High Pressure Behaviour of Pyroxenes

Demelza Alice Hugh-Jones

Department of Geological Sciences,
University College London

Submitted for the Degree of Doctor of Philosophy,
University of London.

August 1995.

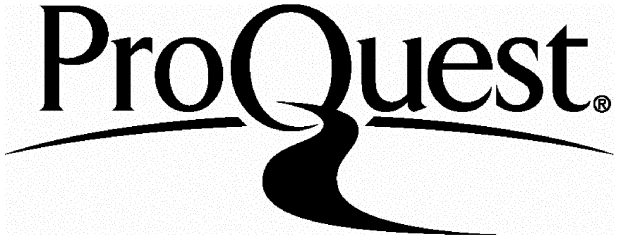

Let the words of my mouth,

and the meditation of my heart,

be always acceptable in thy sight,

O Lord my rock and my redeemer.

Psalm 19:14

ABSTRACT

Pyroxenes make up almost 25% by volume of some mineralogical models of the Earth's upper mantle, with their transformation to the higher density garnet structure at ~ 400 km contributing to the seismic discontinuity at this depth. At depths shallower than this, both orthorhombic and monoclinic structures of $(Mg,Fe)SiO_3$ pyroxenes are stable. In order to try to understand their behaviour at depth, a single crystal X-ray diffraction study has been carried out on both synthetic and natural ortho- and clinopyroxenes along or near the $(Mg,Fe)SiO_3$ join using a diamond anvil cell.

Synthetic $(Mg,Fe)SiO_3$ orthopyroxenes undergo a distinct change in compression mechanism at ~ 4 GPa and ambient temperature, characterised by the onset of shortening of the previously incompressible Si-O bonds, with associated changes in the degrees of kinking and tilting of the silicate chains. This change in compression mechanism causes a discontinuous break in their equation of state (EOS). The addition of impurities such as Ca^{2+} to the orthopyroxene causes the M2 cation sites to become significantly stiffer, thus inhibiting any change in compression mechanism of the natural orthopyroxenes at any pressure, and also any break in their EOS's.

Both low-clinopyroxene (space group $P2_1/c$) and orthopyroxene (Pbca) transform to the higher pressure C2/c clinopyroxene structure at high pressures; both transitions are first order in character involving a ~ 3 % volume discontinuity. However, whilst the low- to high-pressure clinopyroxene transition is displacive, involving a major reconfiguration of the silicate chains, the ortho- to high-pressure clinopyroxene transformation is highly reconstructive, with the newly-formed C2/c phase reverting preferentially to the $P2_1/c$ polymorph upon pressure release. This high-pressure C2/c structure differs from that of the C2/c phase stable at high

temperatures predominantly in the degrees of kinking of their tetrahedral chains. The possibility of a "cross-over" transition between these structurally distinct C2/c phases at extreme conditions is discussed.

Changing the composition of a pyroxene from $MgSiO_3$ to $FeSiO_3$ has very little effect on the topology of the equilibrium phase diagram, although the triple point and phase boundaries are shifted to lower pressures with increasing iron content.

ACKNOWLEDGEMENTS

Firstly and most importantly, this work would never have been completed without the constant support of my supervisor, Dr. Ross Angel, throughout my three years at UCL. I would also like to thank Dr. Nancy Ross for her continued interest in the project, and for keeping me fit with regular squash matches! Within the Crystallography and Mineral Physics Group at UCL, I would also like to acknowledge the help and encouragement of Prof. David Price, Dr. Ian Wood and John Sowerby, and the technical assistance of Pete Woods.

Financially, I acknowledge the receipt of a Research Studentship (grant number GT4/92/223/G) from the Natural Environment Research Council. The experiments performed at the Bayerisches Geoinstitut (in Bayreuth, Germany) were financed by the EC "Human Capital and Mobility - Access to Large Scale Facilities" programme (Contract No. ERBCHGECT940053 to D.C. Rubie).

I would like to thank Dr. Ann Chopelas and Dr. Steve Mackwell for giving me the natural orthopyroxene samples on which to perform high-pressure X-ray diffraction experiments, and Prof. Fritz Siefert and Prof. Dave Rubie for welcoming me to the Bayerisches Geoinstitut in February 1994, August 1994, and March 1995. During these three research visits, I undertook both synthesis experiments (under the watchful eye of Dr. Alan Woodland, now at the University of Heidelberg), and TEM characterisations, for which I am very grateful to Dr. Tom Sharp and Andre Hogrefe for their patience and guidance.

Finally, I must also thank Mum (for her painstaking attempts to understand this research), Dad (for the incentive to publish more papers than he has!), and Tristan, Rupert and Carenza all for their support. Last, but by no means least, I must thank Renny just for being there whenever I need him.

CONTENTS

LIST OF FIGURES

Chapter 1: Introduction

Chapter 2: Experimental Details and Sample Characterisation

Chapter 7: Determination of the (Mg,Fe)SiO_3 Phase Diagram

LIST OF TABLES

Chapter 1: Introduction

Chapter 2: Experimental Details and Sample Characterisation

Chapter 3: Structural Compression of $(Mg,Fe)SiO_3$ Orthopyroxenes

Chapter 6: Crystal Chemistry of High-Pressure C2/c Pyroxenes and their Behaviour at High Pressures

Chapter 7: Determination of the $(Mg,Fe)SiO_3$ Phase Diagram

CHAPTER 1

INTRODUCTION

1.1 EARTH STRUCTURE AND IMPORTANCE OF PYROXENES

The Earth is presently considered to consist of a series of radially symmetric shells separated by sharp seismic discontinuities. Each of these shells is characterised by either a unique chemical composition or distinctive physical properties. Phase transitions between different polymorphs of the constituent minerals present at depth are generally assumed to be responsible for the discontinuities between the shells; laboratory studies of the precise pressures and temperatures of such transitions have enabled tentative identification of the major seismic discontinuities with particular polymorphic phase transformations in the $(Mg,Fe)SiO_3$ and $(Mg,Fe)_2SiO_4$ systems.

From both the PREM model (Dziewonski and Anderson, 1981) and seismological studies at depths below the crust-mantle boundary (ie, depths greater than $\sim$40 km in continental areas), the seismic structure of the upper mantle of the Earth is dominated by a velocity increase at a depth of $\sim$400 km, which is followed by an anomalously high velocity gradient to $\sim$600 km, marking the uppermost limit of the lower mantle (shown schematically in Figure 1.1). The division of the upper mantle and the transition zone is defined by the $\sim$400 km discontinuity, which has been characterised by a $\sim$5% increase in both the shear (V_s) and compressional (V_p) wave velocities, and a density contrast of some 3-4% (eg., Revenaugh and Jordan, 1991). Although the transformation of pyroxenes to higher density garnet structures is likely to contribute to this discontinuity (Gasparik, 1989), experimental equilibrium studies in the $(Mg,Fe)_2SiO_4$ system (eg, Katsura and Ito, 1989) confirm that the olivine to wadsleyite transition also occurs at pressures and temperatures appropriate to this depth, and over a narrow pressure interval.

The boundary between the transition zone and lower mantle (Figure 1.1) is defined by a sharp velocity increase of about 6-8% at $\sim$600 km, and a density contrast of $\sim$6% (Revenaugh and Jordan, 1991; Shearer, 1990), and may in part be identified with the breakdown of spinel and the transformation of garnet to an assemblage

dominated by $(Mg,Fe)SiO_3$ perovskite and magnesiowüstite, (Mg,Fe)O.

The presence of two other smaller velocity increases at depths of ~220 km and ~520 km has recently been confirmed (eg., Hales et al., 1980; Shearer, 1990; Vidale and Benz, 1992; Karato, 1992); the higher pressure wadsleyite to spinel transition (in the $(Mg,Fe)_2SiO_4$ system) may be associated with the ~520km discontinuity (Ringwood, 1975). Because there are no phase transitions in this system at appropriate depths, it is likely that the orthorhombic to monoclinic inversion in $(Mg,Fe)SiO_3$ pyroxenes at high pressures could be related to the Lehmann discontinuity found between ~180km and ~280km depth in subcontinental mantle (eg, Angel et al., 1992a; see also Chapter 5 for details of the transition). Addition of less than about 10% iron to the the mantle alters the phase relations (Herzberg and Gasparik, 1991) in both the $(Mg,Fe)_2SiO_4$ and $(Mg,Fe)SiO_3$ systems by spreading out the univariant phase boundaries of the simple systems into divariant fields in pressure-temperature space. The presence of more than ~10% Fe^{2+} and/or other cations such as Al^{3+}, Ca^{2+}, Na^+, K^+,... may, in addition, stabilise further structural phases.

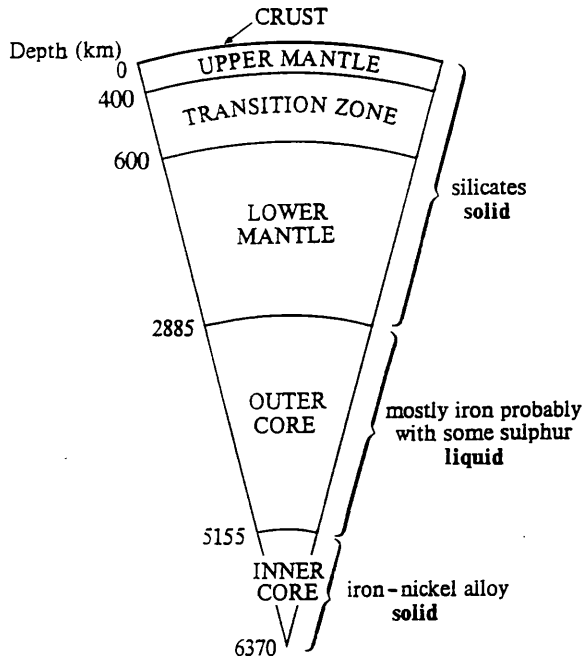

Figure 1.1: A schematic section of the Earth, showing the boundaries between the crust, upper and lower mantle, transition zone and inner and outer core.

Two discrete models are currently accepted as an adequate description of the mineralogy of Earth's mantle (Weidner, 1986) - the "piclogite" model, in which the lower mantle is more silica- (and iron-) rich than the upper mantle, and the "pyrolite" model for which it is assumed that there is no chemical difference between the upper and lower mantle. The mineral assemblages for both models are presented in Table 1.1. Although experiments to determine the phase relations in the MgO-FeO-SiO_2 system (Ito et al., 1984) have shown that the density and bulk modulus constraints imposed by the PREM model are consistent with those expected for an upper mantle of pyrolitic composition, there is insufficient evidence to eliminate the possibility of an upper mantle of piclogitic (or intermediate) composition.

Oxide	Pyrolite	Piclogite
Norm		
MgO	40.3	21.0
FeO	7.9	5.7
CaO	3.0	7.0
SiO_2	45.2	48.9
Al_2O_3	3.5	14.4
Na_2O	0.0	3.0
Mode		
Olivine	61	16
Orthopyroxene	15	3
Clinopyroxene	10	45
Garnet	14	36

Table 1.1. Mineralogy of the upper mantle (after Weidner, 1986)

Pyroxenes are thus major components of the Earth's upper mantle at depths shallower than ~400 km, where assemblages containing two distinct pyroxene phases are stable - a calcium-poor pyroxene with approximate composition $(Mg,Fe)SiO_3$ and a diopside-jadeite solid solution which contains the sodium and calcium components. Although the calcium-rich pyroxene component remains in monoclinic symmetry

throughout the upper mantle, the calcium-poor pyroxenes exhibit both orthorhombic and monoclinic symmetries depending on the external conditions of pressure and temperature. This thesis concentrates on the effect of pressure on the orthorhombic and monoclinic polymorphs of the Ca^{2+}-poor $(Mg,Fe)SiO_3$ pyroxene solid-solution series.

1.2 STRUCTURE AND CLASSIFICATION OF THE $(Mg,Fe)SiO_3$ PYROXENE POLYMORPHS

The structure of all pyroxene polymorphs may be described in terms of alternating layers of "TO_4" tetrahedra and "MO_6" octahedra lying approximately parallel to the (100) plane (Cameron and Papike, 1980). In each tetrahedral layer the TO_4 tetrahedra share two corners (denoted O3 oxygens) with adjacent tetrahedra, forming infinite chains running parallel to the *c*-axis; the repeat unit in each chain consists of two tetrahedra with formula $(TO_3)^{2-}$. In most natural pyroxenes, the dominant tetrahedral cation is Si^{4+}, and the octahedral sites contain six- to eight-coordinated cations such as Mg^{2+}, Fe^{2+}, Ca^{2+}, Al^{3+}, Na^{+}, K^{+}, etc.

There are two distinct M cation sites in the octahedral layer of all pyroxene structures: the M1 site is the smaller of the two (tending to contain smaller cations with ionic radii in the range 0.53 - 0.83Å; Cameron and Papike, 1980) and is in almost regular octahedral coordination, whereas the M2 site may be six-, seven- or eight-coordinate depending on the cation it contains, with the ionic radius of this cation being generally in the range 0.72 - 1.16Å (Cameron and Papike, 1980). The M2 site is highly distorted, containing four relatively short M-O bonds and two considerably longer, with the degree of distortion depending on both the type of cation contained within the site and the conformations of the tetrahedral chains to which it is linked. The M1 and M2 polyhedra share edges to form sheets that lie parallel to the (100) plane. When the M2 site is 8-coordinated, these sheets appear to form a continuous (100) layer, but when the coordination of the M2 site is reduced to 6-fold, the octahedral layer consists of discrete bands or strips of polyhedra parallel to the *c*-axis separated by elongate continuous rifts (Cameron and Papike, 1980).

Within the layers of SiO_4 tetrahedra, the tetrahedral chains may be rotated in two directions from the fully extended position, denoted O- and S-rotations (Thompson, 1970). The differences between these rotations are most clearly defined in terms of ideal structures with fully rotated chains (Figure 1.2), with the O-configuration having a chain extension angle (as measured by the O3-O3-O3 angle) of 120°, and a resulting structure based on a cubic close-packed arrangement of oxygen atoms. This structure requires a tetrahedral to octahedral edge ratio of 1:1. Hexagonal close-packing of these oxygen atoms produces a structure with S-rotated chains whose chain extension angle is 240° by convention (eg., Cameron and Papike, 1980).

In an O-rotated tetrahedral chain, the basal triangular faces of the tetrahedra (ie. those approximately parallel to (100)) have an orientation opposite to that of the triangular faces of the octahedral strip to which they are linked via the apical O1 oxygen atoms (Figure 1.2a). In an S-rotated chain, however, these triangular faces have the same orientation (Figure 1.2b). Both of these situations represent extreme rotations; in real pyroxene structures, the chain extension angle is never less than about 130°, and is usually in the range 160°-175° (Cameron and Papike, 1980). Fully extended chains in an ideal structure have an extension (O3-O3-O3) angle of 180°; this structure is only viable if the tetrahedral to octahedral edge ratio is $\sqrt{3}$:2 (Figure 1.2c).

Note that the tetrahedral to octahedral edge ratio increases with rotation of the silicate chains away from the fully-extended position (in *either* the O- *or* S-direction) in such a way that increased chain rotation leads to relatively smaller octahedral cation sites (Cameron and Papike, 1980). For this last reason, Pannhorst (1979, 1981) chose to distinguish pyroxenes on the basis of the stacking sequence of layers of *nearly-straight* and *kinked* chains.

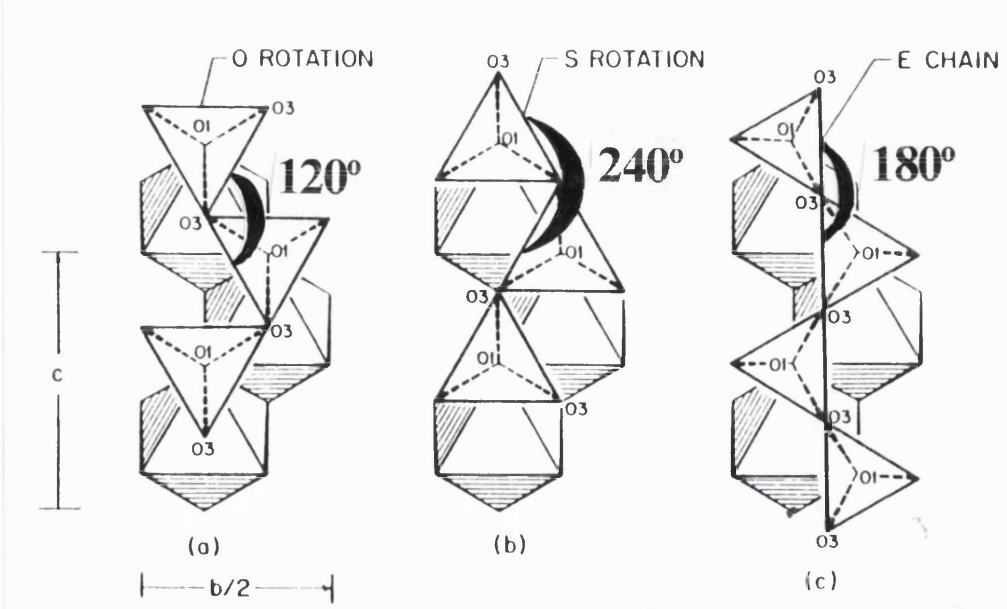

Figure 1.2: Stylised diagram showing the differences between a) O- and b) S-rotations of the tetrahedral silicate chains in ortho- and clinopyroxenes (after Thompson, 1970; Cameron and Papike, 1980); c) Stylised diagram of the pyroxene with fully extended silicate chains.

The "layer classification" proposed by Pannhorst (1979) assumes that both the presence of distinct layers containing either nearly-straight or kinked tetrahedral chains and the linkage between the layers of M1-octahedra and tetrahedral chains, are the two most important factors for the formation of the different pyroxene structures. He considered all silicate chains (both O- and S- rotated) to be "straight" if their chain extension angle (O3-O3-O3) is in the range 150° to 210°; chains which have an O3-O3-O3 angle outside this range were described as "kinked" chains. He further distinguished between layers of kinked chains with O- and S-rotations (ie, those with chain extension angle (O3-O3-O3) of 120° and 240° respectively in the ideal pyroxene

structure; Thompson, 1970) by labelling them K and K' layers respectively. These seemingly arbitrary divisions between the two types of silicate chains actually fall in the gaps observed in the chain angles of real pyroxene structures (few, if any, pyroxene structures exist with O3-O3-O3 angle of 150° or 210°; Cameron and Papike, 1980). The layers of straight tetrahedral chains (with an O3-O3-O3 chain angle of 180°) are denoted S, while M is used to describe an M1 octahedral layer. Positive (+) and negative (-) signs refer to the relative orientations of the octahedral basal faces with respect to the c-axis. This layer classification (Pannhorst, 1979, 1981) appears to reflect the details (eg, temperature dependence and transformation behaviour) of the relationships between the pyroxene polymorphs better than the "I-beam" approach, which was originally developed for wider purposes, such as the classification of biopyriboles (Thompson, 1970).

Schematic "I-beam" diagrams (Papike et al., 1973) have been adapted from Thompson's (1970) ideal I-beam model in order to summarise the topological differences between the principal pyroxene structure types. Within each I-beam unit, two tetrahedral units point inwards and are cross-linked by M1 octahedrally-coordinated cations, forming a highly stylised tetrahedral-octahedral-tetrahedral unit (Figure 1.3). Symbols inside the I-beam units provide information about the symmetry and orientation of the individual coordination polyhedra (Figure 1.4); for example, A's and B's refer to symmetrically distinct tetrahedral chains (when the silicate chains in the structure are non-equivalent) with the rotation of these chains from the fully-extended position being described as either O- or S-rotations (Thompson, 1970).

Following the classifications of Cameron and Papike (1980), the positive (+) and negative (-) symbols within the I-beam units have been used to represent the "skew", "tilt" or direction of stagger of the octahedral layer, with respect to a right-handed set of crystallographic axes. Thus, "+" signs indicate that the apices of the *upper* triangular faces of the octahedra within the strip (ie, those parallel to the (100) plane) point in a $+c$ direction. Note, however, that the upper and lower triangular faces lying approximately parallel to (100) in a single octahedron, are oriented in the opposite sense, while all the faces on one side of the octahedral layer point in the

same direction. Thompson's (1970) parity rule states that "if two tetrahedral strips are rotated in the same sense (ie, both O- or both S-rotated), then the two octahedral strips (one above and one below the tetrahedral layer) to which they are joined across (100) must both have a "tilt" or "skew" in the same sense. If the rotations are in opposite senses, these tilts will be in opposite senses". This parity rule is violated, however, in the real structures of protopyroxene and orthopyroxene, where linkage of the tetrahedral and octahedral layers is achieved by straightening of the "A"-chains relative to the "B"-chains, and by distortion of the cation polyhedra (Cameron and Papike, 1980).

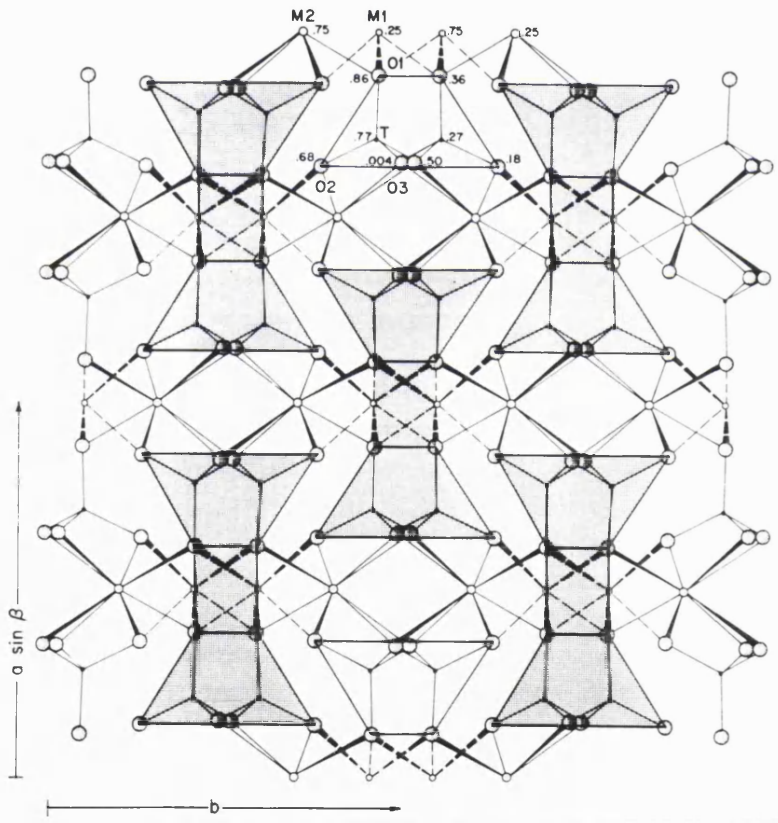

Figure 1.3: The crystal structure of a Ca^{2+}-containing C2/c pyroxene projected down [001]; shaded areas represent the I-beam units (after Cameron and Papike, 1980).

Figures 1.4a and b show schematic I-beam diagrams of $P2_1/c$ and high-temperature C2/c clinopyroxenes projected down [001], identifying the O- and S-rotations (Thompson, 1970) of the tetrahedral silicate chains within the I-beam units. The unit cell parameters, b and $a\sin\beta$, are also clearly shown. Figure 1.4c shows the stylised I-beam structure of the orthopyroxene with space group Pbca, again projected down [001]. In all three cases, the N- and P- rotations (see below; Sueno et al., 1976), and the relative skew (Cameron and Papike, 1980) of the silicate chains are also labelled.

Sueno et al. (1976) chose to characterise the different pyroxene structures by describing the rotations of the tetrahedral chains from the straight position as either *P*- or *N*-rotations, to allow for differences in the lateral arrangement of the tetrahedral chains and octahedral strips. In an N-rotation (Figure 1.5a), the basal triangle of the lateral tetrahedral chains point opposite to the triangles of the octahedra to which they are joined through common O2 atoms, whereas in a P-rotation (Figure 1.5b) they point in the same directions.

Figure 1.5c shows the effect of combining N- and P-rotated chains in the same structure. Combinations of P- and N-rotated chains lead to structures with "N/N", "N/P" and "P/P" geometries, each of which has different size limitations for the M2 site. The P/P configuration (Figure 1.5b) is the most stable since tetrahedra and octahedra do not share edges, and may thus alter their shape and positions independently from each other; P/N and N/N geometries share one and two edges (Figures 1.5c and 1.5a) respectively.

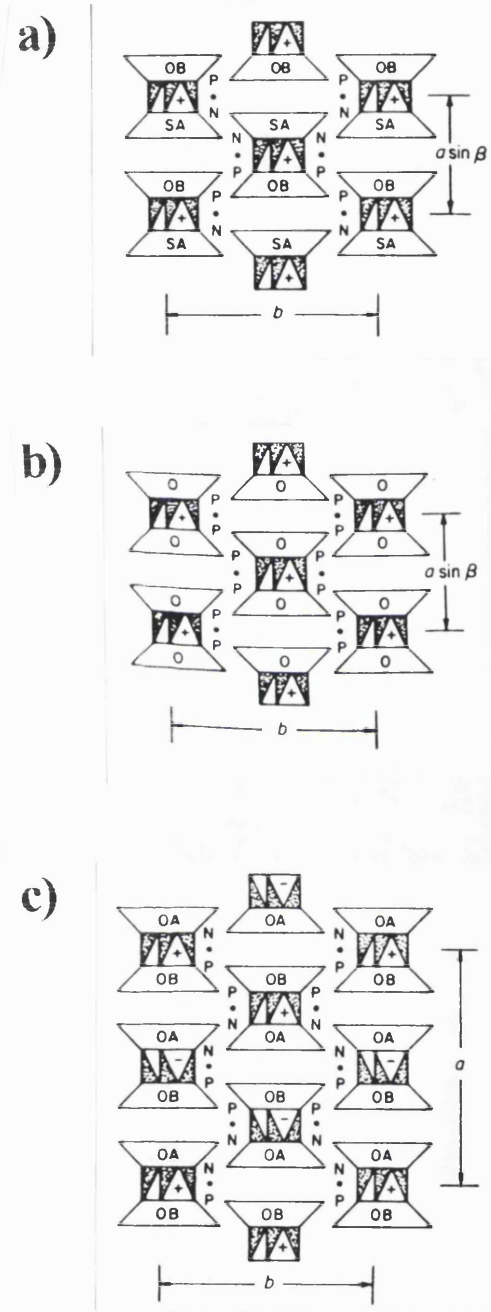

Figure 1.4: Schematic I-beam diagrams of a) $P2_1/c$ clinopyroxene, b) high-temperature C2/c clinopyroxene, and c) Pbca orthopyroxene, showing the O- or S- (and N- or P-) rotations of the silicate chains (after Sueno et al., 1976) and the "A"- and "B" chains where appropriate.

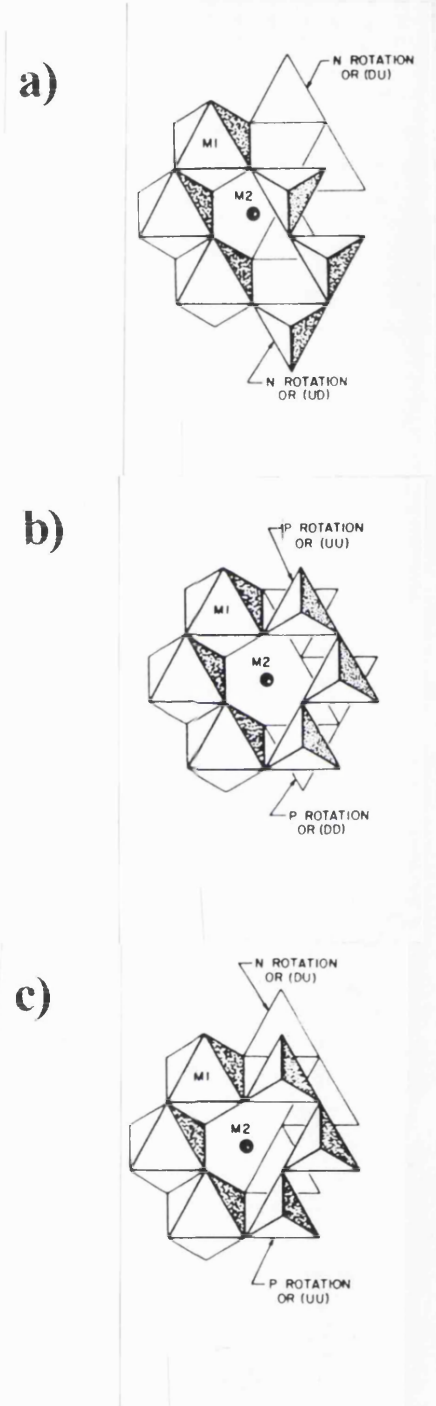

Figure 1.5: Schematic diagram of the configuration of the tetrahedral chains around the M2 site described using a) N/N, b) P/P and c) N/P rotations of the chains (after Sueno et al., 1976). Note that the tetrahedra share a) two edges b) no edges or c) one edge with the M2 octahedron.

The differences between the structurally distinct pyroxene polymorphs of $(Mg,Fe)SiO_3$, are characterised by the differences in both the stacking sequences of their octahedral layers and in the configurations of their silicate chains; the symmetry of all these pyroxene polymorphs is either orthorhombic or monoclinic. Their structures are briefly described below, and are summarised in Table 1.2.

The monoclinic pyroxene structure stable at ambient temperatures and pressures (otherwise known as the "low clinopyroxene" structure) contains two symmetrically distinct tetrahedral chains in adjacent tetrahedral layers; the "A" chain is S-rotated, and is more extended with smaller tetrahedra than the B chain which is O-rotated and considerably kinked (eg., Ohashi, 1984; Burnham, 1966). The edge-sharing of the tetrahedra and M2 site which results from the S-rotation of the "A"-chain makes the M2 octahedral site extremely distorted. In the Cameron and Papike notation (1980), the stacking sequence is (+c/3)(+c/3)..., and under Pannhorst's (1979) description, the stacking sequence of layers of silicate chains and layers of octahedra may be described as *M+SS-M+KK-M*. The space group of low-clinopyroxene is $P2_1/c$.

Orthopyroxene also contains two distinct tetrahedral chains, which are both O-rotated; the more extended chain (as measured by the O3-O3-O3 chain extension angle) with smaller tetrahedra is known as the "A" chain, and the more kinked chain with larger tetrahedra is referred to as the "B" chain (eg., Ohashi, 1984; Burnham, 1966). The stacking sequence of this orthorhombic structure (as described by Cameron and Papike, 1980) is (+c/3)(+c/3)(-c/3)(-c/3)(+c/3)... thus producing zero displacement parallel to *c* for every fourth octahedral layer. Under Pannhorst's (1979) notation, this structure may be described as *M+SS+M-KK+M-SS-M+KK-M*. Although both M1 and M2 sites are octahedrally coordinated, the M2 site is considerably more distorted than the M1 site at ambient pressures. The space group of orthopyroxene is Pbca.

There have been several reports of the existence of an orthopyroxene with space group $P2_1ca$ which has been found in both lunar rocks (eg, Smyth, 1974b) and meteorites (eg, Harlow et al., 1979); recently it has also been identified in terrestrial rocks (Luo et al., 1992). Sasaki et al. (1984) explained the presence of the "forbidden" reflections (ie, those that violate the *b*-glide in Pbca orthopyroxene, causing the change in space group) in the diffraction patterns as occurring as a result of either exsolved C2/c clinopyroxene on (100), diffuse streaking of the ortho- and/or clinopyroxene from neighbouring levels of the (*0kl*) plane, or multiple diffraction effects. These explanations were subsequently discounted by Luo et al. (1992), who observed all the *k*-odd reflections in an (*0kl*) electron diffraction pattern of two orthopyroxene samples, confirming the existence of terrestrial pyroxenes with space group $P2_1ca$, as well as the more common orthopyroxene with space group Pbca.

The high temperature monoclinic structure (or "high-T clinopyroxene") contains a single symmetrically distinct tetrahedral chain, which is O-rotated and considerably extended (eg., Sueno et al., 1984). Adjacent tetrahedral layers are related by a two-fold rotation axis parallel to *b*. This high-temperature phase has a stacking sequence of octahedral layers of (+c/3)(+c/3).., and the sharing of edges between neighbouring tetrahedra and M2 octahedra is now prohibited (Cameron and Papike, 1980). The M2 site in this high temperature structure is 8-coordinate and highly distorted, whilst the cation in the M1 site remains in regular octahedral coordination at all temperatures studied. This structure has stacking sequence *M+SS-M+SS-M*, using Pannhorst's (1979) classification. The space group is C2/c.

The high temperature protopyroxene structure is only stable for pyroxenes containing > 87% Mg^{2+} (Dallwitz et al., 1966). This structure is orthorhombic, containing only one distinct tetrahedral chain which is O-rotated (eg., Smyth, 1971). The M2 polyhedra share two edges with adjacent tetrahedra. Protopyroxene has stacking sequence (+c/3)(-c/3)(+c/3)..., under the Cameron and Papike (1980) notation, *M+SS+M-SS-M* under the Pannhorst (1979) notation, and has space group Pbcn.

The final pyroxene polymorph described here is the high pressure monoclinic structure (or "high-P clinopyroxene"), containing a single distinct O-rotated tetrahedral chain which is highly kinked. Both M1 and M2 cations are in regular octahedrally coordinated sites (eg., Angel et al., 1992a; this work). This high pressure phase has an octahedral stacking sequence of (+c/3)(+c/3).... (after Cameron and Papike, 1980) and under Pannhorst's (1979) description, the stacking sequence of polyhedral layers may be identified as *M+KK-M+KK-M*. The space group is C2/c.

	Orthopyroxene	Protopyroxene
Space Group	Pbca	Pbcn
Number of symmetrically distinct chains	2	1
Chain rotations - Thompson, 1970	A chain: O B chain: O	All O
Pannhorst notation, 1979	M+SS+M-KK+ M-SS-M+KK-M	M+SS+M-SS-M
N-P notation - Sueno et al., 1976	P-N	N-N
M1 coordination	6	6
M2 coordination	6	6
Cameron and Papike notation, 1980	(+c/3)(+c/3)(-c/3) (-c/3)(+c/3)..	(+c/3)(-c/3)(+c/3)
No. edges shared between M2 octahedron and tetrahedron	1	2
Reference: $MgSiO_3$ $FeSiO_3$	Ohashi (1984) Burnham (1966)	Smyth (1971)

Table 1.2. Summary of pyroxene polymorph classification schemes.

	Low-clinopyroxene	High-T cpx	High-P cpx
Space Group	$P2_1/c$	C2/c	C2/c
No. symmetrically distinct chains	2	1	1
Chain rotations - Thompson, 1970	A chain: S B chain: O	All O	All O
Pannhorst notation, 1979	M+SS-M+KK-M	M+SS-M+SS-M	M+KK-M+KK-M
N-P notation - Sueno et al., 1976	P-N	P-P	P-P
M1 coordination	6	6	6
M2 coordination	6	8	6
Cameron and Papike notation, 1980	(+c/3)(+c/3)(+c/3)	(+c/3)(+c/3)(+c/3)	(+c/3)(+c/3)(+c/3)
No. edges shared between M2 octahedron and tetrahedron	1	0	0
Reference: $MgSiO_3$ $FeSiO_3$	Ohashi (1984) Burnham (1966)	- Sueno et al. (1984)	Angel et al. (1992a) This work

Table 1.2: (cont.)

In 1935, Ito proposed that the "rhombic" enstatite polymorph of $MgSiO_3$ was formed from finely twinned monoclinic cells on (100); by 1950, he had developed a theory of structures containing regularly twinned space groups on a submicroscopic scale, to which he assigned the name "polysynthetic structures". He predicted the symmetry of the previously unidentified monoclinic subunit of the twinning to be

$P2_1/c$; this was confirmed by Morimoto (1956) who successfully refined the structure of low-clinoenstatite in this space group. Buseck et al. (1980) further elaborated this idea of polysynthetic structures in order to interpret electron diffraction patterns from various pyroxene polymorphs (see Chapter 2). Ito's theory may also be considered to be a case of "isochemical one-dimensional polytypism" (Smith, 1969a), in which the same structural subunit is stacked differently along one axis, while keeping the same lattice repeats in the plane perpendicular to the axis. Although there is some distortion of the pyroxene structure at the boundaries between the individual subunits, such twinning of the pyroxene on a unit-cell scale may still be considered to be polytypism provided the structure of the actual boundaries remains unchanged (Angel, 1986).

Following the work of Ito (1935, 1950), Ohashi (1984) described several possible twinning relationships between the low-clinoenstatite and orthoenstatite space groups as a result of detailed structure determinations using X-ray diffraction techniques. The twin law that required the least structural adjustments to produce orthopyroxene from low-clinopyroxene twinned on a unit cell scale, was determined to be parallel to the close-packed oxygen layers, so that polytypes could be characterised by differences in stacking of the octahedral and tetrahedral layers. Slight atomic readjustments after twinning were found to be most significant in polyhedra involving bridging oxygens. Lattice strain and structural distortions caused multiple-unit polytypes (eg, orthoenstatite) not to have cell volumes exactly integer multiples of unit-layer polytypes (eg, low-clinoenstatite). Although he drew no analogies, this scheme of characterisation of the enstatite polymorphs closely resembles that of the "layer-classification" developed by Pannhorst (1979, 1981).

Cation substitutions (eg, replacing Mg^{2+} with Fe^{2+} in the enstatite polymorphs) affect both the size of the octahedral layer and its linkage with the tetrahedral chains. Structural adjustments of this type may also involve extension (or kinking) of the chains (measured by changes in the O3-O3-O3 chain angle), distortion of the tetrahedra or a change in "out-of-plane" tilting (ie, the degree of tilt of the bases of the SiO_4 tetrahedra from the (100) plane). Such substitutions also cause changes in the

rate of polyhedral expansion as a result of increasing the temperature, with the M1 and M2 octahedra generally expanding faster than the tetrahedra. For example, Smith et al. (1969) suggested that increasing the iron content of a pyroxene increases all three cell parameters, *a*, *b*, and *c*, whereas increases in the calcium content cause a marked increase in *a* only (see Chapter 4). It will also be seen in Chapter 3 that the structural changes occurring in the orthopyroxene structure with increasing either the temperature or pressure are virtually the opposites to each other; for example, the tetrahedral chains tend to kink (as measured by the O3-O3-O3 chain extension angle) with increasing pressure, while they straighten upon temperature increase.

From a study of pyroxenes of several compositions and of all space groups, Cameron and Papike (1980) determined a series of relationships between the ionic radius of the cation in either or both of the M sites, and other structural parameters such as the internal Si-O bond lengths and chain extension angles. An increase in the average radius of the cations in the M1 and M2 sites generally results in an increase in the average Si-O bond distance. For example, a change in M2 cation radius from that of Mg^{2+} to that of Fe^{2+}, causes the average Si-O bond lengths in the high temperature C2/c structure to increase by about 0.005 Å, and the average M2-O bond lengths by about 0.009 Å; the O3-O3-O3 chain angle is predicted to decrease by up to about 5°. However, in the $P2_1/c$ structure, the average Si-O bond length in both silicate chains is predicted to shorten as the radius of the octahedral cation increases, while the average M2-O bond length should still increase. Both "A"- and "B"-chains are estimated to rotate towards the fully-extended position by approximately 7° as Fe^{2+} replaces Mg^{2+} in the M cation sites. These latter trends are identical to pyroxenes of the orthorhombic (Pbca) structure (Cameron and Papike, 1980), although the amount of rotation of the silicate chains towards the fully-extended configuration due to the above cation substitution is approximately 2° less.

1.3 COMPRESSIBILITY STUDIES OF PYROXENES

In order to understand more clearly the behaviour at depth within the Earth's upper mantle of the $(Mg,Fe)SiO_3$ ortho- and clinopyroxenes, it is important to determine both the responses of the structures of these pyroxenes to non-ambient conditions, as well as their equations of state (ie. the volume variation with pressure and/or temperature). Although these Ca^{2+}-poor pyroxenes transform to higher density garnet structures at depths in excess of 400 km (Gasparik, 1989), there are several polymorphic phase transitions which occur at the lower pressures and temperatures characteristic of the pyroxene stability field (see Chapters 5 and 7), which may be responsible, at least in part, for other seismic discontinuities present at shallower depths. Such transitions include the orthopyroxene to high-pressure clinopyroxene phase transition (which is described for the $FeSiO_3$ system in Chapter 5), which may contribute to the Lehmann discontinuity at depths of $\sim$200km in sub-continental mantle. The high-pressure clinopyroxene phase produced as a result of this transformation is non-quenchable, reverting to the lower symmetry ($P2_1/c$) clinopyroxene phase upon pressure release. Thus all experiments on the high-pressure clinopyroxene phase (and other such non-quenchable phases), and also experiments to determine the effect of pressure on the pyroxene structure, must be performed *in situ*. The diamond-anvil cell (DAC; see Chapter 2 for details) is an ideal tool for investigating such non-quenchable high-pressure phases, since it may be designed to be suitable for X-ray diffraction experiments at pressures of up to $\sim$12 GPa, thus enabling the measurement to a high degree of precision of the structural and volume variations with pressure.

Other experimental techniques regularly used for determining the compressibilities and EOS's of pyroxenes and other minerals include Ultrasonics and Brillouin spectroscopy. The ultrasonic technique involves the measurement of transit times of ultrasonic waves between parallel faces of the crystal (held at a constant temperature and pressure) using a pulse superimposition method. Although ultrasonic measurements have been performed for more than 25 years, Webb and Jackson (1993) have recently determined a reliable method for measuring the travel times of ultrasonic waves through crystals, and their experimental details will be outlined briefly below.

Transducers of a given size are bonded to the single crystals and travel-time measurements are made for waves of the fundamental frequency propagating through the crystals. In order to measure the actual travel-time through the crystal alone, the relative contributions from the propagation and reflection phase shifts may be determined by comparative one- and two-transducer experiments (see Jackson et al., 1981). The elastic moduli of the crystal were then calculated from the twelve modes of propagation using Cook's algorithm for crystals of orthorhombic symmetry (see Webb, 1989).

Brillouin spectroscopy involves the interaction between electromagnetic waves and vibration modes of the crystal due to acoustic phonons. The sample is generally (eg, Bass and Weidner, 1984; Kandelin and Weidner, 1988a, 1988b; etc.) immersed in a fluid of similar refractive index to the sample, in order to reduce both refraction and the intensity of elastically scattered light at the crystal surface. Light from an Ar-ion laser is focused onto the sample, and analysed at 90° to the incident direction, the crystal orientation within the Brillouin spectrometer having been determined to within $\sim 0.5°$ by back-scattering of the laser light from the crystal faces. A small portion of this scattered light is Doppler-shifted due to the interaction with thermally generated phonons in the sample - this is the Brillouin-scattered component of the spectrum. The magnitude of the frequency shift gives the acoustic velocity for each orientation of the crystal. Compressional and shear modes are separated by controlling the polarisation of the incident and scattered light; elastic constants (c_{ij}) may then be calculated from the wave velocities in particular crystallographic directions.

Finally, it is important to note that while X-ray diffraction experiments measure the *isothermal* bulk modulus (K_T), both ultrasonics and Brillouin spectroscopy measure the *adiabatic* bulk modulus (K_S) of the material. This isothermal bulk modulus is determined at constant temperature, whereas the adiabatic bulk modulus is measured at a constant heat content (ie., with no heat exchange with the surroundings), and therefore generally results in an increase in temperature.

The conversion factor between these two bulk moduli is given below:

$$K_S = (1+\alpha\gamma T)\ K_T \qquad (1.1)$$

where α represents the volume thermal expansion coefficient of the material, and γ is its Grüneisen parameter, defined as:

$$\gamma = \frac{\alpha\ K_T}{\rho\ C_V} = \frac{\alpha\ K_S}{\rho C_P} \qquad (1.2)$$

Thus the magnitude of K_T is always somewhat less than that of K_S. Due to inconsistencies in the published data for both α and γ for Ca^{2+}-poor pyroxenes, the difference in magnitude of K_S and K_T is assumed to be of the order of $\sim 1\%$ throughout this work. Table 1.3 illustrates this problem, giving a range of published values of α and γ for Mg^{2+}-rich orthopyroxenes.

Author(s)	α (K^{-1})	γ	$\alpha\gamma T$ (298K)
Frisillo, A.L. and Barsch, G.R. (1972)	47.0×10^{-6}	1.56	0.02
Dietrich, P. and Arndt, J. (1982)	20.8×10^{-6}	0.84	0.005
Skinner, B.J. (1966)	24×10^{-6}		
Saxena, S.K. and Eriksson, (1983)	24.1×10^{-6}		
Saxena, S.K. (1988)	12.7×10^{-6}		
Yang, H. and Ghose, S. (1993)	23×10^{-6}	0.88	0.006

Table 1.3: Comparison of some of the published values of the volume thermal expansion coefficient, α, and the Grüneisen parameter, γ, at 298K for Mg^{2+}-rich orthopyroxenes.

1.4 ORGANISATION OF THE THESIS

This thesis reports the results of a series of compression experiments on Ca^{2+}-poor and Ca^{2+}-free ortho- and clino-pyroxenes along or near the enstatite - ferrosilite join, using high-pressure single-crystal X-ray diffraction techniques. In Chapter 2, details of the methods of synthesis of the pyroxene samples, the design and operation of the diamond anvil cells used to generate pressure on the samples, details of the X-ray diffraction experiments and data reduction are described. Chapter 2 also presents the results of characterisation of all the pyroxene crystals used in this study using Transmission Electron Microscopy. Structural data collected from three synthetic $(Mg,Fe)SiO_3$ orthopyroxene samples and a natural orthopyroxene of approximate mantle composition allow identification of the compression mechanisms operating in these structures at pressure; they are described in detail in Chapter 3. Unit cell data collected from all the orthopyroxene samples at pressure intervals of $\sim$0.4 GPa were used to determine their EOS's which are presented in Chapter 4; the observed values of both the isothermal bulk modulus ($K_{0,T}$) and its pressure derivative, K_0', are also compared with the available published data for orthopyroxenes of similar compositions using different experimental techniques.

Since phase transitions between pyroxene phases of different symmetries are probably responsible, at least in part, for some of the seismic discontinuities within the Earth's upper mantle, experiments demonstrating that both the low-clinoferrosilite (space group $P2_1/c$) and orthoferrosilite phases of $FeSiO_3$ transform to a previously unidentified C2/c phase at high-pressures are presented in Chapter 5. The crystal chemistry of this newly characterised high-pressure C2/c clinoferrosilite is discussed in Chapter 6, and, with the assistance of other data from the available literature, this crystal chemistry is then extended to include all clinopyroxenes along the $(Mg,Fe)SiO_3$ join. The structures of the high-pressure C2/c $(Mg,Fe)SiO_3$ clinopyroxenes are demonstrated to be distinct from those of either high-temperature or Ca^{2+}-containing clinopyroxenes. Chapter 6 finally describes the compressional behaviour of the high-pressure C2/c clinoferrosilite structure and its EOS.

The history of the determination of the pyroxene phase diagrams across the $MgSiO_3$ - $FeSiO_3$ join since 1906 is reviewed in Chapter 7, in which all the compressibility data of these Ca^{2+}-poor pyroxenes is also consolidated into phase diagrams. From these data, and from the slopes of the equilibrium phase boundaries, estimates of ΔS, ΔH, and ΔV of the transformations between the low-clino, ortho- and high-pressure clinopyroxene polymorphs of end-member compositions are calculated. A short summary of the conclusions reached during these experiments is given in Chapter 8 with a few suggestions for future work in the field.

CHAPTER 2

EXPERIMENTAL DETAILS

AND SAMPLE CHARACTERISATION

2.1 SYNTHESIS OF SINGLE PYROXENE CRYSTALS

Although single crystals of some of the pyroxene phases studied in this thesis were available from either public collections (for example, the synthetic $MgSiO_3$ orthoenstatite was acquired from Smithsonian Collection, Washington, U.S.A.) or private collections (eg, the natural orthopyroxenes were donated by Dr. Ann Chopelas (OPX1) and Dr. Steve Mackwell (OPX2)), crystals of the remaining compositions and/or structure-types had to be synthesised using either the piston-cylinder apparatus or the multi-anvil press at the Bayerisches Geoinstitut, Bayreuth, Germany.

Starting materials for all such syntheses were mixtures of fayalite (Fe_2SiO_4), MgO and quartz (SiO_2); the relative quantities of each of these were calculated so as to give the required bulk composition of the product. Approximately 5% by weight BaO - B_2O_3 (78 wt% BaO, 22 wt% B_2O_3) was added to each sample capsule to act as a flux. It was intended that this flux would melt by the target pressure and temperature of the run in order to promote the growth of large single crystals of the pyroxene phase. A slight excess of quartz was also added in all runs to compensate for the dissolution of SiO_2 into the flux. Silver was used as the capsule material to prevent loss of Fe^{2+} to the capsule during the experiment. The sample assembly and experimental details for all ortho- and clinopyroxene synthesis experiments were essentially the same as those reported in Woodland and O'Neill (1993).

The piston cylinder apparatus was used to synthesise orthopyroxenes at pressures below ~5 GPa. Talc-Pyrex pressure cells (diameter 1.905 cm) were used to enclose the sample capsule. The temperature was controlled by means of Pt - $Pt_{90}Rh_{10}$

thermocouples, and the experiments were carried out at 1100°C. Although no correction was made for the effect of pressure on the emf, this uncertainty was estimated to be approximately $\pm$ 20°C. The duration of the experiments at pressure and temperature was in the range 10 - 12 hours. The pressure had previously been calibrated from the position of several well-characterised phase equilibria: a) the olivine - spinel transition in Mg_2GeO_4 (Ross and Navrotsky, 1987), b) the albite + jadeite + quartz equilibrium (Holland, 1980), c) the ferrosilite + fayalite + quartz equilibrium (Bohlen et al., 1980), and d) the pyroxene - garnet transition in $CaGeO_3$ (Ross et al., 1986). Based on the widths of these calibration brackets, uncertainties in the pressure measurements are estimated to be approximately $\pm$ 0.1 GPa.

To obtain pressures in excess of 5.5 GPa, necessary for the synthesis of $FeSiO_3$ clinopyroxene, experiments were conducted in the Sumitomo 1200 multi-anvil press at the Bayerisches Geoinstitut, using Toshiba F grade tungsten carbide cubes with an 11mm truncated edge. The pressure cells were MgO octahedra, measuring 18mm along their edges. The silver sample capsule was heated by a graphite resistance heater with the temperature being monitored using axially inserted Pt - $Pt_{90}Rh_{10}$ thermocouples; again no correction was made for the effect of pressure on the emf. The multi-anvil press had been calibrated using both of the transitions in Bi (I-II, III-IV) at ambient temperature, and the following transitions at 1000°C and 1450°C: a) quartz - coesite (Bohlen and Boettcher, 1982), b) coesite - stishovite (Yagi and Akimoto, 1976), and c) fayalite - γ spinel (Yagi et al., 1987). The accuracy of the pressure measurements, based on the widths of the reversal brackets and repeated checks of these reversals, is estimated to be $\pm$ 0.3 GPa. The duration of the experiments at pressure and temperature were in the range 10.5 - 12.5 hours. After this time, the temperature was quenched to the ambient temperature while the pressure was released slowly over a period of about 10 hours. The synthesis conditions of the $Mg_{0.3}Fe_{0.7}SiO_3$ and $FeSiO_3$ orthopyroxenes and the $FeSiO_3$ clinoferrosilite are given in Table 2.1.

Composition	Phase	Equipment	Pressure	Temperature
$Mg_{0.3}Fe_{0.7}SiO_3$	ortho	Piston Cylinder	3.0 GPa	1100 °C
$FeSiO_3$	ortho	Piston Cylinder	3.0 GPa	1100 °C
$FeSiO_3$	clino	Multi-Anvil	8.0 GPa	1200 °C

Table 2.1: Synthesis conditions for $Mg_{0.3}Fe_{0.7}SiO_3$ and $FeSiO_3$ orthopyroxenes and $FeSiO_3$ clinopyroxene.

2.2 INITIAL CRYSTAL SELECTION

The compositions of several crystals from each sample were analyzed using energy-dispersive X-ray analysis with a Phillips CM20-FEG transmission electron microscope (at the Bayerisches Geoinstitut), which gave the relative proportion of elements in the sample to a precision of about $\pm$ 1% (see also Section 2.5). Crystals of both the orthorhombic and monoclinic phases of the $MgSiO_3$ and $FeSiO_3$ end-members showed no impurities; compositions of all other pyroxenes studied are reported in Table 2.2. Mössbauer experiments on representative samples of the orthoferrosilite and clinoferrosilite crystals (McCammon, personal communication) displayed no peaks due to the presence of Fe^{3+}, implying that the concentration of Fe^{3+} in both samples was less than 0.8 %.

Sample	Average composition	ΔMg^{2+}	ΔFe^{2+}	ΔCa^{2+}	ΔAl^{3+}
$En_{0.6}Fs_{0.4}$	$Mg_{0.59}Fe_{0.41}SiO_3$	1 -3 %	1 - 3 %	-	-
$En_{0.3}Fs_{0.7}$	$Mg_{0.29}Fe_{0.71}SiO_3$	2 -7 %	2 - 7 %	-	-
OPX1	$(Mg_{0.85}Fe_{0.13}Ca_{0.02})(Si_{0.96}Al_{0.04})O_3$	1 -5 %	1 - 2 %	< 0.5%	0.5 - 1%
OPX2	$(Mg_{0.83}Fe_{0.12}Ca_{0.006}Al_{0.04})(Si_{0.97}Al_{0.03})O_3$	1 - 2.5 %	0.5-1.5%	< 0.5%	< 1%

Table 2.2: Compositional variation in natural and synthetic $(Mg,Fe)SiO_3$ samples determined using energy-dispersive X-ray analysis with the TEM. The Δ's represent the percentage variation in the concentrations of the respective cations.

Crystal fragments from all the samples were selected initially according to their dimensions and optical quality; in all cases they measured between about 125 x 80 x 40 μm and 60 x 30 x 20 μm, and were free from obvious twins and optical imperfections. In order to check that they were also of a suitable quality for high pressure X-ray diffraction, preliminary data collections were carried out at ambient pressure and temperature with a conventional glass-fibre mount. The crystal was accepted for high-pressure experiments if the widths of the diffraction profiles were sufficiently narrow (ie, having a width of less than approximately 0.35° in ω-scans), if the estimated standard deviations (*esd*'s) of the unconstrained unit cell parameters were within ~0.01% of their full value, if the unconstrained unit cell angles, α and γ, were within ~0.02° of the expected values of 90° (for both ortho- and clinopyroxenes), and if the intensity data refined easily to a structure with an R-value (denoted R(avg) in Tables 2.3a-e) of less than ~4%; within the experimental uncertainties, the positional parameters of the $MgSiO_3$ and $FeSiO_3$ end-members at ambient conditions had to be equal to the literature values.

Figures 2.1a and b show the relative widths of "narrow" and "broad" X-ray peak profiles respectively, collected from different orthopyroxene samples at ambient conditions using conventional glass fibre mounts. It was not possible to obtain reasonable structure refinements from pyroxenes which exhibited peak profiles much broader than the "broad" one in Figure 2.1b (ie., having peaks with full widths at half maximum height (FWHM) much greater than ~0.35° on ω). For this reason, intensity data was not collected from either the natural orthopyroxene (OPX1) or the synthetic orthopyroxene with approximate composition $Mg_{0.3}Fe_{0.7}SiO_3$. Subsequent microstructural analyses of all the pyroxene phases studied in this thesis using the transmission electron microscope (see Section 2.5) have revealed a possible explanation for this variation in the widths of the X-ray peak profiles between the samples.

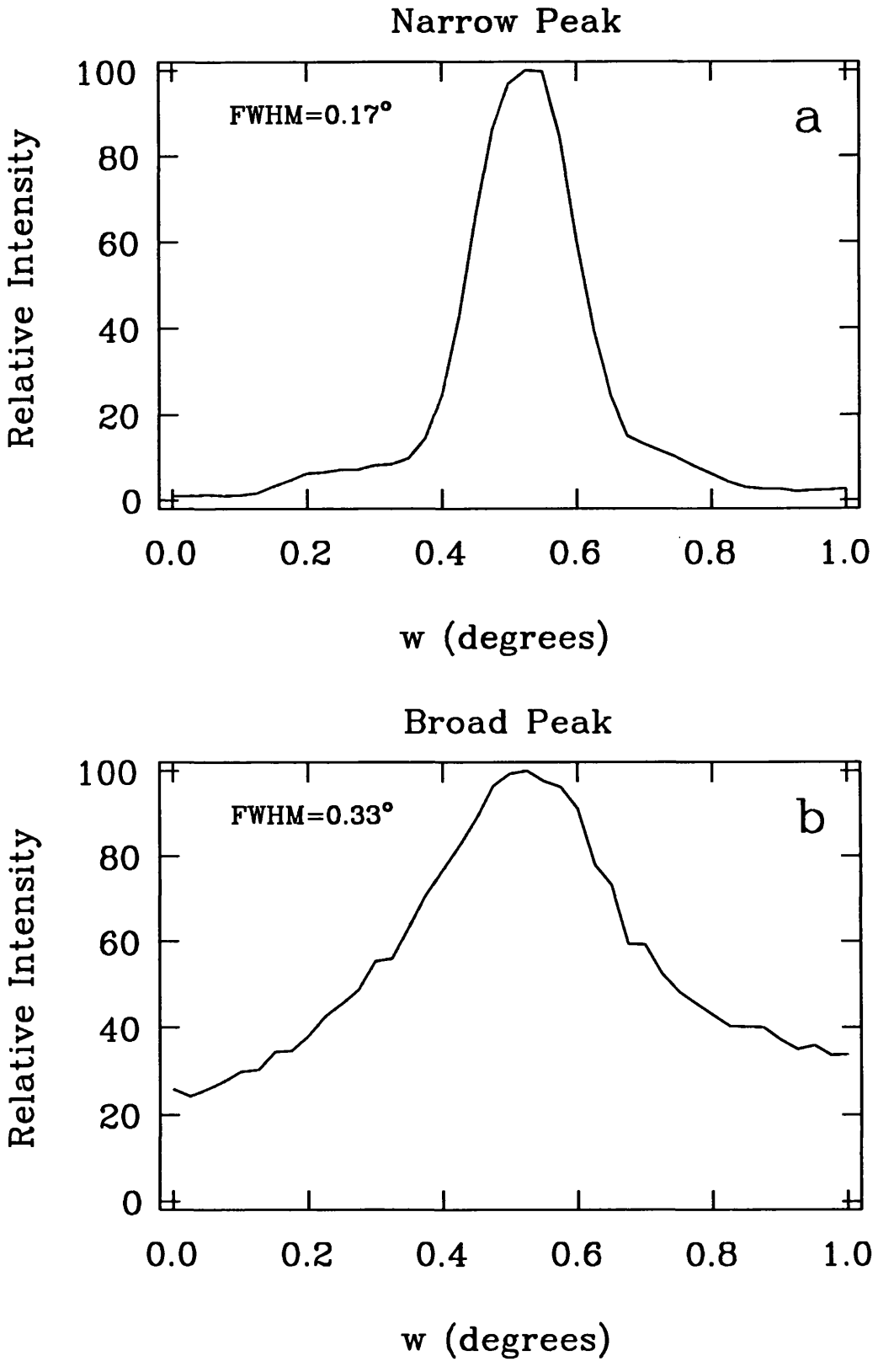

Figure 2.1: Typical a) "narrow" and b) "broad" X-ray diffraction peak profiles collected from the $(Mg,Fe)SiO_3$ orthopyroxenes in air at ~ 16° 2θ. In both cases, the full widths at half maximum (FWHM) are given.

2.3 THE DIAMOND ANVIL CELL

In order to study the effect of pressure on the crystal structure of the pyroxenes using X-ray diffraction techniques, the crystals were mounted in a diamond anvil cell (DAC), which is capable of generating high pressures in a hydrostatic environment whilst also guaranteeing the accessibility of the X-ray beam to the sample. The use of diamonds to transmit pressure to the sample chamber is ideal for two reasons: firstly, they are partly transparent to many ranges of electromagnetic radiation, including X-rays, and secondly because they are the hardest material known. The DAC's used in these experiments were also light enough to be mounted on a goniometer head of an X-ray diffractometer, while being able to generate pressures of up to ~ 12 GPa.

2.3.1 Design and Operation of the DAC

In their simplest form, DAC's consist of two opposed diamond anvils which generate pressure in a sample chamber formed by their culet faces and a metal gasket (Figure 2.2; described in detail in Hazen and Finger, 1982; Angel et al., 1992b). The diamonds are supported on platens, which are driven together by means of a clamping device to produce pressure in the sample chamber; the precise alignment of the diamond anvil faces must be maintained at all times. Since single crystals suitable for high-pressure X-ray experiments must be small enough to remain uncrushed between the diamond anvils, and unshielded from X-rays by the gasket, but large enough to provide sufficient diffracting volume for intensity measurements, the design of the DAC must minimise the absorption of the X-ray beam passing through the cell, and also increase the number of diffracted beams from the sample that can be observed.

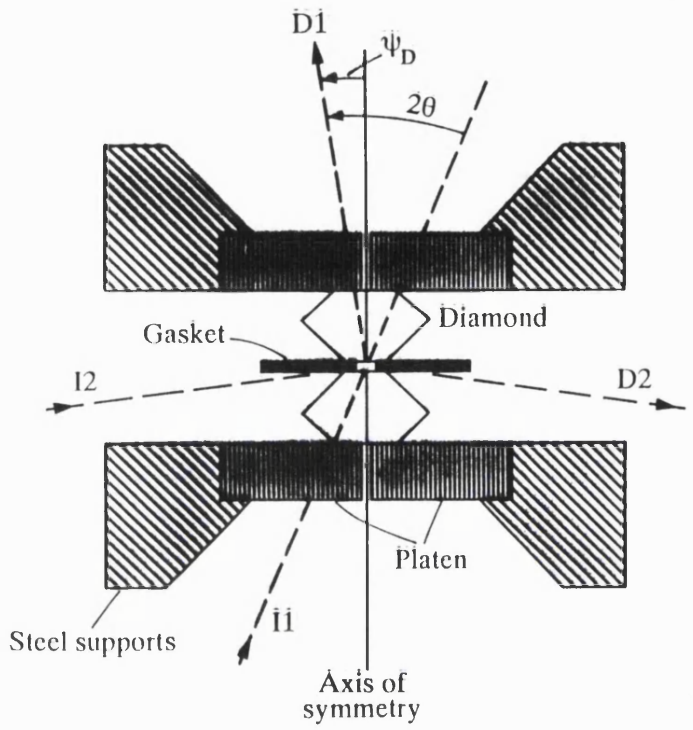

Figure 2.2: Schematic diagram of a diamond anvil cell (DAC) in transmission geometry (after Angel et al., 1992b). The arrows marked I1 and I2 represent the paths of typical incident X-ray beams to the sample in transmission and transverse geometry respectively; the arrows marking paths D1 and D2 represent the corresponding diffracted beams.

In transmission geometry (Figure 2.2), the X-ray beam passes through one platen and diamond anvil before reaching the crystal, and the diffracted beam passes through the other diamond anvil and platen before its detection, making it important that the platen is made of a material that has a low absorption coefficient to X-rays, generally beryllium. This beryllium may be hardened (both by the introduction of a small amount of BeO, and by substantial mechanical work hardening) to reduce indentation by the diamonds when it is held at high pressure, and also reducing the possibility of mechanical failure of the cell. The area of reciprocal space accessible for X-ray examination is then only restricted by the size of the steel supports for these

platens, and the size of pressure-generating mechanism. The maximum angle between the diffracted beam and the straight-through position (known as the "opening angle", ψ) is usually of the order of $\psi \sim 40°$. For DAC's with this geometry, about one third of all reflections may be collected (Merrill and Bassett, 1974); experimental corrections for absorption of both incident and diffracted beams by the platens and diamond anvils can be easily measured (Finger and King, 1978), or calculated.

There are several designs of DAC which make use of this transmission geometry, the simplest of which is the modified Merrill-Bassett type diamond-anvil cell (Figure 2.3; Hazen and Finger, 1982), which is capable of reaching pressures of up to $\sim$7 GPa. The pressure is applied by means of three screws, whilst alignment of the diamond anvils is maintained by three pins passing through both of the steel supports. The diamond culets are generally 750μm in diameter, though smaller culet faces of the diamond anvils allow higher pressures to be reached, in approximately inverse proportion to the culet area.

A recent modification of the Merrill-Bassett DAC is the "DXR4" type diamond anvil cell (Angel et al., 1992b; Figure 2.4). Pressures of up to $\sim$12 GPa may be generated in the DXR4 cell by means of two counter-threaded screws which join the steel backing plates together. Hemispherical beryllium platens ease the calculation of absorption corrections, while a conical access hole in each platen increases the optical access to the sample; these holes are filled with Be plugs during intensity data collections to simplify the calculation of such absorption corrections.

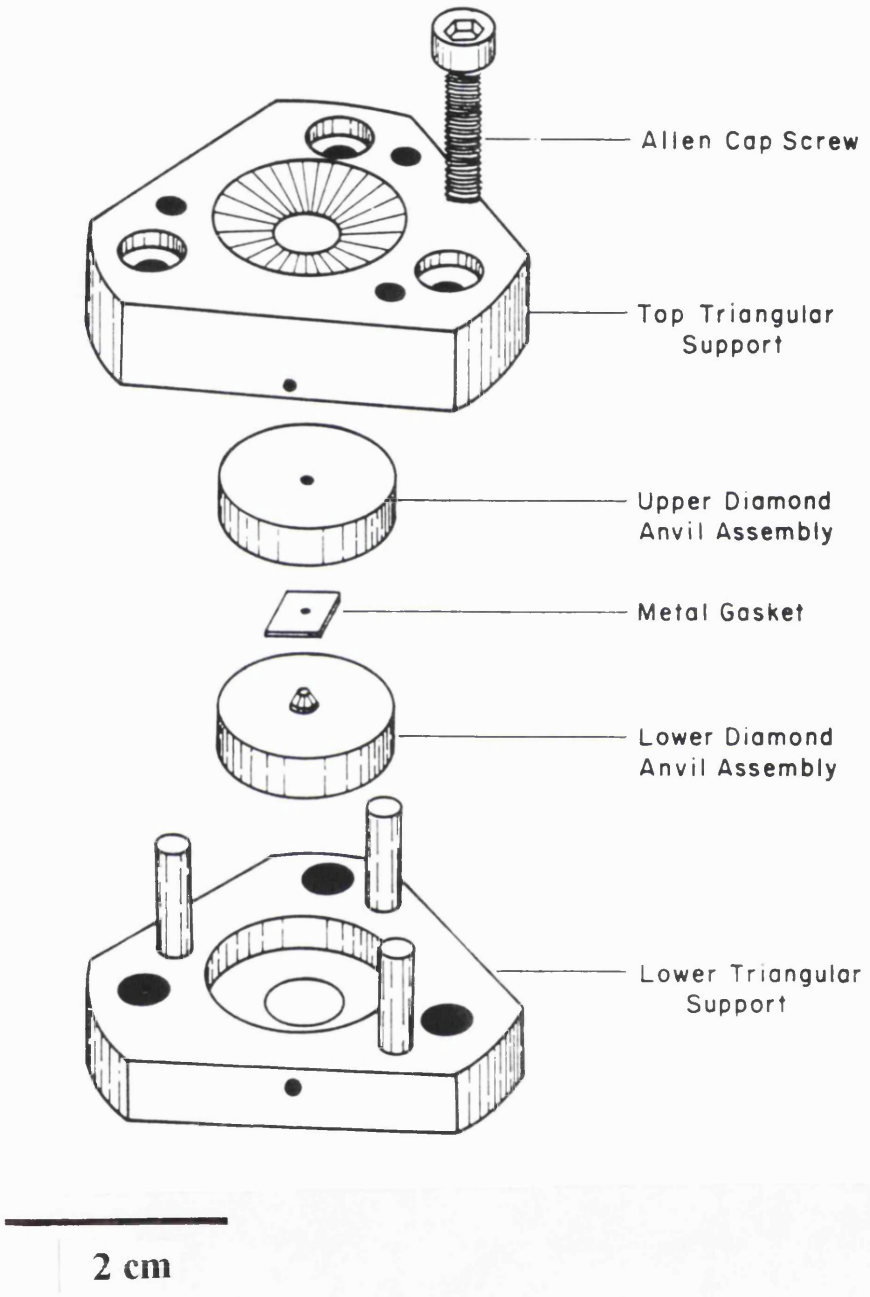

Figure 2.3: Exploded view of a modified Merrill-Bassett DAC (after Hazen and Finger, 1982).

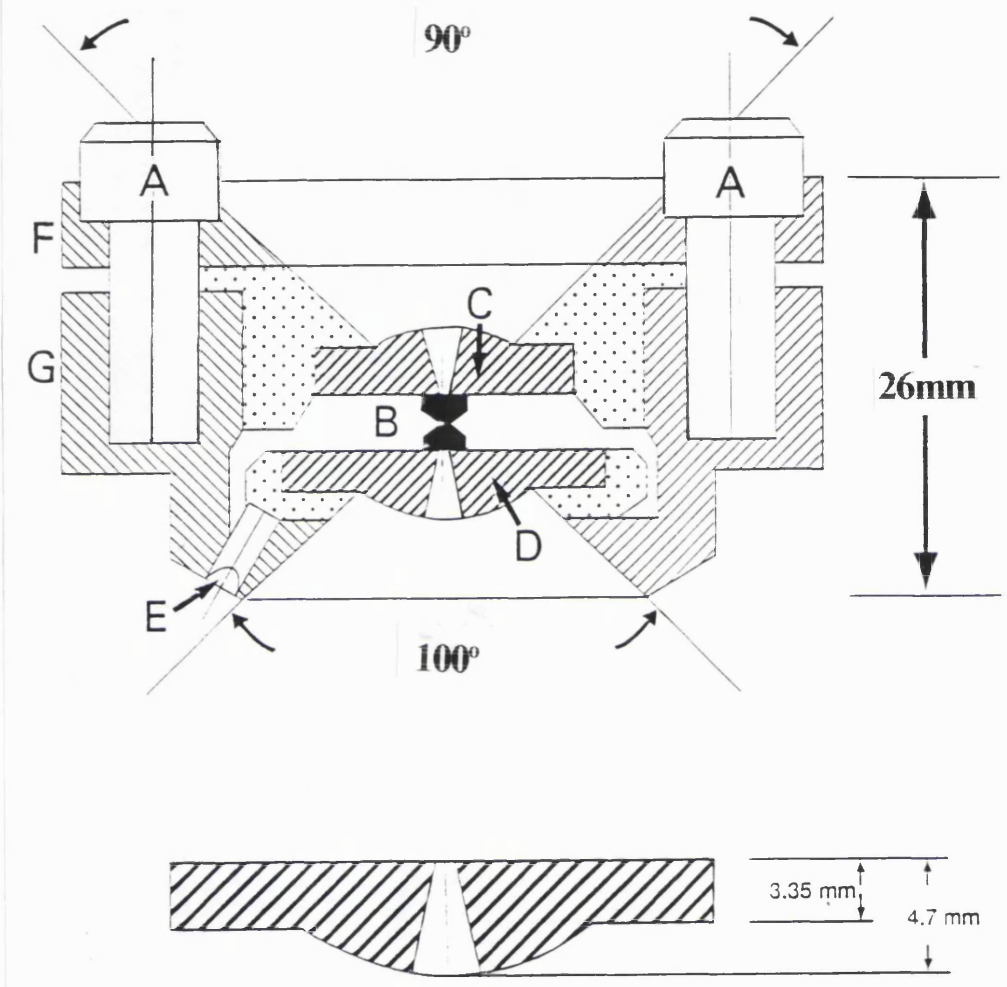

Figure 2.4: Schematic diagram of the DXR4-type DAC, with an enlarged cross-section of the hemisperical beryllium backing plate. A) allen cap screws; B) diamonds; C) upper hemisperical beryllium backing plate; D) lower hemisperical beryllium backing plate; E) lower backing plate adjustment screw; F) upper steel support; G) lower steel support.

Other designs of DAC include the lever-arm cell (Mao and Bell, 1978), the gas-cell (Hazen and Finger, 1982), and a DAC which allows both transmission and transverse geometries to be accessed, as described by Malinowski (1987). However, since the experimental studies in this thesis only employed modified Merrill-Bassett-type and DXR4-type DAC's, detailed descriptions of further designs of DAC may be found in Hazen and Finger (1982), Angel et al. (1992b), Allan (1993) and Hackwell (1994).

For each high-pressure experiment undertaken in this study, the chosen pyroxene single crystal was mounted onto the face of one of the diamond anvils and glued into position with a small amount of the alcohol-insoluble component of petroleum jelly, along with a small ruby chip for pressure determination (see section 2.3.2). A disc of stainless steel or heat-treated inconel 750X foil approximately 250μm thick, containing a central hole of diameter $\sim$200μm, was used to make the gasket which provides the walls of the sample chamber formed between the diamond anvil faces (Figure 2.2). Although higher pressures may be obtained by indentation of the gasket by the diamonds before drilling the hole (Jephcoat et al., 1987), this technique was found to be difficult to perform experimentally. In practice, holes were drilled in the gaskets before they were indented to pressures characteristic of the highest pressures required during the subsequent experiment; the resulting closed-up holes were then re-drilled to a diameter of $\sim$200μm, (ie, considerably less than half the diameter of the diamond culet), and thoroughly cleaned prior to the loading of the crystal in the DAC.

The pressure medium used in all the high-pressure experiments was a 4:1 methanol-ethanol mixture, which remains hydrostatic to pressures up to that of its glass transition at 10.4 GPa (eg., Jayaraman, 1983). However, it is interesting to note that the addition of water to give a 16:3:1 methanol:ethanol:water mixture appears to extend this range to about 14.5 GPa (Jayaraman, 1983).

2.3.2 Pressure Measurement

The pressure acting on the sample chamber was determined by measuring the wavelength shift of the R_1 laser-induced fluorescence from the ruby chip included in the cell, a method first described by Forman et al. (1972). The shift of these ruby fluorescence lines is nearly linear to pressures in excess of 100 GPa (Mao et al., 1986). Since the ruby fluorescence wavelength is extremely sensitive to the external pressure and temperature (a $\sim 5^{\circ}$ increase in temperature may shift the fluorescence wavelength by the equivalent of a 0.1 GPa increase in pressure (Barnett et al.,1973)), the fluorescence wavelength from a reference sample of ruby held at ambient conditions was always measured at the same time as the wavelength emitted from the ruby chip included in the DAC. The measurement of this room pressure spectrum also eliminates the effect of instrumental drift in the monochromator. The instrument used for these pressure measurements was a *Jobin-Yvon* spectrometer, the specifications of which included a 640mm path length, a grating with 1800 lines per mm, and a photomulitplier tube as the detector.

The complete fluorescence spectra of both rubies, including both components of the doublet, were collected, and the wavelength of the R_1 and R_2 lines and their separation were obtained by fitting the spectrum with an empirical modified Lorentzian function, of the form described by Wood et al. (1980). A characteristic plot of the fluorescence doublets at room pressure and ~ 1.5 GPa are shown in Figure 2.5. The presence of non-hydrostatic stresses introduced from the pressure-transmitting fluid cause both broadening of the ruby fluorescence lines (eg, Forman et al., 1972) as well as a change in the R_1-R_2 split (Adams et al., 1976). The wavelength shift of the fluorescence of the ruby in the DAC from that at room pressure was converted to pressures using the calibration of Mao et al. (1986) and the precision (ie, reproducibility) of the pressure measurements is estimated to be better than $\pm$ 0.03 GPa (this work; Angel et al., 1992b). Within a single set of pressure measurements, taken at the same time, the precision is generally better than $\pm$ 0.005 GPa.

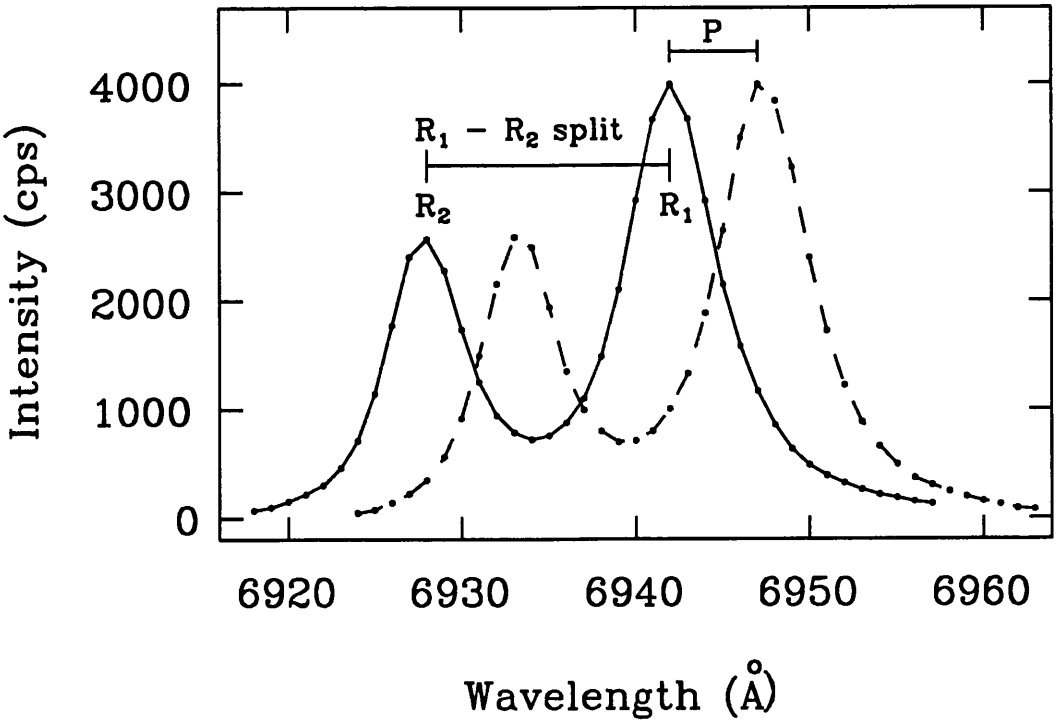

Figure 2.5: Plot of the ruby fluorescence spectrum taken from the ruby held at ambient conditions (solid line) and at ~1.5 GPa (dashed line), indicating the pressure shift (calculated from the wavelength shift of the R_1 peaks; denoted P), and the positions of the R_1 and R_2 peaks and their separation at 1 atm.

2.4 XRAY DIFFRACTION EXPERIMENTS

2.4.1 Experimental Technique

A Picker four-circle diffractometer (Figure 2.6a) equipped with a Mo X-ray tube (with K_α radiation obtained by β-filtering) was used throughout the course of the experiments. (Note that molybdenum K_α radiation is ideal for high-pressure X-ray diffraction since it has a very low absorption by both diamond and beryllium metal). The diffractometer is automated by Krisel electronics, and the control software used, including all peak centring algorithms, was the SINGLE code (authors Finger and Angel). The loaded and pressurised DAC was mounted in the centre of the χ-circle of the diffractometer, using a specially designed goniometer head (Figure 2.6b).

a)

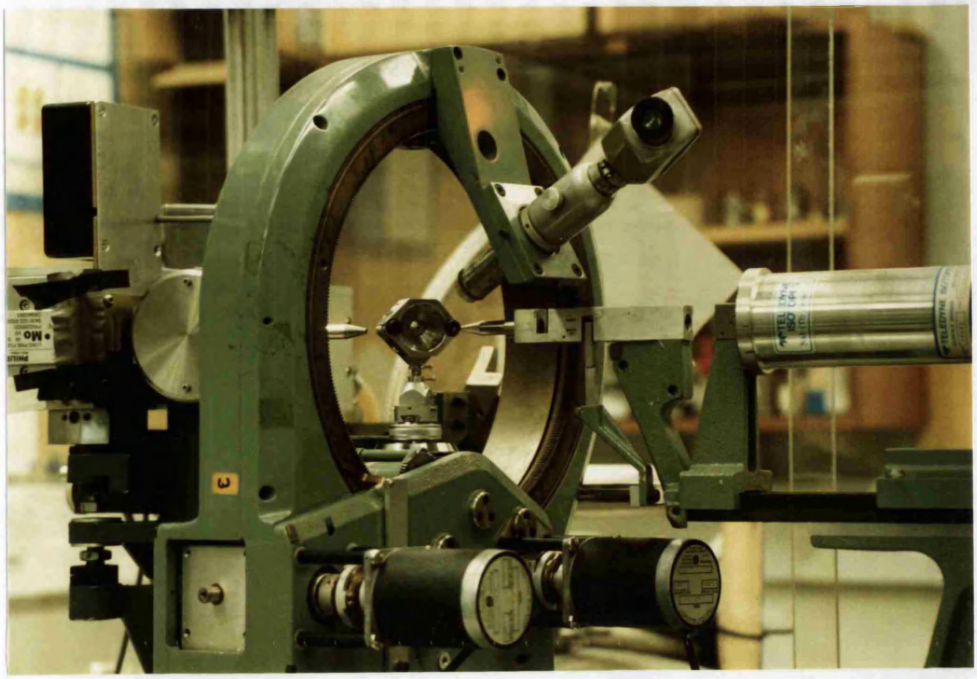

b)

Figure 2.6: a) Photograph of the Picker four-circle diffractometer used for all the X-ray diffraction experiments located inside a radiation enclosure; b) a close-up of the modified goniometer head supporting a DXR4-type DAC.

At each pressure, the positions of between 25 and 32 accessible low-angle reflections in the range $12° < 2\theta < 28°$ were centred by the method of King and Finger (1979). The reflections were centred (ie., their intensities were maximised) by adjusting 2θ, ω, and χ at eight equivalent settings for each reflection. Note that, since DAC's cannot be used in bisecting mode as most of the reflections would be obscured by the body of the cell, ϕ remained fixed at either ϕ or $\phi+180°$ throughout the centring procedure in all cases. This "eight-position centring" procedure ensures that the errors introduced from uncertainties in the diffractometer zeros, offsets due to poor optical centring of the crystal, and misalignment of the diffractometer may be calculated with more accuracy. Unit cell dimensions were determined by a vector least-squares fit (Ralph and Finger, 1982) to the corrected positions of these reflections.

Intensity data were collected from most of the pyroxene samples at pressure intervals of approximately 1 GPa. For each of these data collections, the intensities of *all* accessible reflections to $2\theta = 60°$ in one half of reciprocal space were collected with ω-scans of 1° total width and a step size of 0.025°, in a constant precision mode to obtain $I/\sigma_I > 10$ subject to the restriction of a maximum count time per step of 8s. Room pressure data from each crystal mounted in the DAC containing no fluid was also collected in order to eliminate the possibility of systematic errors in the refined parameters arising from either restricted access to the reflections or uncertainties in the corrections for diamond-anvil cell absorption. Standard reflections were collected every 200 minutes to check for drift of the diffractometer and intensity decrease (for example, due to failure of the X-ray tube). Datasets with significant or systematic variations in these standard reflections were discarded, and the data collection re-started

Since the geometry of the DAC causes restricted access of the reflections, occasionally intensities at only one or two of the four possible symmetrically-equivalent positions could be collected, thereby preventing identification of incorrect diffracted intensities. In some experiments, entire sets of symmetry equivalent reflections were absent, preventing some of the structural parameters (generally along

one particular crystallographic axis) to be determined with sufficient accuracy. In extreme cases, when many of these symmetry-equivalent reflections were absent from the diffraction pattern, it was necessary to unload the DAC and remount the crystal in another orientation on the face of the diamond (ideally $\sim 90^{\circ}$ from the initial orientation) and then to repressurise the cell to a pressure within one estimated standard deviation (*esd*) of the original pressure. This considerably improved the data coverage along the appropriate axis. This technique was successfully employed in the determination of the structure of the high-pressure clinoferrosilite phase at several different pressures (see Chapter 5).

2.4.2 Data Reduction - Structure Refinements

Integrated intensities were obtained from the step-scans using a modified Lehmann-Larsen algorithm (Grant and Gabe, 1978), with the option to reset backgrounds interactively. Since there was a high chance of interference from diffraction profiles from other DAC components, much care was taken to ensure that only the Bragg intensity from the crystal itself was integrated and any diffuse background excluded.

Intensities were then corrected for absorption by the diamonds, Lp effects, shadowing by the gasket, and absorption by the crystal itself (typically, $\mu_l \sim 10\,cm^{-1}$ for the $MgSiO_3$ polymorphs, and $\mu_l \sim 72\,cm^{-1}$ for $FeSiO_3$ polymorphs). The absorption corrections were calculated using the program ABSORB (written by Angel), which is based, in part, on ABSORB (Burnham, 1966a) as modified by Finger and Prince (1975). The reflections were averaged in the Laue Groups mmm for orthopyroxenes, and 2/m for clinopyroxenes. Refinements to structure factors with $F > 6\sigma_F$ were carried out with the RFINE90 program, a development version of the RFINE4 program (Finger and Prince, 1975), with reflections assigned weights of σ^{-2}, where σ was derived from counting and averaging statistics. The averaging criteria and rejection of outliers also followed the recommendations of Blessing (1987). Refinement parameters for all the pyroxene phases studied are given in Tables 2.3 a-e.

These refinement parameters are defined as follows: R(avg) is the internal R-value determined using the *esd*'s calculated for the structure factors, F_C, during averaging of the reflections in Laue Group 2/m. R_u is the unweighted R-value obtained during the final cycle of refinement using the program RFINE90, and is calculated from all the available reflections using the expression:

$$R_u = \frac{\Sigma |F_O - F_C|}{\Sigma |F_O|} \qquad (2.1)$$

R_w represents the weighted R-value obtained during the final cycle of refinement using the program RFINE90; it is calculated from the observed reflections (with $I > 3\sigma_I$) using an expression similar to that shown in Equation 2.1. G_{fit} is a measure of the goodness-of-fit of the observed structure factors, F_O, to the calculated ones, F_C.

P (GPa)	No. refs. before averaging	No. obs. $I > 3\sigma_I$	R (avg)	R_u	R_w	G_{fit}
0.00	1232	681	0.029	0.049	0.047	1.57
1.04†	1235	642	0.036	0.058	0.055	1.44
1.95	1226	657	0.032	0.074	0.066	1.85
3.27	1199	687	0.034	0.056	0.048	1.40
4.09	1268	723	0.031	0.064	0.056	1.69
4.95	1102	605	0.033	0.074	0.069	1.83
5.85†	1187	613	0.043	0.068	0.057	1.70
7.00†	1121	668	0.045	0.056	0.060	1.32
8.10†	1142	672	0.046	0.069	0.074	1.64

Table 2.3a: Refinement parameters for synthetic $MgSiO_3$ orthoenstatite. Entries marked with a cross (†) represent the data collections carried out in a DXR4-type DAC; unmarked entries were performed on the same crystal contained in a Merrill-Bassett type DAC.

P (GPa)	No. refs. before averaging	No. obs. $I > 3\sigma_I$	R (avg)	R_u	R_w	G_{fit}
0.00	1262	625	0.032	0.047	0.042	1.25
1.54	1249	628	0.036	0.047	0.043	1.40
2.50†	1227	755	0.030	0.043	0.039	1.31
3.17	1121	627	0.032	0.052	0.046	1.39
4.14	1105	632	0.041	0.066	0.055	1.49
4.76	1127	661	0.042	0.075	0.068	1.53
5.77†	1093	728	0.028	0.045	0.039	1.30
6.59†	1201	737	0.034	0.050	0.045	1.37
7.50†	1189	712	0.032	0.051	0.045	1.48

Table 2.3b: Refinement parameters for $Mg_{0.6}Fe_{0.4}SiO_3$ orthopyroxene Note that the unmarked entries in the above table were collected from crystal #1 mounted in a Merrill-Bassett DAC, and data collections at pressures marked with a cross (†) were obtained from a second crystal, #2, mounted in a DXR4 cell.

P (GPa)	No. refs. before averaging	No. obs. $I > 3\sigma_I$	R (avg)	R_u	R_w	G_{fit}
0.00	2254	1604	0.024	0.024	0.024	1.16
0.83	1313	730	0.028	0.044	0.040	1.50
1.71	1192	703	0.028	0.050	0.041	1.45
2.84	1270	684	0.028	0.057	0.047	1.62
3.65	1268	653	0.036	0.052	0.051	1.35

Table 2.3c: Refinement parameters for $FeSiO_3$ orthoferrosilite. Note that all data collections for the $FeSiO_3$ orthoferrosilite were carried out on the same crystal in a DXR4-type diamond anvil cell.

P (GPa)	No. refs. before averaging	No. obs. $I > 3\sigma_I$	R (avg)	R_u	R_w	G_{fit}
0.00	1201	651	0.039	0.056	0.052	1.42
1.04	1185	619	0.038	0.059	0.054	1.35
1.90	1179	614	0.038	0.073	0.064	1.65
3.00	1138	594	0.039	0.063	0.052	1.55
4.03	1134	598	0.038	0.070	0.059	1.72
4.93	1143	589	0.043	0.063	0.050	1.42
6.01	1001	539	0.042	0.074	0.071	1.60

Table 2.3d: Refinement parameters for natural orthopyroxene OPX2. All these data collections were carried out on the same natural orthopyroxene crystal contained in a DXR4-type diamond anvil cell.

P (GPa)	No. refs. before averaging	No. obs. $I > 3\sigma_I$	R (avg)	R_u	R_w	G_{fit}
1.87	570	344	0.038			
1.87*	348	199	0.036	0.055	0.047	1.27
2.83	582	354	0.042			
2.83*	348	186	0.055	0.100	0.093	1.92
3.49†	620	395	0.052	0.115	0.108	1.99
4.28*	646	339	0.041	0.100	0.096	1.95
4.94†	612	393	0.048	0.090	0.083	1.79
6.51†	608	412	0.051	0.103	0.098	1.79

Table 2.3e: Refinement parameters for high-pressure C2/c $FeSiO_3$ clinoferrosilite. Unmarked entries were collected from crystal #1, in its original orientation in a Merrill-Bassett type DAC; those marked with a star (*) were collected in the same DAC from the same crystal in a new orientation of $\sim 90°$ from the old one; entries marked with a cross (†) were collected from a second crystal, #2, in a DXR4-type DAC.

2.5 SAMPLE CHARACTERISATION BY TRANSMISSION ELECTRON MICROSCOPY

2.5.1 Introduction

Transmission Electron Microscopy is an ideal way to characterise the microstructural details of a pyroxene sample. Since electrons have a considerably shorter wavelength than X-rays (0.037Å for 100keV electrons compared with 0.7093Å for MoK_{α} X-rays), many more diffracted beams may be observed simultaneously resulting in a large section of the reciprocal lattice being analysed. Since the resolution of the image is defined by the wavelength of the incident radiation, the small wavelength of the electrons allows imaging of Ångström-scale detail of the sample. As electrons also interact strongly with crystals, diffraction patterns recording both space group and microstructural information may be photographed in merely a few seconds. The most useful crystallographic orientation for characterisation of pyroxenes is the projection down the *b*-axis onto the *a*-*c* plane, which allows the imaging of both stacking disorder and twinning. In most transmission electron microscopes (TEM's), the sample crystal may be tilted by between 10° and 60° on two different tilt axes in order to obtain the required crystallographic orientation.

Diffraction contrast, obtained by forming the image using different individual reflections in the diffraction pattern, is very useful for examining the microstructure of the crystal on a local scale. There are two different diffracting conditions possible for obtaining this type of image: the first, known as bright-field (*BF*) imaging, forms the image with only the direct electron beam passing through the objective aperture, while dark-field (*DF*) imaging requires that the direct or straight-through electron beam is excluded, and only a diffracted beam is used for image formation; details of the two methods may be found in eg., Putnis, 1992 and Buseck et al., 1980. Dark-field imaging is particularly useful for imaging parts of a crystal that have slightly different structures or orientations relative to the rest of the crystal, such as twins or antiphase domains (see Chapter 5). By tilting the crystal in the correct manner, it is thus possible to identify specific diffracted beams with individual microstructural features.

In order to fully understand the microstructures observed in the samples, it is convenient to describe the structures of the pyroxene polymorphs in a slightly different way to that outlined in Chapter 1. The orthopyroxene structure may be considered to be made up of clinopyroxene unit cells twinned on a unit-cell scale (eg, Ito, 1935, 1950; Section 1.2). These monoclinic cells may be defined by blocks ~ 4.5Å wide in the a^* direction, with the boundaries parallel to (100) passing through the tetrahedral chains common to all the pyroxene polymorphs (Figure 2.7a and b). These blocks may be in two different orientations denoted + and - , with the + and - directions being related by a *b*-glide on (100). In low-clinopyroxene all the blocks have the same orientation, denoted +++... or ---..., depending on their orientation relative to the unit cell axes (Buseck et al., 1980). The low-clinopyroxene unit cell consists of two of the monoclinic blocks, since they are not equivalent by translation, resulting in cell dimension a ~ 9 Å (Figure 2.7a). Orthopyroxenes consist of blocks in the stacking sequence ++--++--..., with a ~ 18 Å (Figure 2.7b).

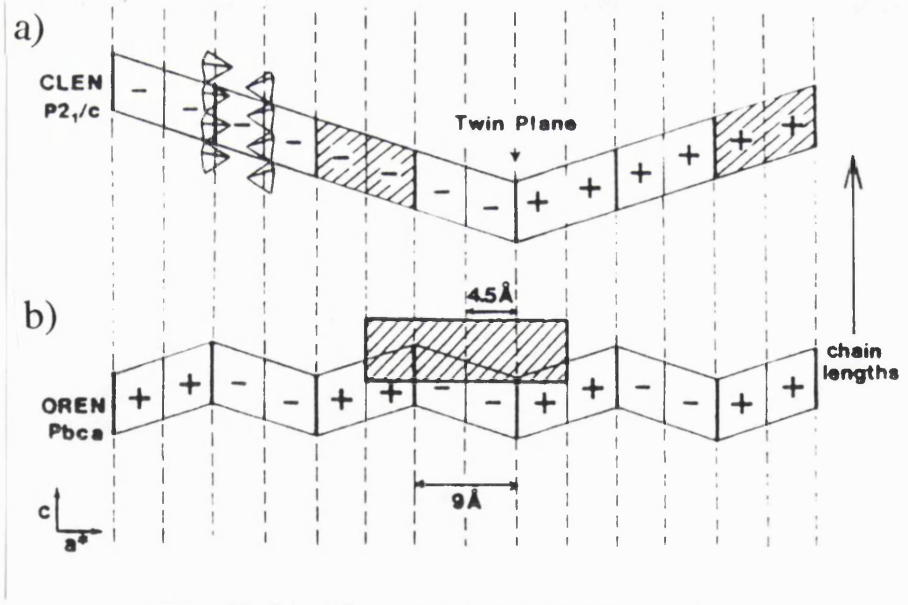

Figure 2.7: Schematic diagram of the structures of a) low-clinoenstatite and b) orthoenstatite projected along [010], after Buseck et al., 1980. The + and - orientations of the blocks reflect the relative displacements of adjacent chains; the conventional unit cell in each case is shaded.

Low-clinopyroxene and orthopyroxene are therefore both constructed from the same monoclinic building blocks; mistakes in the overall stacking sequences of the monoclinic units may cause twinning or stacking faults, which may be observed as streaking along the a^* direction in the diffraction pattern of the pyroxene (Buseck et al., 1980). Although large scale twin intergrowths would not cause streaking in the diffraction patterns, the streaking in the a^* direction (see Figures 2.9b - 2.15b) is due to interlayering of smaller units of ortho- and clinopyroxene.

Although it is not possible to directly image the high-pressure C2/c clinopyroxene phase (since it quenches to the lower symmetry $P2_1/c$ phase upon pressure release; see Chapter 5), there is much information about this phase preserved in the microstructure of the low-clinopyroxene. The presence of antiphase domains within the $P2_1/c$ clinopyroxene suggest that a transformation from the higher-symmetry C2/c phase to the lower symmetry $P2_1/c$ phase has occurred (as first suggested for the C2/c to $P2_1/c$ transition which occurs on cooling in pigeonitic pyroxenes; Morimoto and Tokonami, 1969a); however such antiphase domains can also arise from growth mistakes of the pyroxene, depending on the morphology of the particular crystal. During the C2/c $\rightarrow P2_1/c$ transition, ordering of the previously symmetry-equivalent silicate chains into "A" and "B" chains occurs simultaneously in many parts of the crystal, forming numerous primitive domains. These domains will be either in registry, or out of registry by $1/2(a+b)$, (Morimoto and Tokonami, 1969a). This vector of $1/2(a+b)$ corresponds to the C-centring translational symmetry that is lost as a result of the transition.

Antiphase domain structures have also been observed for omphacites (Champness, 1973; Phakey and Ghose, 1973) in which cation ordering may cause reversion from the space group C2/c to P2/n, either on a local scale causing relatively small domains, or a more widespread one. However, the formation of such antiphase domains in omphacite by cation ordering is due to the differentiation of the M1 and M2 sites into M1a, M1b, M2a and M2b sites respectively, rather than a change in conformation of the silicate chains. Such a symmetry-breaking transformation is therefore not really analogous to the displacive C2/c $\rightarrow P2_1/c$ transition which occurs in these $(Mg,Fe)SiO_3$ clinopyroxene phases during pressure release (see Chapter 5).

Due to the increased symmetry of the high-pressure clinopyroxene phase caused by its *C*-face centring, the associated $h+k=odd$ reflections are not observed in its diffraction pattern. However, since there are no systematic absences caused by the primitive cell of the low-clinopyroxene (although there are absences due to both the 2_1 screw axis and the *c*-glide), information about the C2/c $\rightarrow$P2_1/c transition (and also mistakes occurring during the formation of antiphase domains) will be contained in these $h+k=odd$ reflections, which are absent from the diffraction pattern of the C2/c pyroxene. Antiphase domains are thus imaged in the TEM using the $h+k=odd$ reflections (eg, Putnis, 1992). Dark-field images obtained using the $h+k=even$ reflections of the low-clinopyroxene diffraction pattern ought to show no contrast due to the antiphase structure, since these reflections are present in both the P2_1/c and C2/c diffraction patterns. Antiphase domains produced as a result of pressure decrease at ambient temperature are generally very small (eg, Carpenter, 1979); overlap of the antiphase boundaries generally tend to form an image in which the domains themselves are difficult to identify. If the crystal grain is also thicker than the domain size, this overlapping effect will become more pronounced.

2.5.2 Sample Preparation and Experimental Details

Since nearly all the single crystals studied by X-ray diffraction were chosen from sample capsules containing small pyroxene crystals embedded in a matrix of the BaO - B_2O_3 flux (see section 2.1), the pyroxene crystals used for characterisation in the TEM initially had to be separated from the flux by hand, and washed thoroughly in ethanol. Once the selected crystals had dried, they were transferred to a clean glass slide and placed close together in its centre. An identical clean glass slide was then lowered onto these crystals; the two glass slides were then squeezed gently together until the pyroxene crystals had been crushed to a fine powder. A small drop of ethanol was placed on a standard holey-carbon TEM grid, and this grid was lowered into the pile of pyroxene powder. Once a suitable amount of the crushed pyroxene was absorbed up into the grid, the grid was left to dry naturally in air for at least 24 hours before observation in the TEM.

The TEM used in all characterisations of the pyroxenes was the Phillips CM20 FEG electron microscope at the Bayerisches Geoinstitut, Bayreuth, Germany. Since it also had the facility for energy dispersive X-ray analysis of the samples suspended on the holey carbon grids, the compositions of some the grains of each of the pyroxenes were also measured, giving estimates of the composition of the crystals with a precision of approximately $\pm$ 1% (Table 2.2) and a measure of the degree of local chemical inhomogeneity of the sample. A typical spectrum obtained for such compositional analysis is given in Figure 2.8. Approximately ten grains of each of the pyroxene samples were photographed to give an estimation of the stacking fault densities, and a similar number of grains used to determine the amount of local chemical hetergeneity within each sample.

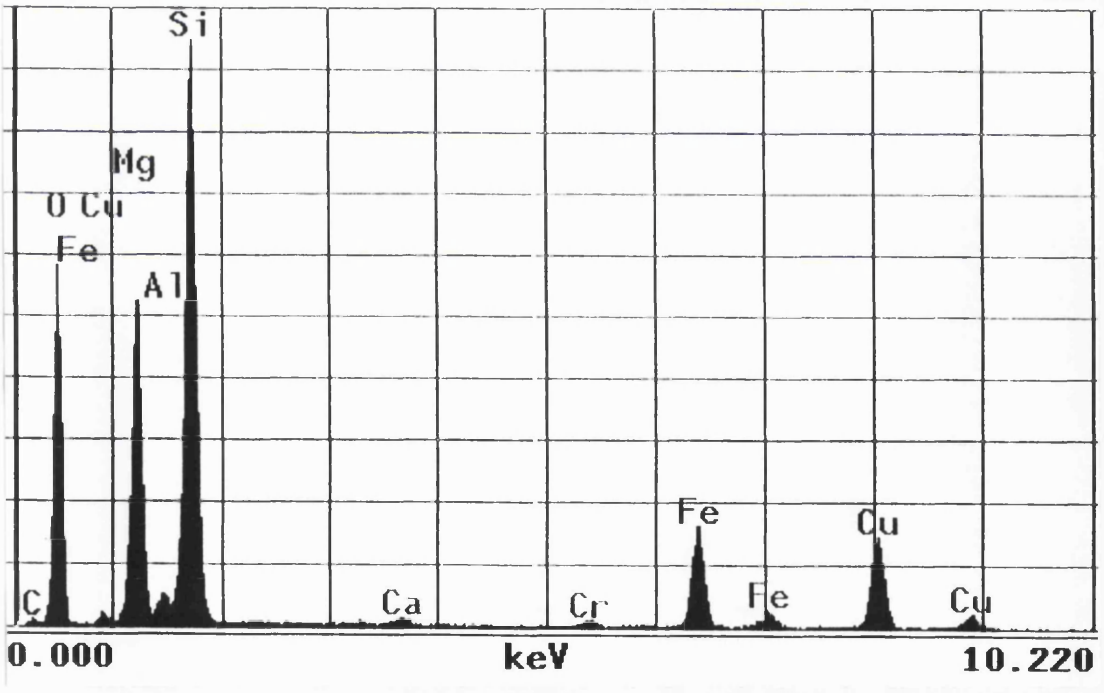

Figure 2.8: Typical spectrum taken using the TEM to determine the relative proportions of the atomic species present. In this case, the spectrum is from the OPX2 natural orthopyroxene, showing peaks from the sample at the energies characteristic of Mg^{2+}, Fe^{2+}, Ca^{2+}, Al^{3+}, Si^{4+}, and O^{2-}. Further Cu^{2+} and C peaks obtained from the TEM grid (on which the sample was suspended) are also observed.

2.5.3 RESULTS

The crushed-grain samples of all the ortho- and clinopyroxenes were examined at both low and high magnifications, and were characterised according to their relative densities of stacking faults and overall microstructures. It is important to note here that the method of preparation of the samples sometimes induced a small amount of deformation of the crystal grains, which led to further contrast being observed in some of the images. Although thickness fringes observed in some specimens (ie. bands of alternating brightness and darkness parallel to the edges of the grains) do not necessarily derive from such grain deformation, Moiré effects (due to the relative mis-orientation of layers of the grains perpendicular to the observation direction) and asterism (ie., slight curvings of the diffraction spots due to small rotations of sub-domains relative to their neighbours, especially noticable in the reflections furthest from the 000 reflection along a^*,) were seen in some samples. The microstructures for each of the samples used as starting materials for the high-pressure experiments are briefly described below; the variations in stacking fault densities are summarised in Table 2.4.

Sample composition	Symmetry	Fault density (faults per μm)
$MgSiO_3$	Pbca	30 ± 20
$Mg_{0.6}Fe_{0.4}SiO_3$	Pbca	20 ± 10
$Mg_{0.3}Fe_{0.7}SiO_3$	Pbca	70 ± 20
$FeSiO_3$	Pbca	30 ± 10
OPX1 $(Mg_{0.85}Fe_{0.13}Ca_{0.02})(Si_{0.96}Al_{0.04})O_3$	Pbca	25 ± 10
OPX2 $(Mg_{0.83}Fe_{0.12}Ca_{0.006}Al_{0.04})(Si_{0.97}Al_{0.03})O_3$	Pbca	15 ± 15
$FeSiO_3$ (starting material)	$P2_1/c$	60 ± 20
$FeSiO_3$ (transformed; see Chapter 5)	$P2_1/c$	70 ± 10

Table 2.4: Variation in stacking fault densities of all ortho- and clinopyroxene samples used in high-pressure experiments.

a) Synthetic $MgSiO_3$ orthoenstatite

The orthoenstatite sample had a moderate degree of stacking disorder (of the order of $\sim 30 \pm 20$ faults per μm). Figure 2.9 clearly shows these stacking faults, imaged along [010]. From closer examination of the area of the grain shown in the figure, it is possible to see the ~ 9Å spacing of the lattice fringes within each of the faults, which corresponds to small regions of the clinoenstatite structure within the orthoenstatite matrix.

b) Synthetic $Mg_{0.6}Fe_{0.4}SiO_3$ Orthopyroxene

This orthopyroxene sample also displayed a moderate density of stacking faults along the [100] direction of the crystal (approximately 20 ± 10 faults per μm). Larger intergrowths of ortho- and low-clinopyroxene were also observed in a few of the crushed grains studied causing the a^* direction in the diffraction patterns of the a^*-c^* plane to become somewhat streaked. A typical TEM photograph of this intermediate orthopyroxene showing some stacking disorder is shown in Figure 2.10a, with its corresponding diffraction pattern (Figure 2.10b). From close examination of Figure 2.10a it is also possible to observe the characteristic 18Å repeat of the orthopyroxene between the stacking faults; high resolution TEM studies of the grain clearly showed that the stacking faults were indeed small bands of clinopyroxene. Energy-dispersive X-ray analysis of this intermediate orthopyroxene has shown that the chemical heterogeneity of the sample on a scale of < 1 μm is of the order of $\pm$ 2% (Table 2.2). Since the analysis has a precision of approximately $\pm$ 1%, this represents a fairly homogeneous sample composition.

c) Synthetic $Mg_{0.3}Fe_{0.7}SiO_3$ Orthopyroxene

This iron-rich orthopyroxene exhibited a high degree of stacking disorder, with about 70 ± 20 faults per μm along [100]. Figures 2.11a and b show a typical crystal grain with its corresponding diffraction pattern. Energy dispersive X-ray analysis with the TEM revealed that this sample was also chemically inhomogeneous (Table 2.2), giving a maximum of 5% difference in the Mg^{2+} and Fe^{2+} content of the grains on a local scale of < 1 μm. This gives an estimate for the bulk composition of the orthopyroxene as $Mg_{0.24-0.34}Fe_{0.66-0.76}SiO_3$.

a)

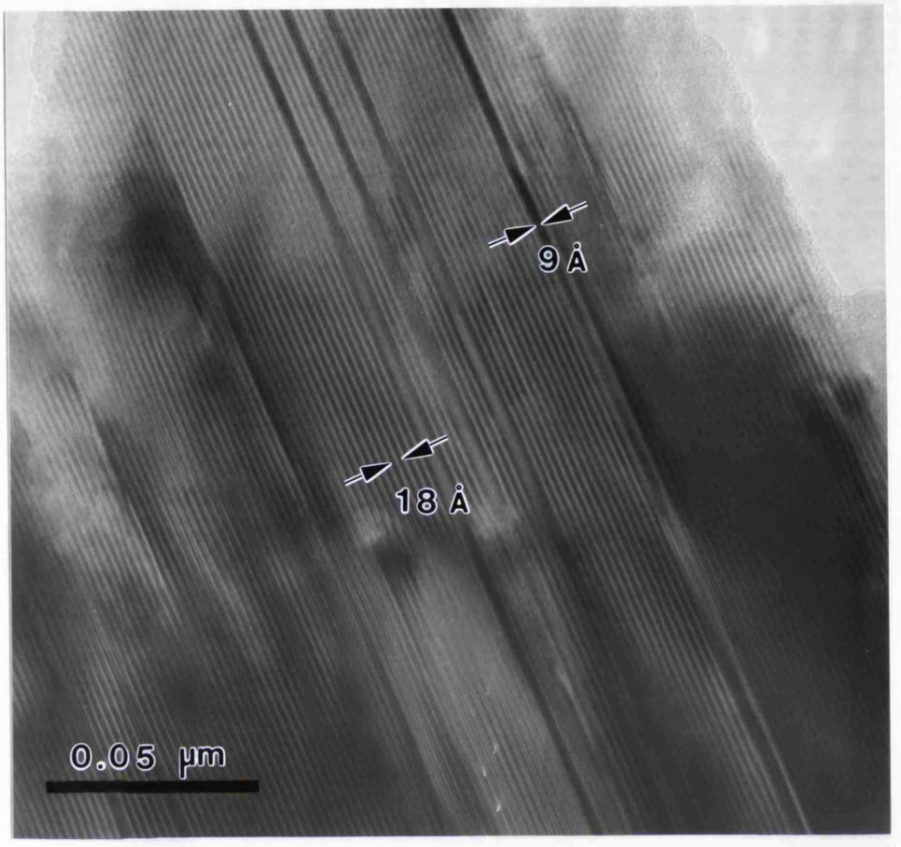

b)

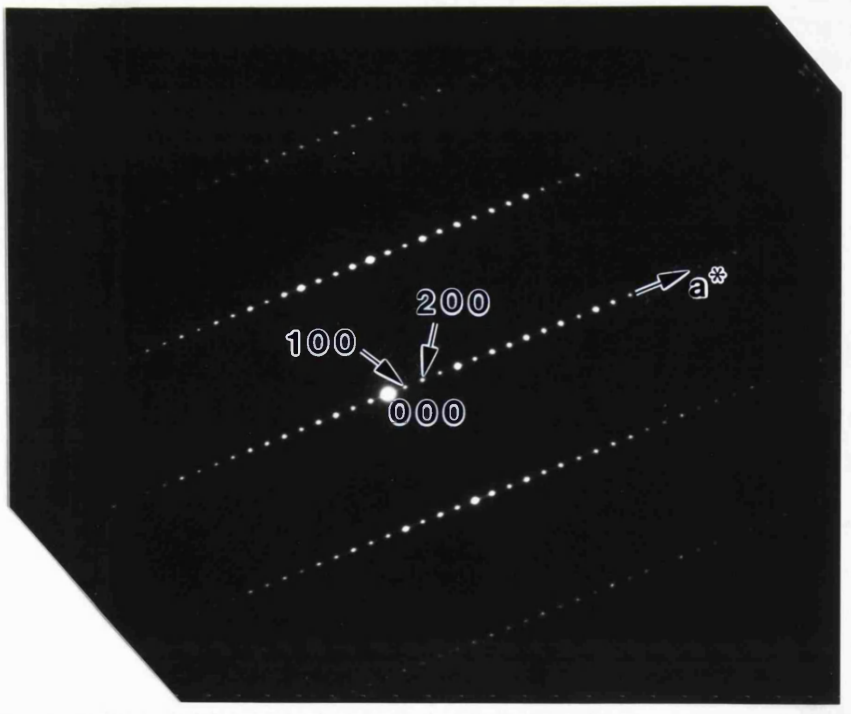

Figure 2.9: a) Bright field TEM photograph of a typical area of a synthetic $MgSiO_3$ orthoenstatite crystal, with b) its corresponding diffraction pattern.

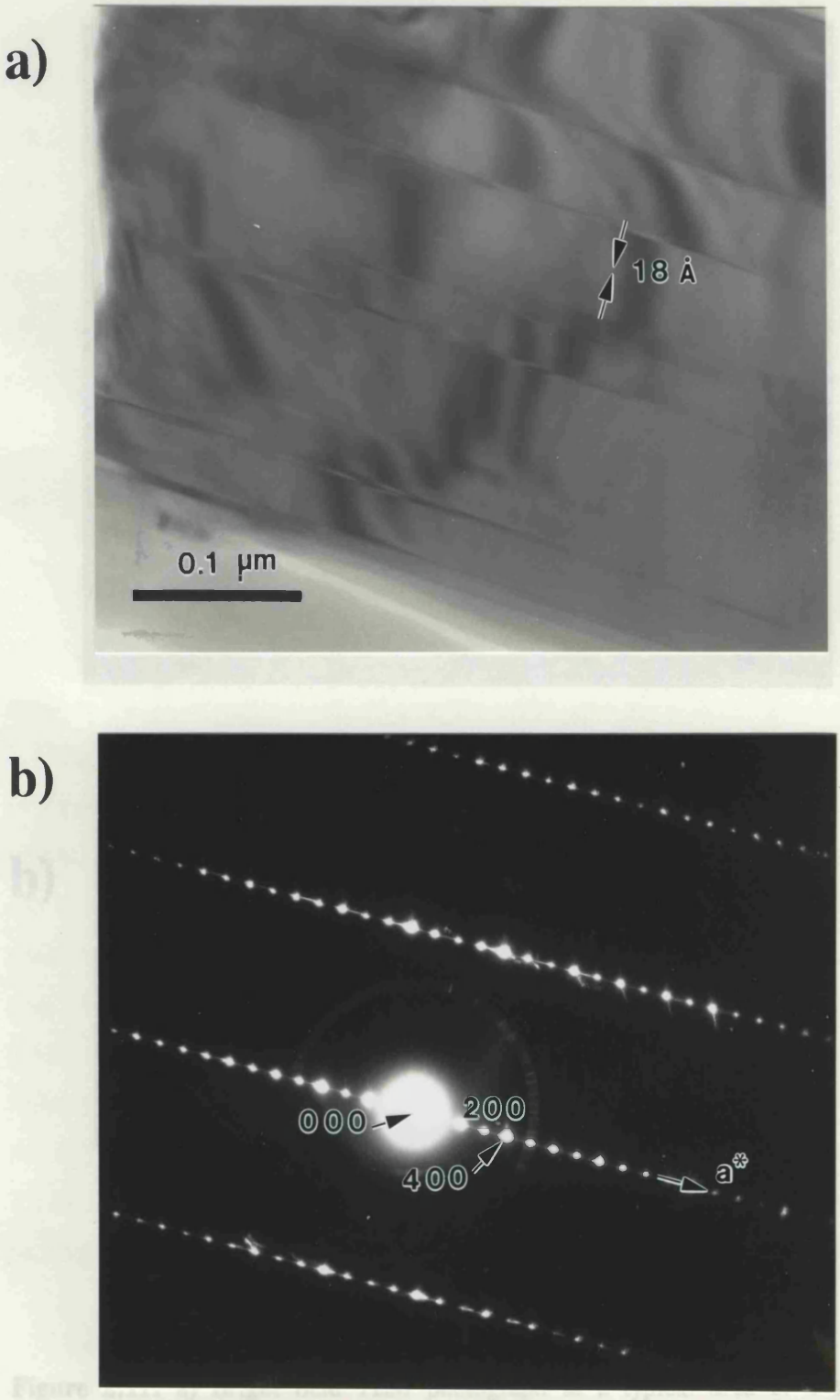

Figure 2.10: a) Bright field TEM photograph of a typical area of a grain of synthetic $Mg_{0.6}Fe_{0.4}SiO_3$ orthopyroxene, showing strain patterns; b) the diffraction pattern of the synthetic $Mg_{0.6}Fe_{0.4}SiO_3$ orthopyroxene, showing streaking of the reflections parallel to a^* caused by the presence of stacking disorder on (100).

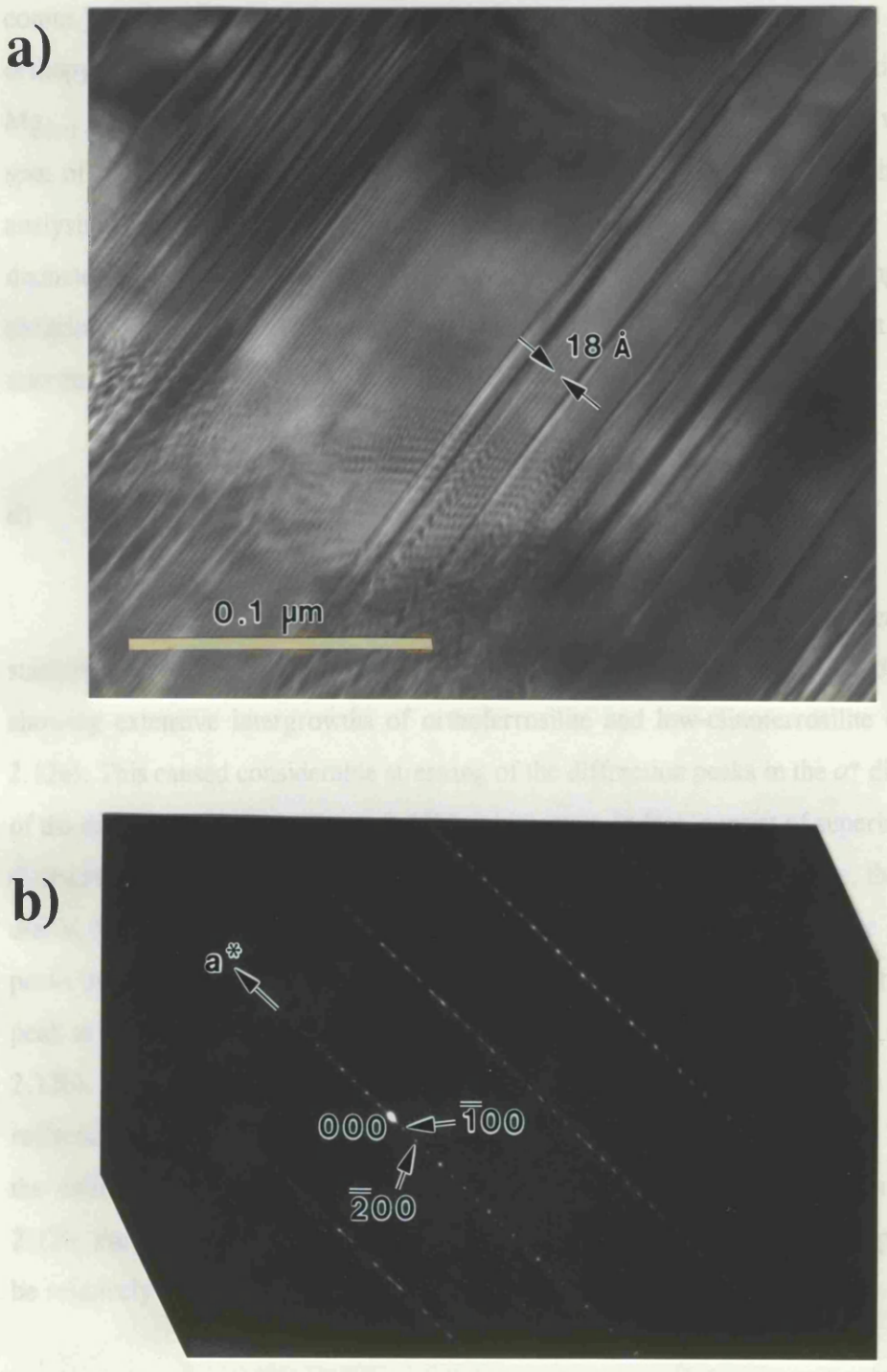

Figure 2.11: a) Bright field TEM photograph of a typical area of a synthetic $Mg_{0.3}Fe_{0.7}SiO_3$ orthopyroxene crystal. Note the Moiré interference due to strains between slightly rotated adjacent domains; b) the diffraction pattern of the synthetic $Mg_{0.3}Fe_{0.7}SiO_3$ orthopyroxene, showing streaking of the reflections parallel to a^* due to stacking disorder on (100).

Further chemical analysis using the electron microprobe (Woodland, pers. comm.) gave a significantly more homogeneous estimate of the composition of this orthopyroxene, with the bulk composition being determined as approximately $Mg_{0.31-0.35}Fe_{0.65-0.69}SiO_3$. However, whilst the TEM analyses were obtained with an spot of approximately 0.05 - 0.1 μm in diameter, the spot size used for chemical analysis with the electron microprobe was considerably larger (approximately 1μm in diameter, and corresponding to a 2 - 3 μm extinction volume), thus causing these chemical heterogeneities on the local scale of 0.1 - 1 μm to be averaged out by the microprobe beam.

d) Synthetic $FeSiO_3$ orthoferrosilite

The $FeSiO_3$ orthoferrosilite crystals generally displayed a moderate density of stacking faults (about 30 $\pm$ 10 faults per μm), with a few of the crushed grains showing extensive intergrowths of orthoferrosilite and low-clinoferrosilite (Figure 2.12a). This caused considerable streaking of the diffraction peaks in the a^* direction of the diffraction pattern (Figure 2.12b), which may, in fact, consist of superimposed diffraction patterns of both the ortho- and low-clinoferrosilites. In this case, the peaks due to the ~ 9Å a-axis of the clinoferrosilite are superimposed on alternate $h = 2n$ peaks originating from the ~ 18Å a-axis of the orthoferrosilite, causing every other peak to appear to be anomalously strong in the combined diffraction pattern (Figure 2.12b). If there were coherent diffraction from both ortho- and clinoferrosilite phases, reflections from each phase should be observed in the *h0l* reflections (with $h > 0$) of the diffraction pattern; since these "doublets" are not clearly observed in Figure 2.12b, the proportion of the $P2_1/c$ component within the orthopyroxene sample must be relatively small.

a)

b)

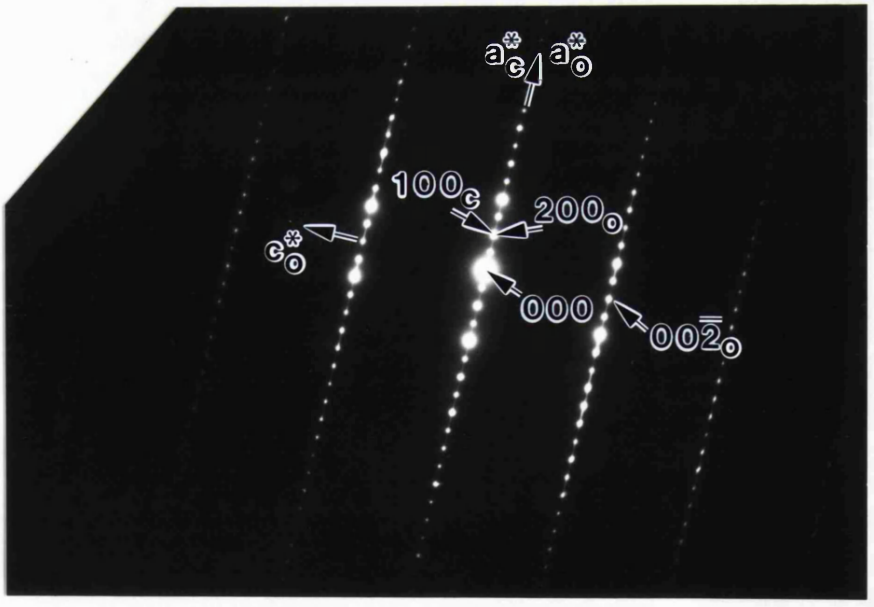

Figure 2.12: a) Bright field TEM photograph of a typical area of an $FeSiO_3$ orthoferrosilite crystal (note that the contrast seen between the stacking faults is due to deformation which occurred during sample preparation), with b) its diffraction pattern. The positions of some of the superimposed reflections from both the ortho- and clinoferrosilites are labelled; note also the streaking of the reflections along a^* due to this ortho/clino intergrowth.

e) Natural Orthoenstatites

Two crystals of natural orthopyroxene from independent sources were used in the high-pressure single crystal X-ray diffraction studies described in Chapters 3 and 4. Although the first crystal (known as OPX1) was found to be compositionally very inhomogeneous on a local scale of $< 1\ \mu m$, the average bulk composition of the crystal used is estimated to be $(Mg_{0.85}Fe_{0.13}Ca_{0.02})^{VI}(Si_{0.96}Al_{0.04})^{IV}O_3$, where the superscripts VI and IV represent the coordination of the cations in the orthopyroxene structure. In terms of the enstatite - ferrosilite solid solution, this crystal may be considered to have approximate Mg-number (ie., defined by the ratio Mg/Mg+Fe) of 0.87. Absorption problems due to the orientation of the grain on the TEM grid relative to both the tilt-axis of the microscope and the position of the X-ray detector were not considered during the analyses of the OPX1 crystal, and therefore the compositional inhomogeneity may actually be somewhat less than that quoted in Table 2.2.

There was generally a moderate degree of stacking disorder in the crushed grains of this OPX1 natural orthopyroxene (with the density of stacking faults along [100] being about $25 \pm 10\ \mu m^{-1}$). A typical TEM photograph of this OPX1 natural orthopyroxene is shown in Figure 2.13a, with its corresponding diffraction pattern (Figure 2.13b). High resolution TEM studies provided some images of the ~18Å lattice planes of the orthopyroxene, and also showed that some of the stacking faults were narrow bands of low-clinopyroxene.

The second natural orthopyroxene crystal (known as OPX2) had approximate composition $(Mg_{0.833}Fe_{0.117}Ca_{0.006}Al_{0.04})^{VI}(Si_{0.970}Al_{0.0285})^{IV}O_3$, calculated as the average number of cations per six oxygen atoms determined from seven independent measurements of the crystal using electron microprobe techniques (Mackwell, pers. comm.; Table 2.5); this crystal may be considered to have Mg-number 0.88. From these analyses, the maximum amount of inhomogeneity of the grains of the crystal are calculated to be $\pm$ 1% for the Mg^{2+} and Fe^{2+}, and less than 0.1% for the Ca^{2+}. Further chemical analysis of this natural orthopyroxene using the TEM (Table 2.2) revealed that, unlike the analyses of the $En_{30}Fs_{70}$ orthopyroxene, this measure of the

chemical homogeneity was reflected on a local scale of $< 1\ \mu m$. The OPX2 crystals were thus of very high quality, with an almost uniform composition throughout.

Cation	1	2	3	4	5	6	7	Mean
Si	1.9390	1.9440	1.9420	1.9394	1.9377	1.9409	1.9418	1.9407
Ni	0.0008	0.0025	0.0006	0.0003	0.0019	0.0000	0.0000	0.0009
Mn	0.0039	0.0022	0.0019	0.0040	0.0028	0.0028	0.0033	0.0030
Fe	0.2394	0.2392	0.2298	0.2353	0.2350	0.2297	0.2262	0.2335
Ti	0.0010	0.0011	0.0006	0.0011	0.0014	0.0013	0.0006	0.0010
Ca	0.0065	0.0057	0.0051	0.0058	0.0061	0.0063	0.0055	0.0059
K	0.0000	0.0001	0.0000	0.0000	0.0007	0.0000	0.0007	0.0002
Cr	0.0008	0.0004	0.0010	0.0004	0.0008	0.0013	0.0010	0.0008
Na	0.0000	0.0004	0.0012	0.0000	0.0000	0.0007	0.0007	0.0004
Al	0.1385	0.1332	0.1361	0.1359	0.1335	0.1383	0.1435	0.1370
Mg	1.6603	1.6595	1.6713	1.6691	1.6742	1.6673	1.6627	1.6663
Total	3.9903	3.9883	3.9895	3.9914	3.9941	3.9884	3.9860	3.9897

Table 2.5: Composition of the natural orthopyroxene OPX2 from electron microprobe analyses (Mackwell, pers. comm.); cations are calculated on the basis of six oxygens.

The microstructures of the OPX2 crystals were also extremely homogeneous; typically very few stacking faults were observed, and the a^* direction in the diffraction patterns was not obviously streaked (Figure 2.14a and b), thus confirming that the OPX2 crystal was indeed of "gem quality". However, Moiré patterns and local strain contrast in the bright field image (Figure 2.14a), and slight asterism in the diffraction pattern (Figure 2.14b) indicate that while crushing the crystals between glass slides during preparation of the TEM grids may produce sub-micron local strains that can interfere with the imaging of other defects, it does not generate stacking disorder into the microstructure.

a)

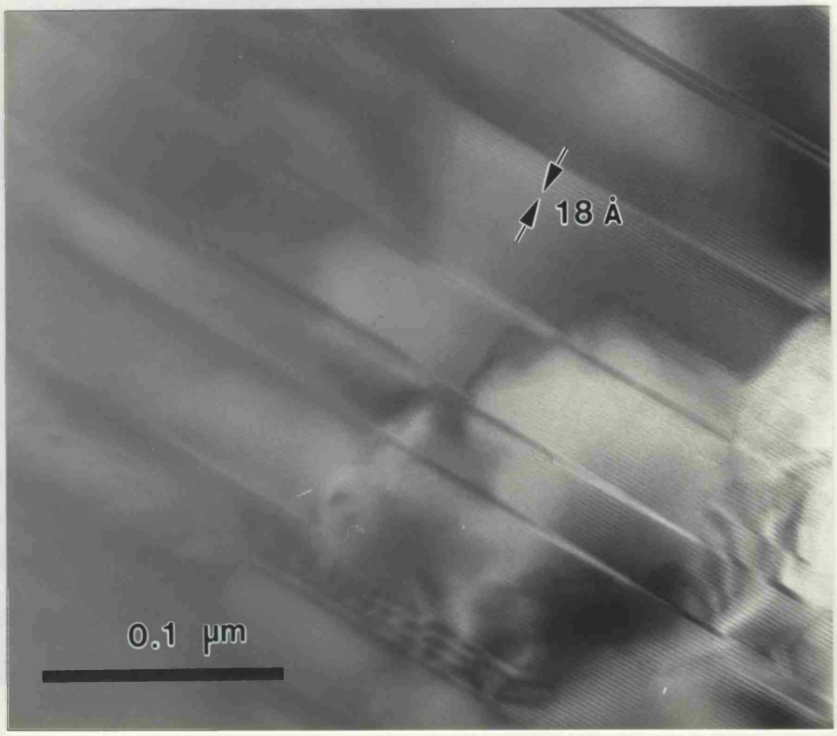

b)

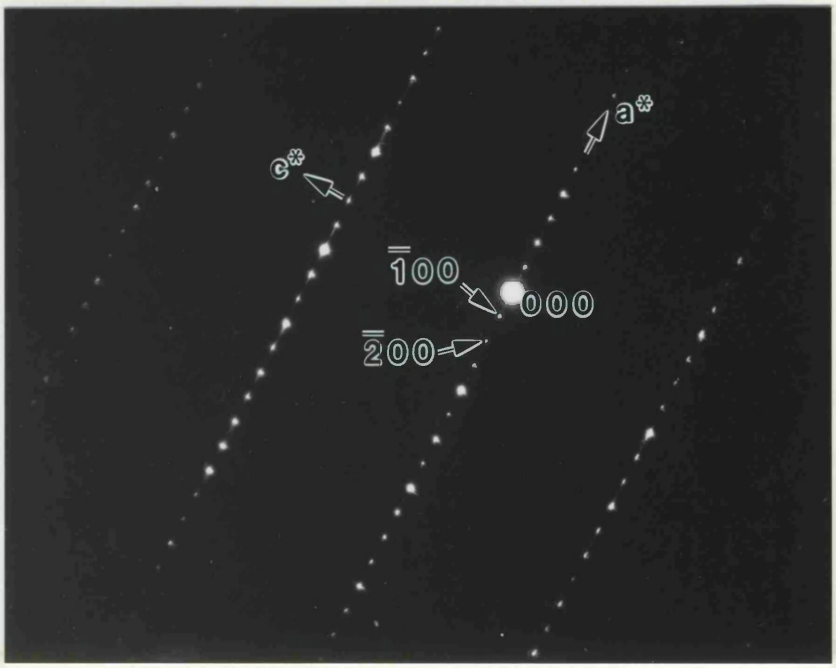

Figure 2.13: a) Bright field TEM photograph of a typical area of an OPX1 natural orthopyroxene crystal, with b) its corresponding diffraction pattern. Note the strain contrast in the lower right-hand corner of the bright field photograph.

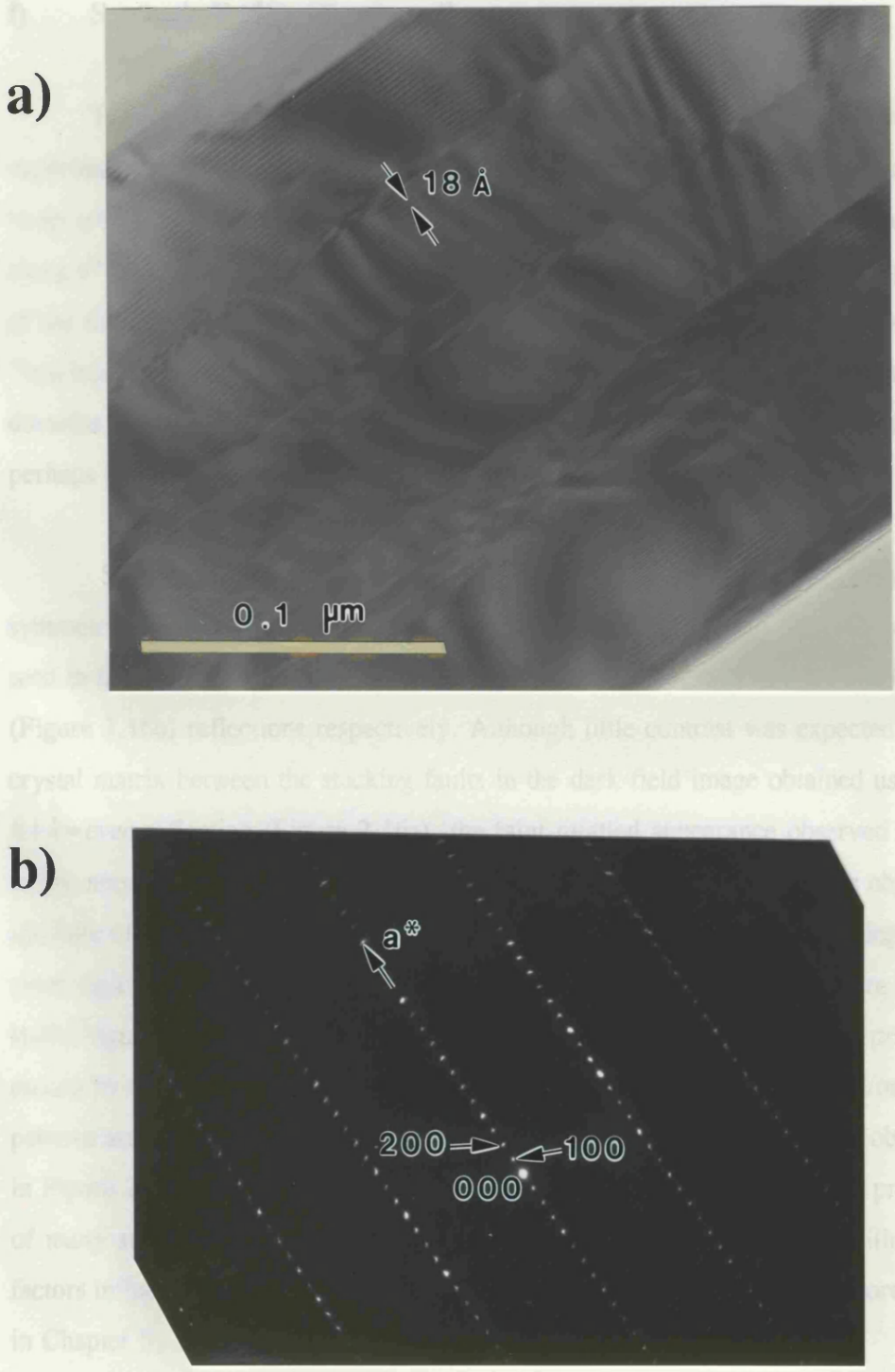

Figure 2.14: a) Bright field TEM photograph of a typical area of an OPX2 natural orthopyroxene crystal, with b) its corresponding diffraction pattern. Moiré patterns in the bright field photograph and asterism of some of the reflections in the diffraction pattern (ie., slight curving of reflections, particularly noticeable far from the 000 reflection) indicate that there is a certain amount of strain in the microstructure.

f) Synthetic $FeSiO_3$ Clinoferrosilite

The low-clinoferrosilite (used as a *starting material* for the compression experiments described in Section 5.2) contained a relatively high density of stacking faults (of the order of 60 $\pm$ 20 faults per μm), with streaking of the diffraction peaks along a^* in the relevant diffraction patterns (Figure 2.15). Since there is close spacing of the diffraction peaks in the a^* direction of the clinoferrosilite, obtaining a good "two-beam" condition needed for dark-field imaging was difficult. Possible antiphase domains produced upon pressure release during synthesis were very difficult to image, perhaps because they were relatively small and irregular.

Strains associated with the formation of such antiphase domains during the symmetry-breaking $C2/c \rightarrow P2_1/c$ transition may be the cause of some of the contrast seen in the dark field images formed with $h+k=even$ (Figure 2.16a) and $h+k=odd$ (Figure 2.16b) reflections respectively. Although little contrast was expected in the crystal matrix between the stacking faults in the dark-field image obtained using an $h+k=even$ reflection (Figure 2.16a), the faint mottled appearance observed in this figure may be due to interference from other diffracted beams through the objective aperture of the TEM, or the strain contrast described above. Dark-field imaging of the same region of the clinoferrosilite grain using an $h+k=odd$ reflection (Figure 2.16b) shows significantly enhanced contrast in the matrix between stacking faults, probably caused by the presence of many small (overlapping?) antiphase domains and/or strain patterns associated by the formation of such domains. The additional contrast observed in Figure 2.16b relative to that in Figure 2.16a must therefore suggest the presence of many small antiphase domains in the microstructure of the clinoferrosilite. The factors influencing the imaging of such antiphase domains are discussed in more detail in Chapter 5, Section 5.3.1.

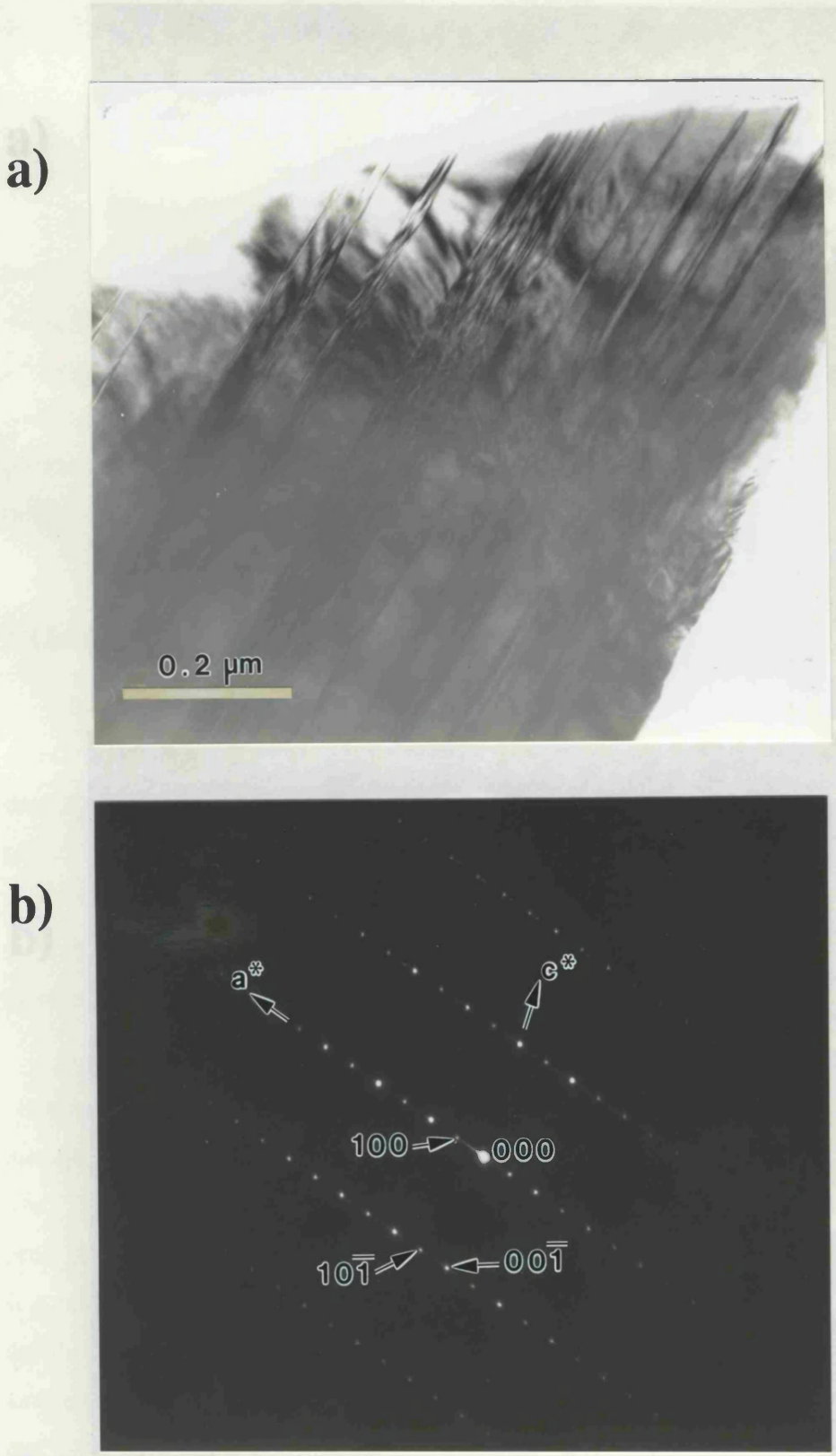

Figure 2.15: a) Bright field TEM photograph of a typical area of an $FeSiO_3$ clinoferrosilite crystal used as the starting material for the high-pressure experiments described in Chapter 5. The contrast is probably due to strains associated with the formation of antiphase domains occuring upon pressure release as a result of the C2/c $\rightarrow$ $P2_1/c$ transition (see Chapter 5 for details); b) the corresponding diffraction pattern, showing some streaking of the reflections along a^* due to the stacking disorder.

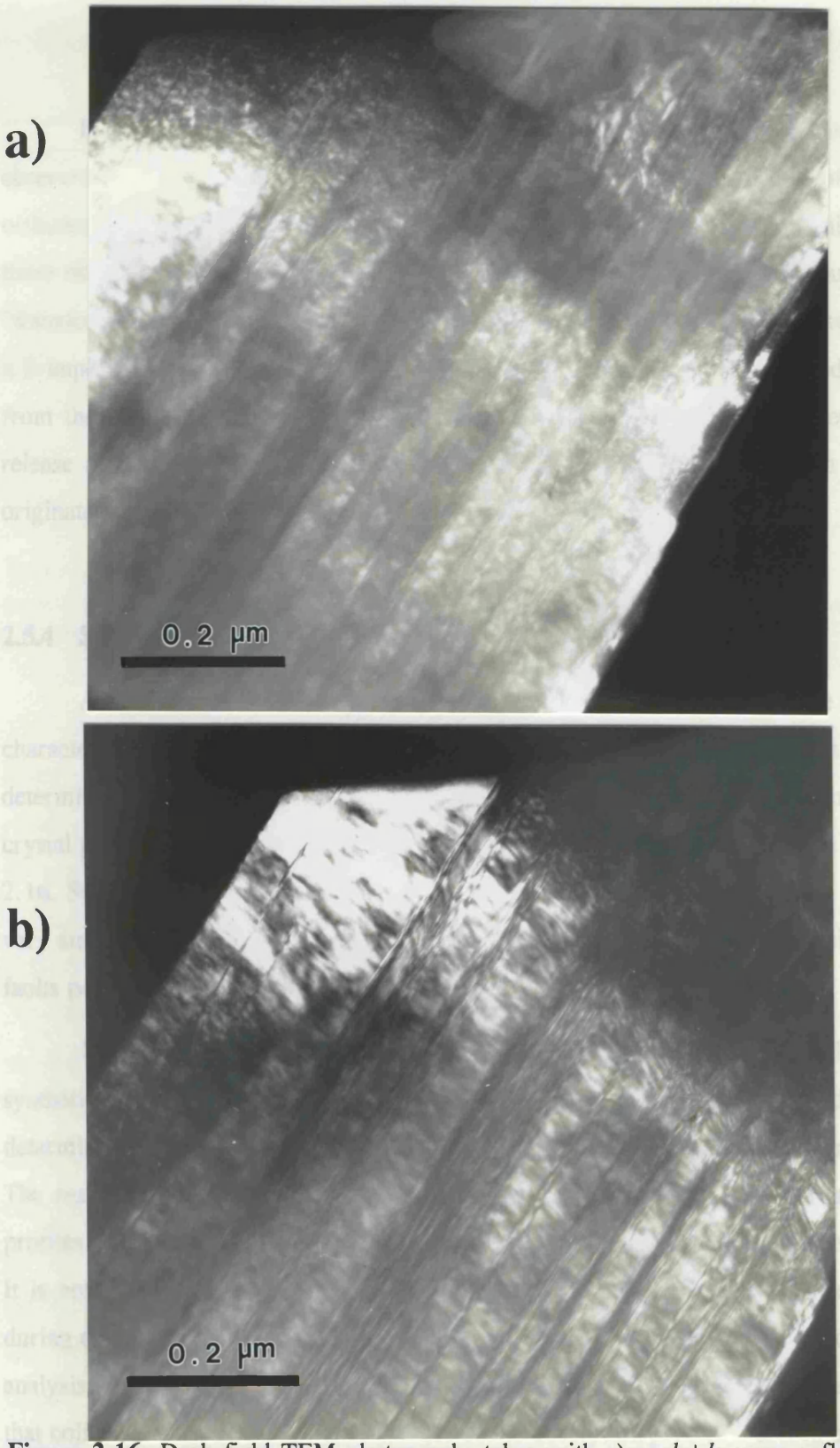

Figure 2.16: Dark field TEM photographs taken with a) an $h+k=even$ reflection from the clinopyroxene diffraction pattern, and b) an $h+k=odd$ reflection. The mottled/tweed contrast in the matrix of the crystal between the stacking faults in a) is probably due to strains associated with the formation of antiphase domains during the symmetry-breaking $C2/c \rightarrow P2_1/c$ transition; the enhanced contrast seen in b) indicates the presence of small, overlapping antiphase domains.

It is interesting to note that both the scale and nature of the microstructure observed for the clinoferrosilite produced as a result of compression of the orthoferrosilite to pressures in excess of ~5 GPa (see Chapter 5) are very similar to those observed for the clinoferrosilite starting material (for more details about the "transformed orthoferrosilite"-type of clinoferrosilite, see Section 5.3.1). However, it is important to note here that both these low-clinoferrosilite samples were produced from the high-pressure C2/c clinoferrosilite phase (see Chapter 5) upon pressure release at ambient temperature, irrespective of the structural state in which they originated.

2.5.4 Summary of TEM Characterisation

All the ortho- and clinopyroxene samples studied in this thesis have been characterised using the TEM. In each case, the density of stacking faults was determined per μm along [100] of the sample, and images of a typical area of the crystal grain, with the appropriate diffraction patterns, are presented in Figures 2.9 - 2.16. Stacking fault densities in both the synthetic and natural orthopyroxenes were very similar, while the clinoferrosilites exhibited approximately twice the density of faults per μm along [100].

For orthopyroxenes of non-end-member compositions (both natural and synthetic), energy dispersive X-ray analysis was carried out in the TEM in order to determine whether there was any local compositional inhomogeneity within the grains. The results of these analyses, with the relative qualities of the X-ray diffraction profiles and the relative amounts of stacking disorder, are summarised in Table 2.6. It is notable that some of these local chemical inhomogeneities were not observed during electron microprobe analyses (Woodland, pers. comm.) since the scale of the analysis obtained with the microprobe was about two orders of magnitude larger than that collected with the TEM. Uncertainties due to absorption problems caused by the relative orientation of the grain on the TEM grid with respect to both the tilt-axis of the microscope and the position of the X-ray detector may cause some reduction in the accuracy of these analyses; however, the quoted uncertainties of $\pm$ 1% ought to be sufficient to cover this.

Sample	Stacking fault density (faults/μm)	Degree of local compositional inhomogeneity	Relative widths of X-ray diffraction peaks
$MgSiO_3$	moderate	-	narrow
$Mg_{0.6}Fe_{0.4}SiO_3$	moderate	moderate	moderate
$Mg_{0.3}Fe_{0.7}SiO_3$	high	high	broad
$FeSiO_3$	moderate	-	narrow
OPX 1	moderate	moderate	broad
OPX 2	low	low	narrow

Table 2.6: Summary of the microstructures of the orthopyroxenes used in high-pressure X-ray diffraction experiments, with the relative quality of the diffraction profiles (see Section 2.2) and degree of stacking disorder, for reference.

It is generally assumed in the available literature that the density of stacking faults present in a particular crystal is the most important factor in determining the relative widths of its X-ray diffraction peaks; however, it is seen from Table 2.6 that for orthopyroxenes on or near the $(Mg,Fe)SiO_3$ join, this is probably not the case. Typical "narrow" and "broad" X-ray peak profiles (with full widths at half maximum (FWHM's) in the ω-scans of 0.17° and 0.33° respectively, measured for peaks at $\sim$ 16° 2θ) were plotted in Figures 2.1a and b. Peak profiles described as of a "moderate" width in Table 2.6 represent those with a FWHM of $\sim$0.25° in ω. From Table 2.6, and from the individual results presented in Section 2.5.3, the quality (ie. relative width) of these X-ray diffraction peaks appears to be more dependent on the presence of compositional inhomogeneities on a sub-micron scale in the $(Mg,Fe)SiO_3$ orthopyroxene crystals, than the density of stacking disorder within their microstructures. It should nevertheless be remembered that this hypothesis is based on the results obtained from only four orthopyroxene samples of appropriate compositions, and therefore caution should be taken when applying it to other mineral systems.

CHAPTER 3

STRUCTURAL COMPRESSION OF $(Mg,Fe)SiO_3$ ORTHOPYROXENES

3.1 INTRODUCTION

The structural response to pressure of orthopyroxenes of several compositions along or near the $MgSiO_3$ - $FeSiO_3$ solid solution join has been determined by high-pressure single crystal X-ray diffraction in the diamond anvil cell (DAC). The synthetic compositions studied were $MgSiO_3$, $Mg_{0.6}Fe_{0.4}SiO_3$, and $FeSiO_3$, and composition of the natural orthopyroxene (OPX2) was approximately $(Mg_{0.83}Fe_{0.12}Ca_{0.006}Al_{0.04})(Si_{0.97}Al_{0.03})O_3$. Data collections for each sample were performed at $\sim$1 GPa pressure intervals, using the method described in Chapter 2, Section 2.4.1. Data reduction and refinement procedures are described in Section 2.4.2. Final refinement parameters for each of the four orthopyroxene compositions have been presented in Tables 2.3a-d, and all of the refined positional parameters, bond lengths and angles are given in Appendix 1. Selected bond lengths, polyhedral volumes and distortions, important for determining the structural response to pressure of each particular orthopyroxene, are given in Tables 3.1a-d. The general orthopyroxene structure at ambient conditions has been described in some detail in Chapter 1, and is shown, for reference, in projection down [100] in Figure 3.1.

This chapter begins by reviewing the individual behaviour of the four orthopyroxenes with increasing pressure, identifying in each the most important structural elements operating during compression. A change in compression mechanism observed in the synthetic Mg^{2+}-rich orthopyroxenes is carefully characterised in terms of changes in the compressibilities of the SiO_4 tetrahedra and associated changes in the degrees of kinking and tilting of the silicate chains. The subsequent section (Section 3.3) describes the differences in the behaviour of the octahedra, tetrahedra and silicate chains with changing composition, both from $MgSiO_3$ to $FeSiO_3$, and then to pyroxenes containing additional natural impurities such

as Ca^{2+} and Al^{3+}. Since it has often been assumed (eg., Hazen and Finger, 1982) that increasing temperature and increasing pressure have opposite effects on a crystal structure, the compressional behaviour of these natural and synthetic orthopyroxenes are compared to the available published data for orthopyroxenes of similar compositions at high temperatures (Smyth, 1973; Sueno et al., 1976; Yang and Ghose, 1995).

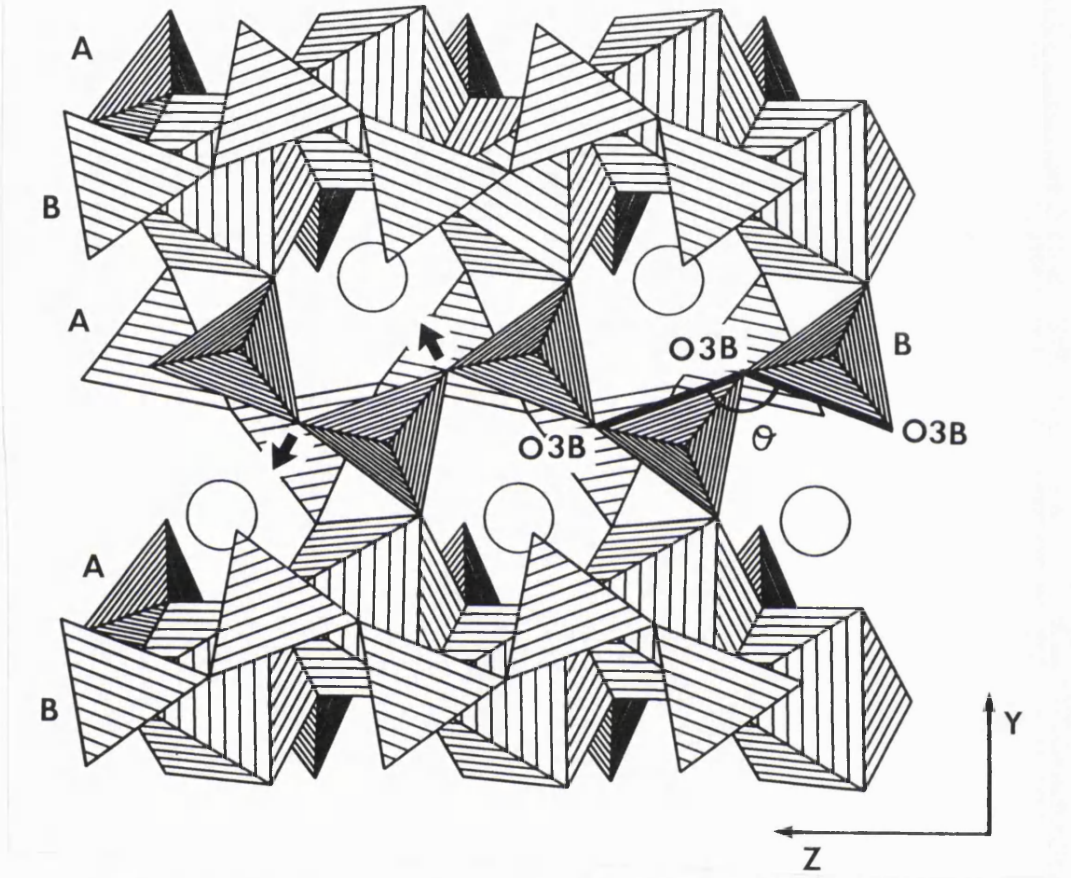

Figure 3.1: Polyhedral representation of synthetic $MgSiO_3$ orthoenstatite at ambient conditions. M1 sites are represented by shaded octahedra; M2 are shown as circles. The arrows indicate the direction of kinking of the silicate chain with increasing pressure (see Section 3.2.1).

In each of the orthopyroxenes studied, both synthetic and natural, the degrees of distortion of the M1 and M2 sites were determined by calculating the octahedral quadratic elongation using the method of Robinson et al. (1971). As the polyhedral bond lengths deviate from their average value, so the octahedral quadratic elongation increases from 1.0, the value defined for a totally regular octahedron of the same volume, using the expression:

$$\lambda \ (mean\ quadratic\ elongation) = \sum_{i=1}^{6} \left(\frac{l_i}{l_0}\right)^2 / 6 \qquad (3.1)$$

where l_i represents the lengths of the individual M-O bonds, and l_0 is the bond length for a regular octahedron of the same volume. An comparable expression was also used to calculate the quadratic elongations of the tetrahedral sites in the "A" and "B" chains.

Linear volume compressibilities of both the octahedral and tetrahedral sites were calculated using the equation:

$$V = V_0(1 - \beta_V P) \qquad (3.2)$$

where β_V represents the linear volume compressibility of the site, measured in GPa^{-1}, V is the volume of the site at high pressure, and V_0 is its volume at ambient conditions. The linear compressibilities of some of the M-O and Si-O bonds were calculated using the similar expression:

$$L = L_0 \ (1 - \beta P) \qquad (3.3)$$

where L is the length of the bond in question at high pressure, L_0 is its length at ambient conditions, and β is the linear compressibility of the bond, measured in GPa^{-1}. Note that for a given octahedron, $\beta_V \sim 3\beta$ if the volume compression is accommodated solely by bond-length shortening.

3.2 COMPLETE DESCRIPTIONS OF STRUCTURAL COMPRESSION OF ORTHOPYROXENES

3.2.1 Compression of Synthetic $MgSiO_3$ Orthoenstatite

The variations of the bond lengths and angles of the synthetic $MgSiO_3$ orthoenstatite with pressure are given in full in Appendix 1. The bond lengths and angles which change most significantly with pressure are given in Table 3.1a.

P (GPa)	0.00	1.04	1.95	3.27
< M1-O >	2.08(1)	2.07(1)	2.06(1)	2.05(1)
M1 volume	11.8(1)	11.6(1)	11.5(1)	11.4(1)
M1 Quad. El.	1.009 (1)	1.008 (1)	1.008 (1)	1.008 (1)
< M2-O >	2.15(1)	2.14(1)	2.13(1)	2.12(1)
M2 volume	12.5(1)	12.3(1)	12.2(1)	12.0(1)
M2 Quad. El.	1.049 (1)	1.046 (1)	1.046 (1)	1.046 (1)
< TA-O >	1.63(1)	1.63(1)	1.63(1)	1.63(1)
TA volume	2.18(1)	2.20(1)	2.18(1)	2.17(1)
TA Quad. El.	1.010 (1)	1.011 (1)	1.011 (1)	1.010 (1)
< TB-O >	1.64(1)	1.64(1)	1.64(1)	1.64(1)
TB volume	2.24(1)	2.26(1)	2.25(1)	2.24(1)
TB Quad. El.	1.005 (1)	1.005 (1)	1.005 (1)	1.006 (1)
O3a-O3a-O3a	158.7(5)	158.9(8)	159.1(9)	158.7(6)
O3b-O3b-O3b	139.0(5)	138.3(7)	137.7(7)	137.1(5)
> A to (100)	4.0(5)	3.8(5)	2.6(5)	2.9(5)
> B to (100)	7.4(5)	7.3(5)	7.2(5)	6.6(5)

Table 3.1a: Selected bond lengths and angles for $MgSiO_3$ orthoenstatite to 8.5 GPa. The symbols < X-O > represent the average X-O bond lengths; "Quad. El." denotes the quadratic elongation of the polyhedral site (determined using equation 3.1); The O3-O3-O3 angles are the chain extension angles (see Figure 3.1); and " >X to (100)" is the degree of tilt of the bases of the tetrahedra in the "X"-chain from the (100) plane.

P (GPa)	4.09	4.95	5.85	7.00	8.10
< M1-O >	2.05(1)	2.04(1)	2.04(1)	2.04(1)	2.03(1)
M1 volume	11.3(1)	11.3(1)	11.2(1)	11.1(1)	11.0(1)
M1 Quad. El.	1.008 (1)	1.008 (1)	1.008 (1)	1.007 (1)	1.007 (1)
< M2-O >	2.12(1)	2.12(1)	2.11(1)	2.11(1)	2.10(1)
M2 volume	12.0(1)	11.9(1)	11.8(1)	11.7(1)	11.6(1)
M2 Quad. El.	1.045 (1)	1.045 (1)	1.045 (1)	1.045 (1)	1.045 (1)
< TA-O >	1.62(1)	1.62(1)	1.61(1)	1.61(1)	1.61(1)
TA volume	2.15(1)	2.13(1)	2.12(1)	2.10(1)	2.09(1)
TA Quad. El.	1.011 (1)	1.011 (1)	1.011 (1)	1.011 (1)	1.011 (1)
< TB-O >	1.63(1)	1.63(1)	1.62(1)	1.62(1)	1.61(1)
TB volume	2.21(1)	2.19(1)	2.18(1)	2.17(1)	2.15(1)
TB Quad. El.	1.005 (1)	1.005 (1)	1.005 (1)	1.005 (1)	1.005 (1)
O3a-O3a-O3a	159.7(8)	159.4(9)	159.3(9)	159.0(9)	158.2(9)
O3b-O3b-O3b	136.8(7)	135.4(8)	136.1(9)	135.5(7)	136.2(8)
> A to (100)	2.9(5)	2.0(5)	2.5(5)	2.0(5)	2.1(5)
> B to (100)	7.0(5)	6.7(5)	6.3(5)	6.4(5)	5.5(5)

Table 3.1a: (cont.).

The volumes of both the M1 and M2 sites of the synthetic $MgSiO_3$ orthoenstatite (and the corresponding average M1-O and M2-O bond lengths) decrease smoothly over the whole 8.1 GPa pressure range studied (Figure 3.2); both the M1 and M2 sites become slightly more regular upon pressure increase. It is interesting to note that while compression of the M1 site is caused by shortening of all the M1-O bonds at approximately the same rate, the volume reduction of the M2 site is due primarily to the anomalously large compression of the M2-O3a and M2-O3b bonds (Appendix 1). The remainder of the M2-O bonds do not shorten significantly over the 8.1 GPa pressure range. It will be seen in Chapter 4 that this unusually large initial compression of the M2-O3 bonds causes the high value of K_0' in the low-pressure equation of state (EOS).

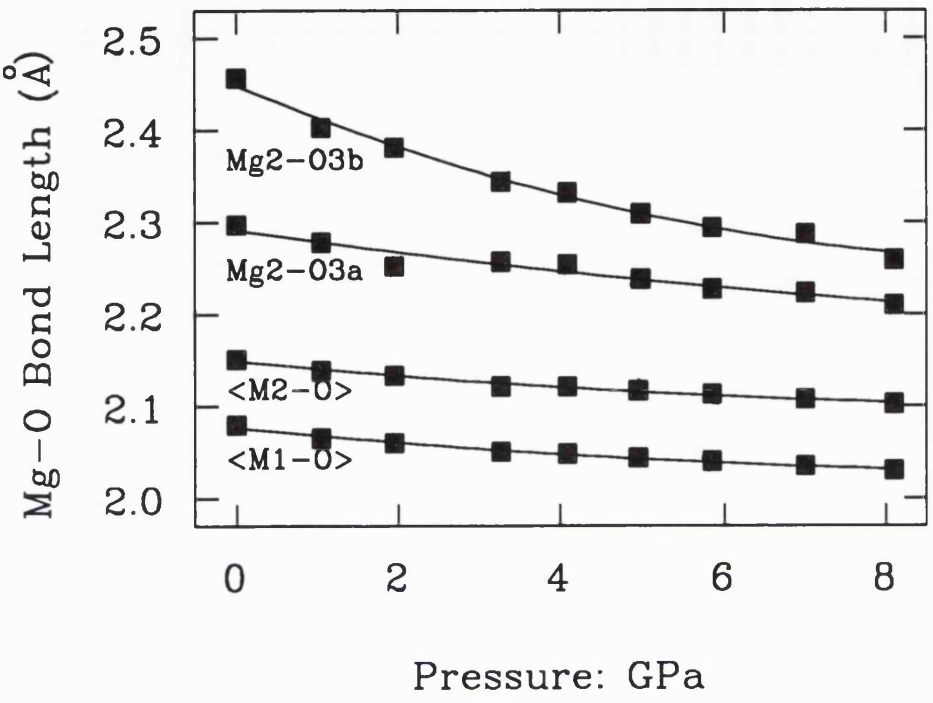

Figure 3.2: Compression of M2-O3a and M2-O3b bonds of synthetic $MgSiO_3$ orthoenstatite, compared to the average M1-O and M2-O bond lengths of the orthopyroxene.

A third-order Birch-Murnaghan EOS fitted to the variation of the octahedral volumes with pressure for $MgSiO_3$ orthoenstatite gives values for the "bulk modulus" and "K_0' ":

M1 site	$K_{0,T}$ = 53.2 (5.4) GPa	K_0' = 31.9 (6.3)
M2 site	$K_{0,T}$ = 63.1 (8.5) GPa	K_0' = 26.7 (7.9)

Ralph and Ghose (1980) determined the structure of an identical synthetic $MgSiO_3$ orthoenstatite at 2.1 GPa. Their data are generally in good agreement with these determinations; from the cube of the average M-O bond length, one can obtain $K_{0,T}$ = 36.8 GPa for the M1 site, and $K_{0,T}$ = 42.4 GPa for the M2 site from their data. Thus, although within one combined estimated standard deviation (*esd*) the compressibilities of the Mg^{2+}-containing M1 and M2 octahedra are identical, both our data and that of Ralph and Ghose (1980) suggest that the M2 site in $MgSiO_3$ orthoenstatite is slightly less compressible than the M1 site.

Below 4 GPa, compression of the $MgSiO_3$ orthoenstatite is accommodated simply by this compression of the M1 and M2 cation sites, with associated changes in the conformations of the chains of essentially rigid SiO_4 tetrahedra: the "B" chain, which is more distorted at room pressure, kinks dramatically whilst keeping the bases of its tetrahedra at an approximately constant orientation of ~7° from the (100) plane, while the "A" chain straightens slightly towards the fully-extended position; the tetrahedra in the "A" chain tilt markedly towards the (100) plane (Figure 3.3a-c). However, above 4 GPa, there is a well-defined change in both the degree of kinking of the tetrahedral chains (as measured by changes in the O3-O3-O3 chain extension angle) and the amount of tetrahedral tilt towards the (100) plane. At these higher pressures, the "B" chain ceases kinking and its tetrahedra begin to tilt steadily towards the (100) plane, whereas the "A"-chain begins to kink slowly while its tetrahedra virtually stop tilting towards (100), as shown in Figure 3.3a-c.

This change in the behaviour of the silicate chains at 4 GPa is accompanied by significant compression of the Si-O tetrahedral bond lengths (Figure 3.4). Although there is a moderate amount of scatter of the individual Si-O bond lengths with increasing pressure (Appendix 1), the non-bridging Si-O bonds in both the tetrahedral "A" and "B" chains (ie, the Si-O1 and Si-O2 bonds) accommodate most of the compression above 4 GPa; there is less change in the lengths of the two bridging Si-O3 bonds. The linear volume compressibilities of both the silicate tetrahedra in this higher pressure compression regime are $\beta_V = 0.006(1)$ GPa^{-1}. Estimation of linear volume compressibilities of the SiO_4 tetrahedra below 2.1 GPa using the cube of the average bond length (Ralph and Ghose, 1980) yield values of 0.007 GPa^{-1} and 0.001 GPa^{-1} for the "A" and "B" chains respectively. Thus although the average SiB-O bond length is incompressible within the experimental uncertainties in both these low-pressure compressional studies, Ralph and Ghose (1980) do observe some shortening of the SiA-O bonds by 2.1 GPa. However, in the absence of *esd*'s, it is not possible to determine whether this shortening is significant.

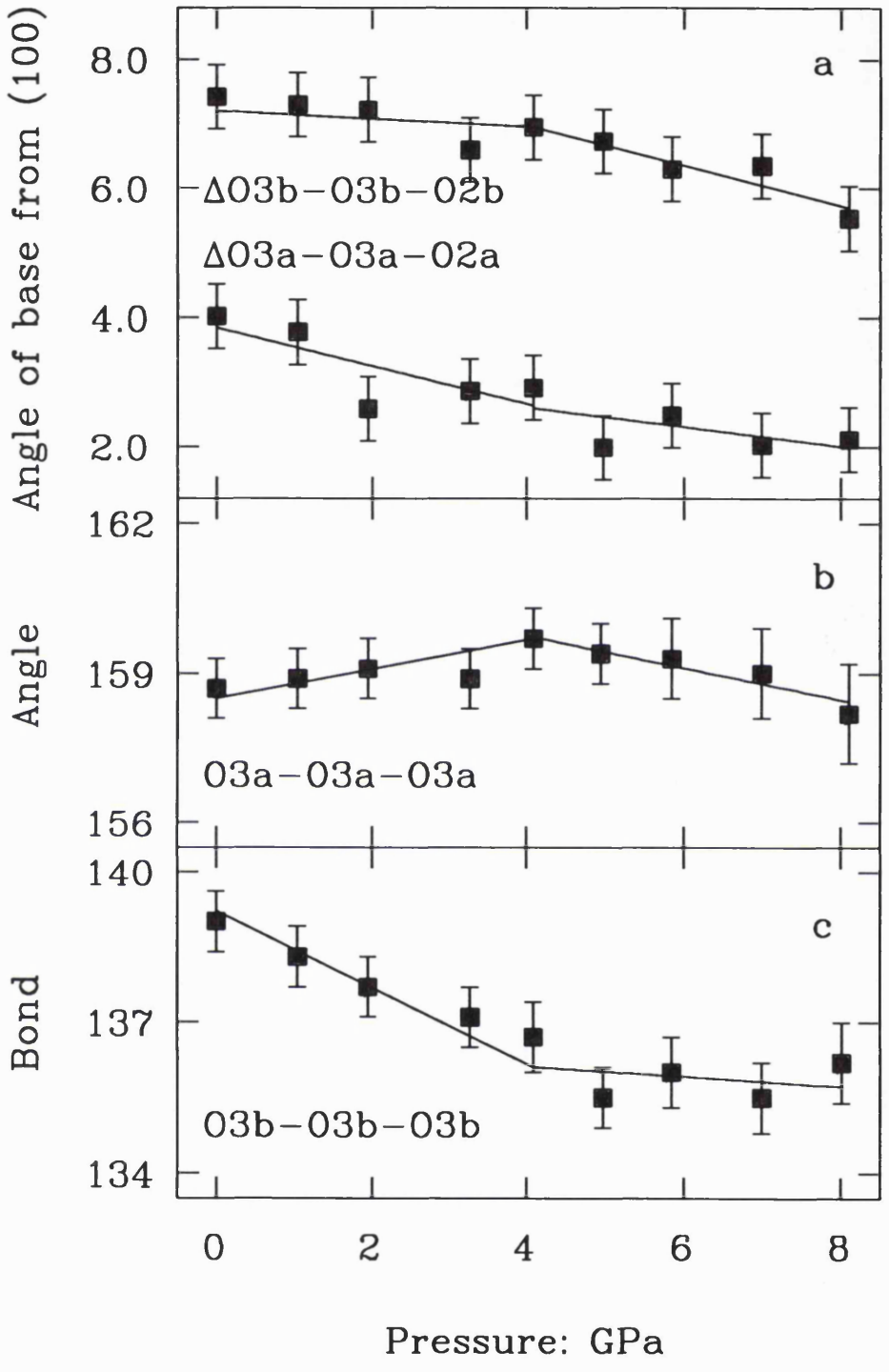

Figure 3.3: a) Changes in the degrees of tilt of the bases of the "A" and "B" silicate tetrahedra in synthetic $MgSiO_3$ orthoenstatite from the (100) plane with increasing pressure, showing a discontinuity at 4 GPa; b) changes in the degree of kinking of the tetrahedral "A"-chain of the synthetic $MgSiO_3$ orthoenstatite with pressure to 8.1 GPa; c) changes in the degree of kinking of the tetrahedral "B"-chain of the synthetic $MgSiO_3$ orthoenstatite with pressure.

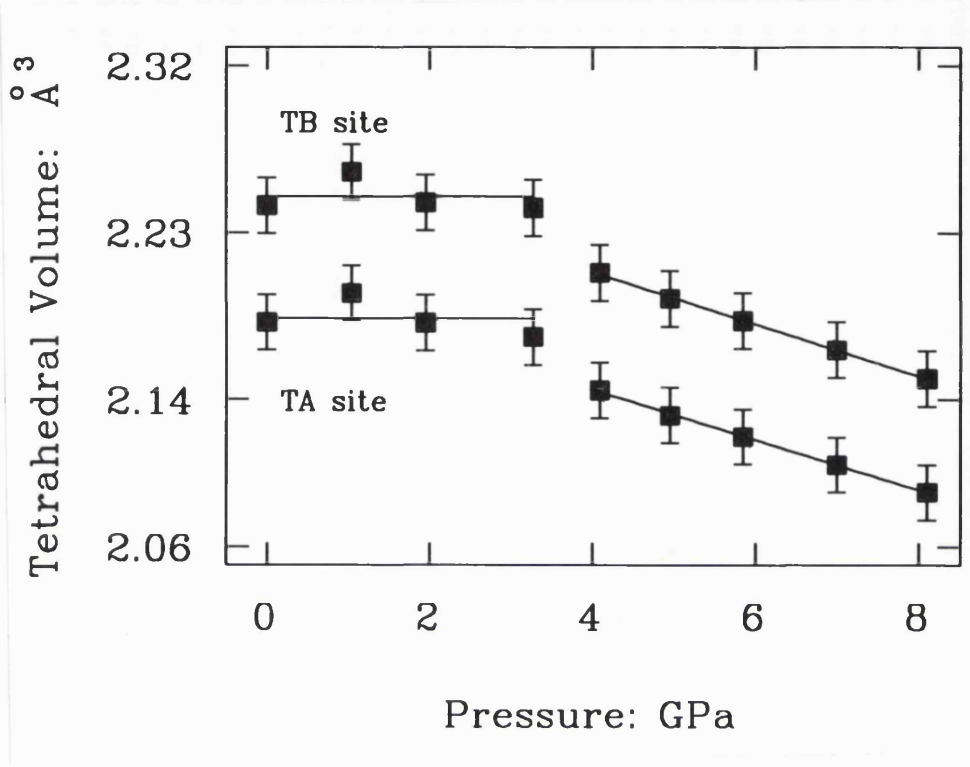

Figure 3.4: Variation in tetrahedral volumes of the TA and TB sites of synthetic $MgSiO_3$ orthoenstatite to ~8 GPa, showing a distinct change in compressibilities above 4 GPa.

This change in compression mechanism observed at 4 GPa for the synthetic $MgSiO_3$ orthoenstatite is reflected in its EOS which shows a distinct break at this pressure (see Chapter 4), and is also apparent in a change in the rate of change, $\delta\upsilon/\delta P$, of the Raman frequencies of $MgSiO_3$ orthoenstatite between 3.5 and 5 GPa (Chopelas and Boehler, pers. comm.; Figure 4.4).

3.2.2 Compression of Synthetic $Mg_{0.6}Fe_{0.4}SiO_3$ Orthopyroxene

Structural data of the $Mg_{0.6}Fe_{0.4}SiO_3$ orthopyroxene was collected at pressure intervals of approximately 1 GPa to 7.5 GPa. Although two different crystals (of identical bulk composition) of the orthopyroxene were used for the data collections, there are no systematic differences in the bond lengths or angles determined from data collections from the two crystals held at ambient conditions (Appendix 1). However, the use of two crystals appears to have somewhat increased the scatter of the data, and thereby reduced the clarity with which the compression mechanisms can be determined. Selected bond lengths and angles from the synthetic $Mg_{0.6}Fe_{0.4}SiO_3$ orthopyroxene at high pressures are given in Table 3.1b; the full list is presented in Appendix 1.

P (GPa)	0.00	1.54	2.50†	3.17
< M1-O >	2.09 (1)	2.07 (1)	2.07 (1)	2.05 (1)
M1 volume	11.9 (1)	11.7 (1)	11.8 (1)	11.4 (1)
M1 Quad. El.	1.010 (1)	1.009 (1)	1.007 (1)	1.011 (2)
< M2-O >	2.19 (1)	2.17 (1)	2.16 (1)	2.15 (1)
M2 volume	12.9 (1)	12.7 (1)	12.5 (1)	12.3 (1)
M2 Quad. El.	1.063 (1)	1.057 (1)	1.053 (1)	1.056 (2)
< TA-O >	1.63 (1)	1.63 (1)	1.63 (1)	1.63 (1)
TA volume	2.19 (1)	2.20 (1)	2.18 (1)	2.20 (1)
TA Quad. El.	1.008 (1)	1.010 (1)	1.010 (1)	1.012 (1)
< TB-O >	1.64 (1)	1.64 (1)	1.64 (1)	1.64 (1)
TB volume	2.26 (1)	2.24 (1)	2.24 (1)	2.26 (1)
TB Quad. El.	1.006 (1)	1.005 (1)	1.005 (1)	1.004 (1)
O3a-O3a-O3a	162.9 (7)	164.1 (7)	162.0 (6)	164.7 (8)
O3b-O3b-O3b	141.9 (6)	140.1 (7)	138.8 (5)	139.4 (7)
> A to (100)	3.6 (5)	3.8 (5)	3.1 (5)	4.5 (5)
> B to (100)	7.4 (5)	6.5 (5)	6.4 (5)	6.6 (5)

Table 3.1b: Selected bond lengths and angles of $Mg_{0.6}Fe_{0.4}SiO_3$ orthopyroxene. The symbols are the same as those described for Table 3.1a. Note also that the data marked with a cross (†) was collected from crystal #2; unmarked data was obtained from crystal #1.

P (GPa)	4.14	4.76	5.77†	6.59†	7.50†
< M1-O >	2.06 (1)	2.06 (1)	2.06 (1)	2.05 (1)	2.05 (1)
M1 volume	11.6 (1)	11.5 (1)	11.5 (1)	11.4 (1)	11.5 (1)
M1 Quad. El.	1.007 (1)	1.007 (1)	1.007 (1)	1.007 (1)	1.005 (1)
< M2-O >	2.15 (1)	2.16 (1)	2.14 (1)	2.14 (1)	2.13 (1)
M2 volume	12.3 (1)	12.4 (1)	12.2 (1)	12.1 (1)	12.1 (1)
M2 Quad. El.	1.055 (1)	1.056 (1)	1.051 (1)	1.054 (1)	1.051 (1)
< TA-O >	1.63 (1)	1.62 (1)	1.62 (1)	1.62 (1)	1.61 (1)
TA volume	2.18 (1)	2.16 (1)	2.16 (1)	2.14 (1)	2.13 (1)
TA Quad. El.	1.008 (1)	1.006 (1)	1.009 (1)	1.009 (1)	1.011 (1)
< TB-O >	1.64 (1)	1.64 (1)	1.63 (1)	1.63 (1)	1.62 (1)
TB volume	2.24 (1)	2.24 (1)	2.19 (1)	2.21 (1)	2.17 (1)
TB Quad. El.	1.004 (1)	1.005 (1)	1.006 (1)	1.005 (1)	1.005 (1)
O3a-O3a-O3a	166.0 (1.2)	164.5 (1.0)	163.6 (1.1)	164.6 (9)	162.5 (7)
O3b-O3b-O3b	138.5 (8)	139.1 (8)	135.8 (9)	138.4 (8)	137.1 (6)
> A to (100)	3.5 (5)	2.8 (5)	2.7 (5)	2.2 (5)	2.1 (5)
> B to (100)	5.5 (5)	5.9 (5)	5.7 (5)	5.4 (5)	5.0 (5)

Table 3.1b: (cont.)

The refined occupancies of the M1 and M2 sites remain unchanged (as expected) at all pressures within the experimental uncertainties (Table 3.2). The compression of the Fe^{2+}-rich M2 sites in the $Mg_{0.6}Fe_{0.4}SiO_3$ orthopyroxene is accommodated mainly by the initial rapid shortening of the M2-O3 bonds, while the remaining M2-O1 and M2-O2 bond lengths are essentially unchanged by the 7.5 GPa pressure increase. Conversely, the lengths of *all* the M1-O bonds decrease somewhat over the same pressure range. The volumes of both the Mg^{2+}-rich M1 and the Fe^{2+}-rich M2 octahedral sites decrease steadily over the whole pressure range studied, with their linear volume compressibilities calculated to be β_V = 0.005(2) GPa^{-1} and 0.008(1) GPa^{-1} respectively. Thus the M2 site is marginally more compressible in synthetic $Mg_{0.6}Fe_{0.4}SiO_3$ orthopyroxene than the M1 site at pressures below 7.5 GPa.

Both the octahedral cation sites become less distorted as a result of increasing the pressure, although the Fe^{2+}-rich M2 site becomes relatively more regular over the 7.5 GPa pressure range than the Fe^{2+}-poor M1 site does (Table 3.1b).

P (GPa)	Mg^{2+} (M1 site)	Fe^{2+} (M1 site)	Mg^{2+} (M2 site)	Fe^{2+} (M2 site)
0.00	0.85 (1) %	0.15 (1) %	0.45 (1) %	0.55 (1) %
1.54	0.86 (1) %	0.14 (1) %	0.47 (2) %	0.53 (2) %
2.50†	0.84 (1) %	0.16 (1) %	0.46 (1) %	0.54 (1) %
3.17	0.86 (1) %	0.14 (1) %	0.48 (1) %	0.52 (1) %
4.14	0.82 (2) %	0.18 (2) %	0.43 (2) %	0.57 (2) %
4.76	0.85 (2) %	0.15 (2) %	0.44 (3) %	0.56 (3) %
5.77†	0.84 (1) %	0.16 (1) %	0.43 (1) %	0.57 (1) %
6.59†	0.85 (1) %	0.15 (1) %	0.43 (1) %	0.57 (1) %
7.50†	0.85 (1) %	0.15 (1) %	0.48 (1) %	0.52 (1) %

Table 3.2: Variation in the occupancies of the M1 and M2 sites of synthetic $Mg_{0.6}Fe_{0.4}SiO_3$ orthopyroxene with pressure. Data marked with a cross (†) was collected from crystal #2, as in Table 3.1b.

At low pressures, the silicate tetrahedra are essentially incompressible, with no significant changes in their Si-O bond lengths or internal O-Si-O bond angles. Above ~3.5 GPa, however, the average Si-O bond lengths for silicate tetrahedra in both the "A" and "B" chains begin to decrease linearly with pressure, with no associated angular distortion of the tetrahedra (Figure 3.5). This decrease in the average Si-O bond lengths is mainly due to shortenings of the non-bridging Si-O bonds (ie., the Si-O1 and Si-O2 bonds) at ~3.5 GPa, while the lengths of the bridging Si-O3 bonds remain almost constant to 7.5 GPa (Appendix 1). The linear volume compressibilities of the tetrahedra in the "A" and "B" chains above ~3.5 GPa are calculated to be 0.007(1) GPa^{-1} and 0.006(1) GPa^{-1} respectively.

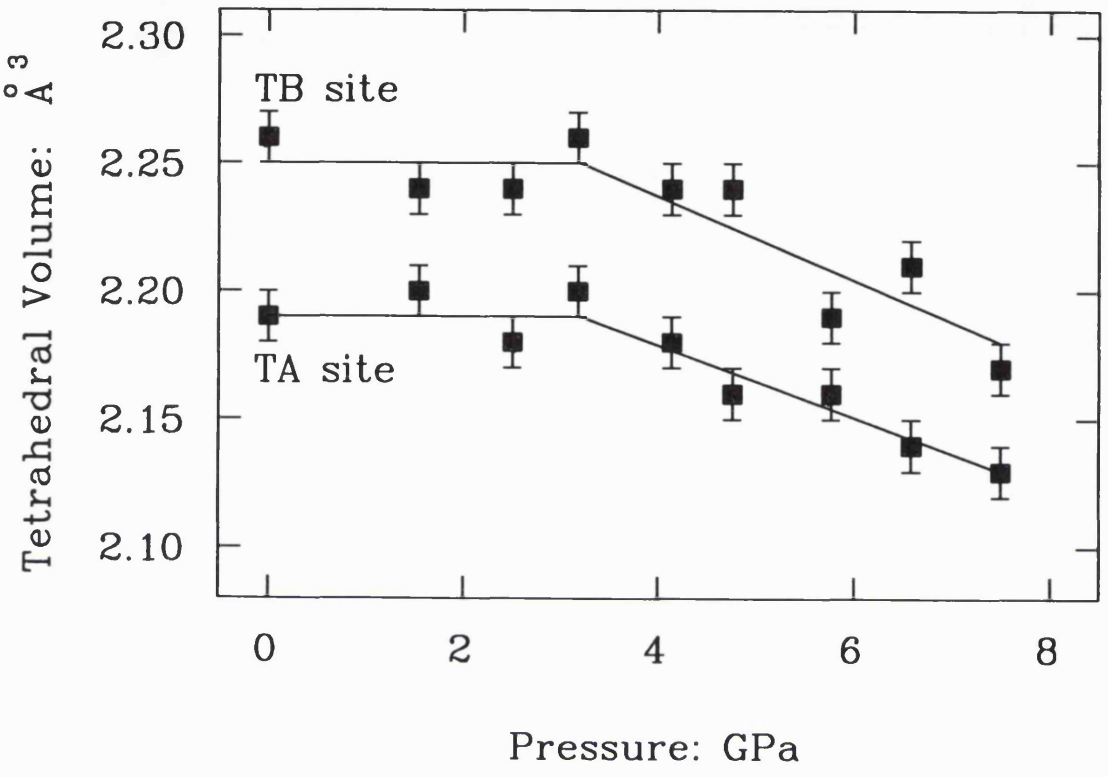

Figure 3.5: Variation in tetrahedral volumes of the TA and TB sites of synthetic $Mg_{0.6}Fe_{0.4}SiO_3$ orthopyroxene to 7.5 GPa, showing a distinct change in compressibilities at ~3.5 GPa.

This change in compressibility of the tetrahedra is accompanied by a discontinuous change in both the degree of kinking of the silicate chains, and the amount of tilt of the constituent tetrahedra from the (100) plane. At pressures below ~3.5 GPa the "B" chain kinks, while above this the rate of kinking is reduced, though it is still in the same direction. The tetrahedra within the "B" chain rotate towards the (100) plane over the whole pressure range studied (Figure 3.6a and b).

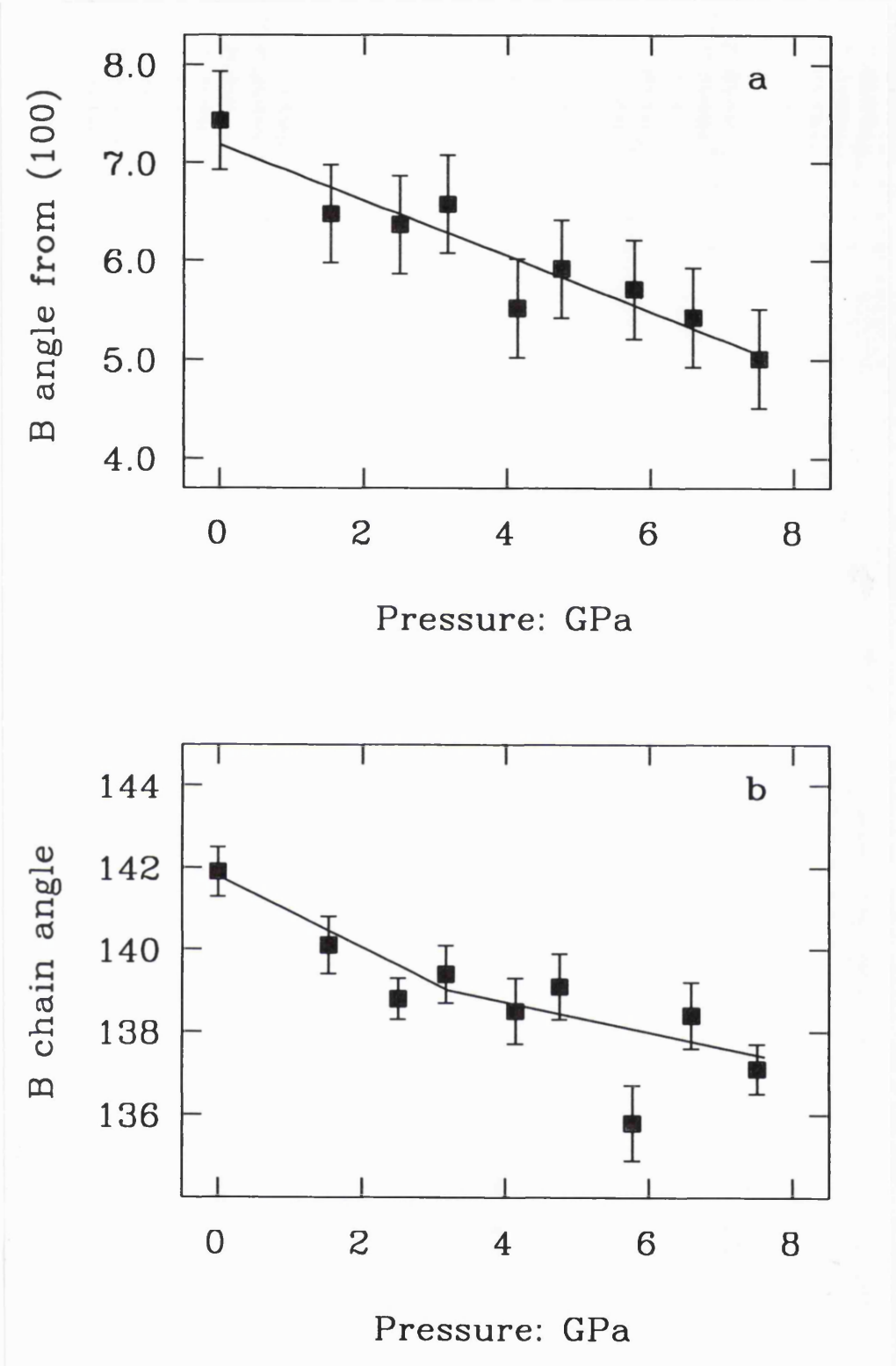

Figure 3.6: a) Variation in the amount of tilt of the bases of the "B"-chain tetrahedra from (100) in synthetic $Mg_{0.6}Fe_{0.4}SiO_3$ orthoenstatite with increasing pressure; b) Changes in the degree of kinking of the "B"-chain with pressure to 7.5 GPa, showing a possible change in behaviour at 3.5 GPa. Note that in both a) and b), the lines are not fitted, but drawn in to illustrate the behaviour of the tetrahedra with pressure.

On the other hand, at low pressures the "A" chain straightens towards the fully-extended position while the bases of its tetrahedra tilt slightly away from the (100) plane to a maximum of ~ 4° from (100); above ~3.5 GPa, this silicate chain begins to kink slightly in the opposite direction, while the bases of its tetrahedra rotate to within 1° of the (100) plane (Figure 3.7a and b).

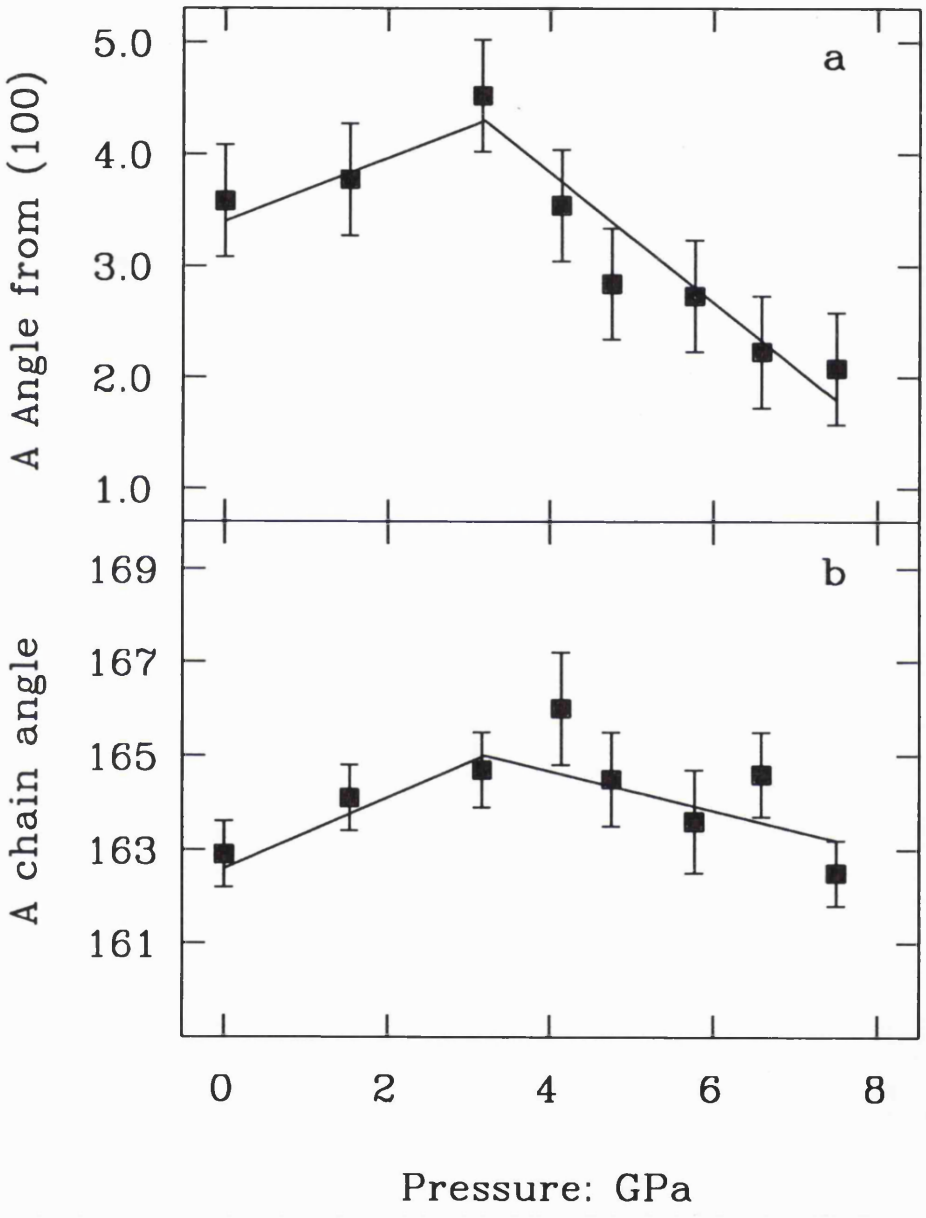

Figure 3.7: a) Variation in the amount of tilt of the bases of the tetrahedra within the "A" chain of synthetic $Mg_{0.6}Fe_{0.4}SiO_3$ orthopyroxene with increasing pressure, showing a distinct discontinuity at 3.5 GPa; b) change in the degree of kinking of the "A" chain with pressure to 7.5 GPa. Note that in both a) and b), the lines are not fitted, but drawn in to illustrate the behaviour with pressure.

3.2.3 Compression of Synthetic $FeSiO_3$ Orthoferrosilite

Intensity data for $FeSiO_3$ orthoferrosilite was collected at approximately 1 GPa intervals, up to ~3.7 GPa; above this pressure, orthoferrosilite transforms irreversibly to the high-pressure C2/c clinoferrosilite phase (see Chapter 5). The variation of selected bond lengths and angles with pressure are given in Table 3.1c; the full list is presented in Appendix 1. Since there is no evidence of compression of the Si-O bonds (or angular deformation of the SiO_4 tetrahedra by "flattening") at any pressure studied, a single mechanism of compression is operating in the $FeSiO_3$ orthoferrosilite below ~3.7 GPa

P (GPa)	0.00	0.83	1.71	2.84	3.65
< M1-O >	2.14 (1)	2.13 (1)	2.13 (1)	2.12(1)	2.10 (1)
M1 volume	12.8 (1)	12.7 (1)	12.7 (1)	12.6 (1)	12.3 (1)
M1 Quad. El.	1.009 (1)	1.009 (1)	1.007 (1)	1.007 (1)	1.007 (1)
< M2-O >	2.22 (1)	2.21 (1)	2.21 (1)	2.20 (1)	2.19 (1)
M2 volume	13.4 (1)	13.2 (1)	13.2 (1)	13.0 (1)	12.9 (1)
M2 Quad. El.	1.070 (1)	1.068 (1)	1.063 (1)	1.063 (1)	1.065 (1)
< TA-O >	1.63 (1)	1.62 (1)	1.62 (1)	1.62 (1)	1.62 (1)
TA volume	2.18 (1)	2.17 (1)	2.15 (1)	2.16 (1)	2.17 (1)
TA Quad. El.	1.008 (1)	1.008 (1)	1.008 (1)	1.008 (1)	1.007 (1)
< TB-O >	1.64 (1)	1.64 (1)	1.63 (1)	1.63 (1)	1.64 (1)
TB volume	2.23 (1)	2.24 (1)	2.21 (1)	2.22 (1)	2.26 (1)
TB Quad. El.	1.005 (1)	1.006 (1)	1.005 (1)	1.004 (1)	1.004 (1)
O3a-O3a-O3a	168.9 (3)	167.2 (9)	167.2 (1.0)	167.6 (1.0)	170.3 (1.2)
O3b-O3b-O3b	143.7 (3)	144.4 (8)	140.9 (8)	139.9 (9)	140.1 (9)
> A to (100)	4.5(5)	4.6(5)	4.8(5)	4.0(5)	3.4(5)
> B to (100)	7.0(5)	7.2(5)	7.0(5)	6.2(5)	6.4(5)

Table 3.1c: Selected bond lengths and angles for $FeSiO_3$ orthoferrosilite. The symbols are the same as those described for Table 3.1a.

To accommodate increasing pressure, the M1 and M2 octahedra of the $FeSiO_3$ orthoferrosilite compress steadily; their linear volume compressibilities are 0.009(2) GPa^{-1} and 0.010(1) GPa^{-1} respectively. The compression of the larger M2 octahedra is mainly accommodated by the rapid shortening of the long M2-O3a and M2-O3b bonds, leaving the lengths of the four remaining M2-O bonds essentially unchanged by ~ 3.7 GPa. Compression of the M1 site is achieved by the shortening of all the M1-O bonds at a similar rate (Appendix 1). Both octahedra become slightly less deformed over the ~ 3.7 GPa pressure range studied. In contrast to this, the silicate tetrahedra remain incompressible over the whole pressure range, with no significant reduction in either the tetrahedral volumes or the average Si-O bond lengths below ~3.7 GPa (Figure 3.8). Although the O-rotated "A" chain does not straighten significantly towards the fully-extended position with increasing pressure, its constituent tetrahedra rotate slightly towards the (100) plane. The tetrahedra in the "B" chain also rotate somewhat towards the (100) plane; this O-rotated chain does become more kinked as the pressure is increased (Figures 3.9a-d).

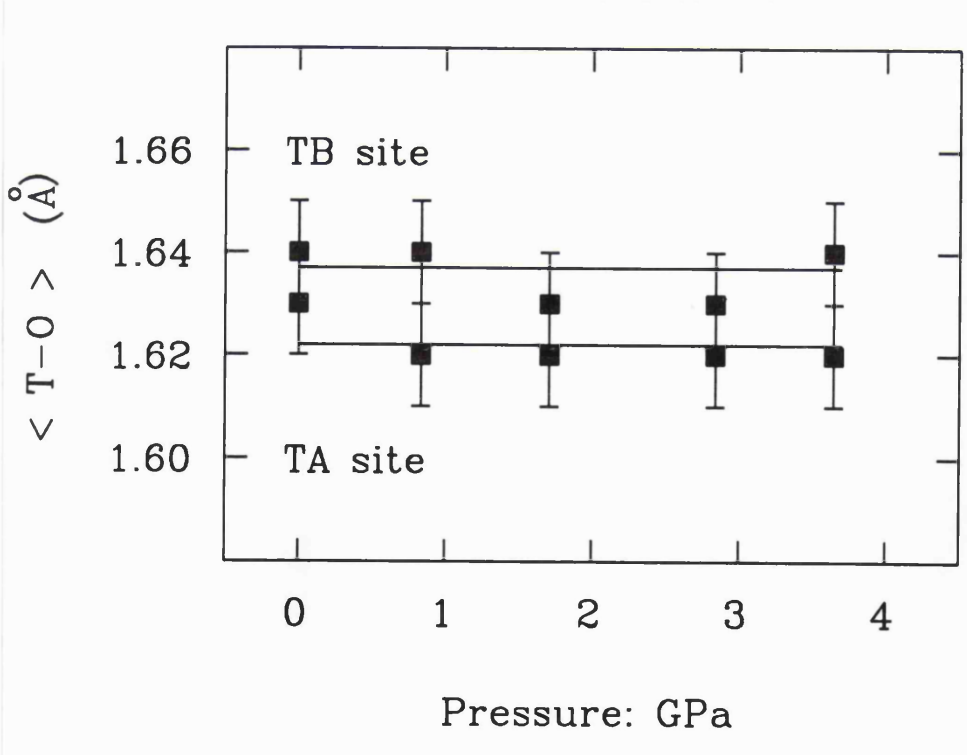

Figure 3.8: Variation in the average tetrahedral bond length of $FeSiO_3$ orthoferrosilite to 3.7 GPa; note that there is no significant shortening of the bonds over this pressure range.

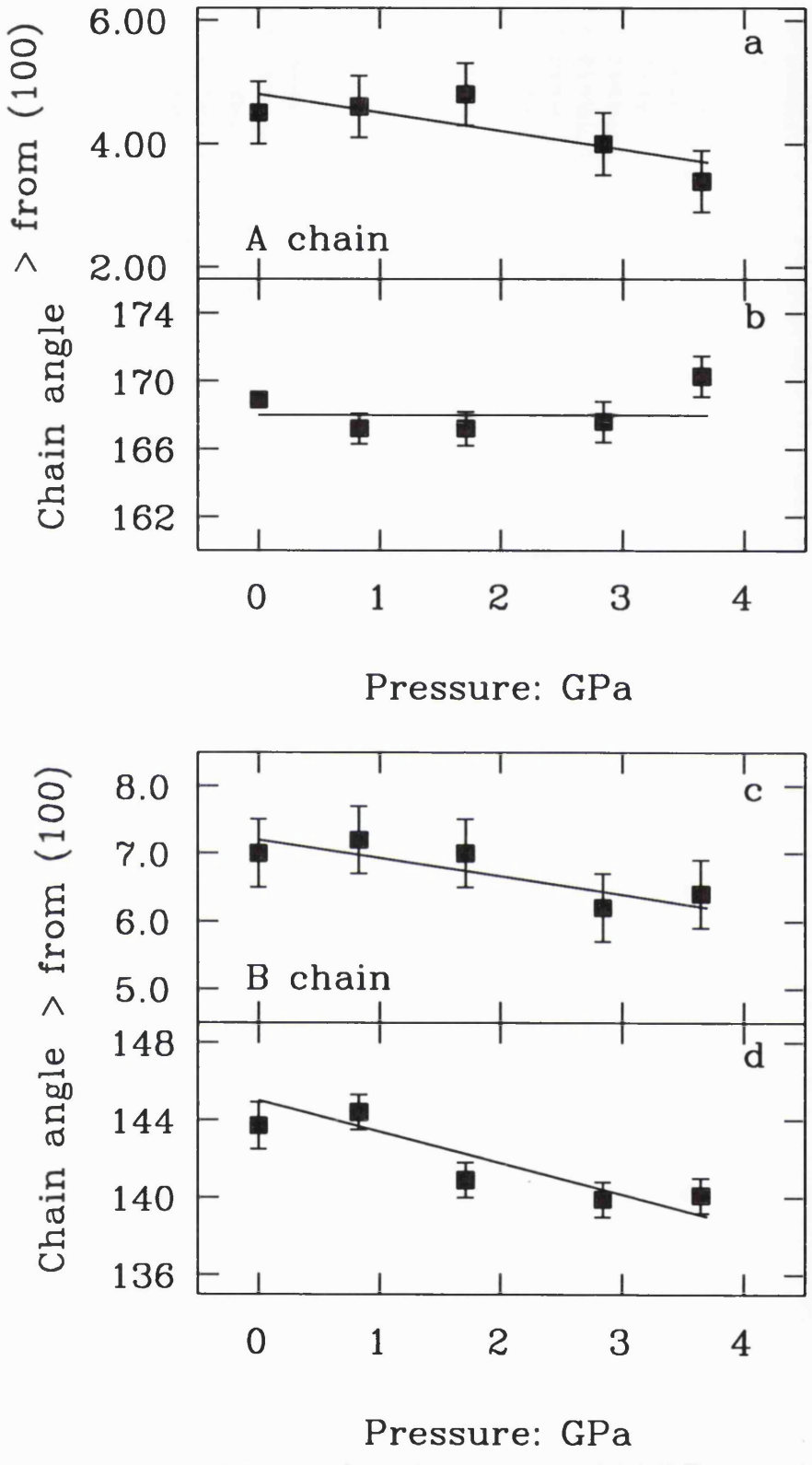

Figure 3.9: Variations in a) the amount of tilt of the bases of the "A"-chain tetrahedra in synthetic $FeSiO_3$ orthoferrosilite from (100) with increasing pressure; b) the degree of kinking of the "A"-chain with pressure to 3.7 GPa; c) the amount of tilt of the bases of the tetrahedral "B"-chain from (100) with increasing pressure; and d) the degree of kinking of the "B"-chain with pressure.

3.2.4 Compression of Natural Orthopyroxene

Structural data was also collected at pressure intervals of ~1 GPa to 6.0 GPa for a natural orthopyroxene (OPX2). All the refined bond lengths and angles are given in Appendix 1, while selected bond lengths and angles, and polyhedral volumes and distortions, are presented in Table 3.1d.

P (GPa)	0.00	1.04	1.90	3.00
< M1-O >	2.06 (2)	2.05 (2)	2.03 (2)	2.01 (2)
M1 volume	11.6 (2)	11.2 (3)	10.9 (3)	10.6 (3)
M1 Quad. El.	1.011 (1)	1.014 (2)	1.017 (2)	1.017 (2)
< M2-O >	2.15 (2)	2.13 (2)	2.12 (2)	2.12 (2)
M2 volume	12.3 (2)	12.0 (2)	11.8 (2)	11.9 (3)
M2 Quad. El.	1.054 (1)	1.054 (1)	1.056 (1)	1.053 (1)
< TA-O >	1.64 (1)	1.63 (1)	1.64 (2)	1.65 (2)
TA volume	2.20 (2)	2.19 (4)	2.24 (4)	2.27 (5)
TA Quad. El.	1.014 (1)	1.011 (1)	1.013 (2)	1.013 (2)
< TB-O >	1.66 (1)	1.68 (1)	1.67 (2)	1.66 (2)
TB volume	2.32 (2)	2.39 (3)	2.38 (3)	2.32 (3)
TB Quad. El.	1.005 (1)	1.008 (2)	1.009 (2)	1.007 (2)
O3a-O3a-O3a	161.1 (7)	160.7 (8)	159.5 (1.0)	161.4 (8)
O3b-O3b-O3b	138.5 (6)	136.7 (7)	136.8 (9)	136.3 (9)
> A to (100)	3.9 (1.0)	2.3 (1.0)	3.7 (1.0)	3.7 (1.0)
> B to (100)	5.1 (1.0)	6.1 (1.0)	7.4 (1.0)	8.7 (1.0)

Table 3.1d: Selected bond lengths and angles for natural orthopyroxene OPX2 to ~ 6 GPa. Note that the symbols used are the same as those described for $MgSiO_3$ orthoenstatite in Table 3.1a.

P (GPa)	4.03	4.93	6.01
< M1-O >	2.03 (2)	2.03 (2)	2.00 (2)
M1 volume	11.1 (3)	11.0 (3)	10.5 (3)
M1 Quad. El.	1.008 (3)	1.011 (2)	1.014 (2)
< M2-O >	2.13 (2)	2.13 (2)	2.11 (2)
M2 volume	12.0 (3)	12.0 (3)	11.7 (3)
M2 Quad. El.	1.051 (2)	1.052 (2)	1.052 (2)
< TA-O >	1.64 (2)	1.62 (3)	1.63 (2)
TA volume	2.21 (4)	2.17 (5)	2.18 (4)
TA Quad. El.	1.012 (2)	1.009 (2)	1.011 (2)
< TB-O >	1.64 (2)	1.64 (3)	1.67 (3)
TB volume	2.25 (4)	2.24 (5)	2.35 (6)
TB Quad. El.	1.007 (2)	1.008 (2)	1.007 (2)
O3a-O3a-O3a	162.1 (1.1)	163.3 (1.0)	160.7 (1.2)
O3b-O3b-O3b	137.2 (1.1)	136.6 (9)	135.9 (1.1)
> A to (100)	2.3 (1.0)	0.9 (1.0)	0.9 (1.0)
> B to (100)	5.1 (1.0)	8.2 (1.0)	6.5 (1.0)

Table 3.1d: (cont.).

From an exhaustive list of the occupancies of the M1 and M2 sites in bronzites and hypersthenes with space group Pbca (Cameron and Papike, 1980), it is assumed that all the available Ca^{2+} will be present in the M2 sites of the orthopyroxene. Compression of the Mg^{2+}-rich M1 sites occurs by the shortening of all the M1-O bonds by a similar amount. Although the initially long M2-O3 bonds compress faster than the rest of the M2-O bonds (which, in this natural orthopyroxene, are almost incompressible to 6 GPa), the M2-O3b bonds compress no faster than the adjacent M2-O3a bonds (Appendix 1). The linear volume compressibilities of the M1 and M2 cation sites are calculated from the experimental data to be 0.013(4) GPa^{-1} and 0.005(2) GPa^{-1} respectively. There is no observable change in the degree of distortion of either the M1 or M2 sites below 6 GPa (Table 3.1d).

There are also no significant changes in the Si-O bond lengths or tetrahedral volumes at any pressure below 6 GPa (Figure 3.10), indicating that the tetrahedra are incompressible to this pressure. The tetrahedra within the "A" chain tilt by approximately 3° towards the (100) plane as the pressure is increased to 6 GPa, while those in the "B" chain tilt slightly away from this (100) plane. Although the "A" chain only straightens very slightly upon pressure increase, the "B"-chain kinks somewhat more away from the straight-through position (Figure 3.11a and b).

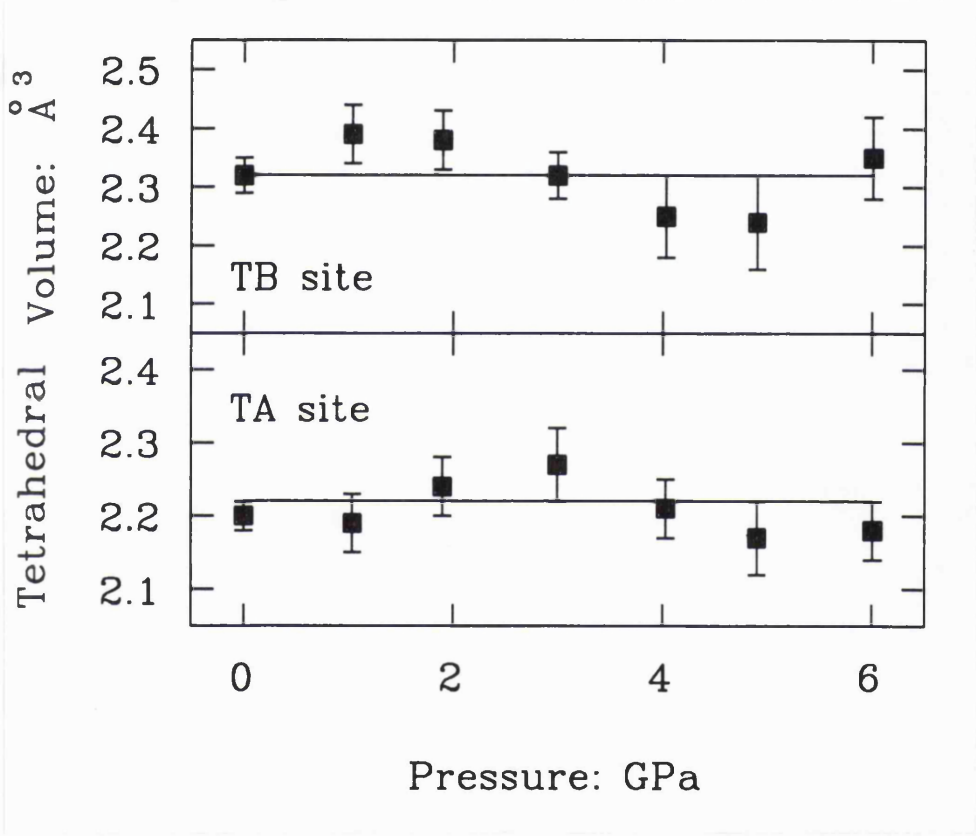

Figure 3.10: The volumes of the silicate tetrahedra in both "A"- and "B"-chains of the natural OPX2 orthopyroxene, measured to ~6 GPa, showing no significant compression at any pressure.

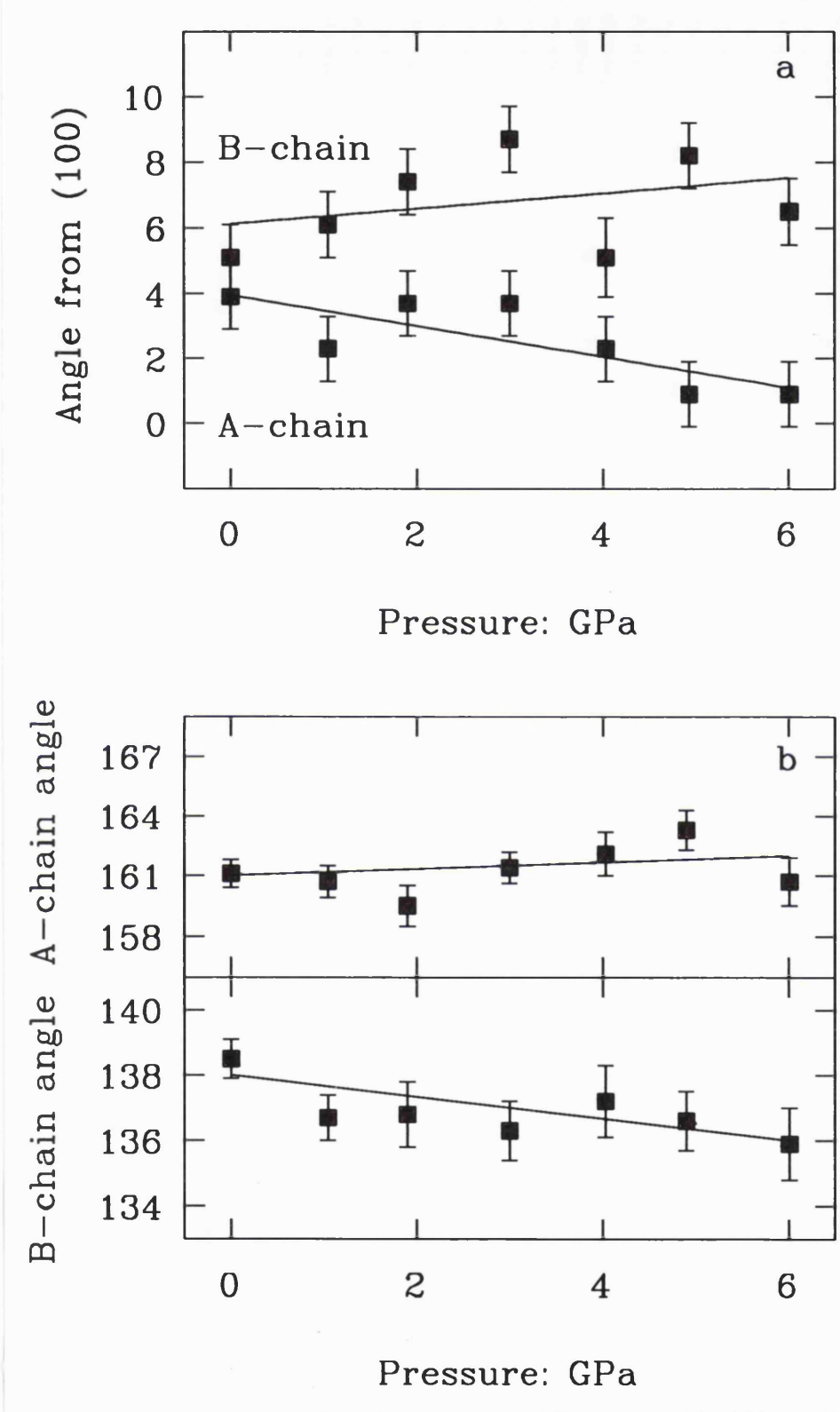

Figure 3.11: a) Changes in the amount of tilt of the bases of the tetrahedral "A"- and "B"-chains in natural OPX2 orthopyroxene from (100) with increasing pressure; b) Variation in the degree of kinking of the "A"- and "B"-chains with pressure to 6 GPa.

3.3 DISCUSSION

a) Compression of the M1 and M2 Octahedra

In orthopyroxenes of intermediate composition along or near the $MgSiO_3$ - $FeSiO_3$ join, there is a tendency for the Mg^{2+} to be more concentrated in the M1 site while the iron (and Ca^{2+} in natural samples) preferentially order onto the M2 site, which is larger and considerably more distorted than the M1 site (this ordering scheme being first detailed by Ghose, 1965). Several further studies on the M1 and M2 site populations and distortions of synthetic $(Mg,Fe)SiO_3$ orthopyroxenes (eg. Cameron and Papike, 1980; Domeneghetti and Steffen, 1992) confirm the ordering scheme proposed by Ghose (1965), and also demonstrate that while the distortion of the M1 site does not significantly increase with increasing Fe^{2+} content, the corresponding distortion of the M2 site does increase considerably. While the state of order of Mg^{2+} and Fe^{2+} can be changed by high-temperature annealing, no movement of the cations between octahedral sites during compression in the DAC was anticipated, because re-ordering is a thermally activated process. The refined distribution of Mg^{2+} and Fe^{2+} between the M1 and M2 sites of the synthetic $Mg_{0.6}Fe_{0.4}SiO_3$ pyroxene studied at high pressure (Table 3.2) confirms that there was no detectable change in the cation ordering.

The presence of Fe^{2+} (and Ca^{2+} in the natural orthopyroxene) in the M2 cation sites of the $(Mg,Fe)SiO_3$ orthopyroxene causes these octahedral sites to be initially more distorted (Table 3.3) than their counterparts in the Mg^{2+}-rich orthopyroxenes. As observed by Domeneghetti and Steffen (1992), the initial distortions of the M1 sites in the orthopyroxenes are essentially independent of the cation contained within the sites, (approximately 1.009(1) for *all* the orthopyroxene samples studied here). From structural analyses at pressure of the three synthetic orthopyroxenes (with compositions $MgSiO_3$, $Mg_{0.6}Fe_{0.4}SiO_3$, and $FeSiO_3$), both the M1 and M2 octahedra were observed to become more regular with increasing pressure, independent of the composition of the orthopyroxene. However, it is interesting to note that the degrees of distortion of the M1 and M2 octahedra in the natural OPX2 orthoenstatite remained essentially unchanged at all pressures (Table 3.1a-d).

Composition	%Mg^{2+} in M1	M1 distortion	%Mg^{2+} in M2	M2 distortion
$MgSiO_3$	100.0	1.009 (1)	100.0	1.049 (1)
$Mg_{0.6}Fe_{0.4}SiO_3$	85 (2)	1.010 (1)	45 (3)	1.063 (1)
$Mg_{0.3}Fe_{0.7}SiO_3$	52 (2)	1.009 (1)	23 (3)	1.064 (2)
$FeSiO_3$	0.0	1.009 (1)	0.0	1.070 (1)

Table 3.3: Distribution of cations in the synthetic $(Mg,Fe)SiO_3$ orthopyroxenes at ambient conditions (determined from the octahedral occupancies refined during structure refinements). The distortions presented in the above table are simply the mean quadratic elongations of the polyhedra (Equation 3.1).

In both the synthetic and natural $(Mg,Fe)SiO_3$ orthopyroxenes studied, the average M1-O and M2-O bond lengths and M1 and M2 polyhedral volumes decreased steadily with increasing pressure. Although in *all* the orthopyroxene samples studied, both synthetic and natural, all six M1-O bonds in each octahedron shortened at approximately the same rate, the anomalously long M2-O3 bonds initially compressed much faster than the other M2-O bonds (see also Ralph and Ghose, 1980). The presence of Fe^{2+} in the M2 site of the synthetic $(Mg,Fe)SiO_3$ orthopyroxenes results in enhanced compressibility of their M2-O3b bonds relative to the corresponding M2-O3b bonds in the Fe^{2+}-free orthoenstatite; the linear compressibilities of the Fe2-O3b and Mg2-O3b bonds (calculated below ~4 GPa) are 0.0196(7) GPa^{-1} and 0.012(1) GPa^{-1} respectively, while the linear compressibilities of both the Fe2-O3a and Mg2-O3a bonds are 0.005(2) GPa^{-1}. The remaining four M2-O bonds in the M2 octahedron are essentially incompressible, to 8.1 GPa, irrespective of the cation contained within the M2 site. This enhanced compressibility of the long M2-O3b bond in the iron-containing orthopyroxenes would therefore account for the greater overall compressibility observed for the Fe^{2+}-rich octahedral sites of the synthetic $(Mg,Fe)SiO_3$ pyroxenes (see Table 3.4).

Composition	Pressure range	β_{M1} (GPa^{-1})	β_{M2} (GPa^{-1})
$MgSiO_3$	0.0 - 8.1 GPa	0.0078 (6)	0.0075 (6)
$Mg_{0.6}Fe_{0.4}SiO_3$	0.0 - 7.5 GPa	0.005 (2)	0.008 (1)
$FeSiO_3$	0.0 - 3.7 GPa	0.009 (2)	0.010 (1)
OPX2	0.0 - 6.0 GPa	0.013 (4)	0.005 (2)

Table 3.4: Linear compressibilities of M1 and M2 octahedra in $(Mg,Fe)SiO_3$ orthopyroxenes.

Due to the limited pressure range of the data for the $FeSiO_3$ orthoferrosilite and the relatively poor data quality of the $Mg_{0.6}Fe_{0.4}SiO_3$ orthopyroxene (since two different crystals were used for structure determinations), only *linear* volume compressibilities of the M1 and M2 octahedra were calculated for the remaining synthetic orthopyroxene phases; these are summarised in Table 3.4, with the linear compressibilities of the octahedra in the $MgSiO_3$ orthoenstatite for comparison. Within the experimental uncertainties, the linear volume compressibilities of the M1 and M2 octahedra are identical within each of the synthetic orthopyroxene samples. The presence of Fe^{2+} in the octahedral sites of two of these samples causes their octahedral sites to become relatively more compressible than the corresponding Fe^{2+}-poor ones; this is clearly seen for the $FeSiO_3$ sample, where both the M1 and M2 sites are more compressible than their counterparts in the $MgSiO_3$ orthoenstatite.

In contrast to this, however, the Mg^{2+}-containing M1 sites of the natural orthopyroxene OPX2 are almost twice as compressible as its M2 sites over the 6 GPa pressure range studied. In other words, while the M1 site of the natural orthopyroxene is somewhat more compressible than the M1 sites of the synthetic orthopyroxenes, its M2 site is significantly stiffer, due to the additional presence of Ca^{2+} in the site. Therefore in order for the orthopyroxene to accommodate pressure increase, compression occurs preferentially at the softer M1 sites.

Comparison of the rate of compression of the M2-O3 bonds of this natural orthopyroxene OPX2 and the synthetic $MgSiO_3$ orthoenstatite (shown schematically

in Figure 3.12) shows that while the M2-O3a and M2-O3b bonds in the natural sample compress at the same rate (with linear compressibilities, β, of 0.006(1) GPa^{-1} and 0.005(1) GPa^{-1} respectively) as the M2-O3a bond of the synthetic orthoenstatite (with β = 0.005(2) GPa^{-1}), the M2-O3b bond in the $MgSiO_3$ orthoenstatite compresses significantly faster than all these (with β = 0.012(1) GPa^{-1}). This remarkably fast compression of the M2-O3b bond in the synthetic $MgSiO_3$ orthoenstatite is responsible for the high value of K_0' in the EOS of the orthoenstatite at low pressures (see Chapter 4). Conversely, the relatively slower rate of compression of the M2-O3b bond in the natural OPX2 orthopyroxene is the predominant cause of the somewhat lower value of K_0' in its EOS (see Chapter 4).

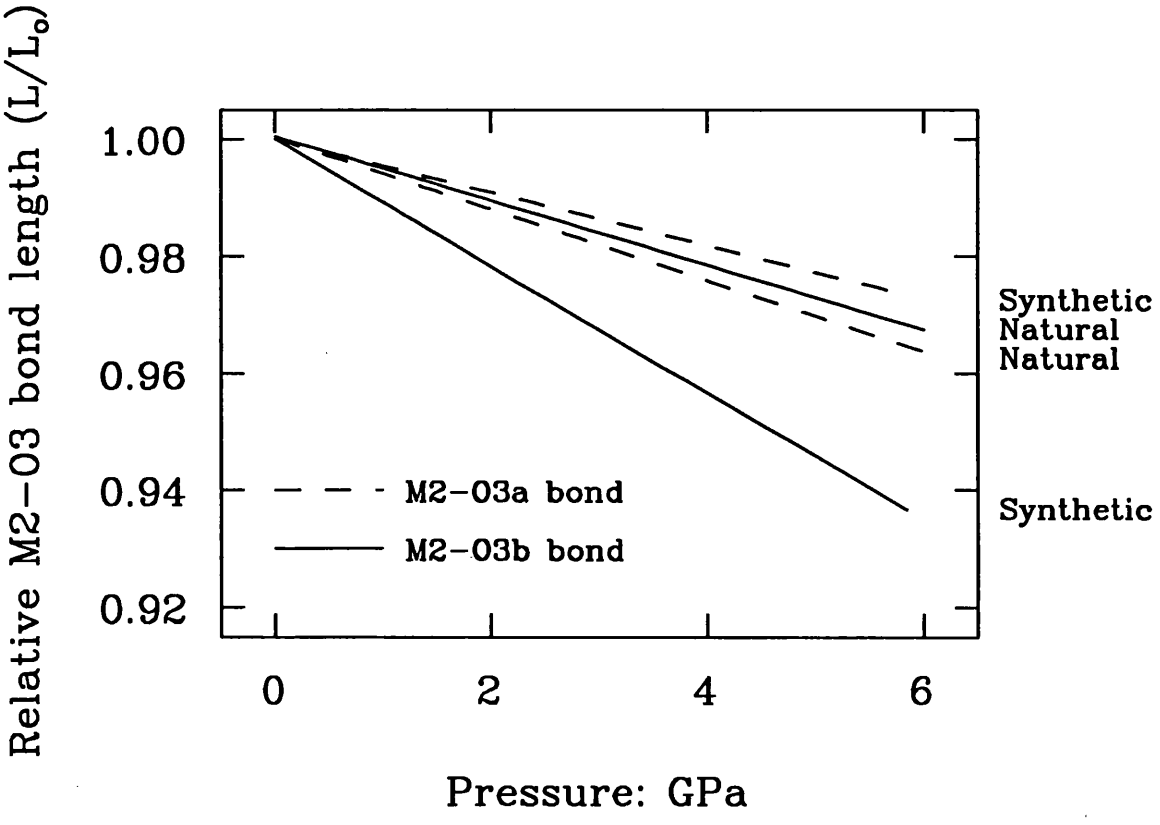

Figure 3.12: Schematic diagram of the differential compression of the M2-O3a and M2-O3b bonds in the synthetic $MgSiO_3$ orthoenstatite and natural OPX2 orthopyroxene samples, to ~6 GPa.

b) Compression of the Tetrahedra

Previous compression experiments on $(Mg,Fe)SiO_3$ orthopyroxenes have regarded Si-O bonds to be incompressible (eg., Levien and Prewitt, 1981; Hazen and Finger, 1977). The SiO_4 tetrahedra in all the synthetic orthopyroxenes studied here are indeed incompressible at low pressures, with no significant change in either Si-O bond lengths or the internal O-Si-O bond angles. Although a single structure refinement of a synthetic $MgSiO_3$ orthoenstatite at 2.1 GPa (Ralph and Ghose, 1980) showed some shortening of the Si-O bonds within the tetrahedra of the "A" chain by 2.1 GPa, both their study and this work are agreed that at low pressures the average SiB-O bond length is incompressible within the experimental uncertainties.

However, at pressures above P_{cr} (defined as a "crossover pressure" between two different compression regimes: 4 GPa for $MgSiO_3$ orthoenstatite (Figure 3.4), and ~3.5 GPa for $Mg_{0.6}Fe_{0.4}SiO_3$ orthopyroxene (Figure 3.5)), there is considerable shortening of the Si-O bonds. While the O-Si-O bond angles remain unchanged within their estimated standard deviations (indicating that there is no associated angular distortion of the SiO_4 tetrahedra), the tetrahedral bond lengths decrease significantly, resulting in a decrease in the volumes of the two SiO_4 tetrahedra. In synthetic orthopyroxenes of both compositions, compression of the tetrahedra above P_{cr} is predominantly caused by the shortening of non-bridging Si-O bonds rather than the bridging Si-O3 bonds. None of the Si-O bond lengths of $FeSiO_3$ orthoferrosilite shorten significantly in the pressure range for which structural determinations were performed (Figure 3.8). However, this range is limited to ~4 GPa because of the instability of the orthoferrosilite (see Chapter 5). It is therefore not possible to determine whether the $FeSiO_3$ undergoes a similar compression mechanism change above 3.65 GPa.

The linear volume compressibilities (β_V) of the SiO_4 tetrahedra in both the "A" and "B" silicate chains of the synthetic $(Mg,Fe)SiO_3$ orthopyroxenes in the higher pressure regime are summarised in Table 3.5. Since these compressibilities in both the synthetic Fe^{2+}-free orthoenstatite and Fe^{2+}-containing orthopyroxene are all identical within the *esd*'s, the volume compressibilities of the silicate tetrahedra must be independent of the bulk composition of the synthetic orthopyroxene.

Composition	Pressure range	β_{TA} (GPa^{-1})	β_{TB} (GPa^{-1})
$MgSiO_3$	4.1 - 8.1 GPa	0.006 (1)	0.006 (1)
$Mg_{0.6}Fe_{0.4}SiO_3$	3.5 - 7.5 GPa	0.007 (1)	0.006 (1)

Table 3.5: Linear compressibilities of SiO_4 tetrahedra of Mg^{2+}-rich orthopyroxenes.

In contrast to the behaviour of the synthetic orthopyroxenes, the tetrahedral bond lengths in the natural OPX2 orthopyroxene do not significantly shorten at any pressure below 6 GPa (Figure 3.10). In addition, there is no observable change in the angular distortion of either tetrahedral site. As a result of this rigidity of the SiO_4 tetrahedra at all pressures, there is a complete absence of any significant kinking of the silicate chains of the natural orthopyroxene with increasing pressure.

High pressure studies of other silicate minerals have shown that SiO_4 tetrahedra are generally incompressible over the pressure range of 0 to ~5 GPa. The few studies that have been performed at pressures significantly in excess of 5 GPa have, however, revealed compression of SiO_4 tetrahedra that is due to, as in the orthopyroxenes, shortening of the Si-O bonds rather than due to deformation (ie. flattening) of the tetrahedra. The compressibility of the tetrahedra in $MgSiO_3$ orthoenstatite is intermediate between that observed for Mg_2SiO_4 olivine, for which a β_V of 0.0071(3) GPa^{-1} can be calculated from the data to 14.9 GPa of Kudoh and Takeuchi (1985), and that of andradite to 19 GPa (Hazen and Finger, 1989) for which β_V = 0.0050(4) GPa^{-1}.

c) Overall compression of structures

Because the octahedral sites are linked directly to the tetrahedral chains of the orthopyroxenes, relative differences in the compressional behaviour of the octahedral sites and the configurations of the silicate chains between samples of different bulk compositions are important in understanding the reasons for the different responses of the natural and synthetic orthopyroxenes to increasing pressure.

It was seen in the previous section that although all the M1-O bonds within a given M1 octahedron (in both natural and synthetic orthopyroxenes) shorten at a similar rate, the M2-O3 bonds shorten more quickly than the other M2-O bonds within the same M2 octahedron. Moreover, while the M2-O3b bonds in all the synthetic orthopyroxenes compress significantly faster than the adjacent M2-O3a bonds, the effect of increasing the overall Fe^{2+} content is to further increase the relative compressibility of the M2-O3b bonds compared to the remaining five M2-O bonds in the M2 octahedron. On the other hand, the M2-O3a and M2-O3b bonds in the natural sample compress at almost identical rates. The presence of the large Ca^{2+} contained within the M2 sites of the natural orthopyroxene must be the cause of these M2 sites being significantly less compressible than either their Ca^{2+}-free equivalents in synthetic $(Mg,Fe)SiO_3$ orthopyroxenes or the neighbouring M1 sites, which appear to accommodate most of the compression of the natural samples.

Changes in the degrees of kinking or extension of the tetrahedral silicate chains with increasing pressure are dictated by (or, alternatively, result from) the relative compressibilities of the adjoining octahedral sites, since the tetrahedra within the chains are connected via their apical O3 atoms to the M2 cations. It is therefore surprising to note that whilst the absolute amount of compression of the individual M2-O3b bonds is highly dependent on the nature of the cation contained within the M2 site, the relative changes in the degrees of kinking and tilting of the silicate chains in all three synthetic $(Mg,Fe)SiO_3$ orthopyroxenes are almost identical in both the low and high pressure compression regimes (Tables 3.1a-c). There is therefore little effect on the high-pressure behaviour of the silicate chains resulting from the substitution of Fe^{2+} for Mg^{2+} in the octahedral sites of the synthetic orthopyroxenes.

Since the presence of a significant amount of Ca^{2+} in the M2 sites of the natural orthopyroxene causes major differences in the compressional behaviour of the octahedra, the behaviour of the silicate chains with pressure in the natural sample are

also different. The "B" chain kinks significantly less than the "B" chains in any of the synthetic orthopyroxenes, whilst the conformation of the "A" chains in the natural sample remain virtually unchanged with the 6 GPa pressure increase. There are no observable discontinuities in either the directions or rates of the degrees of tilting or kinking of these chains at any pressure below 6 GPa, indicating that there is no change in compression mechanism of the natural Ca^{2+}-containing orthopyroxene in this pressure range. This different behaviour of the natural and synthetic samples is important when determining the EOS's of the different phases (see Chapter 4).

The presence of Ca^{2+} in the M2 sites of the natural orthopyroxene causes these sites to become significantly stiffer than the adjacent M1 sites, thus reducing in the amount of chain rotation that is possible, and inhibiting any change in compression mechanism. It was therefore expected that a single structural element could be identified as having reached a critical value in the synthetic samples but not in the natural samples at P_{cr}, which is responsible for inducing the change in compression mechanism in the synthetic orthopyroxenes between 3.5 GPa and 4 GPa. While the estimated standard deviations (*esd*'s) of suitable candidate bond lengths and angles were relatively large, tentative identification of the critical importance of the O3-O3 bond lengths was attained. It is possible that when the O3a-O3a bond length compresses beyond ~2.60Å, and the O3b-O3b bond length below ~2.75Å, the change in compression mechanism is initiated. Although neither bond length reaches these values (beyond their *esd*'s) in the natural orthopyroxene sample, unambiguous confirmation that these O3-O3 bond lengths are the most important structural elements in determining the pressure (and possibility) of a change in compression mechanism of a Ca^{2+}-poor $(Mg,Fe)SiO_3$ orthopyroxene must await more precise high-pressure structural determinations.

3.4 COMPARISON WITH HIGH TEMPERATURE BEHAVIOUR OF ORTHOPYROXENES

It is often assumed that pressure and temperature have opposite effects on the structure of a given phase. Three high-temperature single-crystal X-ray diffraction studies of $(Mg,Fe)SiO_3$ orthopyroxenes have been undertaken - that of Yang and Ghose (1995) for a synthetic $Mg_{0.75}Fe_{0.25}SiO_3$ orthopyroxene, that of Sueno et al. (1976) for synthetic $FeSiO_3$ orthoferrosilite, and that of Smyth (1973) for a natural orthopyroxene with approximate composition $Mg_{0.30}Fe_{0.68}Ca_{0.015}SiO_3$.

3.4.1 Summary of High Temperature Behaviour

In situ structure determinations of the synthetic $Mg_{0.75}Fe_{0.25}SiO_3$ orthopyroxene at temperatures up to 1027°C (Yang and Ghose, 1995) have shown that the "B" chain straightens much faster than the "A" chain, becoming the slightly more extended of the two by 1027°C. Since the conformations of the two chains are similar at such high temperatures, the sizes, distortions and amount of tilt from (100) of the "A" and "B" tetrahedra also become more similar. This involves some "compression" of the tetrahedra within the "B" chain, while the volumes of the tetrahedra within the "A" chains remain unchanged. While the M1 octahedron remains in regular coordination at all temperatures, the coordination of the M2 site becomes seven-fold between 927°C and 1027°C, above which it becomes six-fold again. This change of coordination of the M2 site in this Mg^{2+}-rich orthopyroxene of intermediate composition (Yang and Ghose, 1995) is due to a switching of the bridging O3b atoms coordinated with the M2 cation, due to the rapid straightening of the tetrahedral "B" chain between 927°C and 1027°C. The possibility of a distinct structural state of the orthopyroxene at 1027°C (a so-called "transitional" structure between orthopyroxene and protopyroxene) is also discussed by these authors.

As a result of increasing the temperature to 980°C, Sueno et al. (1976) observed expansion of the Fe1 and Fe2 octahedra of synthetic $FeSiO_3$ orthoferrosilite, virtually no change (or possibly a slight decrease) in tetrahedral volumes, and

significant straightening of both the silicate chains until the "A" chain was almost fully extended. The decrease in Si-O bond lengths observed (Sueno et al., 1976) for the tetrahedra in the "B" chain is slightly greater than the decrease in the bond lengths of the "A" tetrahedra, causing the size difference between the two tetrahedra to be reduced. Note that this is consistent with other pyroxenes (eg. Cameron and Papike, 1980), where the larger silicate tetrahedra occur in the more kinked chains. Although both "A" and "B" chains straighten towards the fully extended position as the temperature is increased (Sueno et al., 1976), unlike the Mg^{2+}-rich orthopyroxene (Yang and Ghose, 1995), the "A" chain of the $FeSiO_3$ orthoferrosilite remains significantly more extended than the "B" chain at all temperatures below 980°C, with the rate of straightening of both chains increasing with increasing temperature.

Both Fe1 and Fe2 octahedra expand substantially with increasing temperature, with mean thermal expansion coefficients (defined in Sueno et al., 1976) of 5.01 for the Fe1 octahedra, and 8.40 for the Fe2 octahedra. Due to anomalous behaviour of the O3 atoms between 600°C and 800°C, the coordination of the Fe2 polyhedra in the orthoferrosilite changes from six to seven in this temperature range, and returns to six-coordinate at higher temperatures, assuming that atomic separations below 3.00Å represent bond lengths. Although the width of this temperature interval of the stability of an M2 site with seven-fold coordination is greater than that observed in the synthetic Mg^{2+}-rich orthopyroxene (Yang and Ghose, 1995), it occurs at significantly lower temperatures than the Mg^{2+}-rich sample.

Smyth (1973) observed similar structural trends of his natural Fe^{2+}-rich orthopyroxene with increasing temperature to 850°C. The silicate tetrahedra also showed zero or slightly negative thermal expansion, while the volumes of both the M1 and M2 octahedra increased by a significant amount. Unlike the iron end-member (Sueno et al., 1976), the thermal expansivity of the M1 octahedra was found (Smyth, 1973) to be slightly greater than that of the M2 octahedra. Both "A" and "B" chains straightened considerably over the temperature range studied, while at all temperatures the "B" chain remained more kinked than the "A" chain. This is again unlike the synthetic Mg^{2+}-rich sample (Yang and Ghose, 1995) where the tetrahedral "B" chain

became more extended than the "A" chain above ~ 927°C. This straightening of the "B" chain in the natural sample (Smyth, 1973) caused the coordination of the M2 site to increase from six to seven at approximately 500°C, again assuming that atomic separations below 3.00Å represent bond lengths.

3.4.2 Comparison with Compressional Behaviour

In many structures, the effects of pressure and temperature are effectively opposite (eg., Hazen and Finger, 1982). Comparison of the compression data presented in Section 3.2 with the published high temperature refinements of orthopyroxene described in Section 3.4.1 shows that the overall situation in orthopyroxenes is far more complex. However, the octahedrally coordinated M1 and M2 sites do behave in an inverse manner. While they become increasingly regular with steadily decreasing volumes upon pressure increase, both the M1 and M2 octahedra become significantly larger and highly distorted (and even seven-coordinate over a short temperature interval) with increasing the temperature (Smyth, 1973; Sueno et al., 1976; Yang and Ghose, 1995). Although this mode of behaviour is independent of the composition of the orthopyroxene, the precise amounts of compression, expansion or deformation of the M1 and M2 sites are, of course, highly dependent on the cations contained within the sites.

The behaviour of the tetrahedral silicate chains at high temperatures and high pressures are not quite as straightforward. In *all* the natural and synthetic samples studied, the tetrahedral "A" and "B" chains straighten as a result of increasing the temperature, irrespective of the bulk composition of the orthopyroxene. However, although the "B" chains in all the natural and synthetic orthopyroxene samples studied do indeed kink during compression (in the low-pressure compression regime at ambient temperature), the "A" chains all straighten to a greater or lesser degree towards from the straight-through position on increasing pressure. The variation in the degree of tilt of the silicate tetrahedra from the (100) plane with increasing temperature was calculated from the reported structures of Yang and Ghose (1995), Smyth (1973) and Sueno et al. (1976); that of the natural sample (Smyth, 1973) is shown in Figure 3.13.

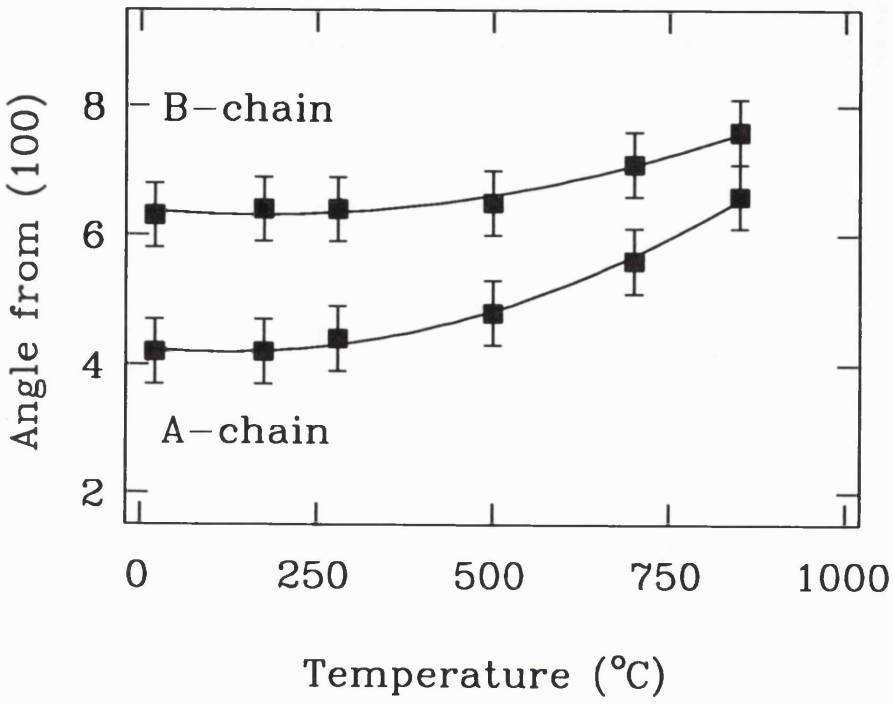

Figure 3.13: Variation in the angle of tilt of the silicate tetrahedra in the "A"- and "B"-chains of a natural orthopyroxene (with approximate composition $Mg_{0.30}Fe_{0.68}Ca_{0.015}SiO_3$) with increasing temperature to ~850°C (data from Smyth, 1973).

Although it is clear for the Fe^{2+}-rich samples (Sueno et al., 1976; Smyth, 1973) that the tetrahedra in both "A" and "B" chains tilt away from the (100) plane on increasing the temperature, the trend of the tilt of the tetrahedra in the Mg^{2+}-rich orthopyroxene (Yang and Ghose, 1995) is harder to define; however, it is probable that these tetrahedra also tilt slightly away from (100) on heating. Upon pressure increase, the tetrahedra contained within the "B" chains of all the synthetic orthopyroxenes studied in this thesis behave in the opposite manner (ie, they tilt towards the (100) plane); those in the "A" chains in the synthetic $MgSiO_3$, $FeSiO_3$ and natural OPX2 orthopyroxenes also tilt towards (100) during initial compression. However, both the tetrahedral "B" chain of the natural OPX2 orthopyroxene and "A" chain of the synthetic $Mg_{0.6}Fe_{0.4}SiO_3$ orthopyroxene tilt away from the (100) plane on initial compression at ambient temperature (Figures 3.3, 3.6, 3.7, 3.9 and 3.11).

Finally, neither temperature increase nor pressure increase have much effect on the Si-O bond lengths and tetrahedral volumes and distortions of orthopyroxenes of several compositions along the $(Mg,Fe)SiO_3$ join (this study; Smyth, 1973; Sueno et al., 1976; Yang and Ghose, 1995).

3.5 SUMMARY

The compression mechanisms of all synthetic orthopyroxenes along the $MgSiO_3$-$FeSiO_3$ join are virtually identical. At a pressure between ~3.5 GPa and ~4 GPa (depending on the composition of the pyroxene) there is a change in compression mechanism, which is the cause of the break in the equation of state (EOS) of the pyroxene (see Chapter 4). This change in compression mechanism has been identified in both synthetic $MgSiO_3$ and $Mg_{0.6}Fe_{0.4}SiO_3$ orthopyroxenes, and is characterised by the onset of shortening of the previously incompressible Si-O bond lengths, with associated discontinuous changes in the degrees of kinking and tilting of the silicate chains. There is no observed angular distortion of these tetrahedra (identified by the lack of significant changes of the internal O-Si-O bond angles) at any pressure below 8.1 GPa. The linear compressibilities of the "A" and "B" tetrahedra in the high-pressure compression regime are identical and independent of the bulk composition of the orthopyroxene. Since the orthoferrosilite transforms irreversibly to the high-pressure C2/c clinoferrosilite at pressures above ~ 4.6 GPa (Chapter 5), it has not been ascertained whether a similar change in compression mechanism also operates in the synthetic $FeSiO_3$ orthoferrosilite at ~3.5 - 4 GPa.

It is not clear from the data in the literature whether such changes in compression mechanism are a general phenomenon, but have not been observed because of insufficient data coverage or insufficient precision in high-pressure structure refinements, or whether these sorts of changes may only occur in structures in which there are sufficient degrees of freedom within the structure to allow smooth compression of the polyhedra of the larger cations (semi)-independently of discontinuous changes in the compression of the silicate tetrahedra. However, it is

interesting to note that $MgSiO_3$ orthorhombic perovskite with SiO_6 octahedra also shows a change in compression mechanism, at 5 GPa (Ross and Hazen, 1990).

There is no evidence of any change in compression mechanism occurring in the natural orthopyroxene at pressures below 6 GPa. The silicate tetrahedra are incompressible to this pressure, and there is little change in the conformations of the silicate chains. This difference in compressional behaviour of the natural orthopyroxene relative to the synthetic samples is due to the presence of either Al^{3+} or Ca^{2+} (or perhaps both) in the M2 cation sites of the pyroxene, although there is evidence from velocity-density systematics collected for a wide range of materials (Shankland, 1972) that the anomalous compressional behaviour of the Ca^{2+}-containing natural orthopyroxene (compared to the behaviour of the synthetic $(Mg,Fe)SiO_3$ orthopyroxenes with pressure) is simply a result of the large ionic radius of the calcium.

In all the orthopyroxenes (both natural and synthetic), the M1 and M2 cation sites compress steadily with pressure. Since compression of the octahedra is intimately connected with the deformation of the tetrahedral chains through the sharing of oxygens, it is somewhat surprising that there is no apparent discontinuity in either the rate of bond-shortening or polyhedral compression of the octahedra in the synthetic orthopyroxenes at P_{cr}. This may, of course, be obscured by the experimental "noise". However, although the linear volume compressibilities of the M1 and M2 octahedra are identical in synthetic orthopyroxenes of end-member composition on the $(Mg,Fe)SiO_3$ join, the effect of additional Fe^{2+} in the M2 sites of the $Mg_{0.6}Fe_{0.4}SiO_3$ orthopyroxene is to enhance the compressibility of its anomalously long M2-O3b bonds, and therefore the M2 site as a whole. The presence of Ca^{2+} in the M2 sites of the natural OPX2 orthopyroxene causes these sites to become significantly stiffer than either the neighbouring M1 sites or the corresponding M2 sites in the synthetic Ca^{2+}-free orthopyroxenes; in order to accommodate pressure increase, compression occurs preferentially at the M1 sites. It is interesting to note that the octahedra, which make up approximately 23% of the total volume of the structure, are softer than the orthopyroxene structure as a whole.

Many of the features of the compression of the $(Mg,Fe)SiO_3$ orthopyroxenes studied here may be considered to be the converse of the structural changes occurring during heating. From a study of three orthopyroxenes of different compositions (Smyth, 1973; Sueno et al., 1976; Yang and Ghose, 1995), it is seen that while the M1 and M2 octahedra behave in essentially opposite ways upon heating or compression, the behaviours of the SiO_4 chains are not so predictable. Whilst the tetrahedral "B" chains in all the orthopyroxenes studied kink upon pressure increase, and straighten upon heating at ambient pressure, the tetrahedral "A" chains in all the orthopyroxenes studied straighten as a result of either increasing the pressure (in the low-pressure compression regime) *or* the pressure. Whereas the tetrahedra tend to tilt away from the (100) plane upon temperature increase and rotate towards (100) during initial compression, this is not a general rule, and some exceptions have been observed in Section 3.4. However, neither temperature increase nor pressure increase have much effect on the Si-O bond lengths and tetrahedral volumes of orthopyroxenes of several compositions along the $(Mg,Fe)SiO_3$ join (this study; Smyth, 1973; Sueno et al., 1976; Yang and Ghose, 1995).

CHAPTER 4

COMPRESSIBILITIES AND EQUATIONS OF STATE OF $(Mg,Fe)SiO_3$ PYROXENES

4.1 INTRODUCTION AND THERMODYNAMICS

The Gibbs free energy, $G_{T,P}$, of a phase is given by:

$$G_{T,P} = H_T - TS_T + \int_{1atm}^{P} V_{T,P}\, dP \qquad (4.1)$$

Both S_T and H_T are essentially independent of pressure, and as a good approximation may be considered to be functions of temperature only:

$$H_T = H_{ref} + \int_{ref}^{T} C_p\, dT \qquad (4.2)$$

$$S_T = S_{ref} + \int_{ref}^{T} \frac{C_p}{T}\, dT \qquad (4.3)$$

where C_p represents the heat capacity of the material at constant pressure, and is usually written as a polynomial function of the temperature, T.

The largest contribution to changes in $G_{T,P}$ with pressure comes from the volume-pressure integral which is the last term in Equation 4.1; this integral can only be evaluated when the variation of the volume of the phase with both pressure *and* temperature is known. The term "Equation of State" (or EOS) is widely used to describe the relationship between pressure, P, temperature, T, and specific volume, V (or specific mass, ρ) of a phase. The EOS can be written for any P-V-T path, but it is often most convenient to consider the volume variation with pressure and temperature separately.

4.1.1 EOS at Constant Pressure

The EOS of a given phase at constant pressure simply describes the effect of temperature on the volume of the phase, and makes use of a thermal expansion coefficient, α, which is often expressed as a polynomial in T.

$$\alpha(T) = \alpha_0 + \alpha_1 T + \alpha_2 T^2 + \alpha_3 T^3 + \ldots = \frac{1}{V}\frac{\delta V}{\delta T} \qquad (4.4)$$

This may be integrated to give an expression for the volume at temperature T, V_T, in terms of the initial volume, V_0, measured at a reference temperature, T_0, and the thermal expansion coefficient, $\alpha(T)$:

$$\int_{T_0}^{T} \alpha(T)\, dT = \int_{V_0}^{V_T} \frac{1}{V}\, dV \qquad (4.5)$$

$$\Rightarrow \ln \frac{V_T}{V_0} = \int_{T_0}^{T} \alpha\, dT \qquad (4.6)$$

$$\Rightarrow V_T = V_0 \exp\left[\int_{T_0}^{T} \alpha(T)\, dT\right] \qquad (4.7)$$

4.1.2 EOS's at Constant Temperature

a) Linear, Murnaghan and Birch-Murnaghan EOS's

The simplest approximation is to assume that the isothermal volume change with pressure ($\delta V/\delta P$) is constant (ie. that the compressibility of a given phase is linear), over the whole pressure range studied.

$$V_p = V_0 (1 - \beta P) \qquad (4.8)$$

where β is the linear compressibility with units of inverse pressure, generally GPa^{-1} or $Mbar^{-1}$. Equation 4.8 may be rewritten as:

$$V_p = V_0 \left(1 - \frac{P}{K_0}\right) \tag{4.9}$$

where $K_0 = \beta^{-1}$, and is known as the linear bulk modulus, measured in GPa or Mbar.

In a real system, however, as the structure is compressed the atoms become closer together and the repulsive forces between them increase, causing the structure to become stiffer as the pressure is increased. Figure 4.1 shows the deviation of real data (in this case data for $FeSiO_3$ orthoferrosilite has been used as an example, see Section 4.2.3) from the linear EOS, measured by the decrease of $\delta V/\delta P$ with increasing pressure.

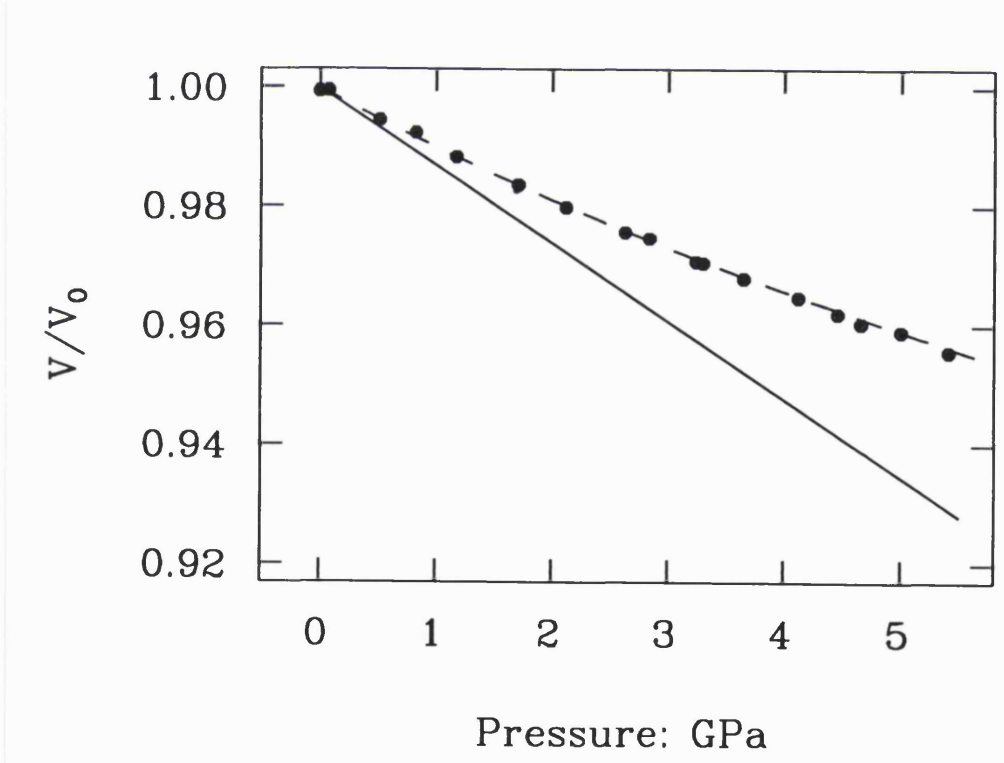

Figure 4.1: Divergence of the "real" compression data for orthoferrosilite (illustrated with a dashed line) from a linear EOS, calculated from the initial compressibility of the pyroxene (solid line).

In order to describe this stiffening of the structure with increasing pressure, the bulk modulus, K_0, must increase with pressure; the simplest assumption is to assign a linear variation of K with P:

$$K = K_0 + K'P \tag{4.10}$$

where:

$$\frac{1}{K} = -\frac{1}{V}\frac{dV}{dP} \tag{4.11}$$

An expression for the volume variation with pressure may be obtained from this equation by integration, as follows:

$$\int_{P_0}^{P} \frac{1}{K}\, dP = \int_{V_0}^{V} -\frac{1}{V}\, dV \tag{4.12}$$

$$\Rightarrow \quad -\ln\frac{V}{V_0} = \int_{P_0}^{P} \frac{1}{K_0 + K'P}\, dP \tag{4.13}$$

$$\Rightarrow \quad \ln\frac{V}{V_0} = \left(-\frac{1}{K'}\right)\left[\ln(K_0 + K'P)\right]_0^P \tag{4.14}$$

$$\Rightarrow \quad \ln\frac{V}{V_0} = \left(-\frac{1}{K'}\right) \times \ln\left(\frac{K_0+K'P}{K_0}\right) \tag{4.15}$$

$$\Rightarrow \quad \frac{V}{V_0} = \left(1 + \frac{K'P}{K_0}\right)^{\left(-\frac{1}{K'}\right)} \tag{4.16}$$

Final rearrangement of this expression gives an expression for V (the volume of the phase at pressure P) in terms of the volume at zero pressure, V_0, the bulk modulus, K_0, and its pressure derivative, K'. This is known as the Murnaghan EOS (Murnaghan, 1937):

$$V = V_0 \left(1 + \frac{K'P}{K_0}\right)^{\left(-\frac{1}{K'}\right)} \qquad (4.17)$$

In this EOS, the bulk modulus, K_0, represents the pressure at which the volume of the phase would theoretically reach zero, were K' = -1. Since the bulk modulus, K_0, increases with increasing pressure due to the stiffening of the material (Equation 4.10), its pressure derivative, K', *must* be positive, causing the Murnaghan EOS to be concave upwards (Figure 4.1). Although many high-pressure mantle minerals (eg. garnet, forsterite, ...) exhibit a K' lying in the range $4 < K' < 6$, orthopyroxenes are an exception, with values of K' (for initial compression to ~ 4 GPa) in the range $10 < K' < 15$ (see later).

However, the Murnaghan EOS appears only to fit the measured pressure-volume relationships to $V_p / V_0 \sim 0.9$. While for most minerals this situation is not reached until the pressure exceeds about 10 GPa at moderate temperatures, solid H_2 reaches this value at merely 0.3 GPa. In this case, and for studying the compression of minerals to above ~ 10 GPa, a more elaborate EOS is needed, such as a second-, third- or fourth-order Birch-Murnaghan EOS. The third order Birch-Murnaghan EOS (Birch, 1947) is derived by considering the variation of the elastic energy of a solid, and by assuming that the free energy is a power series in the finite strain. The integrated expression for the third order Birch-Murnaghan EOS is given below, in Equation 4.18:

$$P = \frac{3K_{0,T}}{2}\left[\left(\frac{V}{V_0}\right)^{7/3} - \left(\frac{V}{V_0}\right)^{5/3}\right]\left\{1 - \frac{3}{4}\left(K_0' - 4\right)\left[\left(\frac{V}{V_0}\right)^{2/3} - 1\right]\right\} \qquad (4.18)$$

Calculation of the EOS of each pyroxene phase (over a defined pressure range) in these studies was carried out using the program 'EOSFIT', in which the equation of state was fitted to the unit cell data using a non-linear least-squares refinement technique which determined a calculated pressure, P_{calc}, for each observed value of V_P / V_0, whilst refining the initial volume, V_0, the room pressure bulk modulus, $K_{0,T}$, and K_0' simultaneously. The refinement was considered to be complete when the pattern of residuals $|P_{obs} - P_{calc}|$ was minimised, generally after about 4 or 5 cycles of refinement. The quality of fit of the various EOS's to the data were assessed by means of an R-value, defined as:

$$R = \frac{\sum |P_{obs} - P_{calc}|}{\sum |P_{obs}|} \qquad (4.19)$$

Fourth-order Birch-Murnaghan EOS's gave no better fit to the data presented in this chapter than the third-order EOS's, with K" refining in all cases to less than its estimated standard deviation.

b) Finite Strain EOS

It is possible to rewrite the third order Birch-Murnaghan EOS (Equation 4.18) in such a way that the finite strain of the material may be determined as a function of its normalised stress (Jeanloz and Hazen, 1991). If the finite strain, f, is of the form:

$$f = [(\frac{V}{V_0})^{-2/3} - 1]/2 \qquad (4.20)$$

the third order Birch-Murnaghan equation of state may be written as:

$$P = 3K_{0,T}\, f(1+2f)^{2.5}(1+af+\ldots) \qquad (4.21)$$

where the constant $a = 3(K_0' - 4)/2$, and $K_{0,T}$ is the bulk modulus at ambient pressure and isothermal temperature, T.

If a normalised stress, F, is introduced (Birch, 1978), the compression data as a function of strain may be analysed. This normalised stress, F, is defined as:

$$F = P / [3f(1+2f)^{2.5}] \qquad (4.22)$$

Substitution into equation 4.21 gives a simplified form of the third order Birch-Murnaghan EOS:

$$F = K_{0,T} (1+af+...) \qquad (4.23)$$

The above rearrangement of the third order Birch-Murnaghan EOS (Equation 4.23) is also known as the Finite Strain EOS.

A plot of finite strain, f, against normalised stress, F, should thus yield a straight line if a third order EOS is an adequate description of the data, with the intercept on the vertical axis giving a value of the bulk modulus, $K_{0,T}$. The slope of this straight line is thus "$aK_{0,T}$" which is equivalent to $3K_{0,T}(K_0' - 4)/2$; this slope will be zero if $K_0' = 4$, as often expected for many mantle minerals. The plots of F versus f for all the $(Mg,Fe)SiO_3$ orthopyroxene data in a single compression regime (see later; also Chapter 3) presented here are essentially linear, with the values of $K_{0,T}$ being within one combined estimated standard deviation (*esd*) of those obtained by direct fitting of the third-order Birch-Murnaghan EOS (Table 4.1). Note that the maximum uncertainties (calculated from the uncertainties in the experimental measurements of P and V) are in the normalised stress, F, and are shown in the plots; uncertainties in f are less than the size of the symbols used.

Table 4.1 is presented on the next page. Note that the values of V_0 used for fitting the Finite strain (Equation 4.23) and Vinet EOS's (Equation 4.27) above ~3.5 - 4 GPa were constrained to the values of V_0 refined from the appropriate third-order Birch-Murnaghan EOS's. (denoted B-M 3; Equation 4.18) In other words, V_0 ($MgSiO_3$) = 829.6(2.3) Å^3, V_0 ($Mg_{0.6}Fe_{0.4}SiO_3$) = 846.8(3.7) Å^3, and V_0 ($Mg_{0.3}Fe_{0.7}SiO_3$) = 859.3(3.1) Å^3.

Composition	Type of EOS	$K_{0,T}$ (GPa)	K_0'	R-value
$MgSiO_3$	B-M 3	95.8 (3.0)	14.9 (2.0)	1.004 %
(P < 4 GPa)	Finite strain	94.9 (1.6)	15.4 (2.6)	0.49 %
	Vinet	95.7 (1.0)	14.1 (1.1)	1.65 %
$MgSiO_3$	B-M 3	122.8 (16.5)	5.6 (2.9)	0.63 %
(P > 4 GPa)	Finite strain	123.2 (1.4)	5.5 (0.4)	3.92 %
	Vinet	122.9 (1.2)	5.5 (0.4)	3.92 %
$Mg_{0.6}Fe_{0.4}SiO_3$ (P < 3.5 GPa)	B-M 3	95.7 (10.6)	14.7 (7.6)	3.32 %
	Finite strain	90.9 (5.3)	14.9 (4.6)	1.50 %
	Vinet	93.8 (5.8)	14.7 (4.3)	4.80 %
$Mg_{0.6}Fe_{0.4}SiO_3$	B-M 3	120.2 (26.4)	3.7 (4.9)	1.07 %
(P > 3.5 GPa)	Finite strain	118.8 (2.9)	4.2 (1.0)	1.20 %
	Vinet	119.3 (3.6)	4.0 (1.1)	5.68 %
$Mg_{0.3}Fe_{0.7}SiO_3$ (P < 3.5 GPa)	B-M 3	99.8 (4.4)	10.0 (2.8)	1.29 %
	Finite strain	99.0 (2.4)	10.4 (1.9)	0.62 %
	Vinet	99.6 (3.0)	9.9 (1.8)	2.04 %
$Mg_{0.3}Fe_{0.7}SiO_3$	B-M 3	110.5 (20.5)	5.9 (4.2)	0.64 %
(P > 3.5 GPa)	Finite strain	109.9 (2.1)	6.2 (0.7)	0.76 %
	Vinet	110.1 (2.2)	6.1 (0.8)	3.44 %
$FeSiO_3$ (P < 5.5 GPa)	B-M 3	94.7 (3.0)	10.7 (1.4)	1.19%
	Finite strain	98.7 (2.4)	9.9 (1.3)	1.10%
	Vinet	99.1 (2.4)	9.6 (1.4)	4.11%
OPX1 (P < 6 GPa)	B-M 3	108.8 (2.7)	9.4 (1.1)	1.18%
	Finite strain	114.6 (1.4)	8.4 (0.8)	0.72%
	Vinet	112.3 (1.1)	8.2 (0.7)	3.14%
OPX2	B-M 3	113.7 (2.0)	7.0 (0.6)	0.82 %
(P < 8.6 GPa)	Finite strain	112.8 (1.0)	7.3 (0.3)	0.68 %
	Vinet	113.3 (1.1)	7.1 (0.3)	3.06 %

Table 4.1: EOS parameters for natural and synthetic orthopyroxenes.

c) Universal or "Vinet" EOS

The other type of EOS used to describe the volume variation of the orthopyroxene data with pressure is the "universal" or "Vinet" EOS (Vinet et al., 1986), which has been used to describe the isothermal pressure-volume (P-V) relationship of a wide variety of materials:

$$P = 3K_{0,T}\,(1-x)\,x^{-2}\,\exp\left[\frac{3}{2}\,(K_0'-1)\,(1-x)\right] \qquad (4.24)$$

where the linear compression, x, is defined as:

$$x = \left(\frac{V}{V_0}\right)^{\frac{1}{3}} \qquad (4.25)$$

The isothermal bulk modulus is designated $K_{0,T}$, and its first derivative with respect to pressure is denoted K_0'. Using Equation 4.24, an expression in terms of the pressure, P, and the volume, V_P, may be derived in the following manner in order to calculate the values of $K_{0,T}$ and K_0':

$$\frac{Px^2}{1-x} = 3K_{0,T}\,\exp\left[\frac{3}{2}\,(K_0'-1)\,(1-x)\right] \qquad (4.26)$$

$$\ln\frac{Px^2}{1-x} = \ln(3K_{0,T}) + \frac{3}{2}\,(K_0'-1)\,(1-x) \qquad (4.27)$$

Plotting $\ln(Px^2/1-x)$ against (1-x) for each of the pairs of P-V measurements yields a straight line with slope $3/2(K_0'-1)$, and intercept on the vertical axis $\ln(3K_{0,T})$. Calculation of the EOS's of the natural and synthetic orthopyroxenes studied here show that the parameters $K_{0,T}$ and K_0' obtained using the Vinet EOS are within one combined *esd* of those determined using the third-order Birch-Murnaghan EOS (Table 4.1).

4.1.3 Calculation of Volume and Linear Compressibilities from Elastic Data

The elastic compliance (or stiffness) of a crystal may be measured by a number of other different techniques, such as Brillouin spectroscopy and Ultrasonic methods (see Chapter 2). In both cases, the symmetry independent elastic moduli may be determined with much accuracy. Both compliance, s_{ij}, and stiffness, c_{ij}, may be written as square matrices of the form:

$$\begin{matrix} s_{11} & s_{12} & s_{13} & s_{14} & s_{15} & s_{16} \\ s_{21} & s_{22} & s_{23} & s_{24} & s_{25} & s_{26} \\ s_{31} & s_{32} & s_{33} & s_{34} & s_{35} & s_{36} \\ s_{41} & s_{42} & s_{43} & s_{44} & s_{45} & s_{46} \\ s_{51} & s_{52} & s_{53} & s_{54} & s_{55} & s_{56} \\ s_{61} & s_{62} & s_{63} & s_{64} & s_{65} & s_{66} \end{matrix}$$

For thermodynamic reasons (Nye, 1957), the compliance and stiffness matrices must also be symmetric, ie., $c_{ij} = c_{ji}$ and $s_{ij} = s_{ji}$. The symmetry of the crystal also reduces the number of independent c_{ij} and s_{ij} components of the matrix. The form of both the orthorhombic c_{ij} and s_{ij} matrices is given below, using the s_{ij} matrix as an example:

$$\begin{matrix} s_{11} & s_{12} & s_{13} & 0 & 0 & 0 \\ s_{12} & s_{22} & s_{23} & 0 & 0 & 0 \\ s_{13} & s_{23} & s_{33} & 0 & 0 & 0 \\ 0 & 0 & 0 & s_{44} & 0 & 0 \\ 0 & 0 & 0 & 0 & s_{55} & 0 \\ 0 & 0 & 0 & 0 & 0 & s_{66} \end{matrix}$$

Since the symmetry of a monoclinic material is lower than that of an orthorhombic one, there are more independent components in the monoclinic s_{ij} and c_{ij} matrix. In the conventional orientation (ie. with the diad parallel to the [010] direction), the form of both the monoclinic compliance (s_{ij}) and stiffness (c_{ij}) matrices are given below:

$$\begin{matrix} s_{11} & s_{12} & s_{13} & 0 & s_{15} & 0 \\ s_{12} & s_{22} & s_{23} & 0 & s_{25} & 0 \\ s_{13} & s_{23} & s_{33} & 0 & s_{35} & 0 \\ 0 & 0 & 0 & s_{44} & 0 & s_{46} \\ s_{15} & s_{25} & s_{35} & 0 & s_{55} & 0 \\ 0 & 0 & 0 & s_{46} & 0 & s_{66} \end{matrix}$$

The volume compressibility, β_V, of a crystal of any symmetry is calculated using the expression (Nye, 1957):

$$\beta_V = (s_{11} + s_{22} + s_{33}) + 2(s_{12} + s_{23} + s_{31}) \qquad (4.28)$$

In other words, the volume compressibility is simply the sum of the nine coefficients in the upper left-hand corner of the compliance matrix. The bulk modulus, $K_{0,T}$ of the material is the reciprocal of the volume compressibility, β_V:

$$K_{0,T} = \frac{1}{\beta_V} \qquad (4.29)$$

The linear compressibility (defined (Nye, 1957) as the relative decrease in length of a line when the crystal is subjected to unit hydrostatic pressure) of the crystal may also be calculated from the compliance matrix; it will vary with direction in a non-isotropic crystal. Unlike the volume compressibility, it also depends on the crystal system; a generalised expression for the linear compressibility is:

$$\beta = s_{ijkk}\, l_i\, l_j \qquad (4.30)$$

where l_i (with $i = 1, 2, 3$) are the directions of the orthogonal unit vectors. For an orthorhombic crystal, the form of the expression for linear compressibility is:

$$\beta = (s_{11}+s_{12}+s_{13})\, l_1^2 + (s_{12}+s_{22}+s_{23})\, l_2^2 + (s_{13}+s_{23}+s_{33})\, l_3^2 \qquad (4.31)$$

and for a monoclinic crystal (in the standard orientation) it becomes:

$$\beta = (s_{11}+s_{12}+s_{13})\, l_1^2 + (s_{12}+s_{22}+s_{23})\, l_2^2 + (s_{13}+s_{23}+s_{33})\, l_3^2 + (s_{15}+s_{25}+s_{35})\, l_1\, l_3 \qquad (4.32)$$

These equations (4.28 to 4.32) allow the results of isothermal compression experiments in the DAC to be compared with measurements of elastic properties by other techniques, provided allowance is made, where necessary, for the isothermal to adiabatic conversion.

4.2 RESULTS

4.2.1 Variation of Orthopyroxene Unit Cell Parameters Across the Mg-Fe Join

Unit cell parameters of four synthetic orthopyroxenes of different compositions along the $MgSiO_3$ - $FeSiO_3$ join were measured at ambient conditions (Tables 4.2, 4.6, 4.7 and 4.8), and are plotted in Figures 4.2a-d. Quadratic equations fitted to these data using a least-squares refinement technique, show that the behaviour of each of the unit cell parameters (*a*, *b*, *c* and *V*) can be described by changes in the iron content (or Mg^{2+} content) only. Within the experimental uncertainties, the ambient pressure unit cell parameters of the synthetic orthopyroxenes used in this study fall on the trend of Smith et al. (1969) determined from a detailed study of thirty-two natural and synthetic orthopyroxenes across the $(Mg,Fe)SiO_3$ join.

4.2.2 $MgSiO_3$ ORTHOENSTATITE

a) Volume Compressibility

Unit cell parameters of $MgSiO_3$ orthoenstatite were determined at approximately 0.3 GPa intervals to 8.5 GPa and are given in Table 4.2. There were no observed hysteresis effects on increasing and decreasing the pressure, and no systematic differences between data collected in the two types of diamond anvil cell used (the modified Merrill-Bassett cell (Hazen and Finger, 1982) and the DXR4-type cell, see Chapter 2). A single EOS fitted to the entire dataset has the parameters $K_{0,T}$ = 103.1(1.9) GPa and K_0' = 9.2(0.6), and the R-value describing the fit of the EOS to the data is R = 0.86%.

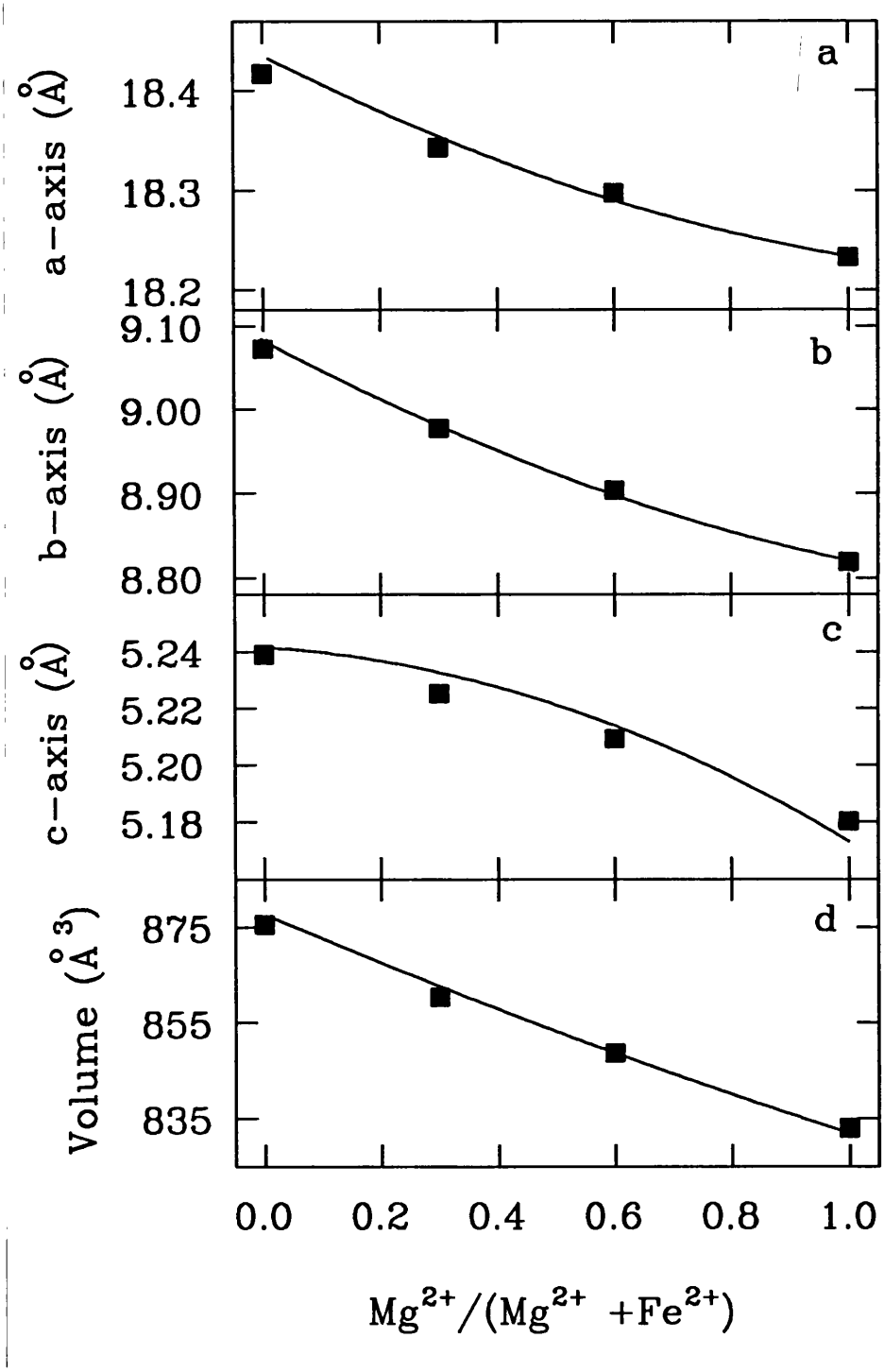

Figure 4.2: Variation of the unit cell parameters a) *a*, b) *b*, c) *c* and d) *V* of synthetic orthopyroxenes with increasing Mg^{2+} content. The data points are taken from this study, with the uncertainties being less than the sizes of the symbols used; the lines are from Smith et al. (1969)

P (GPa)	a (Å)	b (Å)	c (Å)	Volume (Å^3)
0.00	18.233 (1)	8.8191 (7)	5.1802 (5)	833.0 (1)
0.33	18.2143 (9)	8.8105 (8)	5.1735 (5)	830.2 (1)
0.75	18.1969 (7)	8.7926 (5)	5.1671 (4)	826.74 (8)
1.04*	18.186 (1)	8.782 (1)	5.1610 (6)	824.3 (1)
1.28	18.1768 (9)	8.7751 (7)	5.1596 (5)	823.0 (1)
1.71	18.1565 (6)	8.7594 (7)	5.1515 (4)	819.30 (9)
1.95	18.147 (2)	8.756 (1)	5.1493 (7)	818.2 (1)
2.19	18.1441 (6)	8.7477 (5)	5.1465 (3)	816.86 (6)
2.49	18.1280 (5)	8.7381 (4)	5.1418 (2)	814.49 (5)
2.82	18.1175 (5)	8.7289 (4)	5.1381 (3)	812.56 (6)
3.27	18.1045 (6)	8.7181 (4)	5.1327 (3)	810.13 (6)
3.64	18.0884 (7)	8.708 (2)	5.1280 (6)	807.7 (2)
3.88	18.0830 (7)	8.7011 (5)	5.1257 (3)	806.57 (7)
4.09	18.0710 (7)	8.6929 (5)	5.1214 (3)	804.52 (7)
4.26*	18.065 (2)	8.689 (2)	5.119 (1)	803.5 (2)
4.52	18.063 (1)	8.684 (1)	5.1172 (7)	802.7 (2)
4.76	18.0526 (9)	8.6770 (8)	5.1145 (5)	801.15 (9)
4.98	18.0455 (6)	8.6708 (5)	5.1119 (3)	799.86 (6)
5.07	18.0409 (8)	8.6696 (6)	5.1106 (4)	799.34 (8)
5.13	18.037 (1)	8.6686 (9)	5.1102 (5)	799.0 (1)
5.37	18.027 (2)	8.661 (2)	5.1075 (9)	797.5 (2)
5.53	18.023 (1)	8.658 (1)	5.1052 (6)	796.7 (1)
5.85*	18.011 (2)	8.652 (2)	5.102 (1)	795.1 (2)
6.36*	18.007 (2)	8.637 (1)	5.0980 (8)	792.9 (2)
7.00*	17.983 (1)	8.6241 (9)	5.0902 (7)	789.4 (1)
8.10*	17.949 (2)	8.599 (2)	5.0795 (8)	784.0 (2)
8.50*	17.9361 (4)	8.5897 (6)	5.0760 (5)	782.03 (9)

Table 4.2: Unit cell parameters of synthetic $MgSiO_3$ orthoenstatite constrained to orthorhombic symmetry. Note that the data marked with an asterisk was collected from the DXR4-type diamond anvil cell (see Chapter 2 for details); unmarked data was from the modified Merrill-Bassett DAC (Hazen and Finger 1982).

However, the systematic pattern of residuals (P_{obs} - P_{calc}) indicates that this single EOS is not an adequate description of the volume variation of the orthoenstatite with pressure. In fact, the data display a distinct change in behaviour at a pressure of approximately 4 GPa (Figure 4.3).

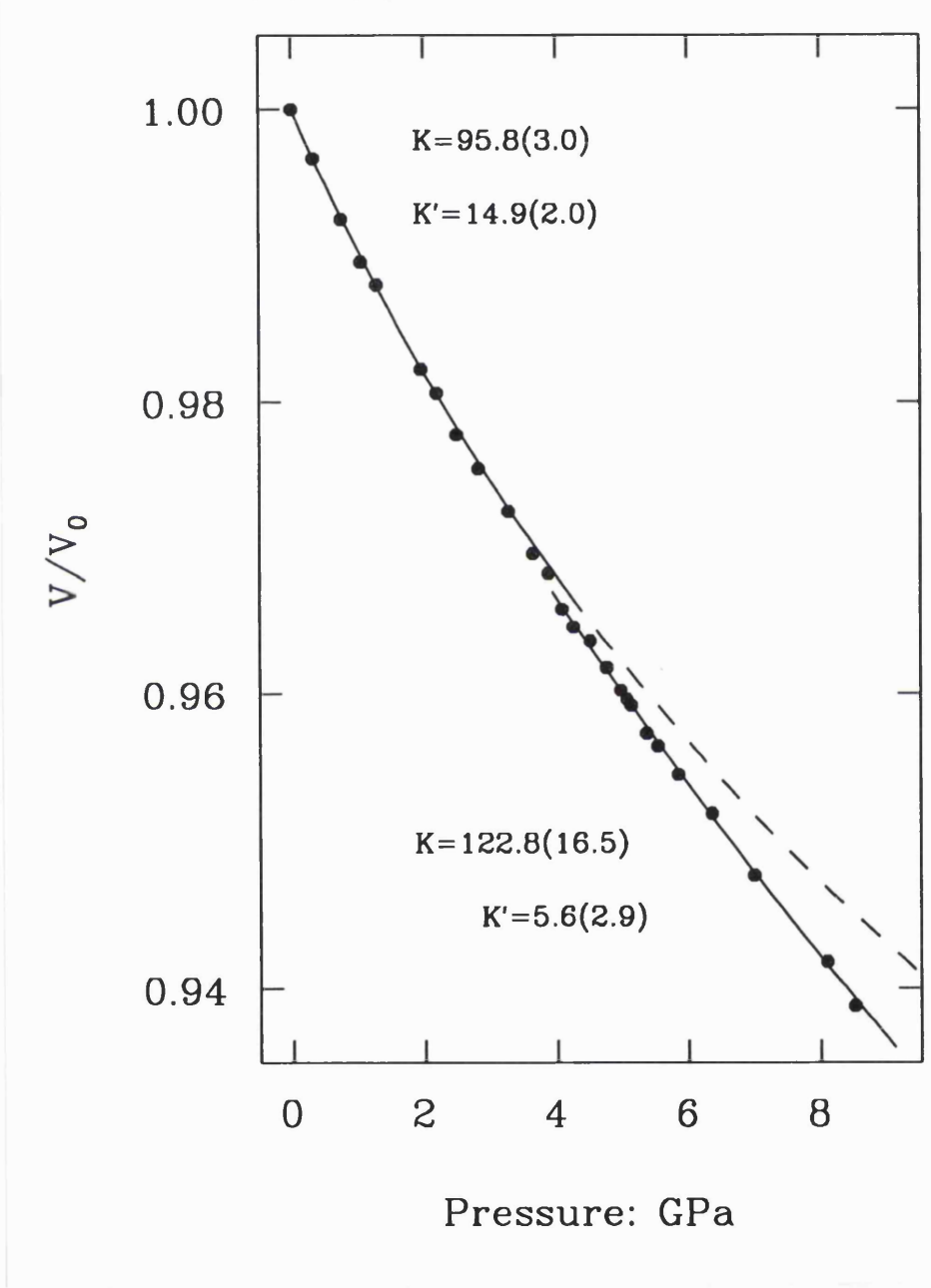

Figure 4.3: Third order Birch-Murnaghan EOS fitted to the volume variation with pressure of synthetic $MgSiO_3$ orthoenstatite, showing a distinct discontinuity at 4 GPa.

This change in behaviour is reproducible and independent of the type of diamond cell employed for the diffraction experiment - note that the data points at 4.09 and 4.26 GPa are from different loadings of the crystal in two different cells of different designs. Two separate EOS's fitted independently to the data 0 - 4 GPa and 4 - 8.5 GPa yield the values:

$P < 4$ GPa	$K_0 = 95.8(3.0)$ GPa	$K_0' = 14.9(2.0)$
$P > 4$ GPa	$K_0 = 122.8(16.5)$ GPa	$K_0' = 5.6(2.9)$

The combined R-value for this pair of EOS's is 0.71%, a significant improvement over the single EOS at the 95% confidence level as assessed by a Hamilton test (Hamilton, 1965). The abnormally large value of K_0' obtained in the low pressure regime was also obtained by ultrasonic measurements of natural orthoenstatite to pressures of ~1 GPa (Frisillo and Barsch, 1972) and to ~3 GPa (Webb and Jackson, 1993). The break in the EOS of the $MgSiO_3$ orthoenstatite also corresponds to a change in the rate of change, $\delta\upsilon/\delta P$, of Raman frequencies with pressure between 3.5 and 5 GPa (Chopelas and Boehler, pers. comm.; Figure 4.4).

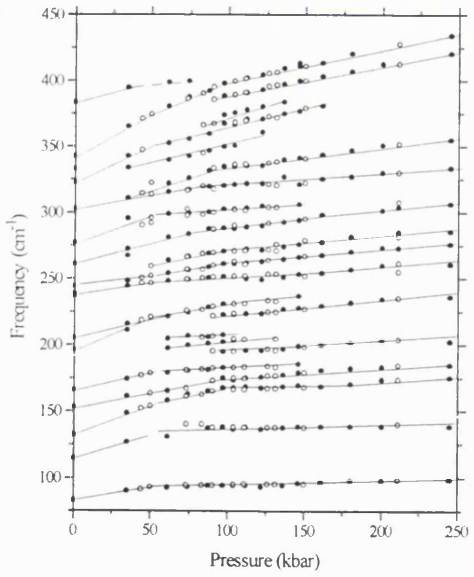

Figure 4.4 Raman data of synthetic $MgSiO_3$ orthoenstatite showing a discontinuity in the rate of change of frequency with pressure ($\delta\upsilon/\delta P$) between 3.5 and 5 GPa (Chopelas and Boehler, pers.comm.).

The difference between the volumes predicted by the two EOS's for the orthoenstatite at 4 GPa is $\sim$ 0.7Å^3 per unit cell, which is of the order of two experimental *esd*'s. It is therefore impossible to determine whether there is a distinct volume step indicative of a first order transition at 4 GPa, or whether it is a continuous change. However, in an attempt to determine whether this volume change is significant, two EOS's were refined simultaneously while being constrained to have the same volume at the crossover pressure, P_{cr}. Free refinement of P_{cr} with the other EOS parameters (V_0, K_0, K_0' for the low pressure regime, and $K_{(P=Pcr)}$ and $K'_{(P=Pcr)}$ for the high pressure regime) partially converges to P_{cr} = 4.27 GPa and oscillates by $\pm$0.03 GPa about this value. The R-value of this fit is 0.86%, significantly worse than the two independent EOS's at the 95% confidence level (Hamilton, 1965).

Thus, although these results are suggestive of the break in the EOS being accompanied by a volume change, this apparent volume change may simply be an artefact, leaving it impossible to resolve whether the EOS has a distinct break or whether there is a continuous "cross-over transition" in the pressure interval $\sim$ 3.9 to $\sim$ 4.3 GPa.

Determinations of the adiabatic bulk moduli of orthopyroxenes have been made at low and ambient pressures by Brillouin spectroscopy and ultrasonic techniques, and are listed in Table 4.3. Weidner et al. (1978) report a room pressure adiabatic bulk modulus (K_S) of 108 GPa for $MgSiO_3$, which corresponds to an approximate value of $K_{0,T}$ ($=K_S(1 + \alpha\gamma T)^{-1}$) of 107 GPa. An EOS fitted to our low pressure data (P < 4 GPa), with $K_{0,T}$ fixed at this value gives V_0 = 832.4(1) Å^3, K_0' = 8.4(7) and R = 1.5%, a poor fit with V_0 differing from the observed value by more than four combined *esd*'s. Even allowing for uncertainties in the conversion of adiabatic moduli to isothermal moduli due to the large uncertainties in the factor $(1 + \alpha\gamma T)$ for orthopyroxenes, the value of K_S determined by Weidner et al. (1978) is inconsistent with the data given in Table 4.2. This may be an artefact of small chemical differences between the samples used in the different experiments, or due to an overestimate by Weidner et al. of the elastic constant c_{12}, as suggested by Duffy and

Vaughan (1988). Using the value of K_S determined by Brillouin spectroscopy for a natural orthoenstatite (containing ~6% iron and significant calcium) by Duffy and Vaughan (1988), it is possible to refine a corresponding value of K_0' to 12.1(0.5). This is within one combined *esd* of the K_0' refined from the above experimental data.

Author(s)	Date	Composition	K_S GPa	K_T GPa	K_0'	Method
Weidner	1978	$MgSiO_3$ (s)	108(3)	107(3)	-	Brillouin
Duffy & Vaughan	1988	$Mg_{0.94}Fe_{0.06}SiO_3$	103.3 (0.4)	102.3(0.4)	-	Brillouin
Watt & Ahrens	1986	$Mg_{0.86}Fe_{0.14}SiO_3$	106(2)	105(2)	-	Shock-wave
Kumazawa	1969	$Mg_{0.84}Fe_{0.16}SiO_3$	96.3 (0.8)	95.3(0.8)	-	Ultrasonics
Frisillo & Barsch	1972	$Mg_{0.8}Fe_{0.2}SiO_3$	103.5	102.5	9.6	Ultrasonics
Webb & Jackson	1993	$Mg_{0.8}Fe_{0.2}SiO_3$	109.4 (0.5)	108.3(0.5)	10.8 (0.8)	k"-1.6(2) Ultrasonics
Bass & Weidner	1984	$FeSiO_3$ (s)	101(1)	100(1)	-	Brillouin

Table 4.3: Comparison of previous Bulk modulus and K' data of synthetic and natural $(Mg,Fe)SiO_3$ orthopyroxenes obtained by different experimental techniques. Note that the orthopyroxenes marked with (s) are synthetic samples; all the rest contain natural impurities such as Ca^{2+}, Al^{3+},...

Both the finite strain EOS (equation 4.23) and the Vinet EOS (equation 4.27) may also be applied to the orthoenstatite data in the two compression regimes (Figures 4.5a and b respectively). Using V_0 = 829.6(2.3) Å^3 for the high pressure compression regime, (determined from fitting of the volume variation with pressure using a third-order Birch-Murnaghan EOS), these EOS's give values for the bulk modulus, $K_{0,T}$ = 94.9(1.6) GPa and $K_{0,T}$ = 95.7(1.0) GPa, and its pressure derivative, K_0' = 15.4(2.6) and K_0' = 14.1(1.1), respectively (Table 4.1). These EOS's fitted to the data in the higher pressure regime are also consistent with the third order Birch-Murnaghan EOS.

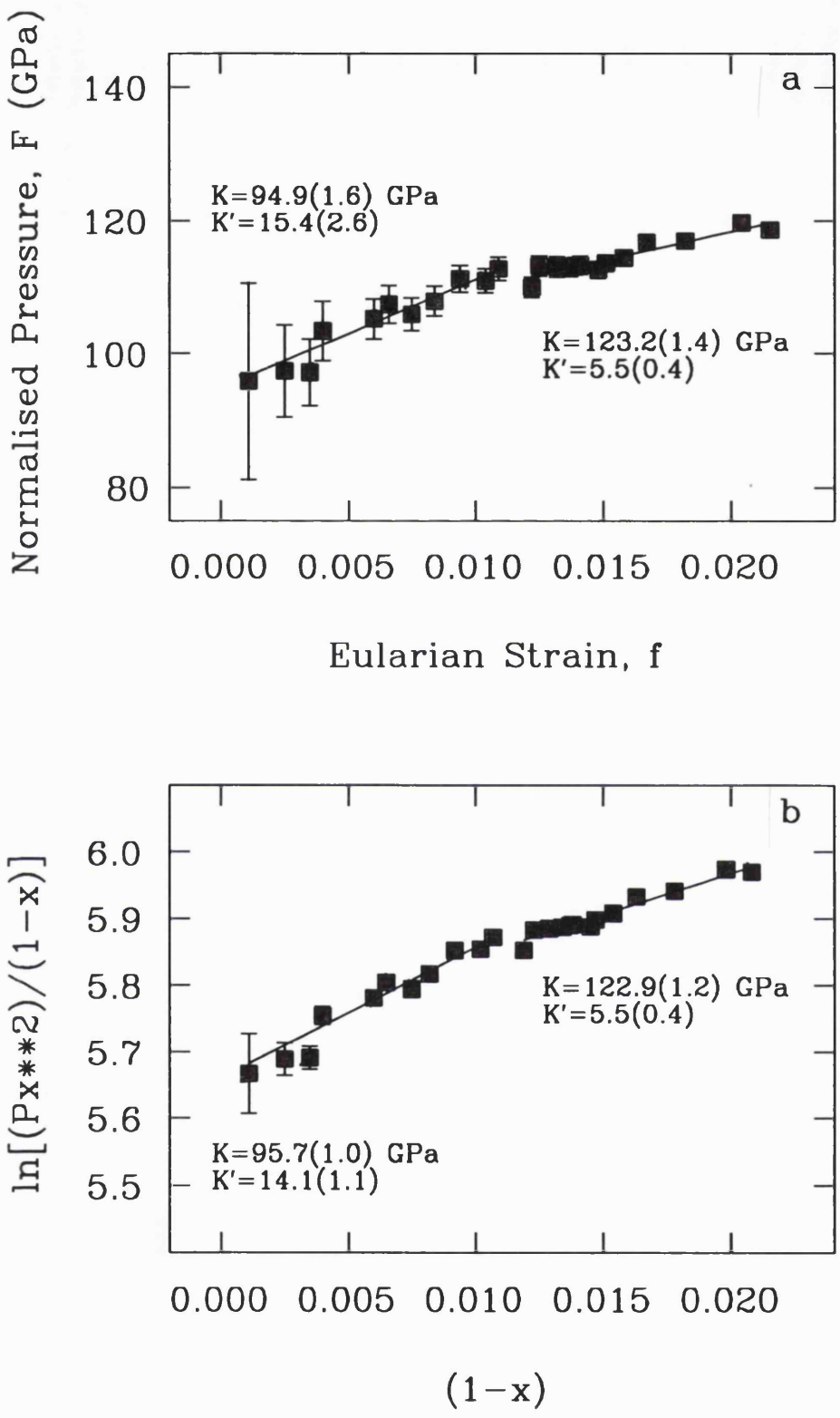

Figure 4.5: a) Finite strain EOS fitted to X-ray diffraction data for the synthetic $MgSiO_3$ orthoenstatite, showing fitting parameters, $K_{0,T}$ and K_0'; b) "Universal" or Vinet EOS fitted to the pressure-volume data for the synthetic $MgSiO_3$ orthoenstatite.

The stress-strain plot and the Vinet EOS require V_0 to be fixed. Since the V_0 appropriate for the high-P data is not unambiguously known, the room pressure value of V_0 may be chosen instead of the V_0 refined from the third order Birch-Murnaghan EOS (used in Figures 4.5a and b). Using this ambient pressure value, the Finite strain plot and the Vinet EOS yield values of $K_{0,T}$ and K_0' similar to the direct fitting of the third order Birch-Murnaghan EOS; these are summarised in Table 4.4. The break in the EOS of the synthetic $MgSiO_3$ orthoenstatite at 4 GPa is unmistakeable using either value of V_0.

Pressure range	Type of EOS	V_0 (Å^3)	$K_{0,T}$ (GPa)	K_0'
4.0 - 8.5 GPa	Finite strain	829.6 (2.3)	123.2 (1.4)	5.5 (0.4)
4.0 - 8.5 GPa	Finite strain	833.0 (0.1)	101.0 (1.5)	9.7 (0.6)
4.0 - 8.5 GPa	Vinet	829.6 (2.3)	122.9 (1.2)	5.5 (0.4)
4.0 - 8.5 GPa	Vinet	833.0 (0.1)	101.6 (1.1)	9.2 (0.5)

Table 4.4: Summary of refined parameters of Finite Strain and Vinet EOS's in the high pressure compression regime, fitted with different V_0's: V_0 = 833.0(0.1) Å^3 corresponds to the initial volume of the $MgSiO_3$ orthoenstatite at ambient conditions and V_0 = 829.6 (2.3) Å^3 is the volume refined from a third-order Birch-Murnaghan EOS fitted to the volume variation with pressure of the orthoenstatite at pressures above 4 GPa.

Although this exceptionally high value of K_0' ($\sim 14 < K_0' < 16$) as observed below 4 GPa seems unlikely at first, is has been demonstrated to be a genuine representation of the data collected by X-ray diffraction, ultrasonic and Brillouin methods. It has been seen in Chapter 3 that it is caused by the initial rapid compression, at low pressures, of the long M2-O3 bonds in the deformed M2 octahedra of the pyroxene, accompanied by changes in the degree of kinking and tilting of the tetrahedral chains. The change in the EOS behaviour of $MgSiO_3$ orthoenstatite at 4 GPa is caused by the change in compression mechanism at this pressure, characterised by the onset of compression of the Si-O bonds (Chapter 3).

b) Axial Compressibilities

The variation of the unit cell parameters of the synthetic $MgSiO_3$ orthoenstatite with pressure are given in Table 4.2, and plotted in Figure 4.6. Two independent third order Birch-Murnaghan EOS's were fitted to each of the axial shortenings, since all three exhibit a small but significant discontinuity at about 4 GPa (Figure 4.6). All three directions are significantly curved, each becoming stiffer in the higher pressure region (ie., with $P > 4$ GPa) where they exhibit higher bulk moduli and lower K_0's than those observed at lower pressures ($P < 4$ GPa). Calculation of the relative compressions of the axes (ie. "d/d_o") up to 8.5 GPa shows the [010] direction to be the most compressible, and [100] the least. From consideration of the structure of the orthopyroxene (Chapters 1 and 3; and Figure 3.1), the [010] direction is the direction between the tetrahedral and octahedral chains, and thus the direction of maximum "free-space". This means that compression in along [010] is relatively unaffected by interatomic bonding. The [001] direction runs along the lengths of the tetrahedral chains; compression in this direction is essentially taken up by kinking and tilting of these chains (see Chapter 3).

The relative linear compressibilities of the three orthogonal axes are identical (within one combined *esd*) to those determined for both natural and synthetic orthoenstatites using both Brillouin spectroscopy and ultrasonic techniques, as shown in Table 4.5. The data of Weidner et al. (1978) are the only independent determinations of the linear compressibilities of synthetic $MgSiO_3$ orthoenstatite, with each of their values for β_x, β_y and β_z being within one combined *esd* of the results presented above. The data for the other natural Mg^{2+}-rich orthopyroxenes (eg., Duffy and Vaughan, 1988; Webb and Jackson, 1993; etc.) do, however, show very similar linear compression behaviour to the synthetic samples.

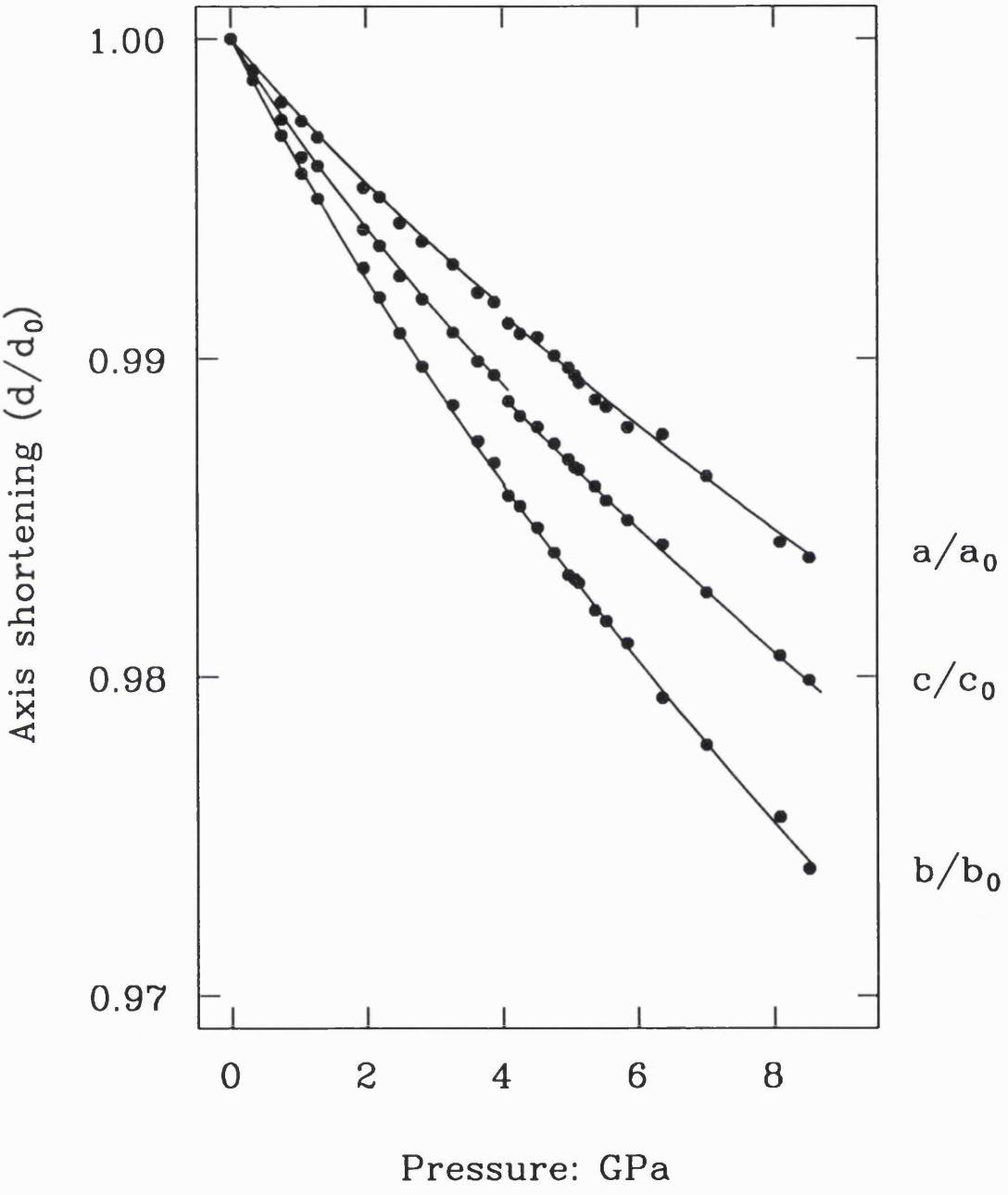

Figure 4.6: Relative compressibilities of the *a*, *b* and *c* axes of the synthetic $MgSiO_3$ orthoenstatite, showing a discontinuity in each at 4 GPa.

Author(s)	Composition	a x 10^3 (GPa^{-1})	b x 10^3 (GPa^{-1})	c x 10^3 (GPa^{-1})
This work	$MgSiO_3$ (s)			
	P < 4 GPa	2.5 (0.1)	4.2 (0.2)	3.6 (0.1)
	P > 4 GPa	2.1 (0.5)	3.7 (0.7)	2.7 (0.4)
Weidner 1978	$MgSiO_3$ (s)	2.5 (0.1)	3.7 (0.1)	3.1 (0.1)
Duffy & Vaughan 1988	$Mg_{0.94}Fe_{0.06}SiO_3$	2.3 (0.1)	4.0 (0.1)	3.6 (0.1)
This work	$Mg_{0.85}Fe_{0.13}Ca_{.02}SiO_3$ (OPX1)	2.3 (0.1)	3.98 (0.09)	3.0 (0.1)
This work	$Mg_{0.83}Fe_{0.12}Ca_{.006}SiO_3$ (OPX2)	2.1 (0.1)	3.6 (0.1)	2.8 (0.1)
Kumazawa 1969	$Mg_{0.84}Fe_{0.16}SiO_3$	2.3 (0.1)	4.1 (0.1)	3.2 (0.1)
Frisillo & Barsch 1972	$Mg_{0.8}Fe_{0.2}SiO_3$	2.3 (0.1)	4.3 (0.1)	3.2 (0.1)
Webb & Jackson 1993	$Mg_{0.8}Fe_{0.2}SiO_3$	2.14 (0.01)	4.00 (0.01)	3.12 (0.01)
This work	$Mg_{0.6}Fe_{0.4}SiO_3$ (s)			
	P < 3.5 GPa	2.3 (0.2)	4.2 (0.2)	3.6 (0.3)
	P > 3.5 GPa	2.2 (0.1)	4.0 (0.4)	3.1 (0.1)
This work	$Mg_{0.3}Fe_{0.7}SiO_3$ (s)			
	P < 3.5 GPa	2.0 (0.1)	3.8 (0.1)	2.8 (0.1)
	P > 3.5 GPa	1.6 (0.1)	3.0 (0.1)	2.1 (0.1)
This work	$FeSiO_3$ (s)	1.55 (0.06)	5.0 (0.5)	4.1 (0.5)
Bass & Weidner 1984	$FeSiO_3$ (s)	1.8 (0.2)	4.9 (0.4)	3.5 (0.3)

Table 4.5: Linear compressibilities of synthetic (marked with (s)) and natural orthopyroxenes. Note that a) the uncertainties quoted in this table represent the maximum errors in the measurement of the linear compressibility of the orthopyroxenes, and b) adiabatic compressibilities were not converted to isothermal compressibilities since the differences are less than the experimental uncertainties.

4.2.3 $FeSiO_3$ ORTHOFERROSILITE

a) Volume Compressibility

The volume and axial variation with pressure of synthetic $FeSiO_3$ orthoferrosilite are given in Table 4.6. Unit-cell data was not collected at pressures in excess of 5.5 GPa, since above this pressure the orthoferrosilite transformed irreversibly to the high-pressure C2/c clinoferrosilite phase (see Chapter 5). This means that it is not possible to determine whether $FeSiO_3$ undergoes a change in compression mechanism (see Chapter 3) and therefore whether it has a change in its EOS, like synthetic $MgSiO_3$ orthoenstatite, at ~ 4 GPa.

P (GPa)	a (Å)	b (Å)	c (Å)	Volume (Å^3)
0.00	18.417 (3)	9.073 (3)	5.239 (2)	875.5 (5)
0.08*	18.421 (6)	9.074 (2)	5.239 (2)	875.6 (4)
0.52*	18.402 (3)	9.054 (1)	5.229 (1)	871.3 (3)
0.83	18.3988 (7)	9.0444 (5)	5.2245 (3)	869.40(7)
1.18*	18.384 (4)	9.027 (1)	5.217 (1)	865.8 (3)
1.71	18.370 (1)	9.006 (1)	5.2084 (6)	861.7 (2)
2.12	18.357 (1)	8.989 (1)	5.2023 (6)	858.4 (1)
2.63*	18.341 (3)	8.9730 (8)	5.1942 (8)	854.8 (2)
2.84	18.341 (1)	8.966 (1)	5.1925 (8)	853.9 (2)
3.24*	18.319 (4)	8.951 (1)	5.1866 (9)	850.5 (3)
3.30	18.325 (2)	8.949 (2)	5.185 (1)	850.3 (2)
3.65	18.311 (2)	8.939 (2)	5.181 (1)	848.0 (3)
4.12	18.302 (1)	8.9232 (9)	5.1750 (5)	845.2 (1)
4.46	18.288 (2)	8.914 (2)	5.171 (1)	842.8 (2)
4.66*	18.277 (7)	8.907 (2)	5.169 (2)	841.4 (5)
5.00*	18.287 (8)	8.896 (2)	5.165 (2)	840.2 (6)
5.41*	18.264 (9)	8.885 (3)	5.160 (2)	837.3 (6)

Table 4.6: Unit cell parameters of $FeSiO_3$ orthoferrosilite constrained to orthorhombic symmetry. Note that the unmarked data was collected from orthoferrosilite crystal #1; the unit cell data marked with an asterisk (*) was obtained from crystal #2. All data was collected using a DXR4-type diamond-anvil cell.

A third-order Birch-Murnaghan EOS fitted to the entire dataset to 5.5 GPa has a bulk modulus, $K_{0,T}$, of 94.7(3.0) GPa, and a K_0' of 10.7(1.4) (see Table 4.1 and Figure 4.7). The high value of K_0' is also found when both Finite Strain and Vinet EOS's are fitted to the data; these give values of $K_{0,T}$ of 98.7(2.4) GPa and 99.1(2.4) GPa respectively, and K_0's of 9.9(1.3) and 9.6(1.4) respectively (Table 4.1). All three of these refined values of the bulk modulus and K_0' are within one combined *esd* of each other, confirming the unusually high value of K_0' observed for orthoferrosilite.

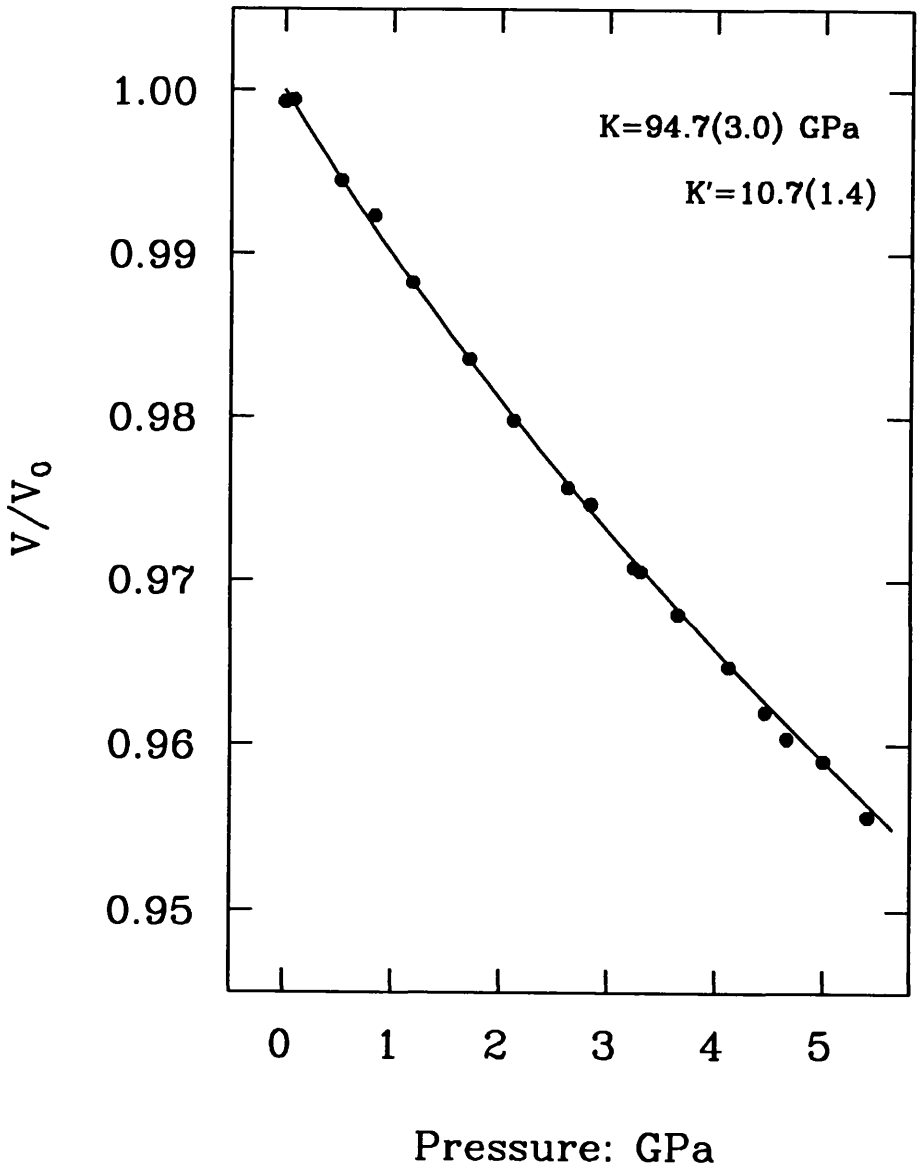

Figure 4.7: Third-order Birch-Murnaghan EOS fitted to the volume variation with pressure of synthetic $FeSiO_3$ orthoferrosilite.

The adiabatic bulk modulus of synthetic orthoferrosilite, K_S, was calculated to be 101(4) GPa from the elastic constants of the pyroxene determined by Brillouin spectroscopy measurements (Bass and Weidner, 1984; Table 4.3). Conversion to the isothermal bulk modulus using the factor $(1+\alpha\gamma T)$, assumed to be of the order of 1% due to uncertainties in both α and γ for orthoferrosilite, gives a value of $K_{0,T}$ of 100(4) GPa. This is consistent with this X-ray diffraction data, with the two values of the bulk modulus agreeing to within one combined *esd*. Refinement of a third-order Birch-Murnaghan EOS while constraining the bulk modulus to be 100 GPa also yields a high K_0' (K_0' = 8.3(0.4))

The EOS fitted to the volume variation of the orthoferrosilite below 4 GPa gives the parameters $K_{0,T}$ = 92.7(3.7) GPa and K_0' = 12.8(1.9). Comparison of this low-pressure EOS with that of the $MgSiO_3$ orthoenstatite (determined at P < 4 GPa) shows that although the values of both the bulk modulus, $K_{0,T}$, and its pressure derivative, K_0', are the same to within one experimental *esd*, the EOS's cannot in fact be superimposed in P-V space; the orthoferrosilite appears to be slightly, but significantly, more compressible than the orthoenstatite (Figure 4.8).

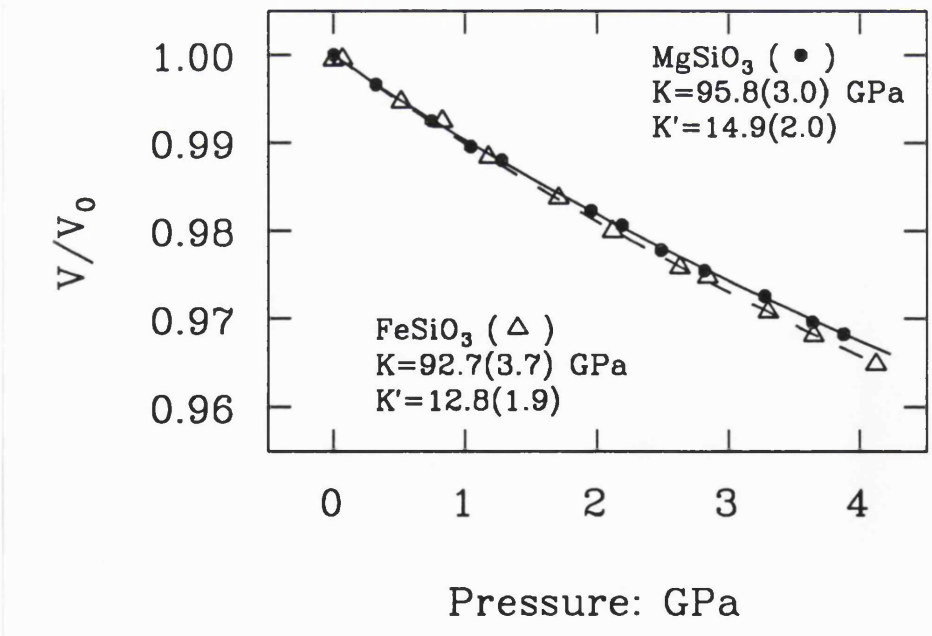

Figure 4.8: Comparison of the third order Birch-Murnaghan EOS's of synthetic $MgSiO_3$ orthoenstatite and $FeSiO_3$ orthoferrosilite to 4 GPa.

b) Axial Compressibilities

The pattern of axial compressibilities of the orthoferrosilite are identical to the orthoenstatite, with the [010] direction being the most compressible, and the [100] being the least compressible (Table 4.5). However, although the [001] and [010] directions are both approximately 15% more compressible than their counterparts in the orthoenstatite, the [100] direction is significantly stiffer (by some ~36%) than observed in the $MgSiO_3$ pyroxene (Figure 4.9). The relative linear compressibilities of the orthoferrosilite are also the same as those calculated from the Brillouin data of Bass and Weidner (1984); the values for these compressibilities are given in Table 4.5.

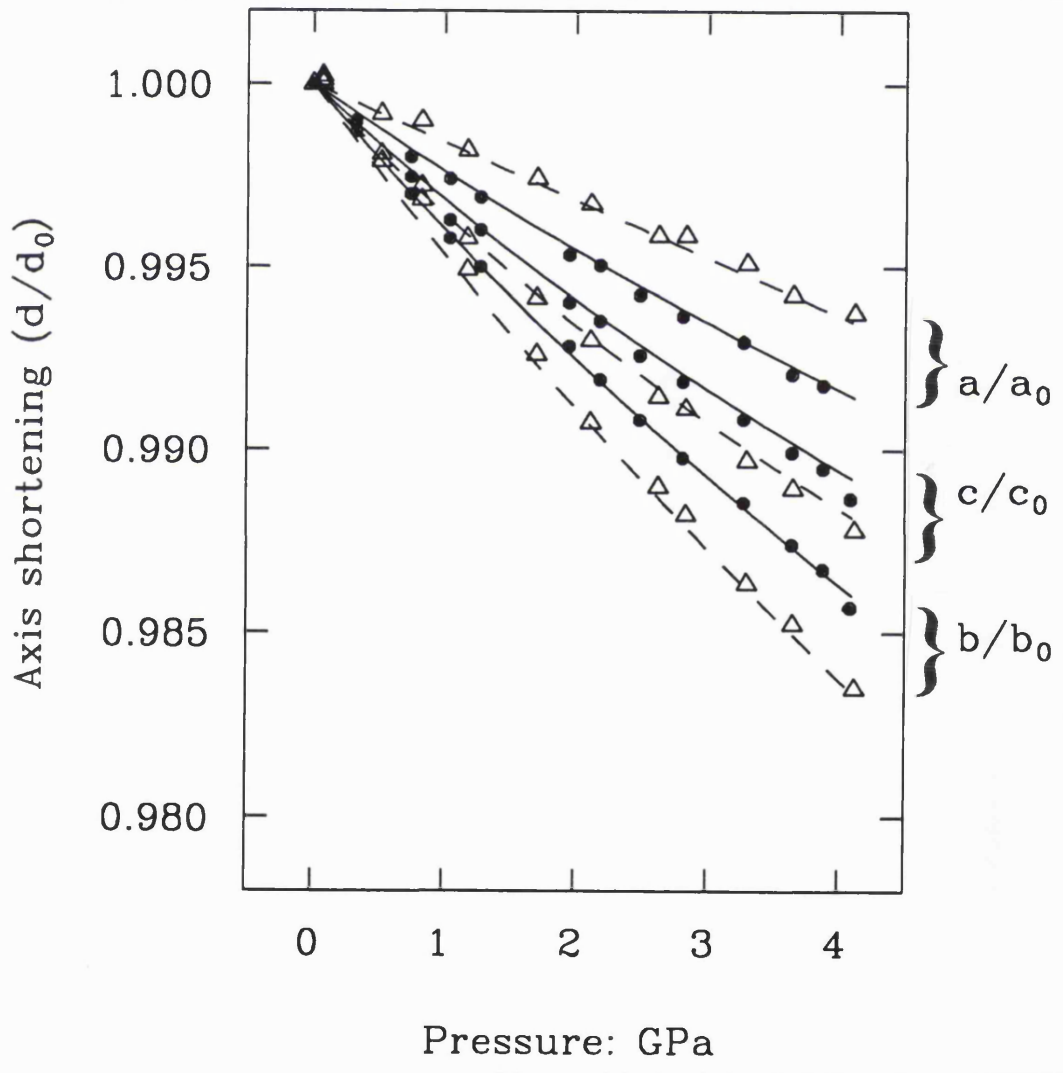

Figure 4.9: Comparison of the relative axial compressibilities of synthetic $MgSiO_3$ orthoenstatite and $FeSiO_3$ orthoferrosilite to 4 GPa.

4.2.4 SYNTHETIC ORTHOPYROXENES OF INTERMEDIATE COMPOSITIONS

a) Volume Compressibilities

The compression of two other synthetic crystals of orthopyroxenes of different compositions along the $(Mg,Fe)SiO_3$ join were also studied to ~7.5 GPa, using *in situ* X-ray diffraction in the diamond-anvil cell. The variation of the unit cell parameters with pressure are given in Tables 4.7 and 4.8. The volume variations with pressure were examined for evidence of discontinuities at ~ 4 GPa, similar to the changes in compressional behaviour seen for the synthetic $MgSiO_3$ orthoenstatite, since structural data collected for the $Mg_{0.6}Fe_{0.4}SiO_3$ orthopyroxene have indicated (Chapter 3) that there is a change in compression mechanism at ~3.5 GPa.

i) $Mg_{0.6}Fe_{0.4}SiO_3$ orthopyroxene

Due to experimental difficulties, several crystals of different qualities taken from the same original sample had to be used, causing increased scatter of the data. This meant that it was difficult to determine whether there is a break or not in the EOS of the orthopyroxene. A single EOS fitted to the entire dataset to 7.5 GPa gave the parameters $K_{0,T}$ = 110.2(4.1) GPa and K_0' = 6.2(1.2), with an R-value of 1.9%.

However, structural data collected from these crystals is indicative of a change in compression mechanism at ~3.5 GPa, involving both changes in the compressibilities of the Si-O bonds, and in the degrees of kinking and tilting of the silicate chains (see Chapter 3). For this reason, it is likely that there is a corresponding break in the EOS at this pressure. Although both the R-values and *esd*'s of the refined parameters are rather large (Table 4.1), the EOS fitted at low-pressures does indeed exhibit a high K_0' of 14.7(7.6), reflecting the high K_0's found for both synthetic $MgSiO_3$ and $FeSiO_3$ orthopyroxenes. Above about 3.5 GPa the value of K_0' decreases to ~ 4. The bulk modulus, $K_{0,T}$, increases from 95.7(10.6) GPa to 120.2(26.4) GPa on entering the higher pressure regime (Figure 4.10)

P (GPa)	a (Å)	b (Å)	c (Å)	Volume (Å^3)
0.00	18.2974 (7)	8.9040 (3)	5.2092 (3)	848.68 (7)
0.00 †	18.284 (1)	8.900 (1)	5.206 (2)	847.1 (3)
0.00 ‡	18.290 (2)	8.902 (2)	5.2061 (2)	847.5 (4)
0.00 +	18.297 (1)	8.9042 (8)	5.2087 (8)	848.6 (2)
0.51 †*	18.276 (3)	8.881 (2)	5.199 (1)	843.8 (3)
0.51	18.268 (2)	8.8818 (7)	5.1976 (7)	843.4 (1)
0.77 +*	18.263 (1)	8.879 (1)	5.1962 (6)	842.7 (1)
1.15	18.244 (2)	8.8600 (7)	5.1881 (7)	838.6 (2)
1.54	18.2351 (8)	8.8492 (4)	5.1839 (4)	836.51 (8)
2.18	18.2123 (9)	8.8294 (4)	5.1750 (4)	832.15 (8)
2.50 +*	18.197 (3)	8.820 (2)	5.171 (2)	829.8 (3)
2.84	18.188 (1)	8.8076 (6)	5.1663 (7)	827.6 (1)
2.85 ‡*	18.183 (2)	8.803 (2)	5.1632 (8)	826.2 (2)
3.17	18.174 (1)	8.7953 (5)	5.1608 (5)	824.9 (1)
3.60 ‡*	18.144 (4)	8.792 (3)	5.157 (2)	822.5 (4)
3.84 †*	18.149 (4)	8.772 (2)	5.152 (2)	820.2 (4)
4.14	18.1418 (9)	8.7682 (7)	5.1495 (5)	819.14 (9)
4.56 +*	18.132 (3)	8.757 (2)	5.146 (1)	816.9 (2)
4.76	18.124 (4)	8.754 (3)	5.144 (2)	816.2 (5)
5.15 †*	18.18 (4)	8.71 (2)	5.14 (2)	813.6 (3.4)
5.58 †*	18.101 (3)	8.728 (2)	5.132 (1)	810.7 (3)
5.77 +*	18.0912 (9)	8.724 (2)	5.1315 (7)	809.8 (2)
5.95 ‡*	18.080 (3)	8.720 (3)	5.127 (2)	808.2 (4)
6.10 +*	18.0778 (8)	8.717 (2)	5.1285 (6)	808.1 (1)
6.59 +*	18.0665 (9)	8.706 (1)	5.1236 (5)	805.8 (1)
7.08 +*	18.057 (2)	8.688 (2)	5.1167 (9)	802.5 (2)
7.50 +*	18.035 (1)	8.682 (2)	5.1138 (8)	800.7 (2)

Table 4.7: Unit cell parameters of synthetic $Mg_{0.6}Fe_{0.4}SiO_3$ orthopyroxene constrained to orthorhombic symmetry. Experiments were performed on crystal #1 in a Merrill-Bassett DAC are unmarked; an asterisk (*) denotes the use of a DXR4-type cell. Experiments on crystal #2 are marked with a cross (†), those on crystal #3 with a double-cross (‡), and those on crystal #4 with a plus-sign (+).

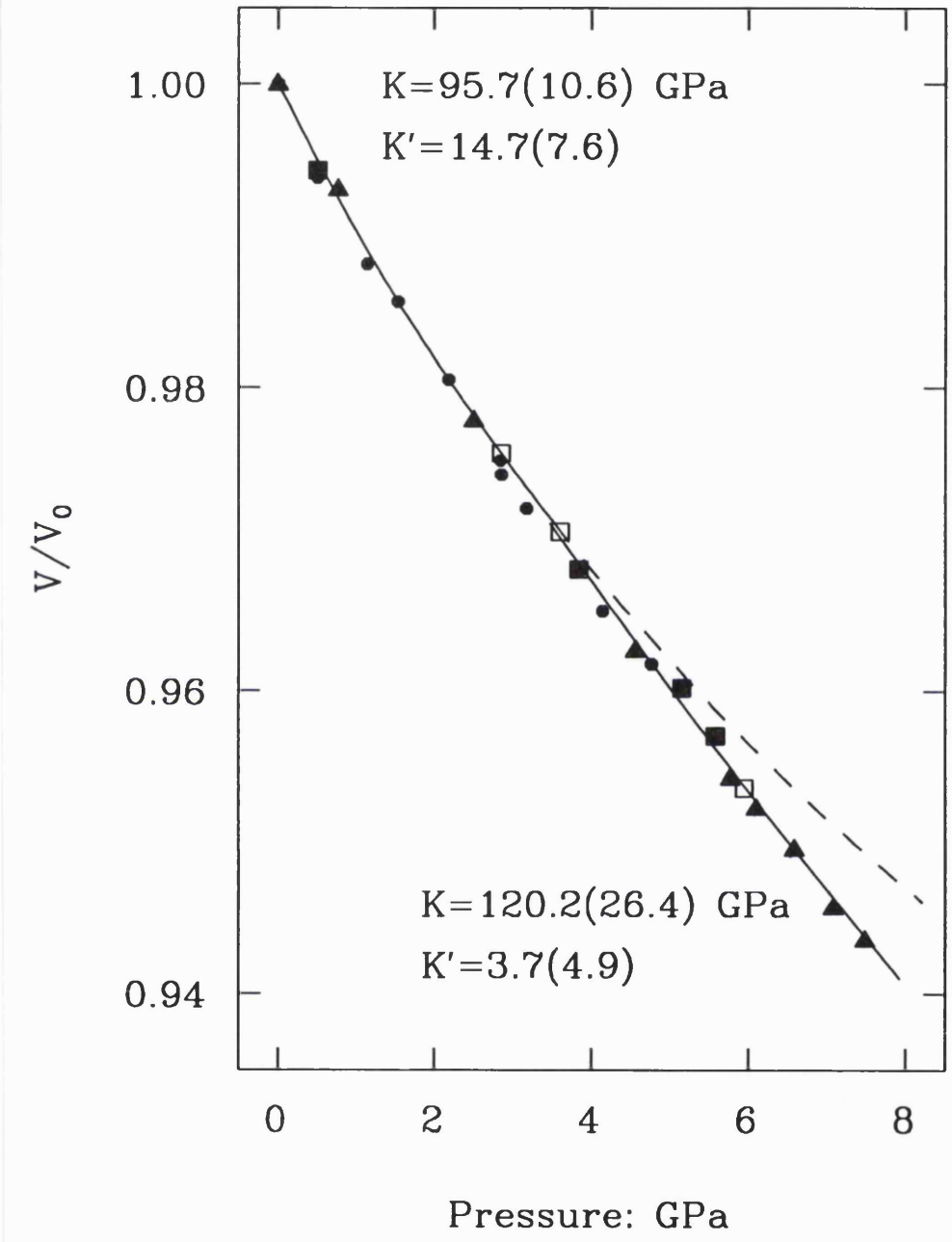

Figure 4.10: Volume variation with pressure of synthetic $Mg_{0.6}Fe_{0.4}SiO_3$ orthopyroxene, fitted with two independent third-order Birch-Murnaghan EOS's and showing a discontinuity at ~3.5 GPa. Data from crystal #1 is shown by filled circles; from crystal #2 by filled squares; from crystal #3 by open squares and from crystal #4 by filled triangles.

The differences in the predicted volume of the unit cell at 7.5 GPa using the one- and two- EOS models is merely of the order of 0.1%, showing that the fit of the split-EOS to the P-V data is not significantly better than the single EOS at the 95% confidence level (Hamilton, 1965).

ii) $Mg_{0.3}Fe_{0.7}SiO_3$ orthopyroxene

It was not possible to determine whether a single or a split-EOS best describes the volume variation with pressure of the synthetic $Mg_{0.3}Fe_{0.7}SiO_3$ orthopyroxene measured to ~7.3 GPa (Table 4.8). A single third-order Birch-Murnaghan EOS fitted to the entire data set to ~7.3 GPa gives the parameters $K_{0,T}$ = 104.1(2.7) GPa and K_0' = 7.3(0.8). However, since a change in compression mechanism was observed for both synthetic $MgSiO_3$ and $Mg_{0.6}Fe_{0.4}SiO_3$ orthopyroxenes between 3.5 GPa and 4 GPa, it is likely that a similar change in compresional behaviour also occurs for this intermediate orthopyroxene, implying that a split-EOS is a better representation of the real volume variation with pressure. Assuming that such a change in compressional behaviour occurs at approximately 3.5 GPa, a split-EOS fitted at pressures both lower and higher than this characterises the low-pressure regime by a relatively high value of K_0', (K_0' = 10.0(2.8)), which is reduced by some 40% at ~ 3.5 GPa to a value of K_0' = 5.9(4.2). The bulk modulus, $K_{0,T}$, is correspondingly increased by approximately 11% from 99.8(4.4) GPa to 110.5(20.5) GPa on entering the higher pressure regime (Figure 4.11). However, it is important to note that this split-EOS does not describe the volume variation with pressure of the synthetic $Mg_{0.3}Fe_{0.7}SiO_3$ orthopyroxene better than a single EOS at the 95% confidence level (Hamilton, 1965).

There are several reasons why the break in the EOS of this intermediate orthopyroxene (and also in the EOS of the $Mg_{0.6}Fe_{0.4}SiO_3$ orthopyroxene) is not significant at the 95% level: the most obvious reason is that the observed data scatter may simply be due to the number of crystals used during the course of both the experiments. Alternatively, the "break" in the EOS may be smeared over a finite pressure interval because of either local chemical heterogeneities or variations in the ordering of the Mg^{2+} and Fe^{2+} cations over the M1 and M2 octahedral sites within the pyroxene crystals of these intermediate compositions.

P (GPa)	a (Å)	b (Å)	c (Å)	Volume (Å^3)
0.00	18.343 (2)	8.9772 (9)	5.2252 (7)	860.4 (2)
0.61	18.338 (4)	8.953 (2)	5.218 (1)	856.6 (3)
0.87	18.309 (5)	8.943 (2)	5.211 (1)	853.3 (4)
0.94*	18.307 (2)	8.939 (3)	5.209 (2)	852.4 (4)
1.49	18.287 (4)	8.921 (2)	5.202 (1)	849.7 (3)
1.77	18.279 (4)	8.905 (1)	5.198 (1)	846.1 (3)
1.79	18.294 (8)	8.910 (2)	5.198 (1)	847.3 (4)
1.91	18.27 (1)	8.908 (3)	5.195 (2)	845.7 (7)
2.31	18.263 (4)	8.891 (1)	5.189 (1)	842.6 (3)
2.61	18.256 (2)	8.8820 (9)	5.1850 (7)	840.7 (2)
3.15	18.233 (2)	8.8636 (8)	5.1776 (7)	836.7 (2)
3.55*	18.218 (1)	8.854 (3)	5.174 (1)	834.5 (3)
4.01*	18.204 (2)	8.841 (3)	5.166 (2)	831.5 (4)
4.05	18.208 (4)	8.837 (1)	5.1661 (9)	831.2 (2)
4.39*	18.193 (1)	8.826 (2)	5.163 (1)	829.0 (3)
4.87*	18.177 (1)	8.814 (2)	5.157 (1)	826.1 (2)
5.25*	18.164 (3)	8.806 (5)	5.152 (3)	824.1 (5)
5.58*	18.154 (3)	8.787 (5)	5.150 (3)	821.5 (6)
5.67*	18.148 (3)	8.788 (5)	5.150 (3)	821.3 (5)
6.21*	18.1377 (7)	8.776 (1)	5.1421 (9)	818.5 (2)
6.48*	18.131 (2)	8.771 (4)	5.140 (3)	817.3 (4)
6.74*	18.117 (2)	8.759 (3)	5.137 (2)	815.2 (3)
7.12*	18.115 (4)	8.756 (7)	5.131 (4)	813.8 (7)
7.33 *	18.104 (1)	8.744 (2)	5.130 (2)	812.0 (2)

Table 4.8: Unit cell parameters for synthetic $Mg_{0.3}Fe_{0.7}SiO_3$ orthopyroxene constrained to orthorhombic symmetry. Note that the unit cells determined at unmarked pressures was collected from crystal #1; those at pressures marked with an asterisk (*) were collected from crystal #2. All unit cells were determined using a DXR4-type diamond-anvil cell.

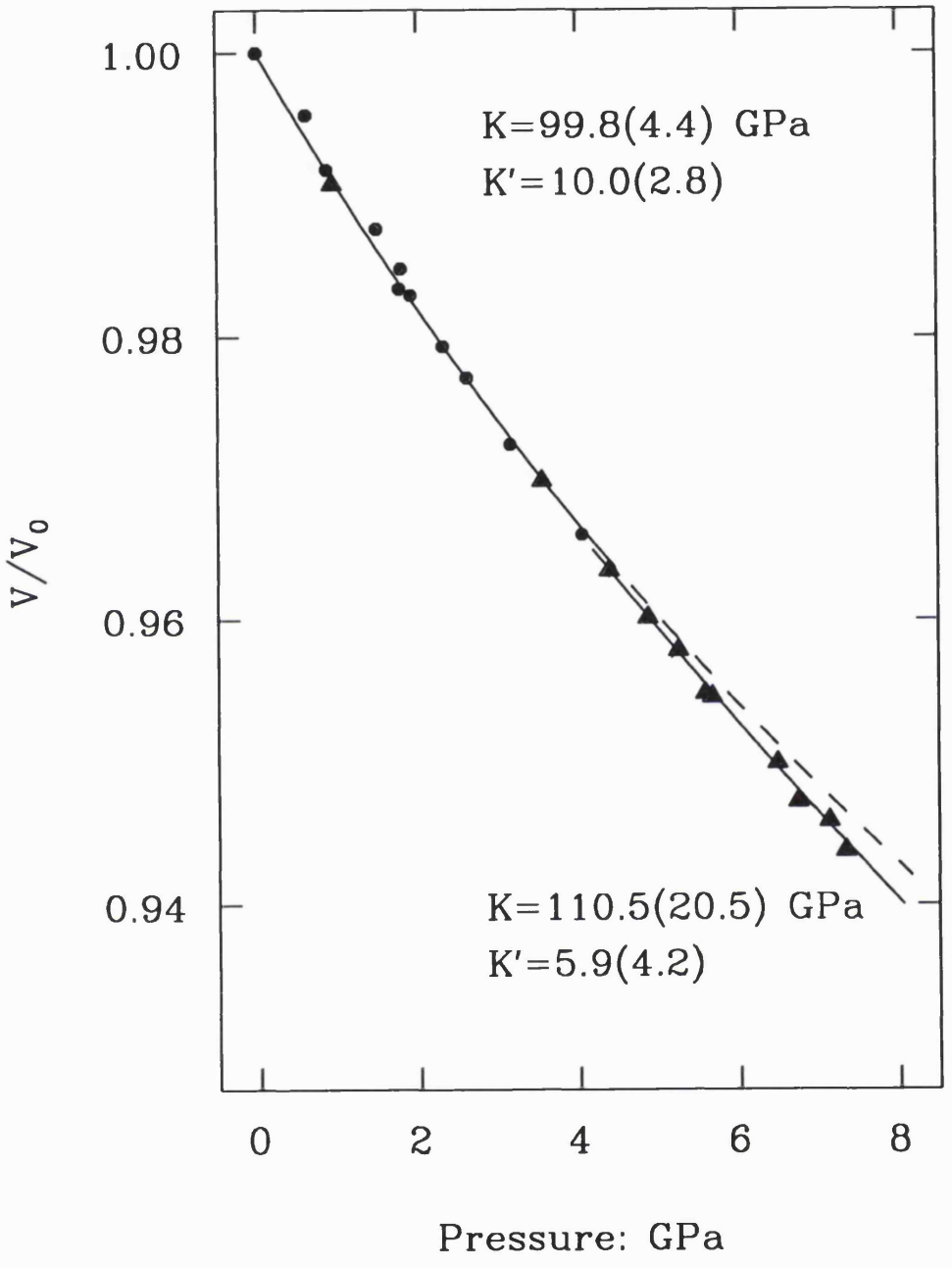

Figure 4.11: Two independent third-order Birch-Murnaghan EOS's fitted to the volume variation with pressure of synthetic $Mg_{0.3}Fe_{0.7}SiO_3$ orthopyroxene, showing a discontinuity at ~3.5 GPa. Data from crystal #1 is shown by circles, and data from crystal #2 by triangles.

b) Axial Compressibilities of $Mg_{0.6}Fe_{0.4}SiO_3$ and $Mg_{0.3}Fe_{0.7}SiO_3$ Orthopyroxenes

The relative axial compressibilities of both the synthetic $Mg_{0.6}Fe_{0.4}SiO_3$ and $Mg_{0.6}Fe_{0.4}SiO_3$ orthopyroxenes in both the low- and high-pressure regimes are identical to those found for the end-member orthopyroxenes (Table 4.5); in both cases, [010] is the most compressible direction, and [100] the least. However, there are significant changes in the absolute axial compressibilities of these orthopyroxenes with increasing Fe^{2+} content (or decreasing Mg^{2+} content). Whilst the *a*-axis becomes progressively stiffer with increasing the Fe^{2+} content of the M1 and M2 cation sites, both the *b*- and *c*-axes become more compressible (Figures 4.12a-c). This effect is most pronounced for the *a*- and *b*-axes, since it is principally the compression of the octahedral sites which affects their compressibilities. Compression of the *c*-axis is due, in addition, to kinking of the silicate chains and is therefore somewhat less dependent on the type of cation contained within the octahedral sites of the synthetic orthopyroxene.

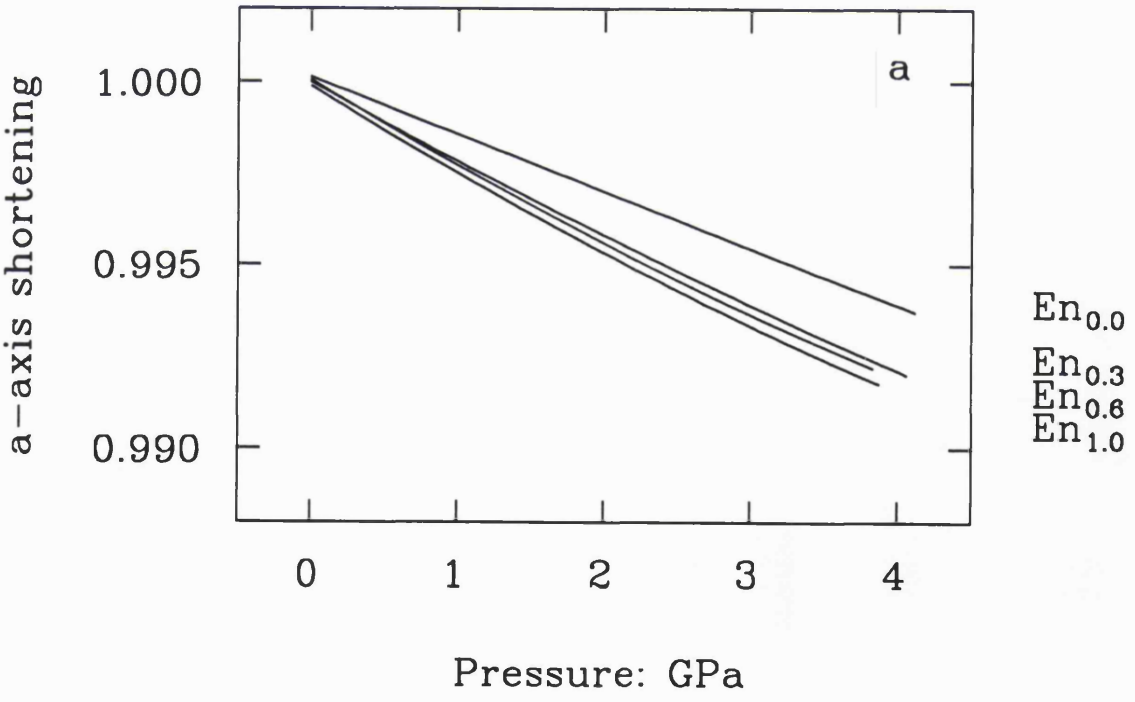

Figure 4.12: a) Effect of increasing Fe^{2+} content of the synthetic $(Mg,Fe)SiO_3$ orthopyroxenes on the relative compressibility of the *a*-axis.

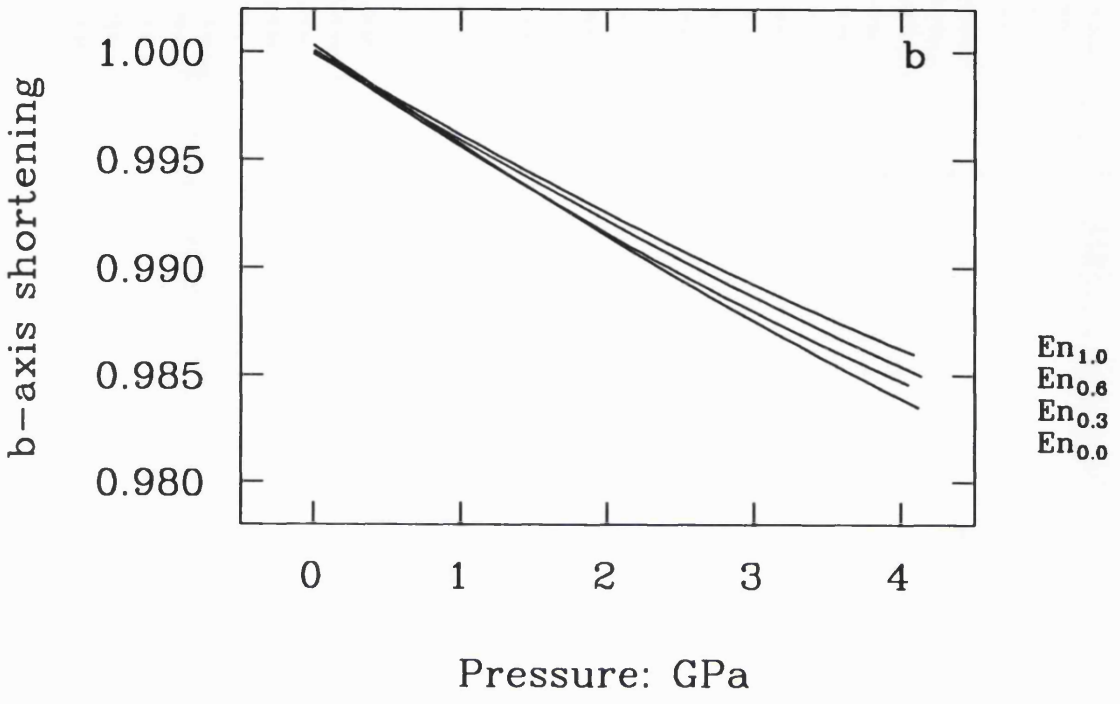

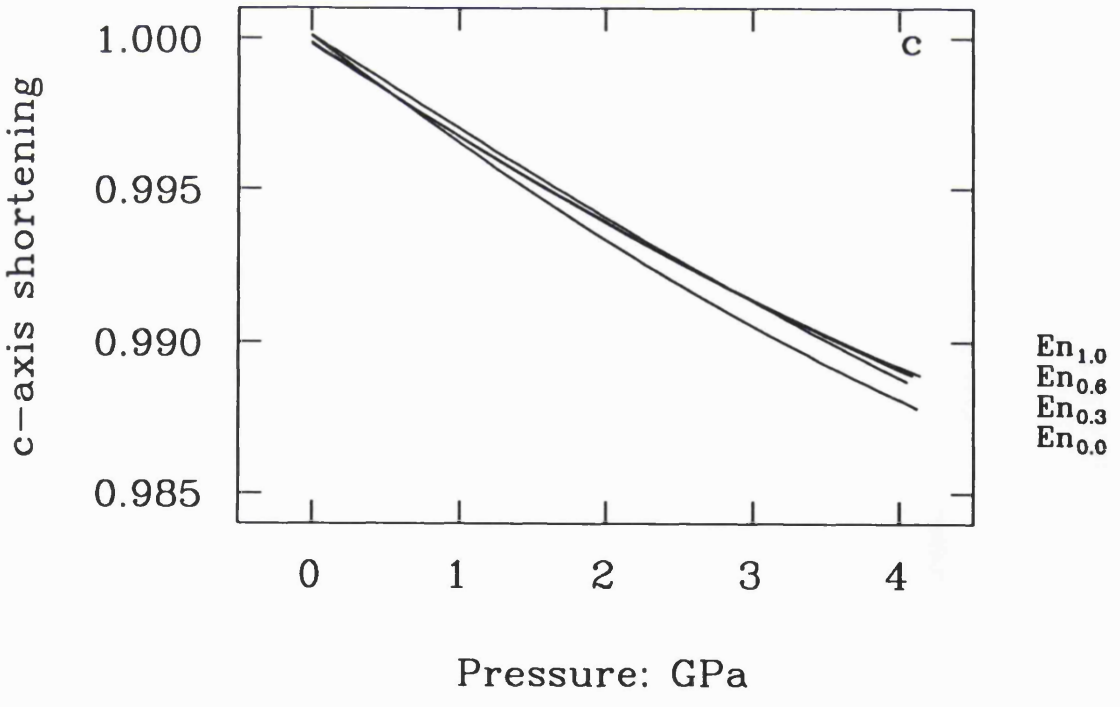

Figure 4.12: b) Effect of increasing Fe^{2+} content of the synthetic $(Mg,Fe)SiO_3$ orthopyroxenes on the relative compressibility of the *b*-axis; c) Effect of increasing Fe^{2+} content of the synthetic orthopyroxenes on the relative compressibility of the *c*-axis.

4.2.5 NATURAL ORTHOPYROXENES

a) Volume Compressibility

Similar compression experiments were undertaken for the two natural orthopyroxene samples; the variations of the unit-cell parameters with pressure are presented in Tables 4.9a and b.

P (GPa)	a (Å)	b (Å)	c (Å)	Volume (Å^3)
0.00	18.237 (4)	8.815 (1)	5.186 (2)	833.7 (3)
0.02*	18.243 (6)	8.809 (1)	5.182 (3)	832.6 (5)
0.48	18.223 (2)	8.8004 (7)	5.1794 (9)	830.6 (2)
0.71*	18.214 (3)	8.7924 (9)	5.175 (1)	828.8 (2)
1.13*	18.196 (4)	8.7759 (9)	5.169 (2)	825.3 (4)
1.20	18.194 (3)	8.7754 (9)	5.1697 (8)	825.4 (2)
1.44	18.183 (2)	8.7667 (6)	5.1654 (7)	823.4 (1)
1.90	18.169 (2)	8.7547 (6)	5.1604 (8)	820.8 (2)
2.14*	18.155 (2)	8.7463 (6)	5.1564 (7)	818.8 (2)
2.63	18.141 (3)	8.733 (1)	5.151 (1)	816.0 (2)
2.92*	18.127 (5)	8.726 (1)	5.148 (3)	814.3 (5)
3.20	18.118 (2)	8.7164 (6)	5.1435 (7)	812.3 (1)
3.57	18.109 (3)	8.708 (1)	5.140 (1)	810.5 (2)
3.93*	18.093 (3)	8.6968 (7)	5.1353 (8)	808.0 (2)
4.22	18.085 (2)	8.6888 (6)	5.1326 (7)	806.5 (1)
4.55	18.075 (2)	8.6822 (7)	5.1288 (6)	804.9 (1)
4.80*	18.064 (3)	8.6775 (8)	5.1270 (8)	803.6 (2)
5.10*	18.061 (3)	8.668 (1)	5.124 (1)	802.1 (2)
5.31*	18.038 (1)	8.6652 (4)	5.1218 (9)	800.6 (1)
5.66*	18.040 (4)	8.6525 (8)	5.122 (3)	799.7 (4)
5.86*	18.026 (4)	8.650 (1)	5.116 (2)	797.7 (4)

Table 4.9a: Unit cell parameters to ~6 GPa of natural orthopyroxene OPX1 constrained to orthorhombic symmetry. Unit cell parameters determined at pressures marked with an asterisk (*) were collected in a DXR4-type diamond-anvil cell; the remainder were collected using a modified Merrill-Bassett diamond-anvil cell (see text).

P (GPa)	a (Å)	b (Å)	c (Å)	Volume (Å^3)
0.00	18.231 (1)	8.8095 (3)	5.1873 (3)	833.12 (8)
0.34	18.220 (1)	8.7989 (5)	5.1822 (5)	830.8 (1)
0.72	18.201 (5)	8.786 (1)	5.1754 (9)	827.7 (3)
1.04	18.189 (2)	8.7765 (5)	5.1723 (5)	825.7 (1)
1.46	18.171 (2)	8.7616 (7)	5.1656 (6)	822.4 (2)
1.90	18.160 (2)	8.7503 (5)	5.1606 (3)	820.1 (1)
1.98	18.156 (3)	8.7477 (9)	5.1598 (8)	819.5 (2)
2.11	18.149 (1)	8.7432 (3)	5.1581 (3)	818.49 (8)
2.74	18.128 (1)	8.7257 (3)	5.1506 (3)	814.73 (8)
3.00	18.115 (1)	8.7184 (3)	5.1472 (3)	812.93 (9)
3.41	18.104 (7)	8.708 (2)	5.145 (3)	811.2 (6)
4.03	18.077 (4)	8.6907 (9)	5.1349 (8)	806.7 (2)
4.59	18.072 (5)	8.683 (1)	5.132 (3)	805.2 (6)
4.93	18.051 (3)	8.6683 (6)	5.1244 (5)	801.8 (2)
5.51	18.026 (6)	8.659 (2)	5.119 (2)	799.1 (4)
6.01	18.00 (1)	8.642 (3)	5.115 (3)	796.0 (9)
6.38	18.00 (1)	8.640 (4)	5.108 (3)	794.6 (7)
6.93	17.983 (4)	8.621 (2)	5.106 (2)	791.6 (3)
7.47	17.972 (5)	8.608 (1)	5.100 (1)	789.1 (3)
8.13	17.944 (3)	8.5965 (9)	5.094 (2)	785.8 (3)
8.62	17.931 (2)	8.5838 (6)	5.0898 (7)	783.4 (2)
9.11	17.918 (7)	8.575 (3)	5.083 (2)	781.0 (5)
9.49	17.89 (2)	8.559 (8)	5.087 (4)	778.9 (1.1)
10.1	17.85 (2)	8.551 (5)	5.078 (4)	775.3 (1.0)
11.0	17.80 (2)	8.543 (6)	5.077 (6)	772.0 (1.3)

Table 4.9b: Unit cell parameters for natural orthopyroxene OPX2, constrained to orthorhombic symmetry. All data was collected using a DXR4-type DAC.

There is no evidence of a change in behaviour of the volume variation with pressure of either of these orthopyroxenes at *any* pressure in the range 0 - 8.6 GPa (Figures 4.13a and b). Structural data collected from the natural orthopyroxene (OPX2) crystal confirms this, showing a single compression mechanism operating up to ~ 6 GPa (see Chapter 3). Therefore, in contrast to the data obtained for the synthetic samples, a *single* third-order Birch-Murnaghan EOS was fitted to the complete dataset for both the first crystal (OPX1) to ~ 6 GPa (giving a bulk modulus $K_{0,T}$ = 108.8(2.7) GPa, and its pressure derivative, K_0' = 9.4(1.1)) and also the second crystal (OPX2) to ~ 8.6 GPa (giving values of $K_{0,T}$ = 113.7(1.7) GPa, and K_0' = 7.0(0.6)); these two EOS's are exactly superimposed to ~ 6 GPa in P-V space (Figure 4.13a and b). The unit cell data collected at pressures in excess of 8.6 GPa for the OPX2 crystal has not been included in the determination of the EOS of the orthopyroxene, since at these pressures the crystal was strained between the two diamond faces in the DAC (see Chapter 2) causing large uncertainties in the refined unit cell parameters; upon pressure release, the crystal became less strained and the unit cell parameters were consistent with those obtained previously. However, these high pressure data are included in Figure 4.13b for completeness.

Comparison of this EOS data with that previously published for natural orthopyroxenes of similar compositions shows that the bulk modulus, $K_{0,T}$, agrees with that of Kumazawa (1969) to within five combined *esd*'s, and that of both Duffy and Vaughan (1988) and Frisillo and Barsch (1972) to within one combined *esd* (Table 4.3). The high K_0' measured in this study also agrees extremely well with the value of 9.6 determined using ultrasonic techniques by Frisillo and Barsch (1972), and of 10.8(8) by Webb and Jackson (1993). Figure 4.14 shows that there is extremely good agreement between the EOS determined by Webb and Jackson (1993) and the single crystal X-ray diffraction data. This agreement between the results of two completely different measurement techniques confirms the abnormally high values of K_0's for Ca^{2+}-poor $(Mg,Fe)SiO_3$ orthopyroxenes.

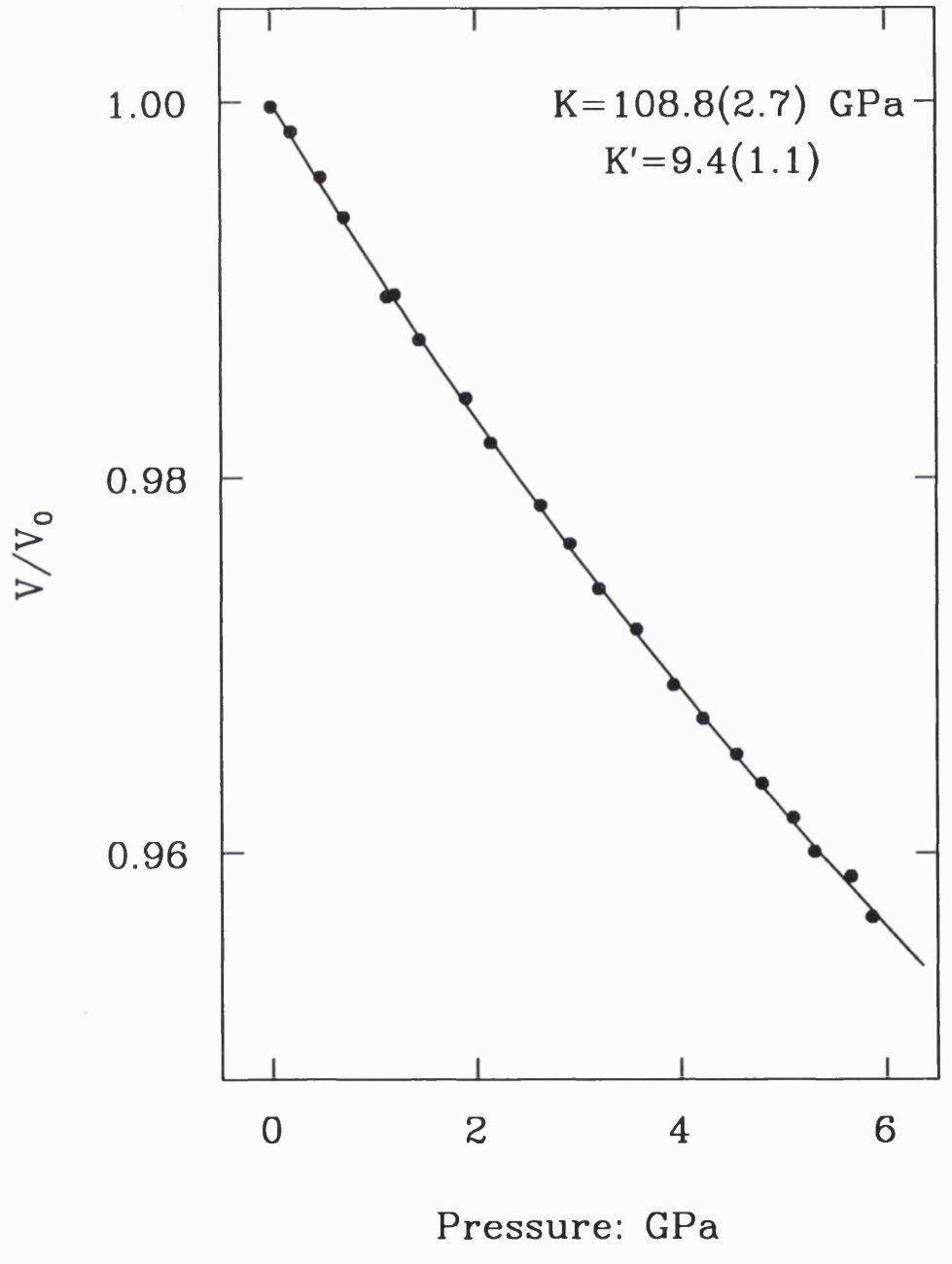

Figure 4.13: a) Volume variation with pressure of the natural orthopyroxene OPX1 to ~6 GPa.

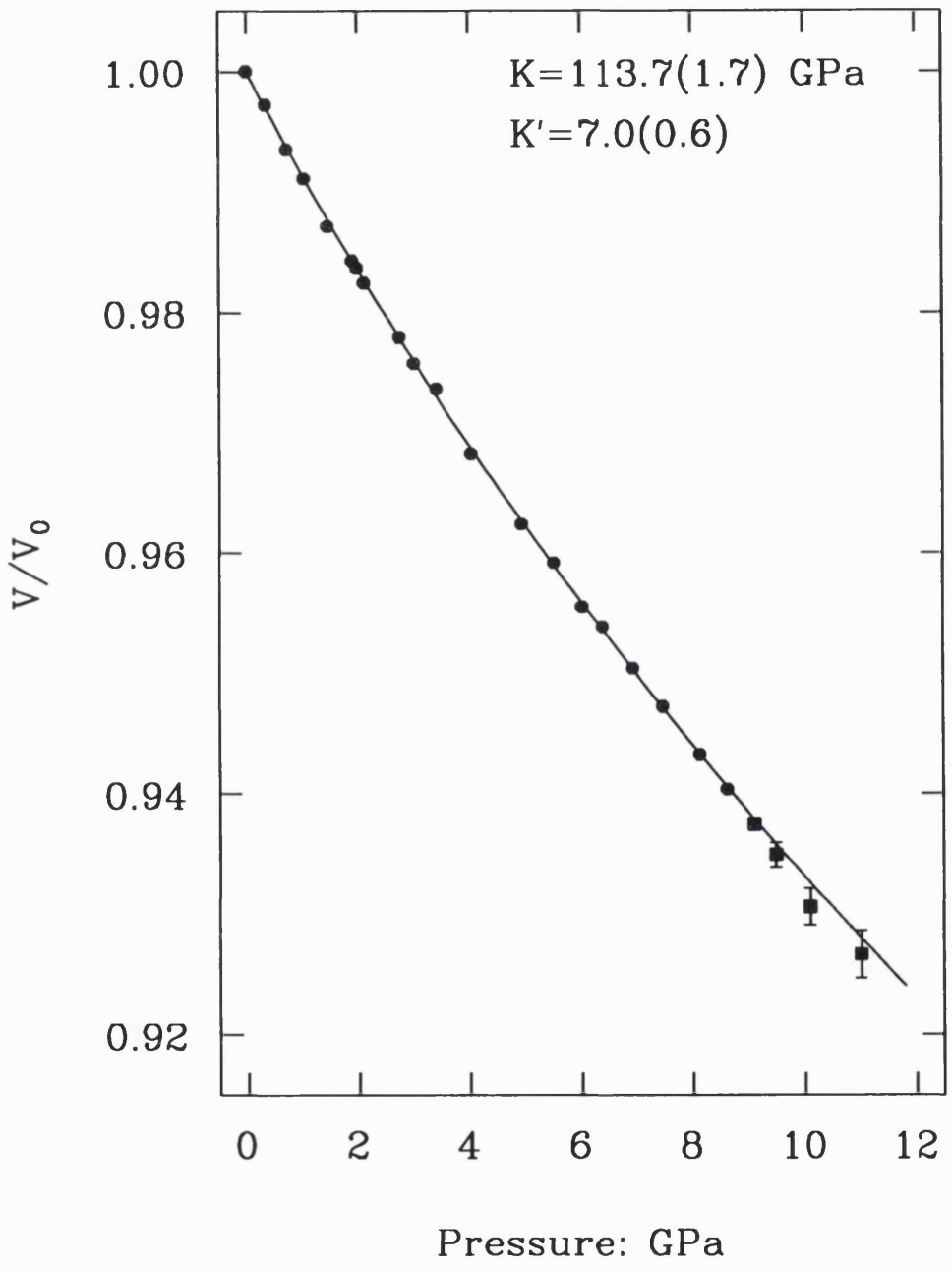

Figure 4.13 b) Volume variation with pressure of the natural orthopyroxene OPX2 with pressure to ~11 GPa (showing the EOS parameters fitted to 8.6 GPa).

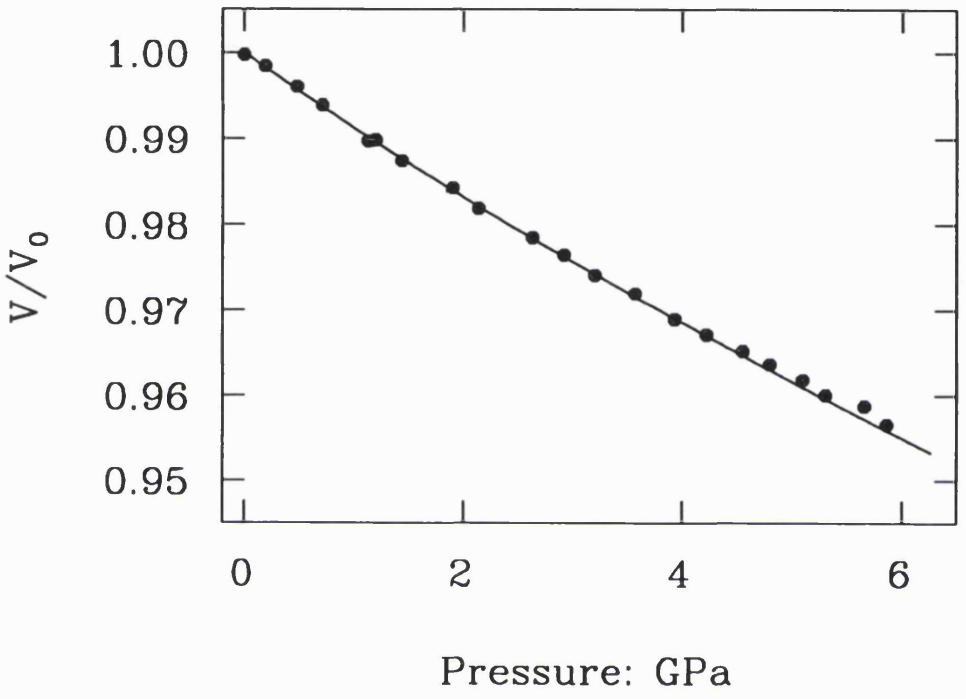

Figure 4.14: Volume variation with pressure of natural orthopyroxene - Data-points to ~ 6 GPa taken from this X-ray study; EOS determined to ~ 3 GPa by Webb and Jackson, (1993) using ultrasonic techniques.

b) Axial Compressibilities

The [010] direction in both the natural orthopyroxenes (OPX1 and OPX2) is the most compressible direction, and [100] the least (Figure 4.15). The axial compressibilities of these natural orthopyroxenes are identical to within one combined *esd* of those calculated for the synthetic $MgSiO_3$ orthoenstatite crystal from both the high-pressure X-ray diffraction results, and also the Brillouin and ultrasonic measurements. (Table 4.5). It is interesting to note that while the stiff *a*-direction compresses at a similar rate to the *a*-direction of the synthetic Mg^{2+}-rich orthopyroxenes, both the *b*- and *c*-directions are somewhat less compressible than those of even the synthetic $MgSiO_3$ orthoenstatite.

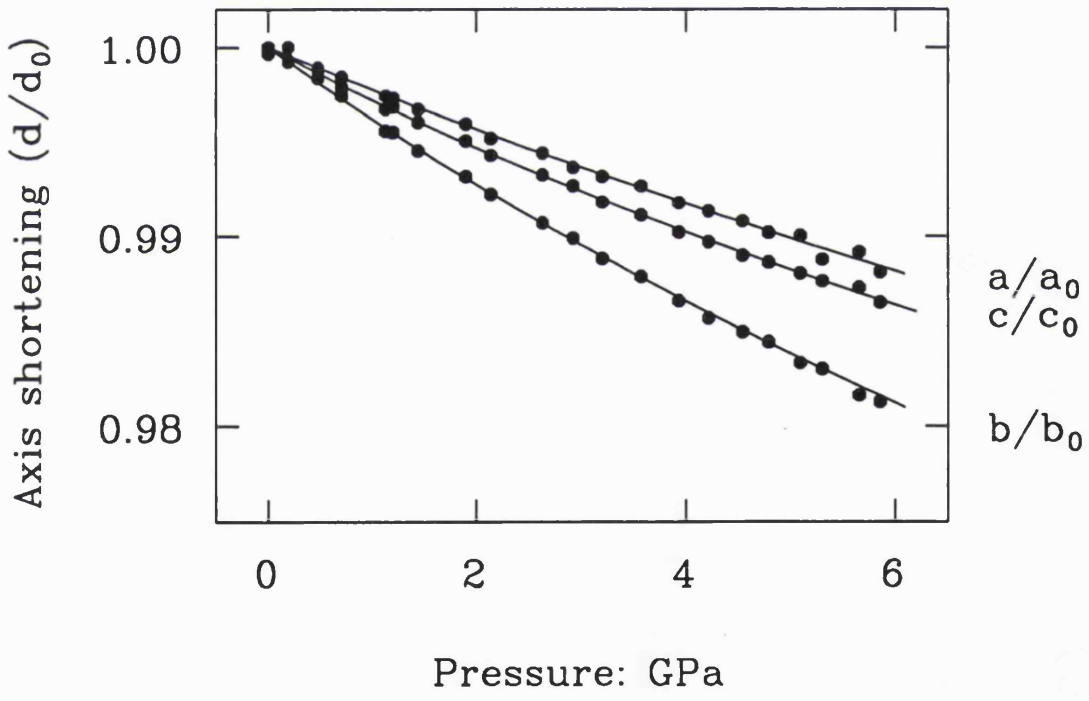

Figure 4.15: Relative axial compressibilities of the natural orthopyroxene OPX1 to ~6 GPa.

4.3 SUMMARY AND STRUCTURAL INTERPRETATIONS

In combination with high-pressure ultrasonic measurements (Frisillo and Barsch, 1972 and Webb and Jackson, 1993), these high-pressure X-ray diffraction data demonstrate that *all* orthopyroxenes with compositions on, or close to, the $MgSiO_3$-$FeSiO_3$ join exhibit anomalously high values of K_0' in their equations of state. This result is independent of the form chosen for the EOS. The structural basis for this unusual behaviour is apparent from the single-crystal structure determinations presented in Chapter 3, which show that at low pressures the longest cation-oxygen bonds within the structure, M2-O3a and M2-O3b undergo much more rapid compression than any other part of the structure.

This rapid compression apparently reaches a structural limit at around 4 GPa in $MgSiO_3$ and ~ 3.5 GPa in $Mg_{0.6}Fe_{0.4}SiO_3$, beyond which the rate of kinking of the silicate chains is reduced and the Si-O bonds start to shorten significantly (see Chapter 3). This change in compression mechanism results in a change in the EOS, causing K_0' to decrease from an unusually high value below 4 GPa to a more "normal" one in the high pressure regime; this is clearly evident in the $MgSiO_3$ end-member. The evidence for such a change in the EOS's of intermediate synthetic compositions is less clear, although structure determinations of $Mg_{0.6}Fe_{0.4}SiO_3$ certainly show the same change in compression mechanism (Chapter 3). The data for the $Mg_{0.6}Fe_{0.4}SiO_3$ orthopyroxene also suggest that the pressure at which this change in compression occurs may decrease with pressure, making it progressively more difficult to detect at increasing Fe^{2+} contents. Part of the reason for this uncertainty is experimental, due to the necessity of using more than one crystal of each intermediate composition; "smearing-out" of the change in compression mechanism over a finite pressure interval as a result of either local heterogeneities in either the composition or state of order of the Mg^{2+} and Fe^{2+} over the M1 and M2 octahedral sites within the orthopyroxene structure may also contribute to the uncertainty.

Direct comparison of the low-pressure ($P < 4$ GPa) P-V data of the end-member $FeSiO_3$ and $MgSiO_3$ orthopyroxenes shows that although the values of both

their bulk moduli, $K_{0,T}$, and their pressure derivatives, K_0', are identical to within one experimental *esd*, the $FeSiO_3$ orthoferrosilite is slightly, but significantly, more compressible than the $MgSiO_3$ orthoenstatite. This is due to the increased compressibility below 4 GPa of the M2 site in the orthoferrosilite compared to the $MgSiO_3$ orthopyroxene (see Chapter 3). The low-pressure EOS's (ie., $P < 4$ GPa) of the two synthetic orthopyroxenes of intermediate compositions fall in between the EOS's of the end-member phases. Similarly, the axial compressibilities below ~ 4 GPa vary steadily with changing composition: while the *a*-axis becomes progressively stiffer with increasing the Fe^{2+} content of the cation sites of the orthopyroxene, the *b*- and *c*-axes become correspondingly more compressible.

Unlike the synthetic $(Mg,Fe)SiO_3$ orthopyroxenes, there is no evidence of a change in compressional behaviour, either from structure determinations (Chapter 3) or from its EOS, of the natural orthopyroxene below ~ 6 GPa. This continuous behaviour of the Ca^{2+}-containing natural orthopyroxenes may be understood in terms of the behaviour of the M2 cation site. Calcium preferentially occupies the M2 cation site (e.g. Ghose, 1965; Cameron and Papike, 1981), and has a larger ionic radius than either Mg^{2+} or Fe^{2+}. Compression of the M2 octahedra of natural orthopyroxenes is therefore less than that observed in the synthetic, Ca^{2+}-free pyroxenes; this is true even for small amounts of Ca^{2+} substitution as the connectivity of the structure allows it to be "braced" by a few stiffer M2 octahedra. As a result there is little change in the degrees of kinking and tilting of either of the symmetrically distinct silicate chains, and the compression limit observed in the Ca^{2+}-free orthopyroxenes (Chapter 3) is never reached in the natural samples. There is therefore no change in compression mechanism and no corresponding change in the P-V behaviour. The stiffening of the M2 cation site also results in an increase over the Ca^{2+}-free samples of the bulk modulus by about 14%.

In conclusion, therefore, addition of Fe^{2+} to $MgSiO_3$ orthopyroxene has no significant effect on the bulk modulus or its pressure derivative, whilst addition of even small amounts of Ca^{2+}, Al^{3+},... to the orthopyroxene (as observed in natural orthopyroxenes of approximate mantle composition) causes significant differences in

the compressional behaviour: the bulk modulus increases by some ~14% to a value closer to that of previous determinations (eg. Frisillo and Barsch (1972); Webb and Jackson, (1993)), its pressure derivative is significantly reduced by some 35% to between 7 and 10, and there is no evidence of any change in compression mechanism of the natural orthopyroxene at pressures below 6 GPa. These measurements confirm the previous Brillouin conclusions (eg., Bass and Weidner, 1984; Duffy and Vaughan, 1988) that Fe^{2+}-Mg^{2+} substitution in orthopyroxenes makes little difference to its EOS.

The effect of Ca^{2+} on the EOS of orthopyroxene is illustrated in Figure 4.16, which shows the difference in the volume variation with pressure of natural orthopyroxene and synthetic $MgSiO_3$ orthoenstatite. At ~10 GPa (the pressure in the Earth's mantle at ~300 km depth), the volume difference is of the order of ~ 0.3%, and the density difference between the two orthopyroxenes is of the order of 3.4%. Thus pure $MgSiO_3$ orthoenstatite is not a good representation of the properties of the pyroxene component of the Earth's upper mantle. The thermodynamic properties of natural orthopyroxenes, which include the large effects of even small amounts of Ca^{2+} and Al^{3+} substitution, are more appropriate for modelling the mineralogical and physical properties of the upper mantle of the Earth.

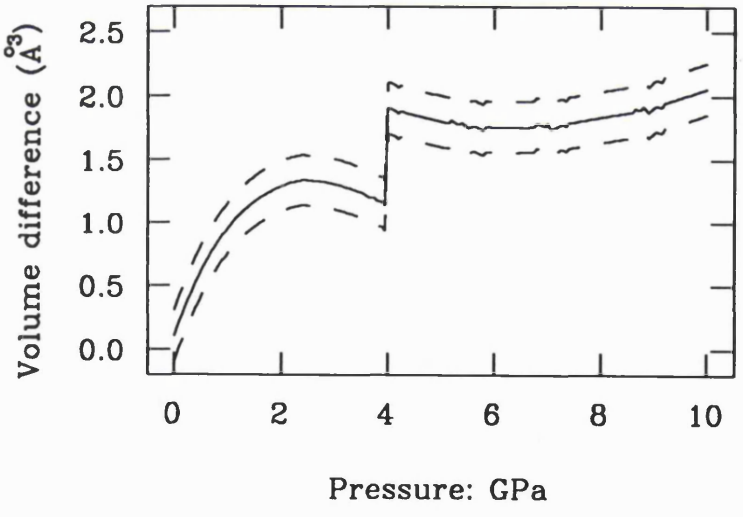

Figure 4.16: Comparison of the third-order Birch-Murnaghan EOS's of natural (OPX1) and synthetic orthoenstatite to 10 GPa. The dotted lines represent the maximum uncertainties in the unit cell volume difference between the natural (OPX1) and synthetic $MgSiO_3$ orthoenstatites. Note the effect of the discontinuity in the EOS of the synthetic $MgSiO_3$ orthoenstatite on the shape of the curve at 4 GPa.

CHAPTER 5

STRUCTURAL PHASE TRANSITIONS IN $FeSiO_3$ PYROXENES

5.1 INTRODUCTION

The presence of polymorphic phase transitions in a mineral system may give some indication about the nature of seismic discontinuities present within the Earth's upper mantle. While it is commonly accepted that the olivine-wadsleyite transition is associated with the discontinuity at 400km depth (eg., Ringwood, 1975), it is possible that the orthopyroxene to high-pressure clinopyroxene transition occurring at high pressures and temperatures (eg, Pacalo and Gasparik, 1990; Kanzaki, 1991; Akimoto et al., 1965; Angel et al., 1992a) may, at least in part, be responsible for the Lehmann discontinuity which is present at ~200 km depth in sub-continental mantle. The positions, in P-T space, of equilibrium phase boundaries between the different structural polymorphs of the $(Mg,Fe)SiO_3$ pyroxenes are also important for determining the overall topology of the pyroxene phase diagram, and thus the thermodynamic relationships between the constituent phases. This final point is discussed in more detail in Chapter 7.

The low-clinoenstatite ($P2_1/c$) to orthoenstatite (Pbca) transition has been successfully reversed at low pressures and modest temperatures by Grover (1972), and another orthoenstatite to clinoenstatite boundary was reversed more recently at much higher pressures and temperatures by both Pacalo and Gasparik (1990) and Kanzaki (1991). In order to reconcile the work of these latter authors with that of Grover (1972), Angel et al. (1992a) compressed a single crystal of $MgSiO_3$ low-clinoenstatite ($P2_1/c$) in a diamond anvil cell (DAC) to ~8 GPa at ambient temperature, and observed a reversible first-order transition to a higher symmetry clinoenstatite phase with space group C2/c. The structure of this high-pressure clinoenstatite phase was determined *in situ*, and was found to be significantly different to the clinoenstatite phase observed at high temperatures (eg, Perotta and Stephenson, 1965; see also Chapter 6).

Since the addition of small amounts of Ca^{2+} or Al^{3+} to the $MgSiO_3$ end-member has only a minor effect on the position of the orthopyroxene to high-pressure clinopyroxene phase boundary (Herzberg and Gasparik, 1991), and Fe^{2+} is likely to be the largest substituent for Mg^{2+} in natural orthopyroxenes, this study of the phase stabilities of $FeSiO_3$ pyroxenes provides end-member data for the subsequent examination of the effect of Fe^{2+} on the phase relations of Ca^{2+}-free pyroxenes (Chapter 7).

The discrepancy observed between the ortho- to clinoferrosilite reversals of Lindsley (1965) and Akimoto et al. (1965) is very similar to that previously described for the reversals of Pacalo and Gasparik (1990), Kanzaki (1991) and Grover (1972) between ortho- and clinoenstatite polymorphs (see also Chapter 7, Figure 7.4). One possible solution would be for the phase diagram of $FeSiO_3$ to have the same topology as that of $MgSiO_3$, with a stability field for a C2/c clinoferrosilite phase at high pressures. By analogy with $MgSiO_3$ this phase would be expected to revert to low-clinoferrosilite upon pressure release. The first part of this chapter describes an *in-situ* high-pressure single-crystal X-ray diffraction study of low-clinoferrosilite ($P2_1/c$), undertaken to attempt to reconcile these differences between the results of Lindsley (1965) and Akimoto et al. (1965), and showing that the low-clinoferrosilite transforms to a C2/c phase at high pressures. The detailed structure and crystal chemistry of this high pressure C2/c clinoferrosilite is discussed at greater length in Chapter 6.

The transformation between orthopyroxene and this high-pressure clinopyroxene occurs for pyroxenes of all compositions along the $(Mg,Fe)SiO_3$ join at pressures and temperatures characteristic of the Earth's upper mantle (Pacalo and Gasparik, 1990; Akimoto et al., 1965; Woodland, unpublished data), with the metastable extension of this boundary at ambient temperatures in the $FeSiO_3$ system falling at approximately 1 GPa at room temperature. Orthoferrosilite thus exists metastably with respect to high-pressure C2/c clinoferrosilite at pressures above this. The second part of this chapter describes compression experiments to $\sim$5.8 GPa on a single crystal of synthetic orthoferrosilite, performed in order to determine the range of metastability of the $FeSiO_3$ orthoferrosilite, and to establish whether its direct

transformation to the high-pressure C2/c phase is indeed possible at ambient temperature.

5.2 THE LOW- TO HIGH-CLINOFERROSILITE TRANSITION

5.2.1 Characterisation of the Transition: Behaviour of Unit Cell Parameters

The structure of the clinoferrosilite crystal with space group $P2_1/c$ was determined at room pressure; selected bond lengths and angles are reported in Table 5.1, (the complete list of refined positional parameters and bond lengths and angles is given in Appendix 2). All structural parameters are within one combined *esd* of those measured by Burnham (1966b).

On compression to 1.43 GPa the clinoferrosilite crystal exhibited $P2_1/c$ cell parameters which are characterised by a relatively large beta angle of $\sim 108°$. At these low pressures there was no significant variation in the intensities of the ω-scans of the $h+k=2n+1$ reflections that are present in the diffraction pattern of low-clinoferrosilite. On increasing the pressure further to 1.75 GPa these reflections disappeared from the diffraction pattern and the unit cell parameters underwent a discontinuous change; while a decreased by $\sim 1.3\%$, c shortened by some 4% and β was reduced by about 5° to a value of 103.07° (Figures 5.1a-d). The transition was accompanied by a 3% volume decrease (Figure 5.1e), which indicates that the transition is first order in character. On releasing the pressure from the crystal the structure once again assumed the low-clinoferrosilite structure, with its large value of β. Subsequent cycles of raising and lowering the pressure around the transition yielded a reversed bracket of 1.48 - 1.75 GPa, and showed that the transformation is both reversible and that the high-pressure phase is non-quenchable.

From diffraction data collected from the crystal at 1.87 GPa it was found that all reflections with $h + k$ = odd were absent, and of the *h0l* reflections those with l=odd were also unobserved. These systematic absences are indicative of space groups C2/c or Cc. An N(z) test (Wilson, 1949) on the intensities of all accessible reflections

indicated that they display the statistics expected from a centric structure. A structure refinement of the combined dataset was therefore carried out in space group C2/c, using as initial coordinates those of high-pressure C2/c $MgSiO_3$ pyroxene (Angel et al., 1992a). Refined positional parameters, bond lengths and angles, and polyhedral volumes and distortions are reported in Table 5.1 and Appendix 2.

	C2/c (1.87 GPa)	$P2_1/c$ "A"-CHAIN	(Room T, P) "B"-chain
Fe1-O1	2.20 (2)	2.08 (1)	2.09 (1)
Fe1-O1	2.109 (8)	2.20 (1)	2.20 (1)
Fe1-O2	2.12 (1)	2.11 (1)	2.13 (1)
Average Fe1-O	2.14 (1)	2.13 (1)	
Fe1 volume	13.0 (1)	12.8 (1)	
Fe1 Quad. El.	1.0083	1.0091	
Fe2-O1	2.12 (2)	2.16 (1)	2.13 (1)
Fe2-O2	1.990 (9)	2.04 (1)	1.99 (1)
Fe2-O3	2.43 (1)	2.45 (1)	2.57 (1)
Average Fe2-O	2.18 (1)	2.22 (1)	
Fe2 volume	13.6 (1)	13.5 (1)	
Fe2 Quad. El.	1.0182	1.0648	
Si-O1	1.61 (1)	1.62 (1)	1.61 (1)
Si-O2	1.60 (1)	1.58 (1)	1.59 (1)
Si-O3	1.67 (1)	1.63 (1)	1.65 (1)
Si-O3	1.66 (1)	1.65 (1)	1.69 (1)
Average Si-O	1.63 (1)	1.62 (1)	1.64 (1)
Si volume	2.22 (2)	2.17 (1)	2.24 (1)
Si Quad. El.	1.0024	1.0063	1.0049
O3-Si-O3	107.4 (0.5)	106.7 (0.4)	110.8 (0.4)
O3-O3-O3	138.4 (0.9)	192.9 (0.9)	144.1 (0.9)

Table 5.1 Bond lengths and angles for the high-pressure C2/c and $P2_1/c$ polymorphs of $FeSiO_3$, at 1.87 GPa and ambient conditions respectively.

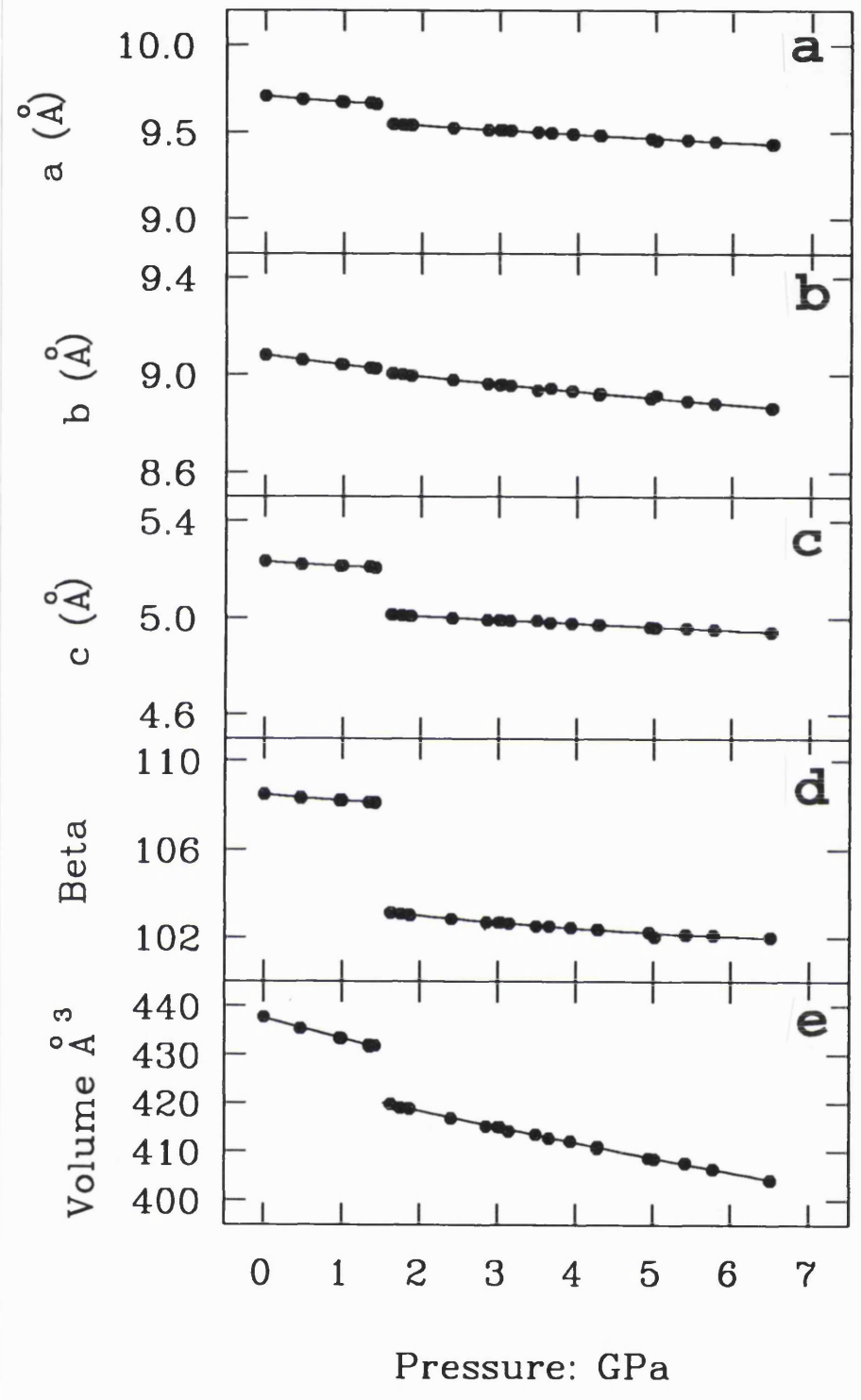

Figure 5.1: Variation of the unit cell parameters a) *a*, b) *b*, c) *c* and d) β of $FeSiO_3$ clinoferrosilite, showing discontinuities in both *a* and *c*, and β during the $P2_1/c$ to C2/c phase transition between 1.48 and 1.75 GPa; e) Variation of the unit cell volume of clinoferrosilite with pressure, showing a discontinuous jump of ~ 12Å^3 between 1.48 and 1.75 GPa. The uncertainties in the measurements of the unit cell parameters, the volume and the pressure are considerably less than the sizes of the symbols used.

The structure of this C2/c polymorph refined from diffraction data collected at 1.87 GPa shows that this clinoferrosilite contains a single symmetrically distinct silicate tetrahedral chain with mean Si-O bond length of 1.63(1)Å, and chain extension angle (O3-O3-O3) of 138.4(9)°. The M1 and M2 cation sites are octahedrally coordinated, with mean bond lengths of 2.14(1)Å and 2.18(1)Å respectively. The structure of this clinopyroxene is discussed in more detail in Chapter 6, and is demonstrated to be the iron analogue of the C2/c phase found in $MgSiO_3$ at pressures above 7 GPa.

Using orientation matrices obtained from diffraction data collected from the clinoferrosilite crystal above and below the transition, the orientational relationship for the transformation of the low- to the high-P clinoferrosilite structures was calculated as:

$$\begin{matrix} 1 & 0 & 0.16 \\ 0 & 1 & 0 \\ 0 & 0 & 1 \end{matrix}$$

Since this relationship between the high- and low-pressure structures consists of two independent components (ie, that due to the crystallographic transition from the low- to the high-clino phases, and also a possible movement of the crystal within the diamond anvil cell between experiments), the above matrix was calculated for several different experimental reversals, giving the estimated uncertainties for each component of the matrix as $\pm$ 0.03. Within these limits, the crystallographic relationship between the $P2_1/c$ and high-P C2/c phases of $FeSiO_3$ is identical to that calculated for $MgSiO_3$ (Angel, pers. comm.).

5.2.2 Nature of the $P2_1/c$ - high-P C2/c Transition in Both Mg and Fe Pyroxenes

The change in symmetry from $P2_1/c$ to C2/c of the clinoferrosilite may be described by differences in the configuration of the silicate chains within the pyroxene framework, in a similar way to the $P2_1/c \rightarrow$C2/c transition in the $MgSiO_3$ end-member (Angel et al., 1992a). The structure of low-clinoferrosilite (space group $P2_1/c$) consists

of two symmetrically distinct silicate chains, which are rotated in different directions. The "A"-chain is S-rotated (defined by Thompson, 1970; also Chapter 1), and is more extended with smaller tetrahedra than the "B"-chain, which is O-rotated and considerably kinked. The edge-sharing of the tetrahedra and M2 site which results from the S-rotation of the "A"-chain makes the M2 octahedral site extremely distorted. The chain extension angles of the low-clinoferrosilite show very large rotations from 180°, indicating that the structure is near its stability limit. Since the SiO_4 tetrahedra are relatively incompressible at low pressures, increasing the pressure will tend to differentially compress the FeO_6 octahedra, thus requiring further rotation of the tetrahedral chains from the straight configuration to stabilise the structure (cf. orthopyroxenes; Chapter 3).

Since the chains are already as kinked as they can readily become, the structure undergoes a major reconfiguration of the silicate chains between 1.43 and 1.75 GPa. Above the transition pressure, the "A"-chain becomes O-rotated (ie, kinked in the opposite sense from the fully extended position relative to its kinking in the low-pressure structure) and becomes symmetrically equivalent the "B"-chain. Note that this chain rotation also involves the breaking of the bonds between each O3 oxygen atom of the "A"-chain and the M2 iron atoms on one side of the chain, and the formation of new bonds between the O3 and the M2 sites on the other side (Schematically shown in Figures 5.2a and b). As a result, the tetrahedra in the "A"-chain no longer share edges with the M2 sites and this allows these octahedra to become significantly smaller. The unit cell volume of the pyroxene is reduced by some 12Å^3 by the transformation to a pyroxene with a small chain extension angle of 138.4°. Under Pannhorst's (1979) description, the transformation involves a change in stacking sequence from *M+SS-M+KK-M* in the $P2_1/c$ phase to *M+KK-M+KK-M* for the high pressure C2/c structure, where *S* denotes a layer of relatively-straight tetrahedral chains, *K* a layer of kinked chains, and *M* represents the octahedral layer.

The nature of this low- to high-P clino transformation is very similar to that occurring above 7 GPa in clinoenstatite (Angel et al., 1992a). In both the $FeSiO_3$ and the $MgSiO_3$ end-member compositions the transition is accompanied by a ~ 3% volume

decrease and a decrease of about 6° in β, (Figures 5.1d and e). However, the magnitude of the hysteresis loop between the high-P (C2/c) and low ($P2_1/c$) structures is much greater in the $MgSiO_3$ end-member (about 2.6 GPa) than in the ferrosilite, which the above reversals demonstrate must be less than 0.27 (5) GPa.

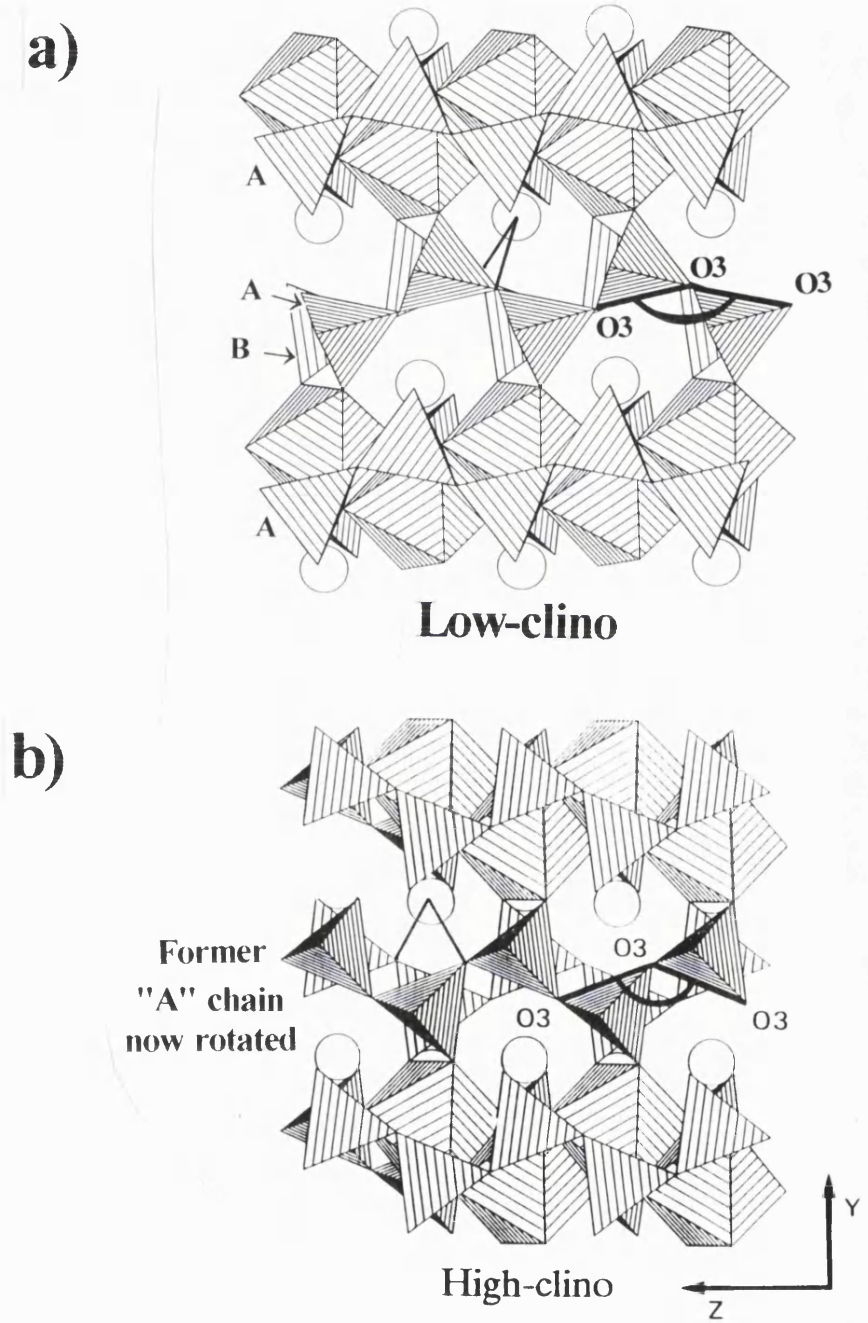

Figure 5.2: Polyhedral representation of the structures of a) low-clinoferrosilite and b) high-pressure C2/c clinoferrosilite projected down [100], showing the positions of the M2-O3 bonds that are broken and re-made during the transition at ~1.6 GPa.

From a study of many pyroxenes of various compositions and all space groups, Cameron and Papike (1980) determined the relationships between ionic cation radius for the octahedral sites and several internal bond lengths and angles. They showed that as the radius of the M2 cation increases the average Si-O bond lengths also increase. For a change in M2 cation radius from that of Mg^{2+} to that of Fe^{2+}, average Si-O bond lengths in the C2/c structure are predicted to increase by about 0.005Å, and the average M2-O bond lengths by about 0.009Å; the O3-O3-O3 chain angle is predicted to decrease by up to about 5°. The above data for the high-P C2/c polymorph of both end-member compositions show that both Si-O and M2-O bond lengths behave as expected, whereas the O3-O3-O3 chain extension angle appears to increase by some 3° as Mg^{2+} is replaced by Fe^{2+} in the M1 and M2 sites.

A similar examination of the behaviour of the low-clino ($P2_1/c$) polymorphs (using the trends determined by Cameron and Papike, 1980) reveals that, on replacing the Mg^{2+} by Fe^{2+}, the average Si-O bond length in both silicate chains shortens, the radius of the octahedral cation increases, and the average M2-O bond length increases, all as expected. Both "A"- and "B"-chains are predicted to rotate towards the straight position by approximately 7° as Fe^{2+} replaces Mg^{2+} in the cation sites; within the experimental uncertainties this is found to be the case for clinopyroxenes of end-member $MgSiO_3$ and $FeSiO_3$ compositions. From these trends it may be assumed that most of the changes of the bond lengths and angles of the monoclinic phases due to changing the composition along the Mg,Fe join can be successfully predicted using the trends of Cameron and Papike (1980), and although the pressure of the low ($P2_1/c$)-high-P (C2/c) transition varies with composition the nature of the transformation does not.

5.3 TRANSITION OF ORTHO- TO HIGH-P C2/c CLINOFERROSILITE

5.3.1 Characterisation of the Transition

A single crystal of $FeSiO_3$ orthoferrosilite was initially compressed in the diamond anvil cell (DAC) to 4.2 GPa. Structure refinements to X-ray intensity data collected at five different pressures between atmospheric pressure and 3.65 GPa inclusive (Chapter 3) showed that compression is accommodated by a smooth decrease in the volumes of the M1 and M2 octahedral sites, with associated tilting and kinking of the two SiO_3 tetrahedral chains. This pattern of compressional behaviour is essentially identical to that observed in $MgSiO_3$ orthoenstatite below 4 GPa (Chapter 3). The total time taken for these experiments was approximately 23 weeks, of which about 18 weeks were at pressures in excess of 1.5 GPa.

After these experiments, the pressure in the DAC was increased to 4.6 GPa, at which pressure the positions of 34 reflections were measured on the diffractometer to determine the unit-cell parameters. The positions and intensities of these reflections clearly indicated that the crystal was still orthopyroxene. An intensity data collection was then initiated. Approximately 3 days after the increase of pressure to 4.6 GPa the reflection intensities had decayed significantly, and the data collection was stopped. Careful searching revealed that the strong reflections used for determining the unit cell parameters of the orthopyroxene had disappeared from the X-ray diffraction pattern of the crystal. A systematic search through reciprocal space found three broad and weak reflections that could not be attributed to diffraction from DAC components. The 2θ angles of these reflections were the same as those of the C2/c high-P clinoferrosilite phase held at $\sim$ 4.5 GPa, and quite distinct from those expected for the orthoferrosilite held at this same pressure. Optical inspection of the crystal in the DAC showed that it had disintegrated into many small pieces, thus providing an explanation of the relative weakness of the reflections. This was confirmed upon unloading of the crystal from the DAC.

A second compression experiment was then performed on another

orthoferrosilite single crystal, grown under the same synthesis conditions. Measurements of unit-cell parameters from atmospheric pressure to 4.7 GPa were undertaken over a period of 32 days. The pressure was then increased to 5.4 GPa (and held at this pressure for approximately 36 hours) for unit-cell determination, and then to 5.8 GPa. The reflections characteristic of the orthopyroxene had disappeared within 12 hours, and before the unit-cell parameters could be determined. At this point, the cell was de-pressurised and unloaded. In both these experiments, the gasket of the DAC was carefully inspected to ensure that the crystal of orthopyroxene had not bridged the anvils and thereby been subjected to non-hydrostatic stresses. Both of the samples were therefore contained within a hydrostatic environment throughout the course of the experiments.

TEM examination of the crystal fragments recovered from the DAC after pressure release revealed that they exhibit a primitive monoclinic diffraction symmetry ($h + k \neq 2n$ reflections present) with d-spacings characteristic of the low-symmetry $P2_1/c$ clinoferrosilite phase (eg, Burnham 1966b). Although some crystal fragments showed distinct twinning on (100), most of them displayed a relatively high degree of stacking disorder (approximately 70 $\pm$ 10 stacking faults per micron along [100]), which caused streaking of reflections in the a^* direction of the diffraction patterns (Figures 5.3a and b). This stacking fault density is considerably higher than the initial degree of stacking disorder observed in the $FeSiO_3$ orthoferrosilite starting material (approximately 30 $\pm$ 10 faults per micron along [100]; see Section 2.5.3).

$P2_1/c$ clinopyroxenes frequently contain anti-phase domains (APD's) that are related by the displacement $1/2(a+b)$ corresponding to the C-face centring translational symmetry present in pyroxenes with C2/c symmetry. Such domains commonly arise as a result of the transformation from C2/c to $P2_1/c$ that can occur, for example, upon cooling (as in the case of pigeonites, e.g. Morimoto and Tokonami, 1969) and/or pressure release. The recovered material in the TEM was therefore carefully examined for evidence of APD's which would provide independent evidence of the material having undergone such a symmetry change upon decompression.

a)

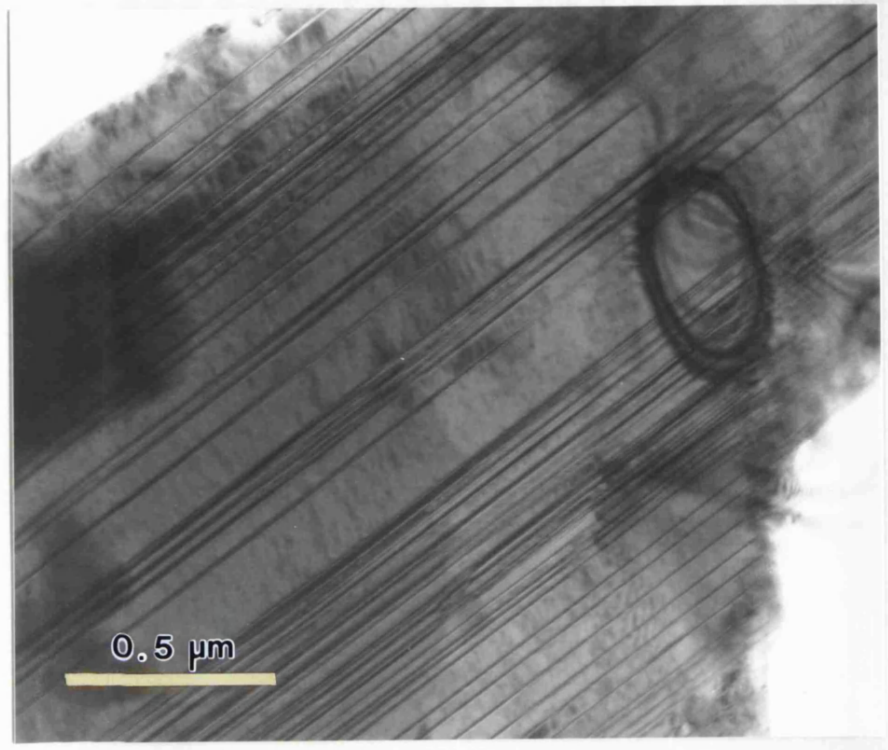

b)

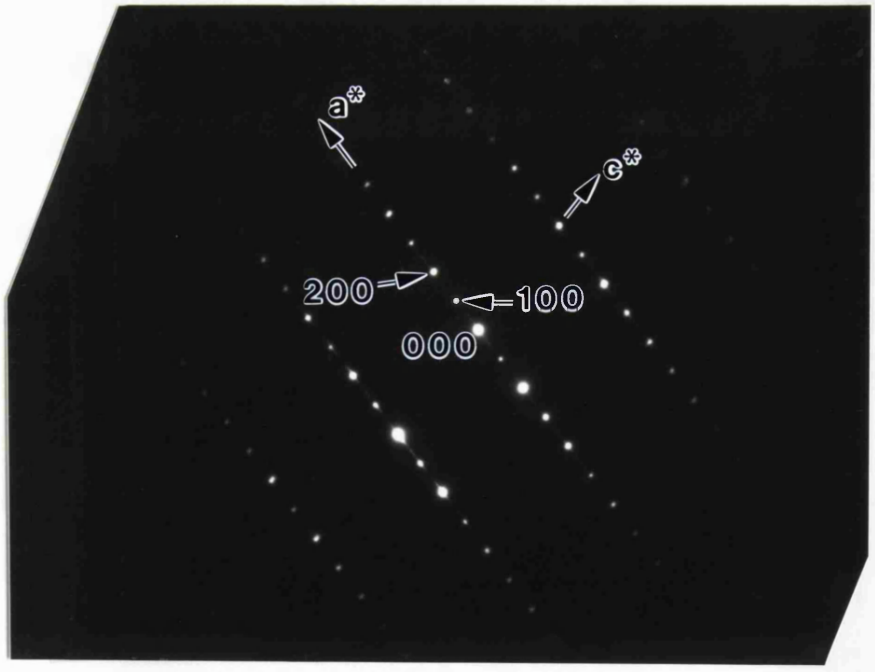

Figure 5.3: a) TEM bright-field image showing numerous stacking faults in a typical area of transformed $FeSiO_3$ ferrosilite, with b) the corresponding diffraction pattern, showing faint streaking along a^* due to these stacking faults.

Such APD's can usually be observed by diffraction contrast imaging in either bright-field or dark-field conditions, with a single $h + k = odd$ Bragg reflection excited (e.g. Nord, 1992). Figure 5.4a shows a typical dark-field image of the recovered material formed with an (h02) reflection where h is odd. Between the (100) stacking faults, the dark field image displays a strong mottled contrast pattern with boundaries generally oriented parallel to (001) which might be interpreted as $1/2(a+b)$ APD's. However, some of this contrast is also apparent in the corresponding dark-field image obtained with an (h02) reflection for which h is even (Figure 5.4b). Under these conditions, such APD's should show no contrast. The fact that the mottled contrast is much stronger in the image obtained where h is odd suggests that while additional microstructures may also contribute to the contrast in dark-field images, much of the contrast originates from fine scale APD's.

There are several experimental reasons why APD contrast in dark-field images collected with $h = even$ may be obtained. First, as with all large unit-cell materials, it is often difficult to obtain pure two-beam conditions because of the small reciprocal lattice spacings along a^* in the $P2_1/c$ pyroxene structure. Slight deviations in crystal orientation can result in intensity on neighbouring reflections such as (h02) with h both even and odd. The objective aperture used for these images is large enough (20 μm) to allow some intensity from a neighbouring reflection to contribute to the images. There is also abundant evidence, in the form of asterism in diffraction patterns as well as Moiré fringes (from misoriented sub-grains) in images, for the presence of substantial nanometre-scale strain in the sample. It is not clear how much of this strain results from the transformation from orthorhombic to monoclinic symmetry or from crushing of the samples in preparation for the TEM (see Chapter 2 for details). Such local strain would give rise to strain contrast in the dark-field images as well as locally varying the diffraction conditions used for imaging. In conclusion, the dark-field images obtained with (h02) reflections and $h = odd$ do not, for experimental reasons, provide unambiguous evidence for the presence (or absence) of $1/2(a+b)$ anti-phase domains within the sample; however it is probable that the contrast observed in Figure 5.4a contains a strong APD component, and that these APD's arise from the transformation of $P2_1/c$ to C2/c.

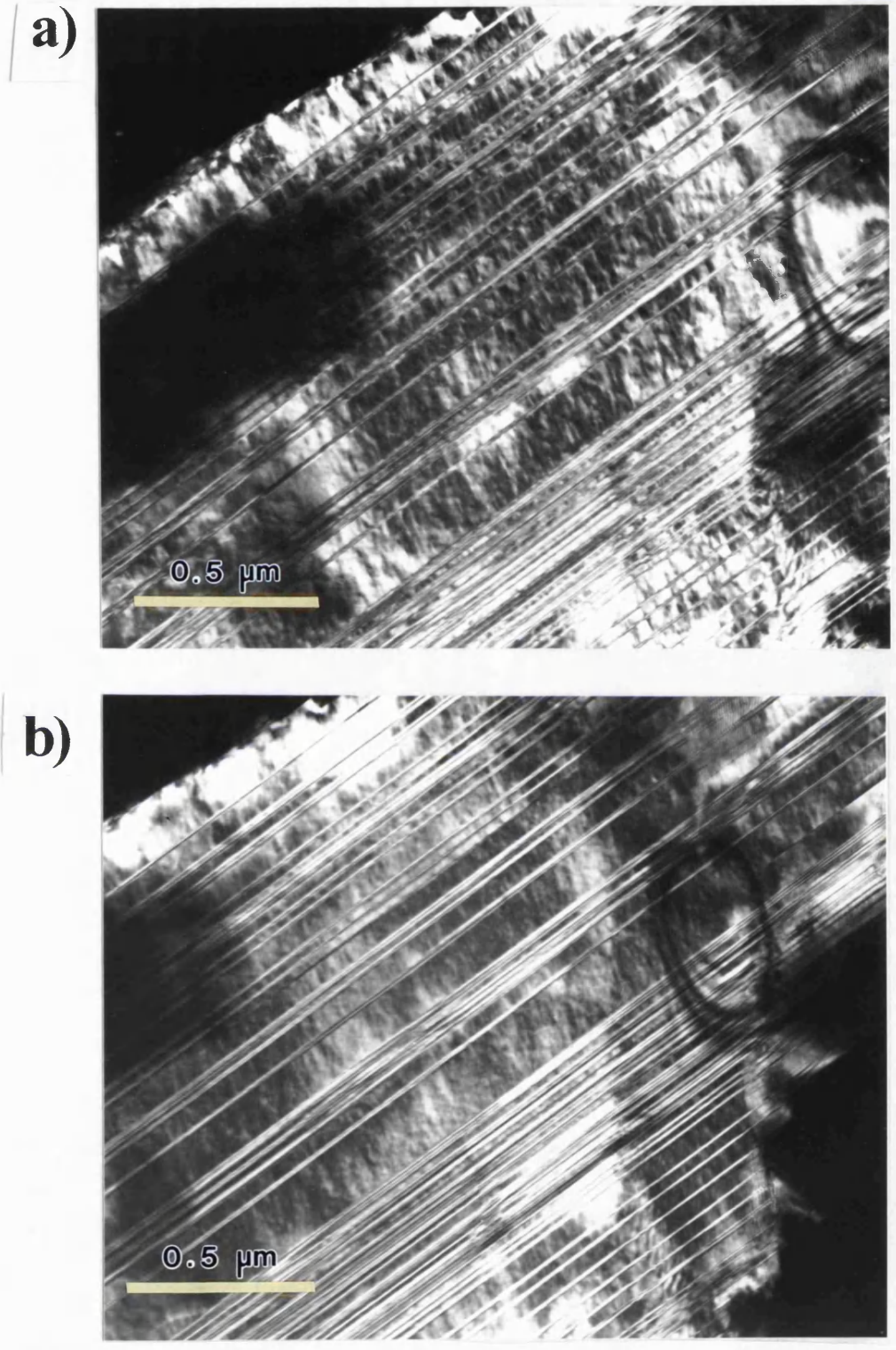

Figure 5.4: a) TEM dark-field image of a typical area of the transformed $FeSiO_3$ ferrosilite, using an $h + k = odd$ reflection of the clinoferrosilite diffraction pattern, and b) dark-field image using an $h + k = even$ reflection of the clinoferrosilite diffraction pattern. Note the enhanced modulated contrast between the stacking faults in a) compared to b).

These TEM observations indicate that the material recovered from the DAC is low-clinoferrosilite with $P2_1/c$ symmetry at room pressure. It was shown above in Section 5.2 that $P2_1/c$ low-clinoferrosilite transforms reversibly to the C2/c polymorph above ~ 1.75 GPa in a methanol:ethanol pressure medium. The C2/c polymorph back-transforms, on decreasing the pressure, to the $P2_1/c$ polymorph at ~ 1.5 GPa; the transition is non-quenchable. The material recovered from the DAC after compression of the $FeSiO_3$ orthoferrosilite must therefore have been either the C2/c polymorph at pressures of 4.6 - 5.8 GPa, or some other phase which also quenches to the $P2_1/c$ polymorph upon decompression. Given that the positions of the diffraction maxima from the transformation product at pressure are consistent with the presence of the C2/c polymorph, the first of these alternatives is the more likely. On this basis, the sequence of transformations was:

Orthoferrosilite (Pbca) $\rightarrow$(P increase above 4.2 GPa) $\rightarrow$High-P Clinoferrosilite (C2/c)

$\rightarrow$(P release below ~ 1.4 GPa) $\rightarrow$Low-clinoferrosilite ($P2_1/c$)

Comparison of the measured equations of state for these polymorphs (see Chapters 4 and 6) indicates that the ortho- to C2/c clinoferrosilite transformation is accompanied by a volume reduction of ~ 2.6% at 5 GPa. This significant volume reduction is presumably the cause of the significant strain contrast and sub-grain mis-orientation observed in the images and diffraction patterns obtained by TEM, and is also responsible, at least in part, for the break-up of the original single crystal of orthoferrosilite. The magnitude of this volume reduction is also another argument in favour of the proposed transformation mechanism. Laying aside for the moment that the survival of low-clinoferrosilite above 2.0 GPa has never been observed in *any* pressure medium (this work; Sowerby and Ross, pers. comm), the volume reduction predicted for the orthoferrosilite to low-clinoferrosilite at 5 GPa is less than 0.2%. Therefore the transformation from orthoferrosilite to C2/c ferrosilite will have a far greater driving force (equal to $\Delta G \sim P\Delta V$) and is thus more likely to occur.

5.3.2 Effect on Unit Cell Parameters

The reduction of the unit cell volume of the order of ~ 22Å^3 (corresponding to a volume discontinuity of ~ 2.6%; Figure 5.5a) is very similar to the ~ 2.8% volume discontinuity determined in Chapter 7 for the corresponding transition in the $MgSiO_3$ end-member of the $(Mg,Fe)SiO_3$ solid solution. Although the lengths of the *b*-axes of both ortho- and high-P clinoferrosilite polymorphs are identical within the experimental uncertainties at 5 GPa, there are distinct changes in the relative lengths of both $d_{(100)}$ (determined relative to the orthorhombic cell) and *c* (Figure 5.5b-d): *c* decreases by some 3.9% at 5 GPa, while d_{100} increases by ~ 1.3%. This compression of the *c*-axis may be identified with the significant kinking of the silicate "A"-chains of the orthopyroxene as a result of the transition, whilst the extension of the *a*-axis (ie, d_{100} in the clinoferrosilite polymorph) may be caused either by the increased out-of-plane tilting of the bases of the tetrahedra from (100) within both silicate chains, or by the exchange of the fairly-regular M1 and more-distorted M2 cation sites during the transition. However, the combined effect of these two axial compression mechanisms is to reduce the volume of the ferrosilite at high pressures, and thus to increase its density.

5.3.3 Nature of the Ortho- to High-Pressure C2/c Clinoferrosilite Transition

Although there are no direct observations from which to draw definite conclusions about the atomic-scale mechanism of the orthopyroxene to clinopyroxene transition, some tentative arguments can be made. Firstly, the duplicate experiments in the DAC show that the transformation is time-dependent and therefore thermally activated. In turn this suggests that bond-breaking is part of the transformation process, but the continued presence of diffraction maxima from the transformation product in the DAC, although weak and broad, indicates that the transformation is not completely reconstructive, and that domains of coherently diffracting single-crystals are preserved. This is confirmed by the TEM observations of the recovered transformation products. Secondly, since the structural changes occurring during the transformation cannot be monitored *in situ*, the following transformation mechanism

has been proposed by studying the initial (orthoferrosilite) and final (high-P clinoferrosilite) structures, and by determining the easiest mode of transition from one to the other.

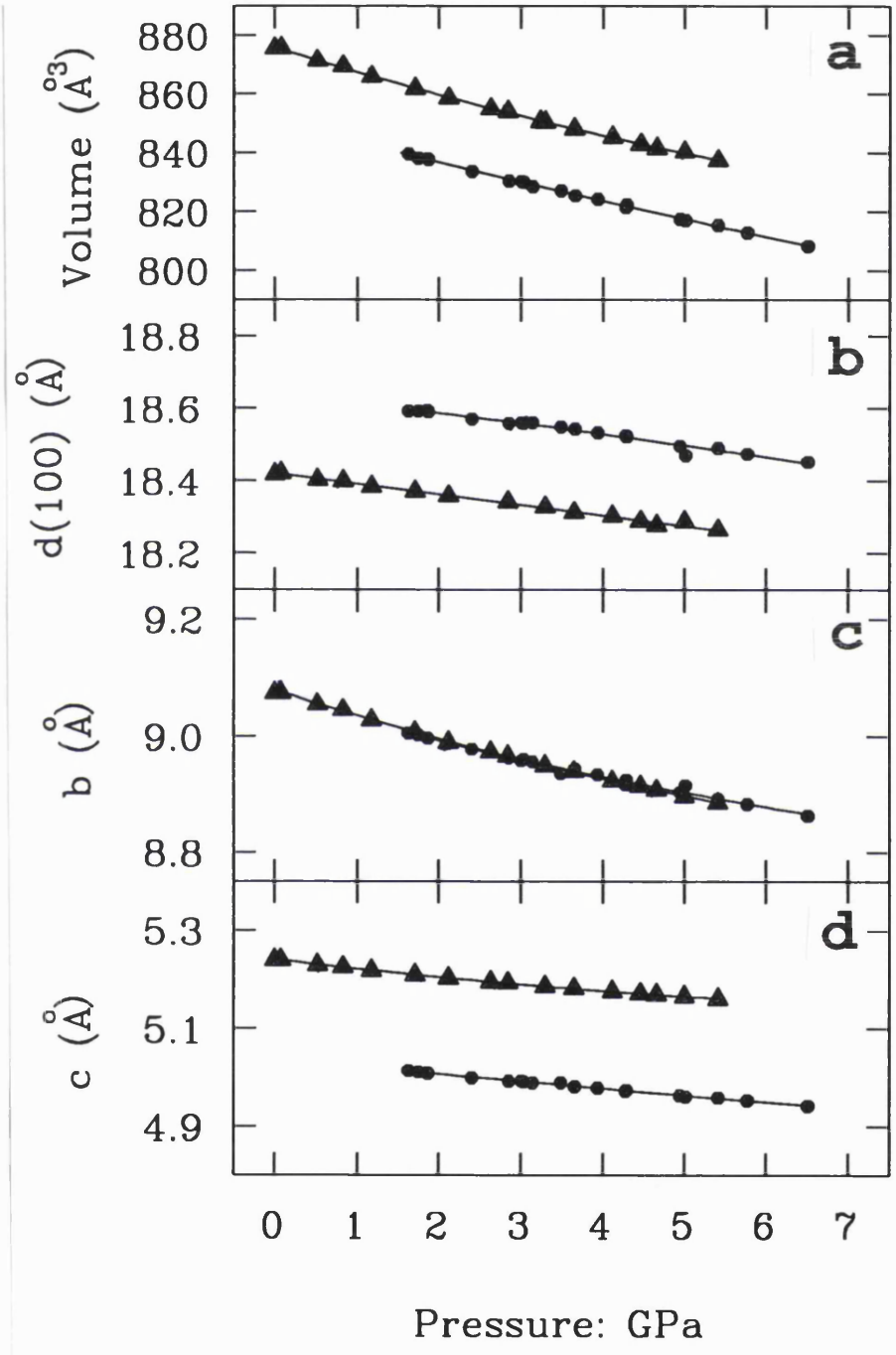

Figure 5.5: Variation of a) the unit-cell volume and the b) *a*, c) *b*, and d) *c* cell parameters (measured relative to an orthorhombic unit cell) of orthoferrosilite (triangles) and high-pressure C2/c clinoferrosilite (circles) with pressure.

Both ortho- and high-pressure C2/c clinoferrosilite consist of alternating layers of SiO_4 tetrahedra and FeO_6 octahedra lying parallel to the (100) plane. Although the silicate chains in both structures are all O-rotated (Thompson, 1970), there are two symmetrically distinct chains in the orthoferrosilite polymorph - the "A" chain is more extended with smaller tetrahedra than the "B"-chain, which contains somewhat larger tetrahedra, and is considerably kinked; both silicate chains are extremely kinked and symmetrically equivalent in the high-pressure C2/c phase (Chapter 6). In both structures, the tetrahedral chains have two different orientations within each (100) layer - with their apical O1 atoms pointing in either the $+a$ direction or the $-a$ direction relative to the basal O2-O3-O3 plane of the tetrahedra respectively; both types of chains are connected to the neighbouring octahedral layers (above and below the tetrahedral layer respectively) by the apical O1 atoms (Figure 5.6).

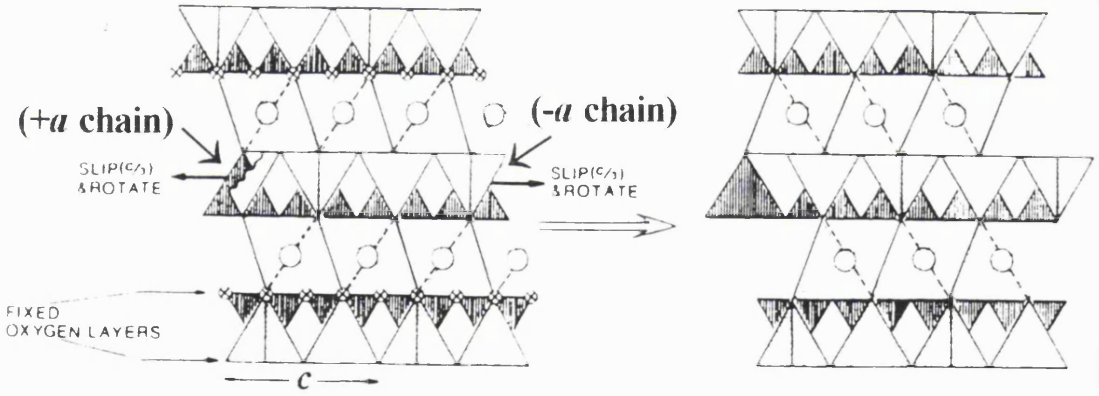

Figure 5.6: Schematic diagram (after Sueno and Prewitt, 1983) of the mechanism for changing the "skew" of two adjacent octahedral layers that have the same sense of skew, as proposed by Sadanaga et al. (1969). In the above diagram, the $+a$ chain and the $-a$ chain in the "B" tetrahedral layer slip in opposite directions by $1/3c$ and rotate.

The structures of orthopyroxene and high-pressure clinopyroxene also differ in the stacking sequence and orientations (or skews) of these octahedral strips within the two structures (Figure 5.7). The orthopyroxene unit cell contains four layers of Fe^{2+} cation sites parallel to (100), between which are layers of tetrahedral chains running parallel to the *c*-axis; the high-P clinopyroxene contains only two cation layers per unit cell. These octahedral layers also have different senses of "skew" (denoted + and -) defined by the direction they point in along the *c*-direction (e.g. Sueno and Prewitt, 1983). Although the skews of the octahedra in the orthoferrosilite structure alternate every two layers (and can therefore be labelled ++--++...), all the octahedral layers in the high-pressure clinoferrosilite phase have the same sense of skew, which can be designated ++++.... When two adjacent octahedral layers in the orthoferrosilite structure have the same sense of skew (ie, ++ or --), the tetrahedral chains between them are known "B"-chains (eg., Figure 5.6); when the skews are different, the chains are "A"-chains.

Before the mechanism of transformation is outlined, it is useful to consider a "double-cell" for the high-pressure clinoferrosilite phase, consisting of two high-pressure C2/c clinoferrosilite unit cells joined together on (100). The corresponding fractional *x*-coordinates of the atoms are halved to give the appearance of a supercell with a dimension close to that of the orthoferrosilite (ie., $a \sim 18$Å), and the *z*-coordinates of all the atoms contained within the unit cell have been corrected for the effect of the β angle of $\sim 103°$. The symmetry-equivalent positions of the Fe1, Fe2 and Si atoms in both the orthoferrosilite and high-pressure C2/c clinoferrosilite are shown, for reference, in Table 5.2. Note that the origin of the fractional coordinates of the orthoferrosilite atoms have been shifted by an arbitrary amount to virtually superimpose the two structures and thus make comparison of the relative fractional coordinates easier.

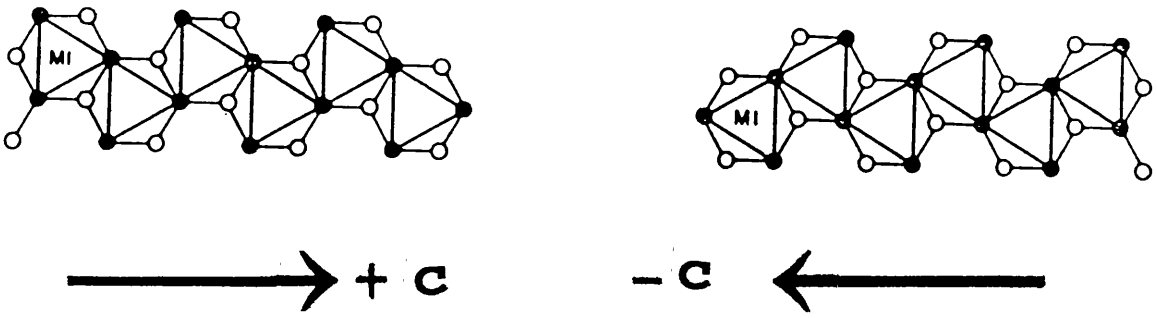

Figure 5.7: Schematic diagram of the different skews of the octahedra within the octahedral strips running parallel to the *c*-axis on the (100) plane.

Atom	Orthoferrosilite (Pbca)	Clinoferrosilite (C2/c)	Corresponding cfs position	M1 - M2 Exchange
Fe1 1	0.000, 0.095, 0.750	0.000, 0.095, 0.750	Fe1 1	no
Fe1 2	0.000, 0.285, 0.250	0.000, 0.905, 0.250	Fe2 1	yes
Fe1 3	0.252, 0.595, 0.750	0.250, 0.405, 0.465	Fe1 4	no
Fe1 4	0.252, 0.785, 0.250	0.250, 0.595, 0.965	Fe2 4	yes
Fe1 5	0.500, 0.095, 0.512	0.500, 0.095, 0.179	Fe1 5	no
Fe1 6	0.500, 0.285, 0.012	0.500, 0.905, 0.679	Fe2 5	yes
Fe1 7	0.752, 0.595, 0.512	0.750, 0.405, 0.465	Fe1 7	no
Fe1 8	0.752, 0.785, 0.012	0.750, 0.595, 0.965	Fe2 8	yes
Fe2 1	0.998, 0.457, 0.741	0.000, 0.272, 0.250	Fe2 2	no
Fe2 2	0.998, 0.923, 0.241	0.000, 0.728, 0.750	Fe1 2	yes
Fe2 3	0.254, 0.457, 0.241	0.250, 0.228, 0.965	Fe1 3	yes
Fe2 4	0.254, 0.923, 0.741	0.250, 0.772, 0.465	Fe2 3	no
Fe2 5	0.498, 0.457, 0.521	0.500, 0.272, 0.679	Fe2 6	no
Fe2 6	0.498, 0.923, 0.021	0.500, 0.728, 0.179	Fe1 6	yes
Fe2 7	0.754, 0.423, 0.021	0.750, 0.228, 0.965	Fe1 8	yes
Fe2 8	0.754, 0.923, 0.521	0.750, 0.772, 0.465	Fe2 7	no

Atom	Orthoferrosilite (Pbca)	Clinoferrosilite (C2/c)	Corresponding cfs position	Shift of chain
SiA 1	0.104, 0.600, 0.425	0.101, 0.412, 0.863	SiA 1	+c/3
SiA 2	0.104, 0.780, 0.925	0.101, 0.588, 0.363	SiA 2	+c/3
SiA 3	0.148, 0.100, 0.425	0.150, 0.088, 0.352	SiA 4	+c/3
SiA 4	0.148, 0.280, 0.925	0.150, 0.912, 0.852	SiA 3	+c/3
SiA 5	0.604, 0.600, 0.837	0.601, 0.412, 0.120	SiA 5	+c/3
SiA 6	0.604, 0.780, 0.337	0.601, 0.588, 0.620	SiA 6	+c/3
SiA 7	0.648, 0.100, 0.837	0.650, 0.088, 0.523	SiA 8	+c/3
SiA 8	0.648, 0.280, 0.337	0.650, 0.912, 0.023	SiA 7	+c/3
SiB 1	0.349, 0.107, 0.172	0.350, 0.088, 0.577	SiB 1	+c/3
SiB 2	0.349, 0.273, 0.672	0.350, 0.912, 0.077	SiB 2	+c/3
SiB 3	0.403, 0.607, 0.090	0.400, 0.412, 0.066	SiB 4	-c/3
SiB 4	0.403, 0.773, 0.590	0.400, 0.588, 0.566	SiB 3	-c/3
SiB 5	0.849, 0.108, 0.090	0.850, 0.088, 0.406	SiB 5	+c/3
SiB 6	0.849, 0.273, 0.590	0.850, 0.912, 0.906	SiB 6	+c/3
SiB 7	0.903, 0.607, 0.172	0.900, 0.412, 0.809	SiB 7	-c/3
SiB 8	0.903, 0.773, 0.672	0.900, 0.588, 0.309	SiB 8	-c/3

Table 5.2. Corresponding fractional coordinates of Fe1, Fe2 and Si atoms in orthoferrosilite and high-pressure C2/c clinoferrosilite, measured at 1.71 and 1.87 GPa respectively. Note that the fractional coordinates of the cations within clinoferrosilite structure have been determined relative to an orthorhombic unit cell; the coordinates of the orthoferrosilite have been shifted by the arbitrary vector (-0.124, -0.060, -0.119), so that the Fe1 atoms in both structures are exactly coincident, and the positions of the remaining cations are almost coincident.

The overall mechanism is characterised by two separate mechanisms occurring simultaneously - a shearing of the tetrahedral chains along [001] within the (100) planes of the structure, and a movement of the M1 and M2 cation sites, involving some exchange of the two.

a) Silicate Chains

Following the mechanism of Sadanaga et al. (1969) for the orthoferrosilite to high-temperature C2/c clinoferrosilite transition, which is reported in considerable detail by Sueno and Prewitt (1983), it is possible to describe the reconfigurations of the silicate chains occurring during the high-pressure transformation in a similar way. This high-pressure transition involves the rotation of the silicate chains until they become symmetrically equivalent, while both chains remain O-rotated throughout. The "B"-chains pointing in the $+a$ and $-a$ directions behave differently in order for this to happen: those pointing in the $+a$ direction slip by $+c/3$ and rotate with respect to the basal triangle of the upper octahedra, whilst the $-a$ chains slip by $-c/3$ in the opposite direction while also rotating their bases (Figure 5.6). The "A"-chains have to kink by more than 30° in order to become symmetrically equivalent to the "B"-chains in the high-pressure C2/c structure. Associated with this kinking during the high-pressure transformation, *all* the "A"-chains (both the $+a$ and $-a$ chains) shift by $+c/3$ causing many bonds between the "A"-chains and the M1 and M2 octahedra to be broken. This is shown schematically in Figure 5.8.

It is interesting to note that the bases of the silicate tetrahedra within the former "A"- and "B"- chains of the orthoferrosilite become tilted approximately 1° away from and towards the (100) plane respectively as a result of the transition. The volumes of the silicate tetrahedra within the former "A" chains of the orthoferrosilite increase by more than 3% during the transition, while becoming significantly more regular in the high-pressure C2/c clinoferrosilite polymorph; the tetrahedra in the "B"-chain remain geometrically unaltered by the transition.

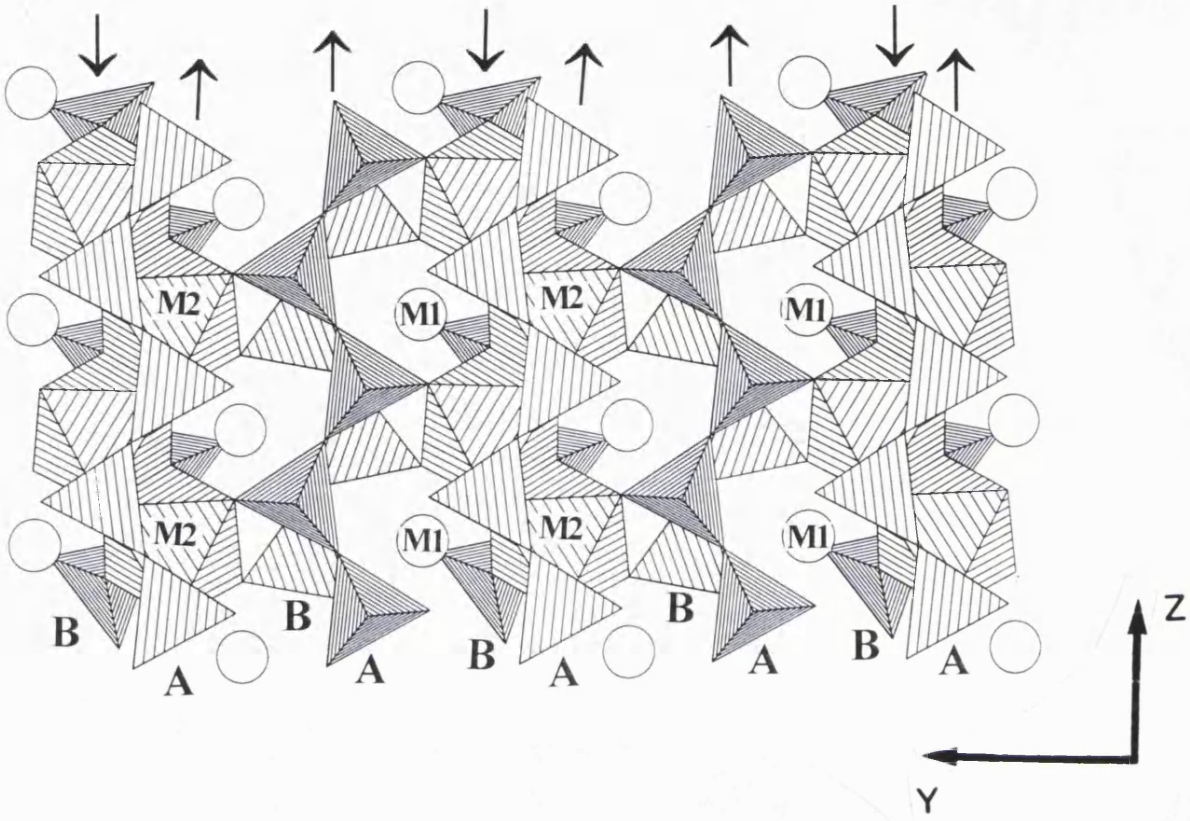

Figure 5.8: Polyhedral drawing of orthoferrosilite showing the mechanism of transformation to high-pressure clinoferrosilite. Shaded octahedra represent M1 sites, and circles represent M2 sites in the orthoferrosilite structure. In this projection, the "B" chains are "-*a*" chains, and therefore translate by -*c*/3; the "A" chains slip by +*c*/3, while also kinking by ~30°; the translations of the chains are shown by the arrows. The unlabelled cation sites remain (in the high-pressure C2/c clinoferrosilite) as the M1 (octahedra) or M2 (circles) sites they are in the orthoferrosilite, whilst the labelled cation sites represent those where exchange of M1 for M2 (and vice versa) occurs during the transition.

b) M1 and M2 Cation Sites

Simultaneously with the shearing of some of the tetrahedral chains in the orthoferrosilite structure, the M1 and M2 octahedra change their direction of "skew". Sueno and Prewitt (1983) outlined several ways in which this reversal of the skew of

the octahedra may be obtained; these involve the movement of the M1 and M2 cations by a vector of magnitude $c/3$ along one or more of three possible directions (see Figure 4 of Sueno and Prewitt, 1983). During the orthoferrosilite to high-pressure clinoferrosilite transformation, the translation vector of the cations proposed by Smyth (1974b) describes their shifts most favourably. This movement requires that the Fe1 and Fe2 cations exchange their positions with each other after the transition with an translation vector of $[c/6 + b/6]$ in the "ideal" pyroxene structure. In other words, M1 becomes M2 and vice versa (Figure 5.8).

The transformation from orthoferrosilite to high-pressure clinoferrosilite may alternatively be described, using Pannhorst's (1979) notation, by the change in stacking sequence of M1 octahedral layers (denoted *M*, with the +/- denoting the sense of shear) and layers of straight (*S*) or kinked (*K*) tetrahedral chains from *M+SS+M-KK+M-SS-M+KK-M* to *M+KK-M+KK-M+KK-M+KK-M*.

Various mechanisms have been proposed for other pyroxene to pyroxene transitions by Sadanaga et al., (1969), Smyth (1974b) and Coe and Kirby (1975), and more recently by Sueno and Prewitt (1983). Sueno and Prewitt (1983) reviewed the previous work, and suggested a detailed mechanism for the transformation of orthoferrosilite to high-temperature polymorph of C2/c clinoferrosilite, the structure of which differs primarily from the high-pressure C2/c polymorph in that it contains extended (ie., O3-O3-O3 = 169.5°) rather than kinked tetrahedral chains (Chapter 6). Because of the highly extended silicate chains in the high-temperature C2/c phase, its M2 sites are substantially larger and more distorted than those observed at high pressures, which are in almost regular octahedral coordination. The general features of the mechanism proposed by Sueno and Prewitt (1983) for the high temperature transformation may also be applicable to the high-pressure transformation outlined above.

However, detailed comparison of the two transition mechanisms shows that although the behaviour of the tetrahedral "B" chains and the exchange of the M1 and M2 cation sites occurring at either high temperature or high pressure are essentially

identical, the "A"-chains in the orthoferrosilite behave somewhat differently under the two conditions. Whilst the degree of kinking of the already extended "A"-chains remains virtually unchanged at high temperature (Sueno and Prewitt, 1983), these chains have to kink by more than 30° during the high pressure ortho- to high-P clinopyroxene transition. The result of this additional kinking and shearing of the "A" chains within the structure is to cause the crystal to disintegrate during the high pressure transformation, whereas the crystals used to characterise the high temperature transition (eg., Sueno and Prewitt, 1983) remained intact throughout the course of their experiments.

5.4 SUMMARY

Both ortho- and low-clinoferrosilites undergo a first order phase transformation at high pressures (and ambient temperatures) to the high-pressure C2/c clinoferrosilite polymorph. Both transitions involve a ~ 3% decrease in the volumes of the unit cells, virtually no change in the lengths of their *b*-axes at the transition pressure, and a ~ 4% decrease in the lengths of their *c*-axes. However, although *a* decreases by ~ 1.3% during the transition of low- to high-pressure clinoferrosilite, it increases by a similar amount during the ortho- to C2/c clinoferrosilite transformation. This is because the structural changes occurring during the two transitions are very different.

The transition of low-clinoferrosilite to high-pressure clinoferrosilite occurs between 1.43 and 1.75 GPa, with a hysteresis of less than ~ 0.27 GPa. It is first order and reversible, with the high-symmetry phase (C2/c) reverting to the low-symmetry phase ($P2_1/c$) on pressure release. The 3% volume decrease associated with the transition is caused predominantly by a decrease in β by about 5° to a value of 103.07° due to a major reconfiguration of the tetrahedral silicate chains of the pyroxene. Above ~ 1.75 GPa, the "A"-chain becomes O-rotated and geometrically equivalent the "B"-chain. This chain rotation also involves the breaking of the bonds between each O3 oxygen atom of the "A"-chain and the M2 iron atoms on one side of the chain, and the formation of new bonds between the O3 and the M2 sites on the other side.

At pressures above ~ 1 GPa, orthoferrosilite transforms reconstructively to the high-pressure C2/c clinoferrosilite phase. This transformation is highly time-dependent, (a conclusion further reinforced by the observation that orthoferrosilite survived pressurisation to 6.0 GPa for 2.5 hours in a multi-anvil experiment; Woodland, pers. comm.), and is first order in character, with a ~ 2.6% volume discontinuity at the transition pressure. It is irreversible, with the newly-formed high-pressure clinoferrosilite reverting preferentially to the low-pressure $P2_1/c$ clinoferrosilite phase upon pressure release.

Unfortunately, there is insufficient data available for the kinetics of the high-pressure transformation to be investigated in more detail at present. However, it is clear from comparison of the crystal structures of the orthopyroxene and high-pressure clinopyroxene that the transformation must be accompanied by major shearing and bond-breaking, which would be expected to result in a high activation energy for the transition. The morphology and microstructure of the recovered transformation products are also suggestive of a transformation mechanism similar to that previously proposed for other orthopyroxene to clinopyroxene transformations. Thus the preferred mechanism is very similar to that suggested for the ortho- to high-temperature clinoferrosilite transition (Sueno and Prewitt, 1983), involving the simultaneous shearing of the tetrahedral chains along [001] within the (100) planes of the structure and some exchange of the M1 and M2 cations sites, although there are some significant differences in the behaviour of the tetrahedral "A"-chains of the orthoferrosilite at high temperature and high pressure.

As a result of these two compressional studies, and earlier reversals of $MgSiO_3$ enstatite phase boundaries (eg., Pacalo and Gasparik, 1990; Angel et al., 1992a), it has been possible to confirm the true stability field of the C2/c phase of $(Mg,Fe)SiO_3$ pyroxenes at high pressures. The possible presence of a kind of "crossover" transition between the structurally distinct C2/c phases stable at high temperatures and high pressures respectively is discussed in some detail in the next chapter.

CHAPTER 6

CRYSTAL CHEMISTRY OF HIGH PRESSURE C2/c PYROXENES AND THEIR BEHAVIOUR AT HIGH PRESSURES

6.1 INTRODUCTION

The first order phase transition between the low-symmetry ($P2_1/c$) and high-symmetry (C2/c) clinopyroxenes occurs above 7 GPa in the $MgSiO_3$ end-member of the $(Mg,Fe)SiO_3$ solid solution (Angel et al., 1992a), and between 1.48 and 1.75 GPa in the $FeSiO_3$ end-member (see Chapter 5). Although there is a much greater hysteresis observed for the $MgSiO_3$ transition, both transformations involve a $\sim$ 3% decrease in the volume of the unit cell when the high-pressure phase is produced. The presence of Fe^{2+} in the cation sites of the pyroxene allows contributions of the crystal field stabilisation energy to the energies of the M1 and M2 sites in the $P2_1/c$ and C2/c structures which are not possible in end-member $MgSiO_3$; the difference in the hysteresis for the low-high pressure transitions in clinopyroxenes of end-member compositions along the $(Mg,Fe)SiO_3$ join may be related to these differences in the crystal field stabilisation energies of the two structures (Ross and Sowerby, 1995). It was shown in Chapter 5 that the structural changes occurring during this transition are essentially independent of the composition of the clinopyroxene along the $(Mg,Fe)SiO_3$ join.

The first part of this chapter compares the crystal chemistry of the high-pressure C2/c phases of both $MgSiO_3$ and $FeSiO_3$ end-member compositions in some detail with other C2/c clinopyroxene polymorphs of the same compositions, to yield insights into the nature of the pyroxene phase diagram at high pressures and temperatures. The high-pressure C2/c phases of $(Mg,Fe)SiO_3$ clinopyroxene have already been characterised in some detail (Angel et al., 1992a; Chapters 1 and 5); the other two C2/c pyroxene structures to be considered are a clinopyroxene stable at high temperatures (which has been identified in both $MgSiO_3$ (Perrotta and Stephenson, 1965) and $FeSiO_3$ (Sueno et al., 1984)), and a calculated structure of a fictive Ca^{2+}-

free end-member of a $Ca_{0.5}(Mg,Fe)_{0.5}SiO_3$ - $(Mg,Fe)SiO_3$ solid solution, modelling the effect of introducing Ca^{2+} to the clinopyroxene structure.

The second part of the chapter discusses the compressional behaviour of the C2/c clinoferrosilite structure to ~ 6.5 GPa, and the equations of state (EOS's) of both the low- and high-pressure $(Mg,Fe)SiO_3$ polymorphs. Structure determinations of the lower-symmetry $P2_1/c$ phase at non-ambient conditions were not possible, since the crystals of $P2_1/c$ clinopyroxenes synthesised at high pressures and temperatures were invariably highly twinned (due to the transformation from C2/c to which occurs on pressure release; see Chapter 5).

6.2 CRYSTAL CHEMISTRY OF HIGH-PRESSURE C2/c CLINOPYROXENES

6.2.1 $FeSiO_3$

The structures of three different polymorphs of clinoferrosilite with space group C2/c will be considered here: firstly, the high-pressure phase obtained during compression of the $P2_1/c$ phase above ~ 1.75 GPa (described in Chapter 5); secondly, a high temperature phase, formed by heating a low-clinoferrosilite crystal to 1050°C, (reported by Sueno et al., 1984); and thirdly, a "high-Ca" or "hedenbergite-like" (*Hd-like*) structure that can be postulated as a fictive $FeSiO_3$ end-member of the hedenbergite-ferrosilite solid-solution.

The structure of this Hd-like phase may be modelled using two slightly different extrapolation techniques. The first involves extrapolating the published unit cell parameters and atomic coordinates for pyroxenes along the hedenbergite-ferrosilite join with space group C2/c and intermediate calcium contents (Cameron et al., 1973; Ohashi et al., 1975) to those for a hypothetical hedenbergite-like $FeSiO_3$ composition (Figures 6.1 a-r). From the atomic positions calculated in this way (Table 6.1), the complete clinopyroxene structure can be generated, and bond lengths, angles and

polyhedral volumes derived (Table 6.2, and Appendix 3). The second method involves direct extrapolation of the bond lengths and angles across the join, using the published bond lengths and angles of Cameron et al., 1973 and Ohashi et al., 1975. The *esd*'s reported in Table 6.2 represent the differences between the results of the two methods. Unit cell parameters for all the monoclinic phases of $FeSiO_3$ that are discussed here are summarised in Table 6.3.

	x	y	z
Fe1	0.0	0.901	0.25
Fe2	0.0	0.263	0.25
Si	0.296	0.085	0.252
O1	0.124	0.090	0.159
O2	0.375	0.240	0.362
O3	0.359	0.031	0.045

Table 6.1. Calculated positional parameters for the Hd-like C2/c phase of $FeSiO_3$.

	a (Å)	b (Å)	c (Å)	β	V (Å^3)
$P2_1/c$ Fs; room T,P	9.7075(5)	9.0807(4)	5.2347(5)	108.46(1)	437.70(6)
C2/c Fs; 1.87GPa	9.540(1)	8.996(3)	5.008(1)	103.01(1)	418.8(2)
C2/c Fs; 1050°C	9.928(1)	9.179(1)	5.338(1)	110.20(1)	456.5(1)
C2/c Fs; "Hd-like"	9.73(1)	9.11(1)	5.23(1)	107.8(9)	441.4(8)
$P2_1/c$ En; room T,P	9.605(4)	8.814(3)	5.169(2)	108.34(4)	415.4(3)
C2/c En; 7.93GPa	9.201(3)	8.621(1)	4.908(1)	101.50(3)	381.5(2)
C2/c En; 1100°C	9.864(6)	8.954(4)	5.333(3)	110.03(4)	442.5(5)

Table 6.3 Unit-cell parameters for $FeSiO_3$ and $MgSiO_3$. Note that the data for $P2_1/c$ and high-P Fs ($FeSiO_3$), and $P2_1/c$ and high-P En ($MgSiO_3$) are from these experiments. High-T C2/c Fs data taken from Sueno et al. (1984); high-T C2/c En data taken from Smith (1969b). "Hd-like" data is extrapolated from data across the CaFe-FeFe join.

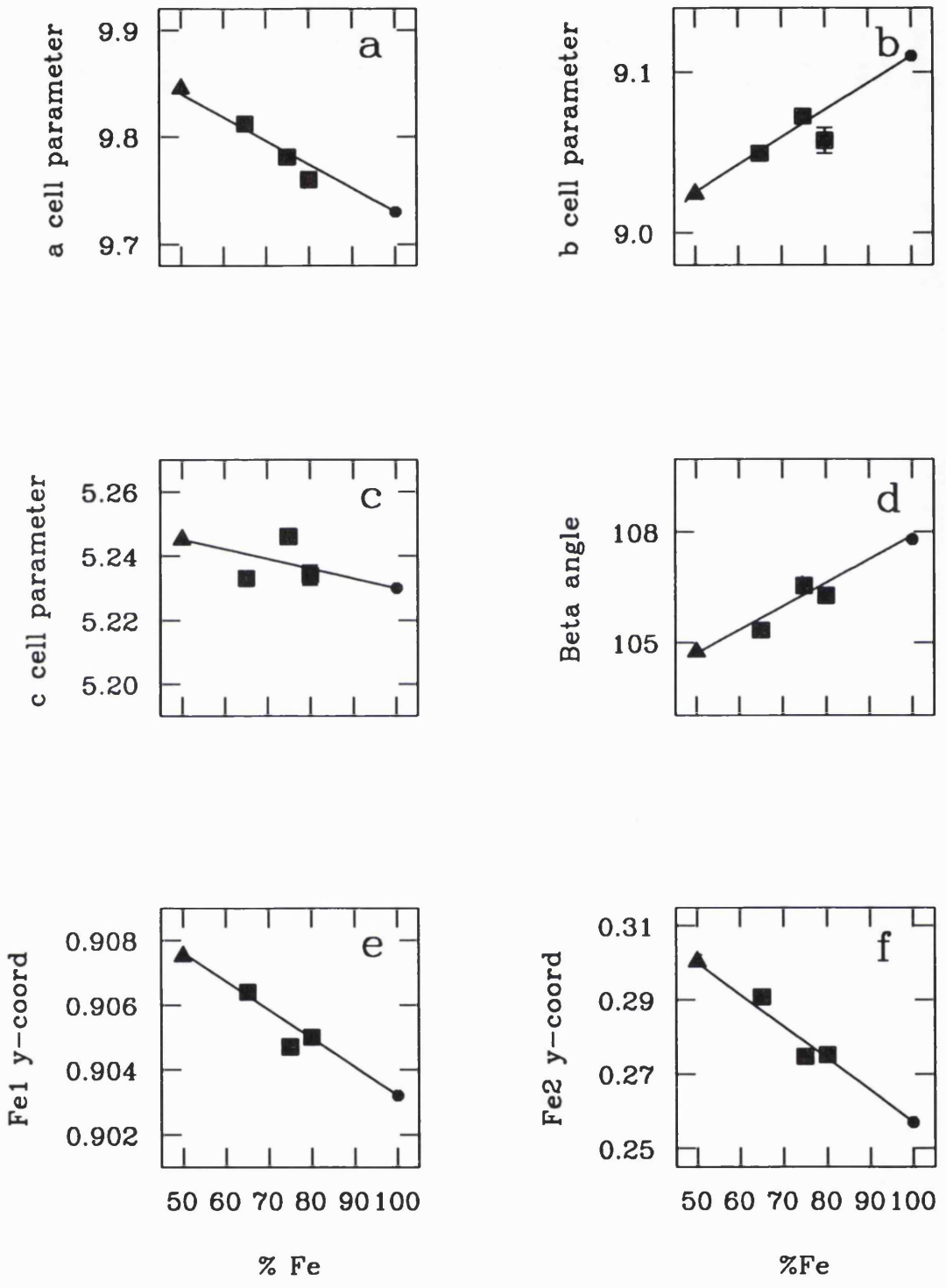

Figure 6.1: a-d) Variation of the cell parameters, and e-r) Fe, Si and O positional parameters of C2/c clinopyroxenes across the Hd-Fs join (data from Ohashi et al, 1975 (squares) and Cameron and Papike, 1980 (triangles)), fitted with linear regression lines, and extrapolated to the fictive Ca^{2+}-free "Hd-like" clinoferrosilite (see text; circles)

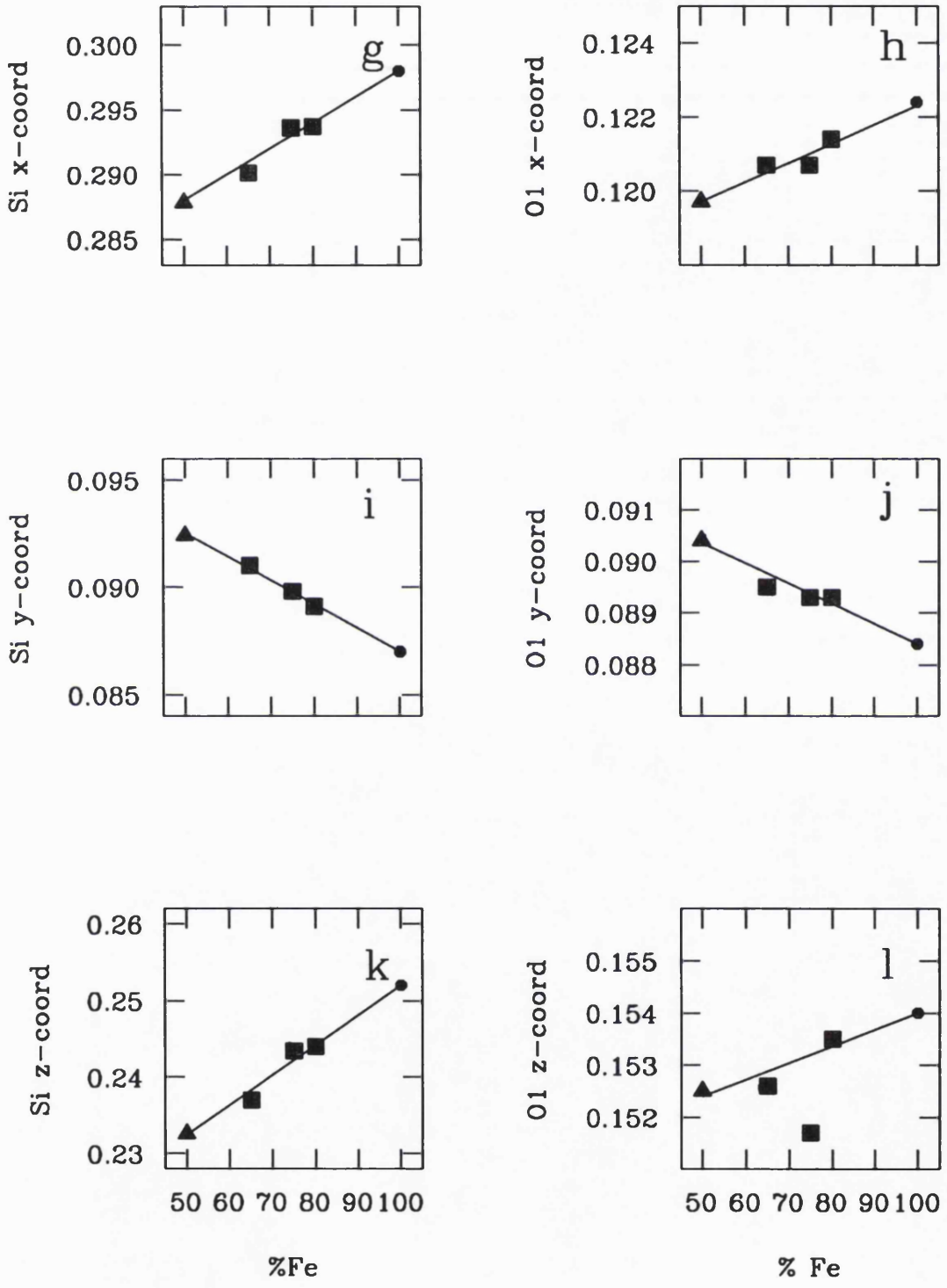

Figure 6.1: (cont.).

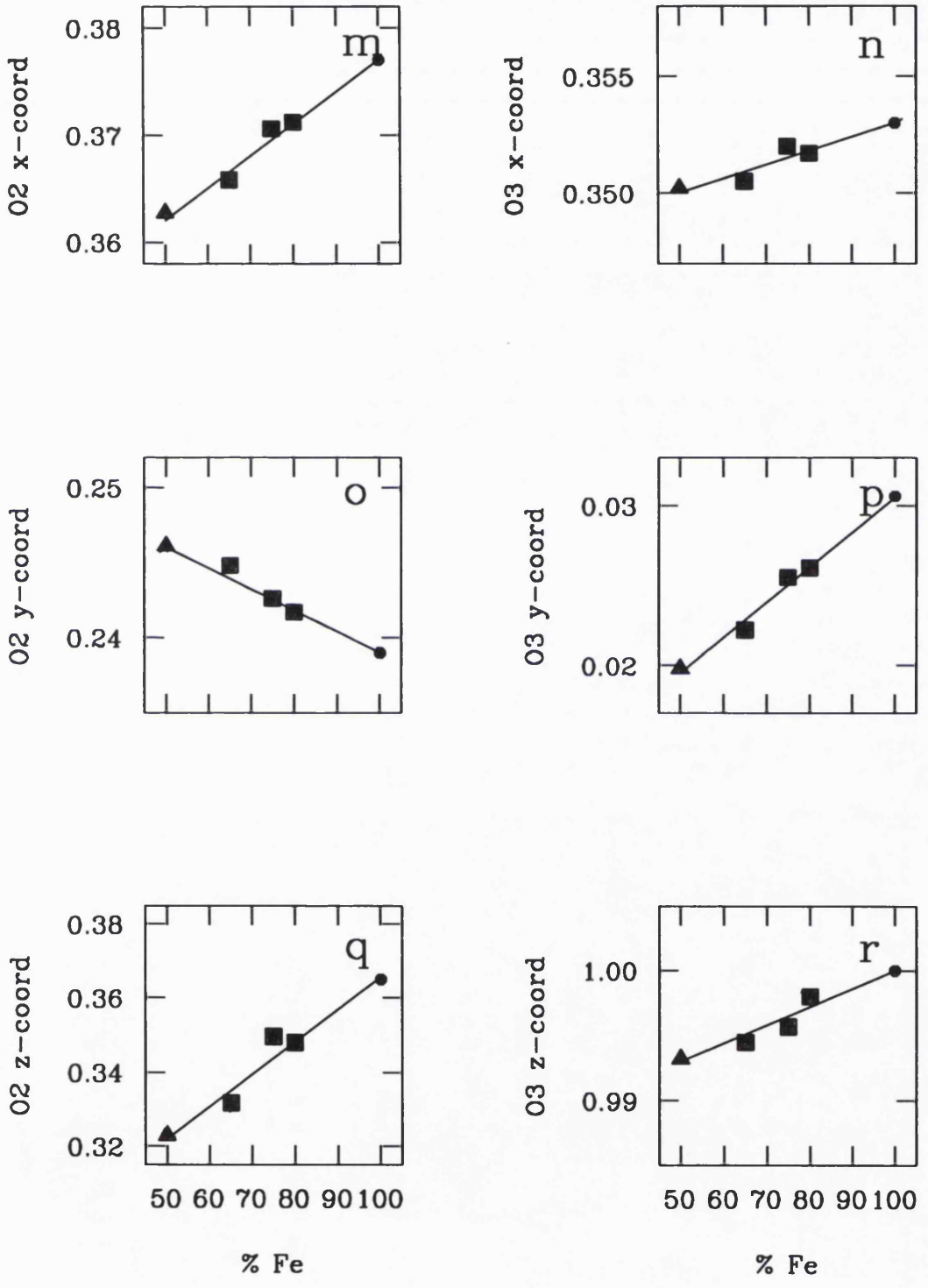

Figure 6.1: (cont.).

	High-P (1.87 GPa)	High-T (1050°C)	Hd-like
Fe1-O1	2.20 (2)	2.28 (2)	2.07 (1)
Fe1-O1	2.109 (8)	2.104 (8)	2.22 (1)
Fe1-O2	2.12 (1)	2.15 (1)	2.105 (9)
Average Fe1-O	2.14 (1)	2.18 (2)	2.13 (1)
Fe1 volume	13.0 (1)	13.5 (1)	12.8 (1)
Fe1 Quad. El.	1.008 (1)	1.010 (1)	1.009 (1)
Fe2-O1	2.12 (2)	2.16 (2)	2.10 (1)
Fe2-O2	1.990 (9)	2.016 (9)	2.005 (5)
Fe2-O3	2.43 (1)	2.72 (1)	2.91 (3)
7/8th Fe2-O		3.19 (2)	3.00 (3)
Average Fe2-O (of 6)	2.18 (1)	2.30 (2)	2.33 (1)
Fe2 volume	13.6 (1)	25.3 (2)	24.0 (2)
Fe2 Quad. El.	1.018 (1)		
Si-O1	1.61 (1)	1.60 (1)	1.625 (5)
Si-O2	1.60 (1)	1.61 (1)	1.605 (1)
Si-O3	1.67 (1)	1.65 (1)	1.64 (1)
Si-O3	1.66 (1)	1.67 (1)	1.641 (1)
Average Si-O	1.63 (1)	1.63 (1)	1.631 (5)
Si volume	2.22 (2)	2.22 (2)	2.215 (8)
Si Quad. El.	1.002 (1)	1.005 (1)	1.003 (1)
O3-O3-O3	138.4 (9)	169.5 (8)	156.3 (4)

Table 6.2. Selected bond lengths, angles, polyhedral volumes and distortions of the high-P (Chapter 5), high-T (Sueno et al., 1984) and Hd-like C2/c phases of $FeSiO_3$.

The most striking difference between these three C2/c polymorphs is the unusually small value of β in the high-P structure. This angle of about 103° is over 7° less than that observed in the high-T phase at 1050°C (Sueno et al., 1984) and nearly 5° less than that calculated for the Hd-like phase. There is evidence to show that β may increase as much as 3° during a temperature rise of 1000°C, (Smyth, 1974a), in which case both high-T and the fictive Hd-like phases will have a value for

β (extrapolated to room temperature) of about 108°. The extrapolated room pressure unit-cell volume of the high-P phase is over 8% less than the volume of the high-T phase; only about 1% of this difference arises from the thermal expansion of the pyroxene at elevated temperatures. The unit cell volume of the high-P form is also ~5% less than that of the Hd-like phase, thus showing that the volumes of both the high-T and the fictive Hd-like polymorphs are very similar at ambient conditions.

The *a*, *b*, and *c* cell parameters of the high-P C2/c phase are all significantly shorter than the corresponding cell parameters of either the high-T or fictive hedenbergite-like polymorphs (Table 6.3), the cell parameters of these latter two phases (after corrections for thermal expansion have been made to the high-T data) being of a similar magnitude. These comparisons seem to suggest that at a superficial level, the structures of the high-T and Hd-like phases are similar, and both are distinct from the C2/c phase found at high pressures.

The O3-O3-O3 chain extension angle of each of the phases (Table 6.2) is very important for characterising the differences between the monoclinic pyroxene polymorphs. There is only one symmetrically distinct silicate chain in the C2/c pyroxene structure, which is O-rotated to differing degrees in all of the polymorphs (Table 6.2). It is slightly more than 10° from the fully extended position in the high-T phase (which has stacking sequence *M*+*SS*-*M*+*SS*-*M* under Pannhorst's (1979) classification; Chapter 1), allowing the M2 sites to become very large and highly distorted from an ideal octahedron. In the fictive Hd-like phase, the chain extension angle is approximately 156° and the Fe^{2+} in the M2 site occupies a distorted 8-coordinate polyhedron, with a correspondingly large volume. Only the high-P clinoferrosilite exhibits a remarkably small chain extension angle, some 20° less than the Hd-like phase, and over 30° less than the extended high-T silicate chains. Extrapolation of this high-T extension to ambient temperature (by noting the effect of temperature on C2/c pyroxenes such as diopside and hedenbergite, Cameron et al., 1973) merely reduces the chain extension angle by about 3°.

As far as the chain extension angles are concerned, the Hd-like structure is therefore intermediate between that of the high-P and high-T structures, but is much nearer to that of the high-T structure (Figure 6.2). The average Si-O bond lengths in all three phases are identical to within one combined *esd*, though the tetrahedra are somewhat more distorted at high temperature. The M1 site does not differ significantly in either shape or size between the three C2/c phases, although it is approximately 5% larger in the high-T structure than the other two: thermal expansion is likely to contribute to up to 1.5% of this difference, while the remainder may be accounted for by the experimental uncertainties.

The most significant variation in size and shape of the cation sites in the high-P, high-T and fictive Hd-like structures occurs at the M2 site, which is connected to the silicate chains via the long M2-O3 bonds; kinking of the chains away from the extended position will inevitably lead to smaller and more regular M2 sites. Since the silicate chains are highly kinked at high pressure (with O3-O3-O3 angle of 138.4° at 1.87 GPa), the M2 octahedron is indeed fairly regular, but becomes almost 8-coordinated and very distorted at high temperatures with a dramatic increase in polyhedral volume (Table 6.2; Figure 6.2). Sueno et al. (1984) calculated the volume of this "8-coordinate" polyhedron to be approximately 25.25Å^3, a volume that is comparable to volumes of the M2 polyhedra found in Na^+- and Ca^{2+}-containing pyroxenes (Cameron et al. 1973). The M2 site in the Hd-like phase is also a distorted 8-coordinated polyhedron, with a similarly large volume to that at high temperature. It is likely that at high temperatures the Fe^{2+} atoms vibrate rapidly in the expanded and distorted M2 sites polyhedra, causing them to resemble the 8-coordinate polyhedra found in Ca^{2+}-containing pyroxenes and also in the fictive Hd-like $FeSiO_3$ structure.

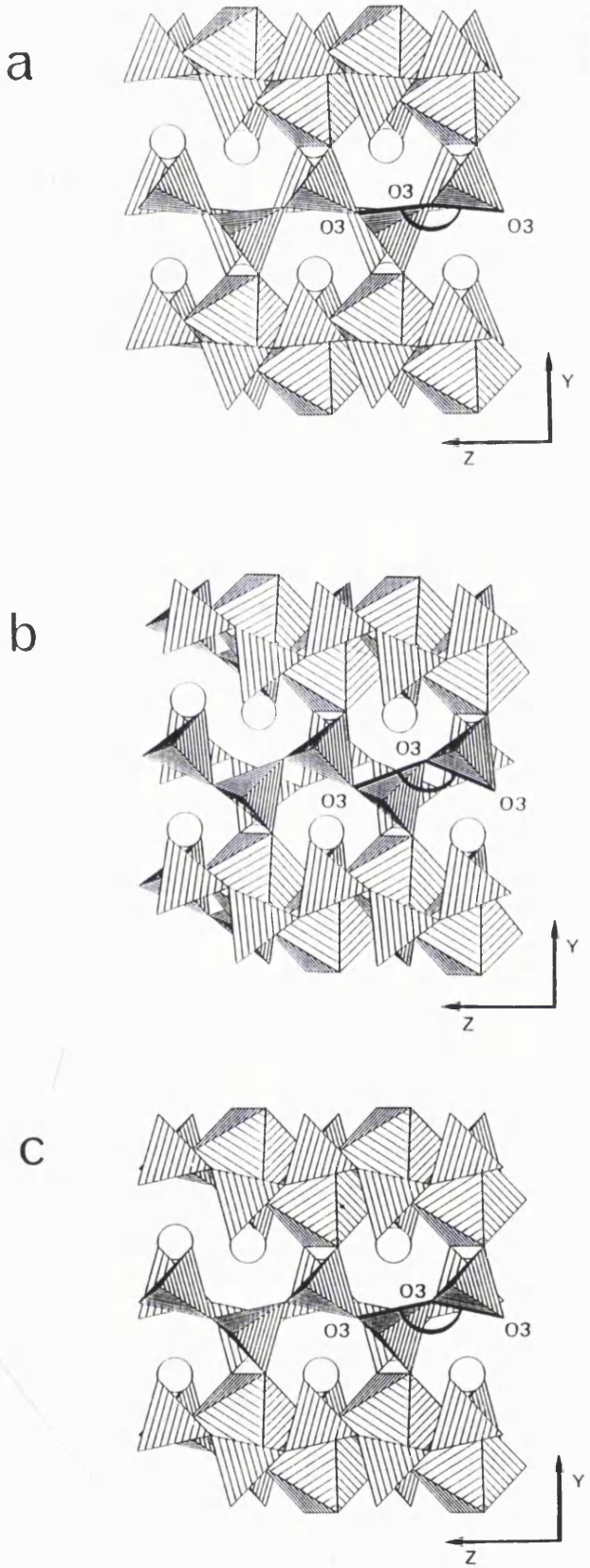

Figure 6.2: Polyhedral representations of the a) high-T, b) high-P and c) Hd-like C2/c clinoferrosilite phases. The M1 sites are shown by shaded octahedra, and the M2 sites by circles. The chain extension angles (O3-O3-O3) are also labelled.

6.2.2 $MgSiO_3$

Since the Ca^{2+}-poor component of pyroxene in the Earth's upper mantle is likely to have approximate composition $Mg_{0.85}Fe_{0.15}SiO_3$ (eg., Ringwood, 1975), the same comparisons have been carried out with three Mg^{2+}-rich C2/c pyroxenes. The structures of the low ($P2_1/c$) and high-P (C2/c) structures of clinoenstatite ($MgSiO_3$) have already been determined (Ohashi, 1984; Angel et al., 1992a), but no published data for a pure $MgSiO_3$ C2/c form stable at high temperatures is available. However, there is much experimental evidence for the existence of such a phase (eg, Perrotta and Stephenson, 1965; Smith, 1969b; Shimobayashi and Kitamura, 1991), with the temperature of the metastable low ($P2_1/c$) to high-T (C2/c) transition increasing as the Mg^{2+} content is increased across the $FeSiO_3$ - $MgSiO_3$ join (Prewitt et al., 1971). The only published structure of a Mg^{2+}-containing C2/c pyroxene at high temperature is that of Smyth (1974a) who determined the structure of a $Mg_{0.32}Fe_{0.68}SiO_3$ clinopyroxene. The structure of a high-T C2/c $MgSiO_3$ phase has been estimated by extrapolation along the Mg-Fe join.

A model of a "high-Ca" structure was formed by extrapolation along the diopside-enstatite join to form a "Diopside-like" (*Di-like*) structure which is less well-defined at the Mg^{2+}-end of the $(Mg,Fe)SiO_3$ solid solution than the Hd-like $FeSiO_3$ structure due to inconsistencies in the published structural data for pyroxenes of intermediate compositions. Unit cell parameters for the Mg^{2+}-rich C2/c clinopyroxenes are given in Table 6.3.

Comparisons of these monoclinic polymorphs of $MgSiO_3$ pyroxene show that the differences between the high-P, high-T and Di-like polymorphs are very similar to those seen in the ferrosilite end-member. As with the high-P ferrosilite phase, the high-P C2/c phase of $MgSiO_3$ may be distinguished by its low β angle of 101.5° and its extremely kinked tetrahedral chain (Angel et al., 1992a). This chain extension angle of 133.4° is the smallest ever reported for *any* pyroxene, and significantly smaller than the "B"-chain of low-clinoenstatite (138.3°). The high-T C2/c structure, on the other hand, has extremely extended silicate chains, with a chain extension angle only ~ 7° from the ideal straight-chain configuration. This substantial extension of the

silicate chain implies that the M2 sites are both large, highly distorted and irregular: a structural determination (Smyth, 1974a) of the intermediate pyroxene with composition $Mg_{0.32}Fe_{0.68}FeSiO_3$ at 825°C shows that this is indeed the case. The M2 site in the fictive Di-like phase of $MgSiO_3$ is also in 8-fold coordination, and although it is more regular than the high-T M2 site, it has a similar overall volume. The silicate chains in the Di-like structure are less extended than the high-T chains, but significantly more extended than those seen at high pressures.

6.2.3 Geochemical Implications of the Presence of High-P C2/c Clinopyroxene

It has often been assumed for geochemical experiments that the stable upper mantle phase of Ca^{2+}-poor pyroxene is the orthorhombic polymorph (with space group Pbca), rather than this newly characterised monoclinic phase with space group C2/c, which for the $FeSiO_3$ end-member composition becomes stable at a depth of about 50-60 km. It is useful therefore to compare the structures of these two phases, in particular the size and distortion of the M2 sites in order to predict the effect the orthorhombic to C2/c phase transition will have on the trace element partitioning behaviour of the pyroxene.

Although there is no significant difference (within the experimental uncertainties) in shape or size of the M1 sites in the Pbca phase (see Chapter 3 for the structural details of orthoferrosilite) and the C2/c phase stable at high-P, the M2 site is somewhat less distorted in the high-P C2/c polymorph. In both phases, this M2 cation is octahedrally coordinated, with identical average M2-O bond length (within one combined *esd*) and polyhedral volume. Within the experimental uncertainties, the average Si-O bond lengths and polyhedral volumes of the tetrahedral sites in both these pyroxene polymorphs are identical. These structural similarities of the high-P C2/c and Pbca polymorphs also apply to the $MgSiO_3$ end-member of the ferrosilite-enstatite solid-solution, with the M2 cation site being less distorted in the high-P C2/c structure and the geometries of both the tetrahedral and M1 octahedral sites being identical within experimental uncertainties.

The stable form of both pure enstatite and pure ferrosilite at the temperatures and pressures of the Earth's upper mantle is thus the high-pressure C2/c pyroxene polymorph. It is reasonable to assume that the transformation of orthoenstatite to the high-P C2/c phase will also occur for Ca^{2+}-containing natural orthopyroxene compositions close to the $MgSiO_3$-$FeSiO_3$ join. Although this transformation has significant effects on the thermodynamic parameters of the pyroxene (see Chapter 7), the comparison of the structures of the C2/c and Pbca polymorphs of both $FeSiO_3$ and $MgSiO_3$ shows that the sizes and distortions of the cation sites are very similar. The transformation at high pressures of orthopyroxene to C2/c pyroxene is therefore unlikely to have any great effect on either the solid solution limits of the pyroxene phase, or upon its ability to take up trace elements. In particular, by use of fictive "high-Ca" end-members it has been shown that the structures of the high-pressure C2/c phases are substantially different from those of C2/c pyroxenes containing calcium. Thus, the miscibility gaps between the orthopyroxenes $MgSiO_3$ and $FeSiO_3$ and their corresponding solid solutions $(Ca,Mg)MgSi_2O_6$ and $(Ca,Fe)FeSi_2O_6$ will also occur between the high-pressure C2/c phases of $MgSiO_3$ and $FeSiO_3$ and these solid solutions.

6.3 COMPRESSION OF C2/c CLINOFERROSILITE

6.3.1 Introduction

A single crystal of the $FeSiO_3$ low-clinoferrosilite was compressed in a diamond anvil cell until it transformed to the high-pressure C2/c phase, and its structure was determined at approximately 0.8 GPa pressure intervals from 1.87 GPa. Since the initial orientation of the crystal within the DAC was not ideal for determining all of the structural parameters with sufficient accuracy, the cell was unloaded and the crystal was remounted in a different orientation (Chapter 2). The DAC was then re-pressurised to the same pressure, and the data collection was repeated. The two datasets were combined for the final structure refinements, giving significant improvements in the precision of the structural parameters at all pressures (see Chapter 2 for more details). Since this original clinoferrosilite crystal was

destroyed during compression above ~ 4.2 GPa, a second $FeSiO_3$ clinoferrosilite crystal was used for subsequent high pressure structure determinations. The unit cell parameters and structures of the two crystals, determined at ambient conditions, were identical to within one combined *esd*. Refined positional parameters, bond lengths and angles for the C2/c clinoferrosilite to ~6.5 GPa are given in Appendix 2; those that are most significant for the determination of the structural response to pressure are also given in Table 6.4.

6.3.2 Structural Compression of C2/c Clinoferrosilite

The M2 site of the high-pressure C2/c clinoferrosilite phase is more distorted than the M1 site at all pressures below ~6.5 GPa. Although the degree of distortion (ie., the quadratic elongation (Robinson et al., 1971; Chapter 3)) of the M1 site does not change with increasing pressure, the M2 site becomes somewhat more regular by 6.5 GPa (Table 6.4). The volumes of both sites decrease steadily with pressure: the six M1-O bonds shorten at fairly similar rates, causing the linear volume compressibility (defined in Chapter 3) of the M1 site to be $\beta_V = 0.016(6)$ GPa^{-1}.

The M2-O3 bonds (which are considerably longer than the remaining four M2-O bonds at all pressures studied) shorten substantially faster than the remaining M2-O bonds, with a linear compressibility of $\beta = 0.008(2)$ GPa^{-1}. Whilst it is possible within the experimental uncertainties that the M2-O1 and M2-O2 bond lengths do not change at all with increasing pressure to ~ 6.5 GPa, it seems more likely (Figure 6.3) that the M2-O2 bonds shorten slightly, with $\beta = 0.002(2)$ GPa^{-1}, and the M2-O1 bond lengths increase with $\beta = -0.005(3)$ GPa^{-1}; this increasing M2-O1 bond length may, in part, be responsible for the decreasing distortion of the M2 site with increasing pressure (Table 6.4). The overall effect of these changes of the M2-O bond lengths over the 6.5 GPa pressure range (Figure 6.3) is to decrease the volume of the M2 site, with a linear volume compressibility of $\beta_V = 0.007(3)$ GPa^{-1}. Therefore, unlike the $FeSiO_3$ orthoferrosilite polymorph, the M2 sites in this C2/c clinoferrosilite are considerably less compressible than the adjacent M1 sites.

P (GPa)	1.87	2.83	3.49†	4.28	4.94†	6.51†
M1-O1	2.20 (2)	2.16 (3)	2.14 (3)	2.09 (4)	2.14 (2)	2.21 (3)
M2-O1	2.109 (8)	2.08 (1)	2.11 (2)	2.12 (3)	2.12 (2)	2.14 (3)
M1-O2	2.12 (1)	2.11 (3)	2.13 (3)	2.12 (4)	2.07 (2)	2.07 (3)
Av. M1-O	2.14 (1)	2.12 (2)	2.12 (1)	2.11 (1)	2.11 (2)	2.14 (3)
M1 vol.	13.0 (1)	12.5 (2)	12.6 (3)	12.4 (4)	12.3 (2)	12.9 (3)
M1 Q.E.	1.008 (1)	1.009 (1)	1.010 (1)	1.010 (1)	1.009 (1)	1.010 (1)
M2-O1	2.12 (2)	2.12 (3)	2.11 (3)	2.14 (4)	2.18 (2)	2.14 (3)
M2-O2	1.990 (9)	1.98 (2)	1.97 (2)	1.98 (3)	1.96 (2)	2.00 (2)
M2-O3	2.43 (1)	2.41 (2)	2.36 (3)	2.36 (3)	2.37 (2)	2.36 (2)
Av. M2-O	2.18 (1)	2.17 (2)	2.15 (3)	2.16 (3)	2.17 (2)	2.17 (3)
M2 vol.	13.6 (1)	13.4 (2)	12.9 (3)	13.2 (3)	13.3 (2)	13.3 (3)
M2 Q.E.	1.018 (1)	1.019 (1)	1.018 (1)	1.019 (1)	1.021 (1)	1.016 (1)
Si-O1	1.61 (1)	1.64 (2)	1.63 (2)	1.63 (4)	1.57 (2)	1.55 (3)
Si-O2	1.60 (1)	1.62 (2)	1.65 (3)	1.59 (3)	1.60 (2)	1.59 (2)
Si-O3a*	1.67 (1)	1.65 (2)	1.68 (2)	1.66 (3)	1.62 (2)	1.59 (3)
Si-O3b*	1.66 (1)	1.65 (1)	1.62 (3)	1.64 (3)	1.69 (2)	1.66 (2)
Av. Si-O	1.63 (1)	1.64 (1)	1.64 (1)	1.63 (1)	1.62 (2)	1.59 (2)
Si volume	2.22 (2)	2.26 (2)	2.27 (3)	2.21 (3)	2.16 (3)	2.07 (4)
Si Q.E.	1.002 (1)	1.003 (1)	1.002 (1)	1.005 (1)	1.008 (1)	1.004 (1)
O3-O3-O3	138.4 (9)	140.4(1.8)	138.1(2.6)	138.3(1.9)	136.1(1.5)	139.1(2.3)
< (100)	5.8 (7)	4.8 (8)	5.7 (1.1)	6.2(9)	7.8 (1.7)	6.2 (1.2)
Si-O3-Si	126.3 (7)	126.1(1.3)	124.8(1.9)	125.1(2.4)	126.0(1.5)	128.1(1.5)
O3-Si-O3	107.4 (5)	107.0(1.0)	108.0(1.1)	107.4(1.8)	107.9(0.7)	107.9(0.9)

Table 6.4 Variation of selected bond lengths, angles, polyhedral volumes and distortions of C2/c clinoferrosilite with pressure. Data marked with a cross (†) was collected from crystal #2; the remaining data was collected from crystal #1.

* Note that although there is only one symmetrically distinct silcate chain in C2/c clinopyroxenes, these 'a' and 'b' symbols are used to distinguish the two Si-O3 bonds in each tetrahedron.

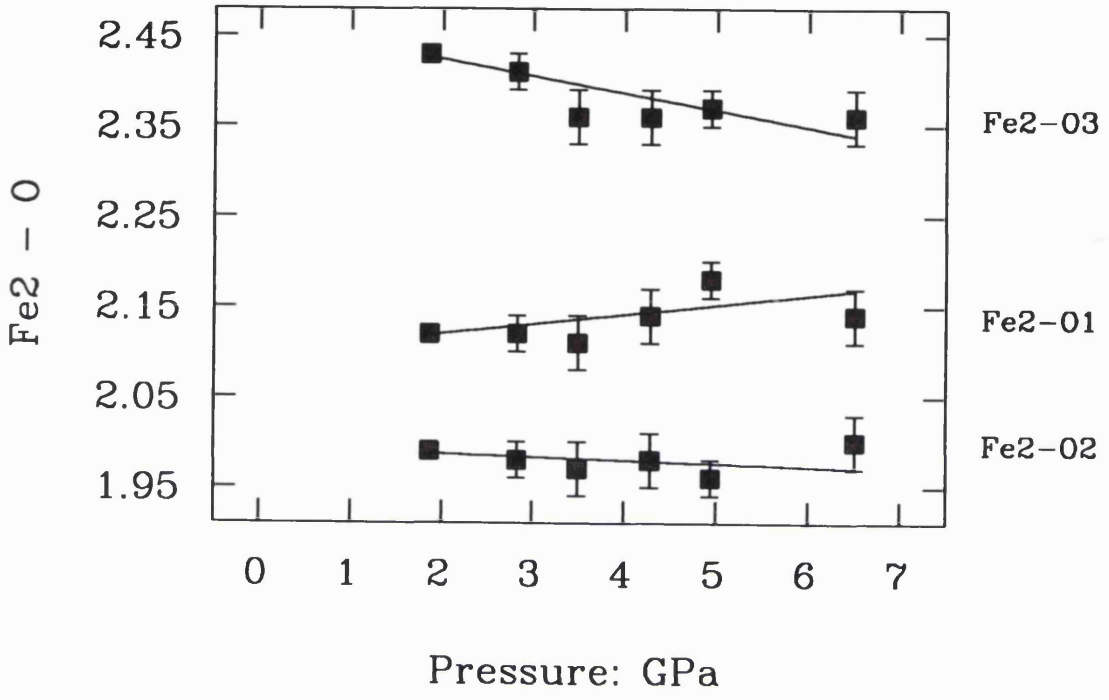

Figure 6.3: Variation of the M2-O bond lengths of the high-pressure C2/c clinoferrosilite phase with increasing pressure.

All the Si-O bond lengths in the high-pressure C2/c clinoferrosilite phase are incompressible to ~ 4.3 GPa, with no associated distortion of the tetrahedra. Above this pressure, the Si-O1, Si-O2 and Si-O3a bonds begin to shorten in a regular way, with no changes in the internal O-Si-O bond angles, and with linear compressibilities in the range ~ 0.008 GPa^{-1} to ~ 0.018 GPa^{-1}; note that, within the *esd*'s, the Si-O3b bond length does not significantly change at any pressure below 6.5 GPa (Table 6.4). The average Si-O bond length behaves in a similar manner: it is incompressible below ~ 4.3 GPa, but at higher pressures it decreases with a linear compressibility $\beta = 0.013(2)$ GPa^{-1} (Table 6.4). This is considerably faster than the rate of decrease of the average Si-O bonds observed in synthetic Mg^{2+}-rich $(Mg,Fe)SiO_3$ orthopyroxenes (Chapter 3) since compression of the SiO_4 tetrahedra in the orthopyroxenes is predominantly due to shortening of the non-bridging (ie., Si-O1 and Si-O2) bonds, rather than the additional compression of one of the Si-O3 bonds, as seen for the C2/c polymorph.

This change in the compressibility of the Si-O bonds in the C2/c clinoferrosilite is reflected in the variation of the volumes of the SiO_4 tetrahedra with pressure. Below ~ 4.3 GPa, the volumes of the silicate tetrahedra are approximately constant at 2.24(3)Å^3, while at higher pressures, these volumes decrease linearly with pressure, with β_V = 0.028(4) GPa^{-1} (Figure 6.4). Over the 2.2 GPa pressure range where compression of the Si-O bonds occurs, the associated reduction in the volumes of the SiO_4 tetrahedra is more than four times as much, per GPa, as that observed for the corresponding tetrahedra in Mg^{2+}-rich $(Mg,Fe)SiO_3$ orthopyroxenes (for which β_V = 0.006(1) GPa^{-1}; Chapter 3). Furthermore, it was seen in Chapter 3 that the rate of volume decrease of the silicate tetrahedra in the orthopyroxenes is essentially independent of the bulk composition of the orthopyroxene, thus implying that the enhanced compressibility of these tetrahedra in the C2/c clinoferrosilite phase above ~ 4.3 GPa is unlikely to simply be due to the effect of the Fe^{2+} in the M1 and M2 cation sites of the clinopyroxene.

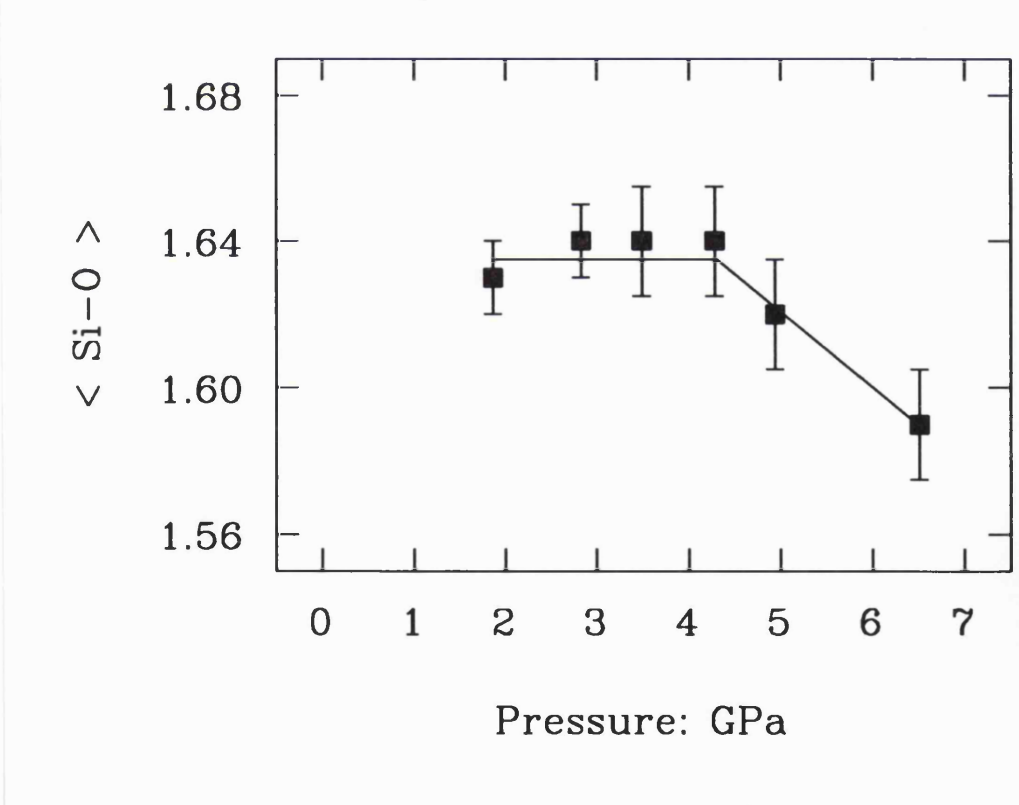

Figure 6.4: Variation of the average Si-O bond lengths of the high-pressure C2/c clinoferrosilite with pressure, illustrating the onset of compression at ~ 4.3 GPa.

The chain extension angle (measured by the O3-O3-O3 angle of the pyroxene; Chapter 1) does not change significantly with increasing pressure to ~ 6.5 GPa (Figure 6.5a). However, the bases of the tetrahedra contained within these chains rotate by almost 2° away from the (100) plane over this pressure range (Figure 6.5b). Since both of these effects are very small, it is impossible to determine whether there is a subtle discontinuous change in the degrees of kinking or tilting of the silicate chains at ~ 4.3 GPa, associated with the onset of compression of the Si-O bonds, as was previously observed for the synthetic orthopyroxenes (Chapter 3).

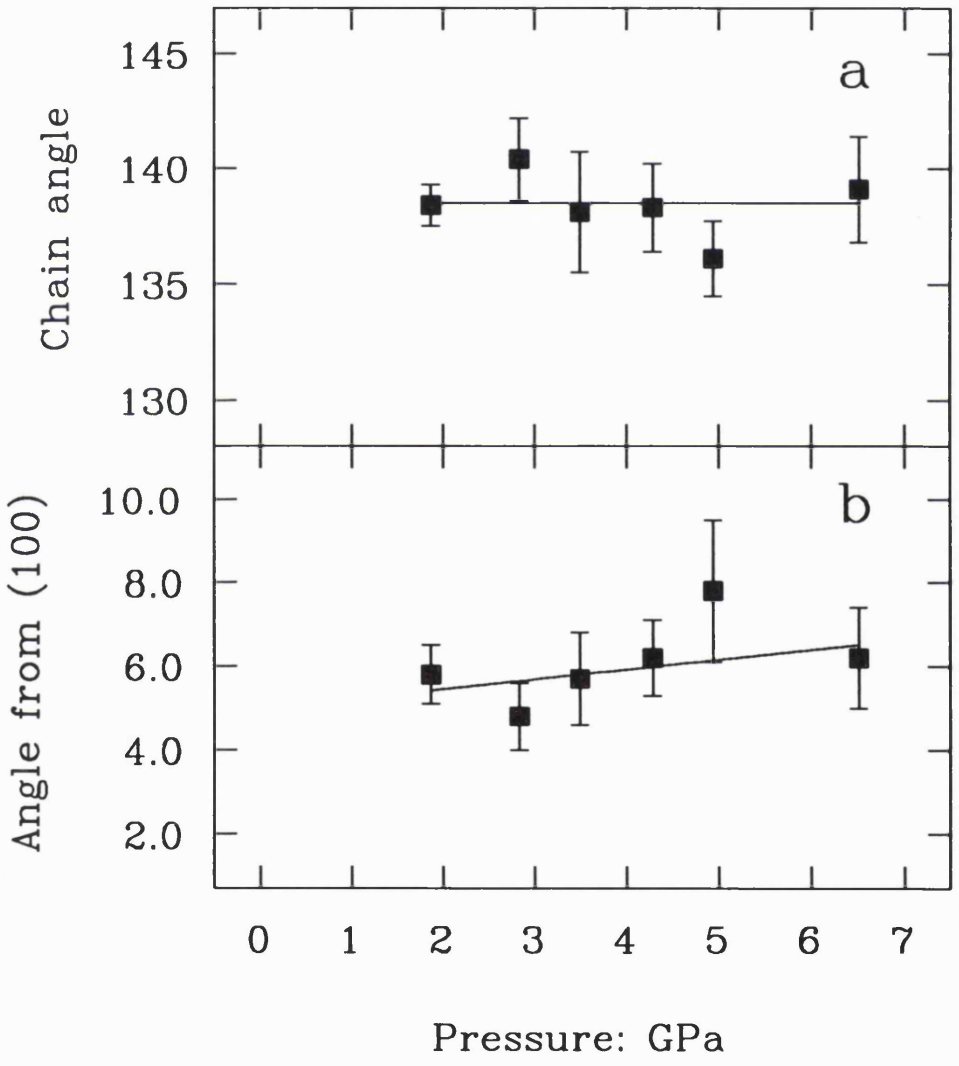

Figure 6.5: Effect of pressure on a) the chain extension angle (O3-O3-O3), and b) the amount of tilt of the tetrahedral bases from (100) of the high-pressure C2/c clinoferrosilite.

The effect of increasing pressure on the structure of the newly characterised high-pressure C2/c clinoferrosilite phase is thus very different to the corresponding response of the orthoferrosilite structure to pressure increase. Below ~ 4.3 GPa in the C2/c clinoferrosilite phase, compression is dominated by the regular compression of the M1 and M2 sites. Above this pressure, the Si-O bond lengths begin to shorten linearly with pressure, with the continued compression of the M1 and M2 sites at their former rates. There is no observable kinking of the silicate chains below ~ 6.5 GPa (Figure 6.5). The mechanism of compression of the high-pressure clinoferrosilite phase therefore resembles that of the natural OPX2 orthopyroxene more closely than that of the synthetic $(Mg,Fe)SiO_3$ orthopyroxenes, in either compression regime. However, both the high-pressure C2/c polymorph of clinoferrosilite and the synthetic $(Mg,Fe)SiO_3$ orthopyroxenes exhibit a distinct change in compression mechanism at ~ 4 GPa, characterised by the onset of compression of the Si-O bonds.

Since there is no observable change in the configuration of the silicate chains in this clinoferrosilite phase at any pressure, the critical parameter for the initiation of shortening of some of the Si-O bonds must be more closely related to the volumes of both (or either?) of the M1 and M2 cation sites, than to the O3-O3 separation. However, there is insufficient data for this parameter to be identified with any certainty at the moment.

6.4 EQUATIONS OF STATE OF $(Mg,Fe)SiO_3$ CLINOPYROXENES

6.4.1 Volume Compressibility of $(Mg,Fe)SiO_3$ Clinopyroxenes

The variation of the unit cell parameters of the low- and high-pressure clinoferrosilite phases with pressure are given in Tables 6.5a and b, and those of the $MgSiO_3$ clinoenstatites (data from Angel and Hugh-Jones, 1994) are given in Tables 6.6a and b. Unit cell parameters of both the low symmetry phases obtained on subsequent decompression of the DAC show no systematic differences from those obtained on increasing the pressure.

P (GPa)	a (Å)	b (Å)	c (Å)	β (degrees)	Volume (Å^3)
0.00	9.7075(7)	9.0807(4)	5.2347(5)	108.462(6)	437.70(6)
0.47	9.690(2)	9.061(4)	5.222(2)	108.29(2)	435.4(3)
0.97	9.675(1)	9.042(3)	5.215(2)	108.19(1)	433.4(2)
1.00	9.672(1)	9.041(3)	5.216(1)	108.19(1)	433.3(2)
1.35	9.668(3)	9.028(1)	5.212(1)	108.10(3)	432.4(2)
1.36†	9.664 (2)	9.028 (2)	5.205 (2)	108.12 (1)	431.6 (2)
1.43	9.661(2)	9.025(4)	5.208(2)	108.09(2)	431.6(2)

Table 6.5a: Unit cell parameters of $FeSiO_3$ low-clinoferrosilite, constrained to monoclinic symmetry.

P (GPa)	a (Å)	b (Å)	c (Å)	β (degrees)	Volume (Å^3)
1.63	9.545(1)	9.005(2)	5.0134(8)	103.12(1)	419.7(1)
1.75	9.543(2)	9.002(2)	5.013(1)	103.07(2)	419.4(2)
1.86	9.5425(6)	8.997(1)	5.0085(5)	103.035(7)	418.94(8)
1.87	9.5400(8)	8.996(2)	5.0083(6)	103.01(1)	418.8(1)
2.40	9.523(1)	8.978(2)	4.9992(8)	102.84(1)	416.8(1)
2.85	9.5111(7)	8.963(2)	4.9922(6)	102.690(8)	415.17(9)
3.00†	9.512 (3)	8.958 (5)	4.993 (2)	102.68 (2)	415.1 (2)
3.03†	9.512 (2)	8.961 (2)	4.991 (2)	102.70 (2)	415.0 (2)
3.14	9.510(3)	8.956(2)	4.989(1)	102.64(3)	414.6(2)
3.49†	9.500 (5)	8.936 (6)	4.989 (4)	102.51 (5)	413.5 (4)
3.66	9.496(4)	8.944(2)	4.981(2)	102.51(4)	413.1(2)
3.94	9.489(1)	8.9339(8)	4.9780(6)	102.45(1)	412.09(9)
4.28	9.483 (2)	8.917 (1)	4.9725 (8)	102.38 (2)	410.7 (3)
4.29†	9.481(1)	8.9247(8)	4.9741(5)	102.37(1)	411.12(8)
4.94†	9.463 (2)	8.904 (2)	4.963 (2)	102.24 (3)	408.7 (2)
5.01†	9.452 (4)	8.915 (4)	4.961 (2)	102.30 (4)	408.4 (4)
5.41†	9.456 (1)	8.8922 (4)	4.9586 (4)	102.13 (2)	407.65 (7)
5.77†	9.447 (2)	8.883 (2)	4.953 (2)	102.10 (2)	406.4 (2)
6.51†	9.432 (2)	8.863 (2)	4.942 (2)	102.00 (2)	404.1 (2)

Table 6.5b: Unit cell parameters of the high-pressure C2/c clinoferrosilite phase, constrained to monoclinic symmetry. Data collected from crystal #1 is unmarked; data from crystal #2 is marked with a cross (†).

P (GPa)	a (Å)	b (Å)	c (Å)	β (degrees)	Volume (Å^3)
0.00	9.605 (4)	8.814 (3)	5.169 (2)	108.34 (4)	415.4 (3)
0.25	9.601 (2)	8.807 (1)	5.167 (1)	108.28 (2)	414.9 (2)
0.78	9.579 (2)	8.794 (2)	5.156 (2)	108.18 (2)	412.7 (1)
1.41	9.569 (2)	8.7746 (9)	5.149 (1)	108.13 (2)	410.9 (1)
1.70	9.564 (2)	8.762 (1)	5.143 (1)	108.08 (1)	409.7 (1)
1.96	9.553 (2)	8.7536 (9)	5.1417 (9)	108.08 (2)	408.7 (1)
2.27	9.542 (2)	8.7444 (8)	5.1367 (9)	108.07 (1)	407.5 (1)
3.20	9.521 (4)	8.720 (2)	5.125 (2)	107.98 (4)	404.7 (3)
3.49	9.514 (2)	8.709 (1)	5.121 (1)	107.94 (2)	403.7 (1)
4.35	9.497 (3)	8.691 (1)	5.112 (1)	107.90 (3)	401.5 (2)
4.80	9.488 (2)	8.6786 (8)	5.1073 (8)	107.86 (2)	400.3 (1)
4.99	9.477 (2)	8.670 (2)	5.102 (1)	107.81 (2)	399.1 (1)
5.30	9.474 (2)	8.6668 (8)	5.1012 (8)	107.84 (2)	398.7 (1)
5.87	9.463 (2)	8.650 (1)	5.094 (1)	107.82 (2)	397.0 (1)
6.06	9.459 (1)	8.6473 (6)	5.0936 (7)	107.81 (1)	396.7 (1)
6.98	9.445 (2)	8.6232 (9)	5.082 (1)	107.75 (2)	394.2 (1)

Table 6.6a. Unit cell parameters of $MgSiO_3$ low-clinoenstatite, constrained to monoclinic symmetry (data from Angel and Hugh-Jones, 1994).

P (GPa)	a (Å)	b (Å)	c (Å)	β (degrees)	Volume (Å^3)
5.34	9.255 (2)	8.684 (1)	4.9332 (9)	101.75 (1)	388.1 (1)
5.78	9.246 (2)	8.670 (1)	4.9299 (9)	101.73 (2)	386.9 (1)
6.43	9.228 (2)	8.6535 (8)	4.9221 (8)	101.62 (2)	385.0 (1)
6.93	9.218 (2)	8.6418 (9)	4.9169 (9)	101.56 (2)	383.7 (1)
7.30	9.207 (2)	8.631 (1)	4.912 (1)	101.51 (2)	382.5 (1)
7.93	9.201 (3)	8.621 (1)	4.908 (1)	101.50 (3)	381.5 (2)

Table 6.6b. Unit cell parameters of $MgSiO_3$ high-clinoenstatite, constrained to monoclinic symmetry (data from Angel and Hugh-Jones, 1994)

Unfortunately, the pressure range of the stability of the $P2_1/c$ phase of $FeSiO_3$ clinoferrosilite was not large enough for all three EOS parameters in the third-order Birch-Murnaghan EOS (defined in Chapter 4) to be refined simultaneously. If the initial volume, V_0, is constrained to the experimentally observed value of 437.7 $Å^3$ at ambient conditions, the values of $K_{0,T}$ and K_0' are very poorly constrained, with large *esd*'s. It has been suggested for the corresponding polymorphs of $MgSiO_3$ (Angel and Hugh-Jones, 1994) that the first derivative of the bulk modulus with pressure, K_0', may be identical for both the $P2_1/c$ and high-pressure C2/c phases. Thus, if K_0' of the low-clinoferrosilite phase is constrained to the value refined for the high-pressure phase, (ie., $K_0' = 4.3$), then the refined parameters for the EOS of low-clinoferrosilite over its 1.4 GPa stability range are:

$$V_0 = 437.6\ (2)\ Å^3 \quad K_{0,T} = 99.9\ (3.6)\ GPa \qquad K_0' = 4.3\ (fixed)$$

It is interesting to note that if V_0 is further constrained to 437.7 $Å^3$ (whilst also constraining K_0' to 4.3) the bulk modulus, $K_{0,T}$, of the low-clinoferrosilite is not significantly altered, or the precision improved (Table 6.7).

Comp^n	Symmetry	Pressure range	V_0 ($Å^3$)	$K_{0,T}$ (GPa)	K_0'
$FeSiO_3$	$P2_1/c$	0.0 - 1.4 GPa	437.7*	88.7 (8.9)	20.9(17.6)
$FeSiO_3$	$P2_1/c$	0.0 - 1.4 GPa	437.7*	97.8 (1.5)	4.3*
$FeSiO_3$	$P2_1/c$	0.0 - 1.4 GPa	437.6 (2)	99.9 (3.6)	4.3*
$FeSiO_3$	C2/c	1.6 - 6.5 GPa	425.5 (4)	113.7(6.8)	4.3 (1.8)
$FeSiO_3$	C2/c	1.6 - 4.3 GPa	426.1(1.0)	98.5(20.3)	10.2 (8.4)
$FeSiO_3$	C2/c	4.3 - 6.5 GPa	425.8(5.6)	111.4(71.5)	4.4 (13.9)
$MgSiO_3$	$P2_1/c$	0.0 - 7.0 GPa	415.6 (2)	111.1(3.3)	6.6 (1.1)
$MgSiO_3$	C2/c	5.3 - 8.0 GPa	405.6(1.1)	104.1(5.7)	6.6*

Table 6.7: Refined EOS parameters for synthetic $MgSiO_3$ (data from Angel and Hugh-Jones, 1994) and $FeSiO_3$ clinopyroxenes. Entries marked with an asterisk (*) were constrained to be constant during refinement of the EOS.

Since the unit cell parameters of the high-pressure C2/c phase of clinoferrosilite were collected over a ~ 5 GPa pressure range, it was possible to simultaneously refine all three EOS parameters to the P-V data of this phase. These are given below:

$$V_0 = 425.5\ (4)\ \text{Å}^3 \quad K_{0,T} = 113.7\ (6.8)\ \text{GPa} \quad K_0' = 4.3\ (1.8)$$

The two fitted EOS's are shown in Figure 6.6; Table 6.7 summarised the refined EOS parameters for various constraints.

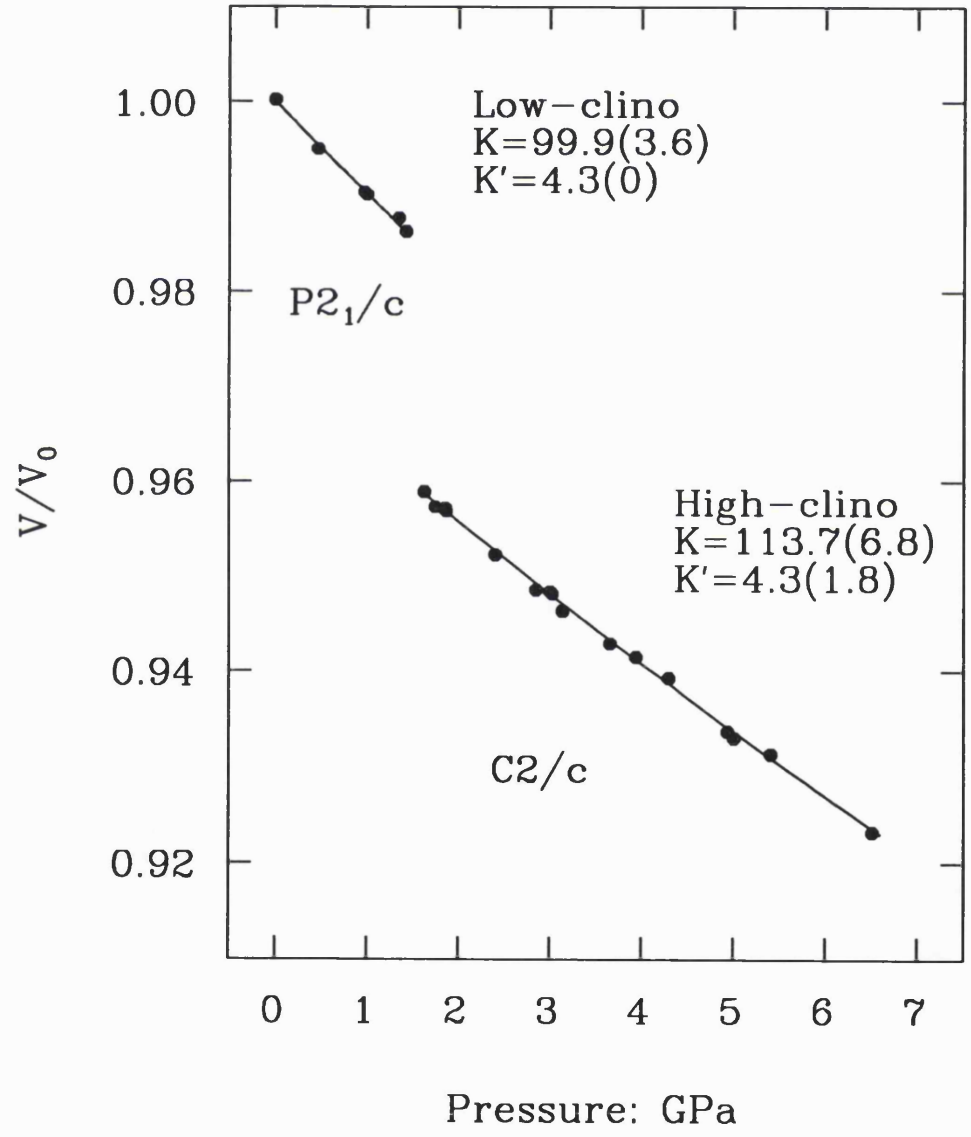

Figure 6.6: Volume variation with pressure of the low- and high-pressure phases of $FeSiO_3$ clinoferrosilite.

Structural data collected for the high-pressure C2/c clinoferrosilite phase between 1.8 GPa and ~ 6.5 GPa (Section 6.3) have suggested that since there is a change in the compression mechanism operating in the clinopyroxene at ~ 4.3 GPa, the volume variation with pressure ought to be represented by two independent EOS's, at pressures lower and higher than this respectively, in a similar way to the corresponding orthopyroxenes (see Chapters 3 and 4). Although it was possible to simultaneously refine V_0, $K_{0,T}$ and K_0' for a split-EOS for the high-pressure C2/c clinoferrosilite (ie., for the P-V data in the ranges 1.6 - 4.3 GPa and 4.3 - 6.5 GPa), the differences between these two sets of refined parameters are not significant within the experimental uncertainties (Table 6.7); the two-EOS fitting to the data is therefore not significant at the 95% level (Hamilton, 1965). However, the lower-pressure compression regime (ie., 1.6 - 4.3 GPa) does have a somewhat higher K_0' ($K_0' \sim 10$) than the higher-pressure regime ($K_0' \sim 4$), as expected by direct comparison with the corresponding orthopyroxenes (Chapter 4), though within one combined *esd* they are identical.

Finally, it is important to note that, while keeping K_0' constrained to 4.3 throughout, the high-pressure C2/c clinoferrosilite phase is less compressible than the low-clinoferrosilite phase. This is obvious from the raw data (Figure 6.6), irrespective of the constraints imposed during the fitting of the EOS.

The EOS's of the $MgSiO_3$ low- and high-clinoenstatite phases are also presented in Table 6.7 (Angel and Hugh-Jones, 1994). Since the range of unit cell data of the high-pressure C2/c clinoenstatite phase is limited to ~ 2.7 GPa, as the DAC used for these compression experiments could not reach pressures higher than ~ 8 GPa, K_0' for this phase has been constrained to the same value as that refined for the low-clinoenstatite. Third-order Birch-Murnaghan EOS's fitted to the volume variation with pressure for the $P2_1/c$ and C2/c phases of $MgSiO_3$ clinoenstatite give the following parameters:

$P2_1/c$: $V_0 = 415.6\ (0.2)$ Å^3 $K_{0,T} = 111.1\ (3.3)$ GPa $K_0' = 6.6\ (1.1)$

C2/c : $V_0 = 405.6\ (1.1)$ Å^3 $K_{0,T} = 104.1\ (5.7)$ GPa $K_0' = 6.6$ (fixed)

The effect of exchanging Fe^{2+} for Mg^{2+} in the cation sites of the clinopyroxenes is to significantly increase the value of K_0'; constraining K_0' to 6.6 reveals that, unlike the $FeSiO_3$ clinoferrosilites, the $P2_1/c$ phase of $MgSiO_3$ is less compressible than the C2/c phase at ambient conditions. However, although the EOS's refined for the two C2/c clinopyroxene phases are virtually superimposable (with only small deviations of the $MgSiO_3$ data from the $FeSiO_3$ EOS in the pressure range 3-5 GPa), the EOS's for the $P2_1/c$ phases are not; this may simply be an artefact of the limited pressure ranges of the data for the low-clinoferrosilite and high-clinoenstatite.

6.4.2 Comparison with EOS's for Other C2/c Clinopyroxenes

Equations of state of Ca^{2+}-containing C2/c clinopyroxene phases of different compositions have also been determined using a variety of different experimental techniques (Table 6.8). The volume variation with pressure of the diopside (Levien et al., 1979) may also be described by a third-order Birch-Murnaghan EOS where K_0' is constrained to 4.0, and the bulk modulus is refined to $K_{0.T}$ = 115.2(1.0) GPa. Although the bulk moduli of the Mg^{2+}-rich diopside phase (Levien et al., 1979; McCormick et al., 1989) are somewhat lower than those of the Fe^{2+}-rich hedenbergite phases (Zhang and Hafner, 1992; Kandelin and Weidner, 1988a), suggesting that the effect of increasing Fe^{2+} content is to cause these Ca^{2+}-containing C2/c clinopyroxenes to become less compressible than their Mg^{2+}-containing counterparts, this effect is small. There is no significant change in K_0' as the composition changes from Mg^{2+}-rich to Fe^{2+}-rich.

Author(s)	Composition	$K_{0.T}$ GPa	K_0'	Technique
Levien et al., 1979	Di_{100} (n)	113 (2)	4.8 (0.7)	X-ray
McCormick et al., 1989	Di_{100} (n)	118 (7)	5.6 (2.5)	X-ray
Zhang & Hafner, 1992	$Di_{40}Hd_{60}$ (s)	82.7 (0.1)	4.0	Mössbauer
Zhang & Hafner, 1992	Hd_{100} (s)	119 (2)	4.0	Mössbauer
Kandelin & Weidner, 1988a	Hd_{100} (s)	120		Brillouin

Table 6.8: Equations of state of C2/c clinopyroxenes of other compositions.

Since the Ca^{2+}-containing clinopyroxenes are known to have significantly different structures to the C2/c phases of the $(Mg,Fe)SiO_3$ clinopyroxenes stable at high-pressures (Section 6.2), it is very surprising to discover that the bulk moduli and K_0's of all the C2/c clinopyroxene phases of all compositions, except pure $MgSiO_3$ and $Di_{40}Hd_{60}$, in the $(Ca,Mg,Fe)SiO_3$ system are identical to within one combined *esd*.

6.4.3 Axial Compressibilities of $(Mg,Fe)SiO_3$ Clinopyroxenes

The variation with increasing pressure of the unit cell parameters for both the low- and high-pressure C2/c clinopyroxene phases are given in Tables 6.5a and b, (for the $FeSiO_3$ clinopyroxenes), and Tables 6.6a and b for the corresponding $MgSiO_3$ phases. The linear compressibilities, β, calculated for the $d_{(100)}$, b, and c orthogonal directions of the four clinopyroxene polymorphs are presented in Table 6.9.

Composition	Symmetry	$\beta_{(100)}$ GPa^{-1}	β_Y GPa^{-1}	β_Z GPa^{-1}
$FeSiO_3$	$P2_1/c$	$1.7(2) \times 10^{-3}$	$4.30(6) \times 10^{-3}$	$3.2(3) \times 10^{-3}$
$FeSiO_3$	C2/c	$1.62(7) \times 10^{-3}$	$3.17(9) \times 10^{-3}$	$2.86(5) \times 10^{-3}$
$MgSiO_3$	$P2_1/c$	$2.00(4) \times 10^{-3}$	$3.10(4) \times 10^{-3}$	$2.41(4) \times 10^{-3}$
$MgSiO_3$	C2/c	$2.0(1) \times 10^{-3}$	$2.8(1) \times 10^{-3}$	$2.04(9) \times 10^{-3}$

Table 6.9: Linear compressibilities of the $FeSiO_3$ and $MgSiO_3$ clinopyroxenes.

In both the $P2_1/c$ and high-pressure C2/c phases of $FeSiO_3$, d_{100} is the least compressible direction, and the [010] direction is the most. This order of axial compressibilities (ie., $b > c > a\sin\beta$) is identical to that already seen for all the Ca^{2+}-poor orthopyroxenes (Chapter 4). All three directions become less compressible on going from the lower-symmetry to the higher-symmetry clinopyroxene polymorph with increasing pressure. Although the response of the low-symmetry $P2_1/c$ structure to increasing pressure has not been determined, the relative compressibilities along

$a\sin\beta$, [010] and [001] for the C2/c phase can be correlated with specific structural elements: compression along [010] is achieved by simply reducing the amount of "free space" between the tetrahedral chains and octahedra, since in pyroxenes of all symmetries, this is the direction of maximum free space; compression along [001] is more restricted in the C2/c phase than in the $P2_1/c$ phase since there is little kinking of the silicate chains in the high-pressure C2/c phase during compression (Section 6.3.2); and finally, compression along $a\sin\beta$ involves the energetically unfavourable compacting together of the (100) tetrahedral and octahedral layers of the clinoferrosilite structure, and is therefore limited.

Comparison of these axial compressibilities with those of the $MgSiO_3$ clinoenstatite phases (Table 6.9; data from Angel and Hugh-Jones, 1994) show that in both the $P2_1/c$ and high-pressure C2/c polymorphs, the [010] direction is the most compressible, and $a\sin\beta$ the least. However, in the C2/c phase of $MgSiO_3$, the compressibility along c and $a\sin\beta$ are the same within the experimental uncertainties; note that the compressibility along $a\sin\beta$ in $MgSiO_3$ does not change on transforming from the $P2_1/c$ structure to the C2/c structure at high pressure.

It was anticipated that changes in the linear compressibilities of C2/c clinopyroxenes due to changing composition along the diopside-hedenbergite join (Table 6.10) could be correlated with the changes in some structural element across the join. From several possible proposed relationships, the most favoured was found to be that between the chain extension angle (ie., the O3-O3-O3 angle) of the clinopyroxenes and their linear (or axial) compressibilities. Papike et al. (1973), and later Cameron and Papike (1980), determined that as the mean ionic radius of the "M" cations (see Chapter 1) decreases, the chains straighten (ie., their O3-O3-O3 angles increase). The effect of changing the chain extension angle of these C2/c clinopyroxenes on their relative linear compressibilities could therefore be determined independently of their compositions (Figure 6.7).

Author	Composition	$\beta_{(100)}$*	β_y	β_z
Levien et al., 1979	Di_{100} (n)	2.18 (5)	4.03 (1)	2.54 (1)
Levien & Prewitt, 1981	Di_{100} (n)	2.58 (3)	3.274 (7)	2.597 (3)
McCormick et al., 1989	Di_{100} (n)	1.94 (5)	3.17 (7)	2.47 (7)
Zhang & Hafner, 1992	$Di_{40}Hd_{60}$ (s)	1.9 (2)	3.1 (2)	2.2 (2)
Zhang & Hafner, 1992	Hd_{100} (s)	2.22 (8)	3.3 (1)	2.6 (2)
Kandelin & Weidner, 1988a	Hd_{100} (s)	2.7 (3)	3.7(1)	1.9 (2)

Table 6.10: Linear compressibilities of C2/c pyroxenes of various compositions, which for the end-member phases are as follows: Di = diopside = $Ca_{0.5}Mg_{0.5}SiO_3$, and Hd = hedenbergite = $Ca_{0.5}Fe_{0.5}SiO_3$. Note that (n) denotes a natural sample, whereas (s) denotes a synthetic sample.
* For comparison the compressibility has been calculated along d_{100} rather than the a axis, to compensate for differing β angles of the clinopyroxenes.

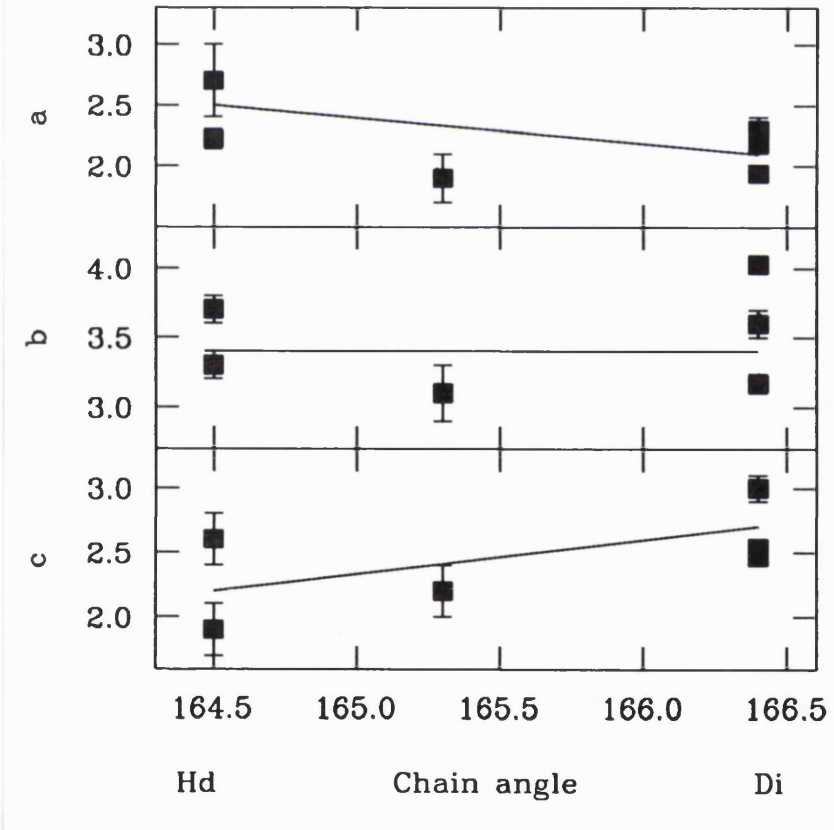

Figure 6.7: Effect of increasing the chain extension angle of Ca^{2+}-containing C2/c clinopyroxenes (hedenbergite and diopside) on the linear compressibilities of these pyroxenes. The data is taken from Levien et al., 1979; Kandelin and Weidner, 1988a; McCormick et al., 1989; and Zhang and Hafner, 1992.

From Figure 6.7, it is seen that as the chain angle (O3-O3-O3) of the clinopyroxene increases, the compressibility of the [010] direction remains unchanged within the experimental uncertainties, the [001] direction becomes more compressible, and the $a\sin\beta$ direction becomes somewhat stiffer. High-pressure C2/c clinoferrosilite has silicate chains some ~ 5° more extended than those of the corresponding high-pressure $MgSiO_3$ phase. From the relationship described above (Figure 6.7), it is expected that the compressibility along [010] will remain unchanged, along $a\sin\beta$ will be less and along [001] will be greater in C2/c clinoferrosilite than in high-pressure C2/c $MgSiO_3$.

Within two combined *esd*'s the experimental data presented in Table 6.9 confirm this, with the compressibility of the [010] direction in the Mg^{2+}- and Fe^{2+} end-members of the $(Mg,Fe)SiO_3$ solid solution staying approximately constant. The compressibility along $a\sin\beta$ is increased by some 23% on substituting Mg^{2+} for Fe^{2+} in the cation sites of the clinopyroxene while the compressibility along [001] is reduced by ~ 29%. These two effects result in the compressibilities of the [001] and $a\sin\beta$ directions in the C2/c phase of $MgSiO_3$ being identical within the experimental *esd*'s.

6.5 SUMMARY

From detailed structural comparisons of all $(Mg,Fe)SiO_3$ clinopyroxenes structures with space group C2/c, the high-pressure C2/c structure is found to differ considerably from both the high-T C2/c phase (eg., Sueno et al., 1984), and also calcium-containing C2/c polymorphs (eg, hedenbergite; Ohashi, 1975), while it is very similar (in terms of the sizes and distortions of the cation sites) to orthoferrosilite. Table 6.11 qualitatively summarises the differences between the three C2/c $FeSiO_3$ clinoferrosilite polymorphs and orthoferrosilite. These structural relationships also hold for the corresponding $MgSiO_3$ ortho- and clinoenstatite phases. The chemical behaviour of the high-pressure C2/c forms of both $MgSiO_3$ and $FeSiO_3$ is therefore expected to resemble that of the corresponding orthopyroxenes.

	High-P	High-T	Hd-like	Ortho
Symmetry	C2/c	C2/c	C2/c	Pbca
β angle	small	large	large	90°
M2 co-ord^{n}	6	8	8	6
M2 volume	small	large	large	small
Chain rot^{n}	O	O	O	All O
Chains	kinked	straight	fairly straight	A: kinked B: straight

Table 6.11: Summary of differences between high-P, high-T, Hd-like C2/c clinoferrosilites and orthoferrosilite.

Since the structures of the high-pressure and high-temperature C2/c clinopyroxenes are very different, the phase diagram for the $MgSiO_3$ - $FeSiO_3$ pyroxene system will contain two structurally distinct C2/c phases, whose stability fields may meet at a kind of isosymmetric "cross-over" transition at very high pressures and temperatures. The possibility of such a "C2/c - C2/c" transition is discussed in more detail in Chapter 7.

At ambient temperature, pyroxenes containing less than ~15% Ca in the $Ca(Mg,Fe)SiO_3$ - $(Mg,Fe)SiO_3$ solid-solution range are stable as a low-symmetry $P2_1/c$ structure (Ohashi et al., 1975); as the temperature is increased, the high-T C2/c structure is stabilised. Since the structures of the high-temperature and "high-Ca" C2/c phases are similar in both $MgSiO_3$ and $FeSiO_3$ end-members (especially in terms of the sizes and distortions of their M1 and M2 cation sites) the structural trends across the hedenbergite-ferrosilite and diopside-enstatite joins would appear to be continuous at some high temperature. Any variation in the structure of this high-T C2/c phase as the composition changes from Ca^{2+}-rich to Ca^{2+}-poor will be caused solely by the substitution of Fe^{2+} for Ca^{2+} in the M1 and M2 sites; the structure of a pyroxene of intermediate Ca^{2+}-content may be estimated using the trends of Cameron and Papike (1980; see Chapter 1).

The response of the high-P C2/c clinoferrosilite phase to increasing pressure is significantly different to that of the corresponding orthopyroxenes, although in both structural polymorphs, there is a change in compression mechanism at about 4 GPa. Below 4.3 GPa, the C2/c clinoferrosilite phase accommodates increasing pressure simply by the contraction of its M1 and M2 cation sites; at higher pressures, the previously incompressible Si-O bonds also begin to shorten (approximately four times faster per GPa than those in orthopyroxenes), with no associated distortion of the tetrahedra. The silicate chains do not significantly kink or straighten below ~ 6.5 GPa.

The EOS parameters of the high-pressure C2/c clinoferrosilite phase are determined to be $K_{0,T}$ = 113.7(6.8) GPa and K_0' = 4.3(1.8). Comparison with the available data for the high-pressure C2/c $MgSiO_3$ phase (Angel and Hugh-Jones, 1994) suggests that the two EOS's are identical to within one combined *esd*; those of the low-symmetry $P2_1/c$ phases of $FeSiO_3$ and $MgSiO_3$ are the same to within two combined *esd*'s. Thus the effect on their EOS's of changing the Fe^{2+} content of $(Mg,Fe)SiO_3$ orthopyroxenes across the join is negligible. In all four $(Mg,Fe)SiO_3$ clinopyroxenes phases studied, the [010] direction is the most compressible, and $a\sin\beta$ the least. All three directions become less compressible in the C2/c phases compared to the $P2_1/c$ phases. The relative differences between the axial compressibilities of the C2/c phases of $MgSiO_3$ and $FeSiO_3$ are explained by differences in the O3-O3-O3 chain angles of the clinopyroxenes.

CHAPTER 7

DETERMINATION OF $(Mg,Fe)SiO_3$ PYROXENE PHASE DIAGRAM

7.1 INTRODUCTION

The sequence of discoveries of the various different structural polymorphs, and the development of the phase relations within the $MgSiO_3$ - $FeSiO_3$ pyroxene solid solution are reviewed in this chapter. Each of the following sections broadly represents the behaviour of pyroxene of a specific structure and composition along the join with respect to either temperature or pressure. From this review and my experimental data (Chapter 5), it is possible to see that the phase relations of *all* Ca^{2+}-poor pyroxenes along the $(Mg,Fe)SiO_3$ join are very similar, differing only in the precise pressures or temperatures of the transitions between the polymorphs. Using the experimentally determined pressures of the low- to high-symmetry clinopyroxene phase transition (Angel et al., 1992a; Chapter 5), the proposed topologies of the equilibrium phase diagrams for both $MgSiO_3$ and $FeSiO_3$ have been confirmed and are presented in Sections 7.2.7 and 7.3.7 respectively; the proposed topology of the metastable phase diagram for $FeSiO_3$ is presented in Section 7.3.8.

Once the phase equilibria between the structurally distinct phases of $(Mg,Fe)SiO_3$ pyroxene have been reviewed, some of the thermodynamic quantities (eg., ΔS and ΔH) of the end-member pyroxene phases are calculated from the previously measured phase boundaries between the phases in P-T space (eg., Grover, 1972; Pacalo and Gasparik, 1990; Lindsley, 1965; Woodland, pers. comm.; Chapter 5) and the experimentally determined equations of state (EOS's; Chapters 4 and 6).

The structural differences between the five existing pyroxene polymorphs were described in Chapter 1, and were summarised in Table 1.2. Briefly, the phases discussed in this chapter are orthopyroxene (with space group Pbca), protopyroxene

(only stable for Mg^{2+}-rich pyroxenes; space group Pbcn), low-clinopyroxene ($P2_1/c$), and high-temperature and high-pressure clinopyroxenes (both with space group C2/c). It has already been demonstrated in Chapter 6 that the structures of the C2/c clinopyroxenes stable at high-temperatures and high-pressures are significantly different; the possibility of a kind of isosymmetric "crossover" transition between them at very high temperatures and pressures proposed in Chapter 6 is discussed in further detail here.

7.2 $MgSiO_3$ ENSTATITE

7.2.1 Historical Background

The first thorough investigation of the phase relations in the $MgSiO_3$ system was the work of Allen et al. (1906), who synthesised pyroxenes and amphiboles of both orthorhombic and monoclinic symmetries. Only the monoclinic pyroxene phase was found to be stable at all temperatures, since the other three phases crystallised metastably below about 1100°C. In 1930, Warren and Modell showed that the amphibole structures of Allen et al. (1906) were simply those of hydrated pyroxenes (containing ~2.2% water), thus limiting to two the number of distinct phases of $MgSiO_3$ pyroxene, namely ortho- (or rhombic) enstatite and clinoenstatite. Although Bowen and Schairer (1935) did not succeed in transforming the monoclinic enstatite to the orthorhombic form, they estimated the temperature of this transition to be 1145°C.

A third polymorph of $MgSiO_3$ enstatite was first obtained at high temperatures by Haraldsen (1930), and was later identified by Büssem et al. (1938) as "protoenstatite". Since it reverted to clinoenstatite on reheating, on grinding at room temperature, and even on long standing, it was assumed to be unstable at all temperatures. However, in 1939, Thilo and Rogge reversed the transition between protoenstatite and rhombic enstatite in the region 900 - 990°C, thus assigning it a true stability field at high temperatures; they also observed the metastable clinoenstatite-protoenstatite transition at ~1260°C.

The structures and unit cell parameters of these three $MgSiO_3$ polymorphs were reviewed and re-evaluated by Atlas (1952) using X-ray diffraction techniques. Additional experiments (Atlas, 1952) to determine the phase equilibria of $MgSiO_3$ favoured the existence of rhombic enstatite up to 985°C, with protoenstatite occurring from 985°C to the point of dissociation into forsterite and liquid (at approximately 1557°C; Kushiro (1972)); clinoenstatite was assumed to be a low-temperature metastable phase formed displacively from protoenstatite by rapid cooling. In 1962, Sarver and Hummel also studied the stability relations of these three $MgSiO_3$ polymorphs, using MgF_2 and LiF as mineralisers to enhance the rate of transformation. They produced protoenstatite from orthoenstatite at ~ 1042°C, with the metastable inversion of this protoenstatite to clinoenstatite occurring at ~ 865°C on cooling (the rate of this latter reaction depending significantly on the external experimental conditions; for example, the substitution of less than 2 % Mn^{2+} for Mg^{2+} was found to inhibit any inversion of protoenstatite below ~ 1042°C).

The following sections briefly describe the history of each of the known phase transformations in the $MgSiO_3$ system, concluding, where possible, with the position of the currently accepted phase boundary in P-T space, which will be used in the thermodynamic calculations in Section 7.2.7.

7.2.2. Ortho- to Protoenstatite Transition

More recent experiments on the transition of orthoenstatite to protoenstatite include those of Lange and Koltermann (1966), who described high temperature X-ray diffraction studies on transformations between enstatite polymorphs using $MgSiO_3$ protoenstatite produced by firing talc as the starting material. They concluded that whilst protoenstatite is indeed the stable high temperature phase of $MgSiO_3$, the initial heating temperature of this protoenstatite merely changes the nature of the transformation to clinoenstatite on cooling. Using the same experimental techniques, Smyth (1974a) found that rapid quenching of protoenstatite from ~ 1000°C produced a twinned clinoenstatite, whereas slower cooling rates produced mixtures of

clinoenstatite and orthoenstatite; orthoenstatite transformed to protoenstatite when left for several days at ~1200°C.

The triangular stability field in P-T space of protoenstatite was determined by Boyd et al. (1964), who showed that orthoenstatite is more stable than protoenstatite at all temperatures for pressures above ~ 1 GPa; clinoenstatite found in runs made at high temperatures and ~ 0.5 - 0.6 GPa was assumed to be the inversion product of protoenstatite. Subsequent experiments (eg., Anastasiou and Seifert (1972); Chen and Presnall (1975)), and the thermodynamic calculations of Gasparik (1990), have determined the precise position of the stability field of protoenstatite in P-T space. The phase boundary between ortho- and protoenstatite is shown, with the experimental data points, in Figure 7.1.

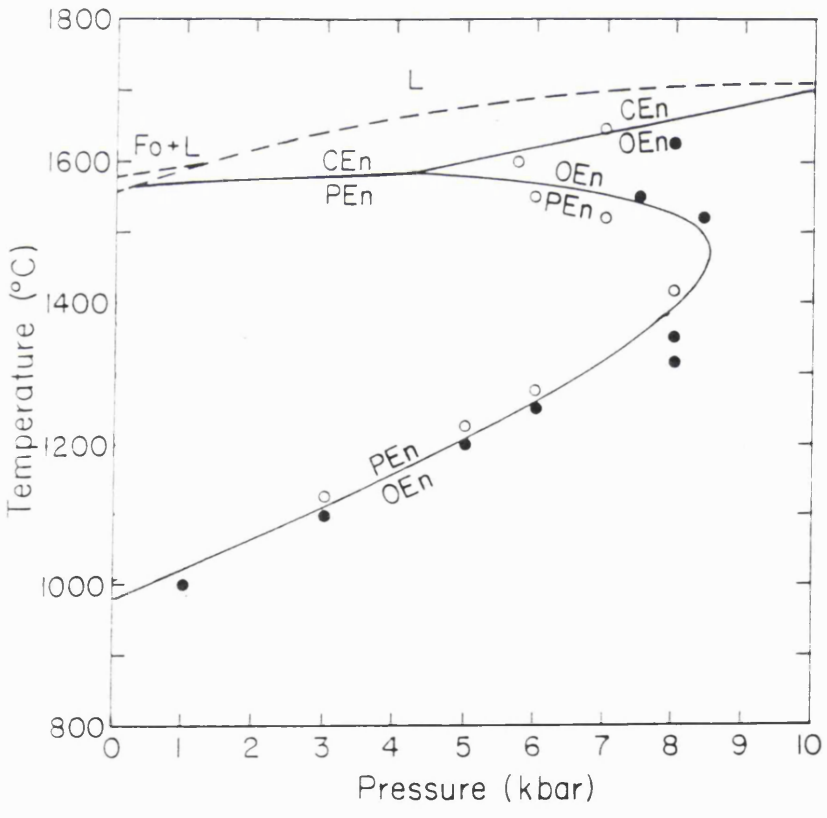

Figure 7.1: The experimental reversals (denoted by circles; data from Boyd et al. (1964), Anastasiou and Seifert (1972) and Chen and Presnall (1975)) and thermodynamic calculations of Gasparik (1990; shown by the solid line) constraining the protoenstatite stability field.

7.2.3 Low-Clino to Orthoenstatite Transition

In 1964, Sclar et al. reversed the orthoenstatite to clinoenstatite transition at moderate temperatures and high pressures, demonstrating that at ambient pressure, clinoenstatite is the stable phase below ~ 540°C. Further reversals of the orthoenstatite to low-clinoenstatite boundary to ~ 5 GPa by Boyd and England (1965) confirmed the existence of such a phase boundary, although their ortho-clino transformation temperature at ambient pressures was some 75°C higher than that of Sclar et al. (1964). In a series of careful hydrothermal experiments and in the absence of shear stresses, Grover (1972) established the true stability field of clinoenstatite at low temperatures and pressures to ~ 0.4 GPa; demonstrating in passing that the clinoenstatite phase could be stabilised at higher temperatures by addition of small amounts of calcium. These three sets of reversals of the ortho- to low-clino enstatite phase boundary are shown in Figure 7.2. The equation of Grover (1972) shown below:

$$T\ (°C) = 566 + 45\ P\ (GPa) \qquad (7.1)$$

is used in the thermodynamic calculations described in Section 7.2.7.

Deformation experiments on the $MgSiO_3$ pyroxene polymorphs indicated that shear stresses also played an extremely important part in the transformations between the polymorphs. Riecker and Rooney (1966) transformed orthoenstatite to low-clinoenstatite at temperatures up to ~1000°C in the presence of shearing stresses; similarly in 1968, Munoz found that application of shear stresses to an orthoenstatite crystal held at pressure and temperature conditions close to Boyd and England's (1965) phase boundary also caused inversion to the monoclinic structure. Coe and Kirby (1975) demonstrated that the rate of formation of clinoenstatite from orthoenstatite is substantially increased by shearing, which significantly enhances the stability of clinoenstatite with respect to orthoenstatite. Their ortho-clino transition was achieved by a macroscopic shear on (100) in the [001] direction, the angle of shear being 12.8 $\pm$ 1.3°. It was found to be coherent and was reversed by annealing under

a variety of conditions. They estimated that the equilibrium transition temperature may be raised by some 300°C per kilobar non-hydrostatic stress.

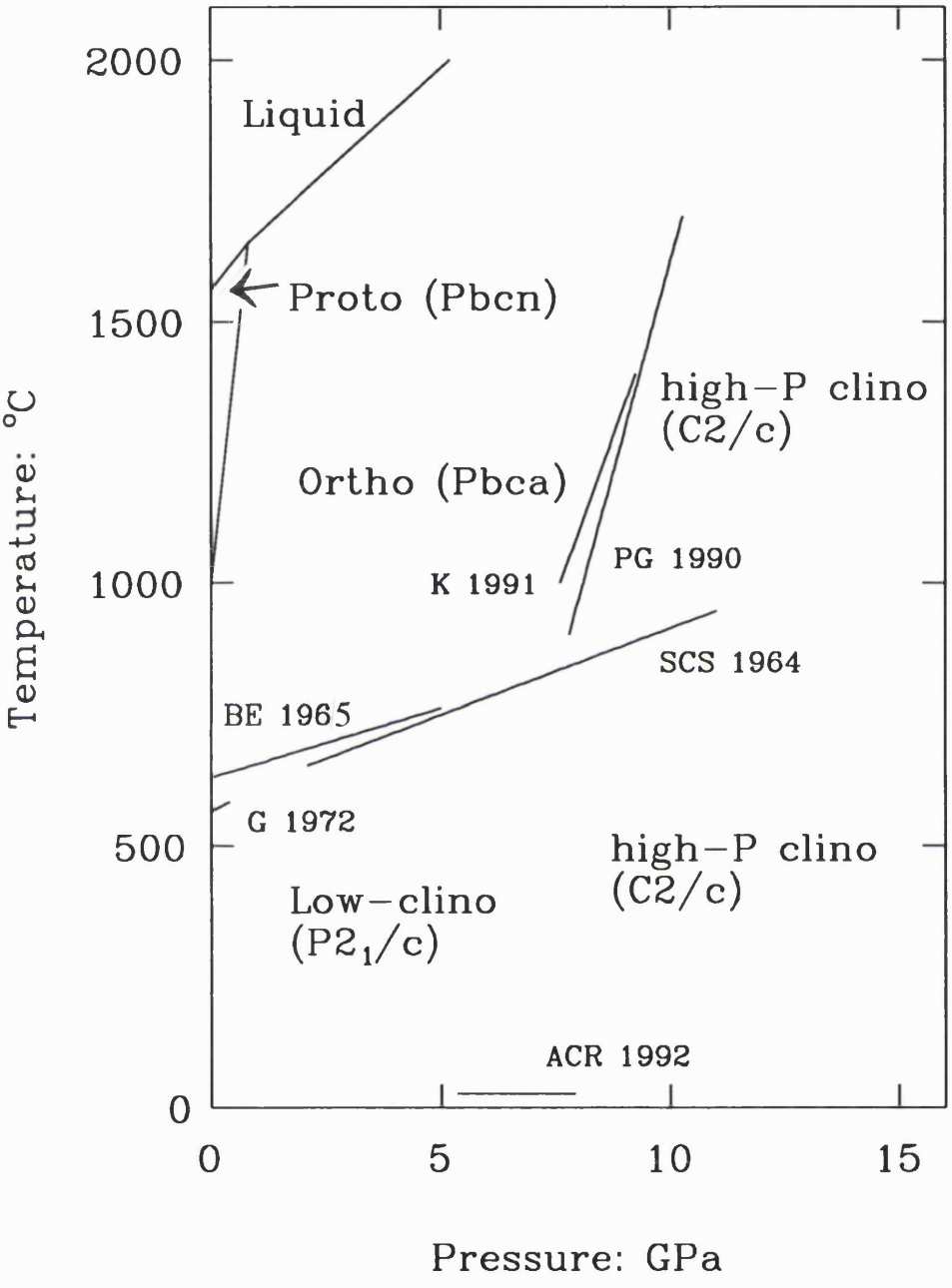

Figure 7.2: The experimental reversals of the phase boundaries in the $MgSiO_3$ enstatite system. The small stability field of high-temperature clinoenstatite shown in Figure 7.1 is included in the protoenstatite field in this diagram. The abbreviated references used are as follows: BE 1965 (Boyd and England, 1965), SCS 1964 (Sclar et al., 1964), G 1972 (Grover, 1972), PG 1990 (Pacalo and Gasparik, 1990), K 1991 (Kanzaki, 1991) and ACR 1992 (Angel et al., 1992a).

7.2.4 Low-Clino to High-Temperature Clinoenstatite Transition

In 1965, Perotta and Stephenson reported the existence of a new fourth phase of $MgSiO_3$ pyroxene, which was produced metastably by a displacive inversion of clinoenstatite at ~ 995°C, persisting over a temperature interval of about 20°C before inverting to protoenstatite; with increasing calcium content the stability field of the new phase was extended by at least 400°C to higher temperatures, with no signs of reversion to protopyroxene. It was indexed on a triclinic unit cell and became known as "high" clinoenstatite, the $P2_1/c$ low-temperature form now becoming known as "low" clinoenstatite. Smith (1969b) reindexed this high clinoenstatite diffraction pattern using a monoclinic cell with space group C2/c, since the X-ray powder pattern of the clinoenstatite formed at high temperatures bore a closer resemblance to diopside than to low-clinoenstatite. However, the *c*-repeat of this new phase is considerably larger than that of low clinoenstatite (which has space group $P2_1/c$), due to a significant straightening of the tetrahedral chains at high temperatures providing larger octahedral cavities for Mg^{2+} vibration (see Chapter 5 for details).

Interestingly, Kuno (1966) independently suggested that for $(Mg,Fe)SiO_3$ pyroxenes containing more than ~15% iron, a "high-clinopyroxene" structure is the stable phase at temperatures above ~1000°C, with the precise temperature of the transformation from orthopyroxene depending on the relative iron content of the pyroxene (see Section 7.4.6). Unaware of the work of Perotta and Stephenson (1965), he identified this high-clinopyroxene with natural pigeonitic pyroxene, naming it "high" simply because it occurred stably at temperatures higher than those of orthopyroxene.

Schwab (1969), and later Ernst and Schwab (1970), identified a further high-temperature phase of $MgSiO_3$ formed from low-clinoenstatite at 1080°C, and from orthoenstatite at 1130°C. Since they claimed minor structural differences between this phase and Perotta and Stephenson's (1965) high-clinoenstatite, a temporary field for "β"-clinoenstatite was introduced between the proto- and orthoenstatite fields.

Sadanaga et al. (1969) performed heating experiments on natural enstatites, and using X-ray diffraction techniques, suggested that this "β"-clinoenstatite may have simply been polysynthetically twinned clinoenstatite. On cooling from 1100°C, their protoenstatite structure persisted to ~ 650°C where it suddenly transformed to low-clinoenstatite, demonstrating the first order character of this transition.

7.2.5 Ortho- to High-Pressure Clinoenstatite Transition

Several later experiments (eg, Akaogi and Akimoto, 1977) performed using high pressure multi-anvil devices also gave clinoenstatite as a product, although it was generally considered to be a metastable phase simply resulting from non-hydrostatic pressure. Kato and Kumazawa (1985) observed clinoenstatite as a liquidus phase at 20 GPa and 2200°C, suggesting that a monoclinic phase may indeed be stable at high pressures and temperatures. For this reason, Kanzaki (1991) investigated a phase boundary between the orthorhombic and monoclinic forms of $MgSiO_3$ at ~ 7-10 GPa using multi-anvil apparatus, successfully stabilising clinoenstatite at 1000°C and pressures in excess of ~7.5 GPa. However, his results gave a slope of much lower $\delta P/\delta T$ than those of previous experiments (eg. Sclar et al. (1964), and Boyd and England (1965), who used piston cylinder and belt apparatus respectively; Figure 7.2), and he explained this discrepancy by either the effect of non-hydrostatic pressure or large differential stresses within the pressure cells of the earlier workers.

Pacalo and Gasparik (1990) reversed the same orthoenstatite-clinoenstatite boundary at 7-11 GPa and 900°C-1700°C using a split-sphere anvil apparatus (Figure 7.2). However, they suggested that the monoclinic phase stable at high pressures and temperatures was a previously unrecognised high pressure polymorph of clinoenstatite, structurally distinct from both the traditional high-temperature clinoenstatite or low-clinoenstatite, although perhaps analogous to $MgGeO_3$ C2/c clinopyroxene (Ross and Navrotsky, 1988).

Using Raman spectroscopy, Chopelas and Boehler (1992) studied the high pressure phases of $MgSiO_3$ pyroxene, heating the sample in a diamond anvil cell with a CO_2 laser to overcome the problem of the non-quenchability of the high-pressure monoclinic phase. Since the spectrum of the high-pressure clinoenstatite bore close resemblance to that of diopside, the new phase was expected to have C2/c symmetry. They also claimed a transition from this high-pressure clinopyroxene phase to orthoenstatite at $\sim$5 GPa upon decompression; subsequent compression experiments using single crystal X-ray diffraction techniques (see Chapter 5 for details) have demonstrated that high-pressure clinopyroxenes in the $(Mg,Fe)SiO_3$ system revert preferentially to the low-clinopyroxene phase rather than to orthopyroxene upon pressure release, due to the highly reconstructive nature of the transformation.

The equation describing the phase boundary of Pacalo and Gasparik (1990) between ortho- and high-pressure clinoenstatite is:

$$P\ (GPa) = 0.0031\ T\ (^{\circ}C) + 5 \qquad (7.2a)$$

which may be rearranged as:

$$T\ (^{\circ}C) = 323\ P\ (GPa) - 1613 \qquad (7.2b)$$

Further experimental work has suggested that the addition of small amounts of Ca^{2+} or Al^{3+} to the $MgSiO_3$ end-member has only a minor effect on the position of the orthopyroxene to high-pressure clinopyroxene phase boundary (Herzberg and Gasparik, 1991).

7.2.6 Low-Clino to High-Pressure Clinoenstatite Transition

Angel et al. (1992a) confirmed the stability of the non-quenchable high pressure clinoenstatite phase (Chopelas and Boehler, 1992) by directly reversing the low-high pressure transition *in situ* in a diamond anvil cell at ambient temperature; the position of this transition is shown in Figure 7.2. The space group of the high-pressure clinoenstatite was verified to be C2/c and from a structure determination at ~ 8 GPa it was possible to identify the mechanism of the transition, which involved a major reorganisation of the silicate chains (see Chapter 5 for details).

7.2.7 $MgSiO_3$ Phase diagram and Thermodynamic Calculations

The currently accepted equilibrium phase diagram for the $MgSiO_3$ enstatite system is that proposed by Angel et al. (1992a), and is shown in Figure 7.3. It is not clear from the available literature whether the high-temperature C2/c phase has a real stability field in P-T space (as suggested by the thermodynamic calculations of Gasparik (1990); Figure 7.1), or whether, in fact, it is metastable at all temperatures and pressures. Because of this uncertainty, the possible stability field of a C2/c clinoenstatite phase at high temperatures has been ignored in Figure 7.3. The metastable phase relations of $MgSiO_3$ are likely to be similar to those of $FeSiO_3$, which are discussed at the end of the next section (Section 7.3.8), although an additional stability field of protoenstatite will be located between the low- and high-clinoenstatite fields at low pressures and very high temperatures.

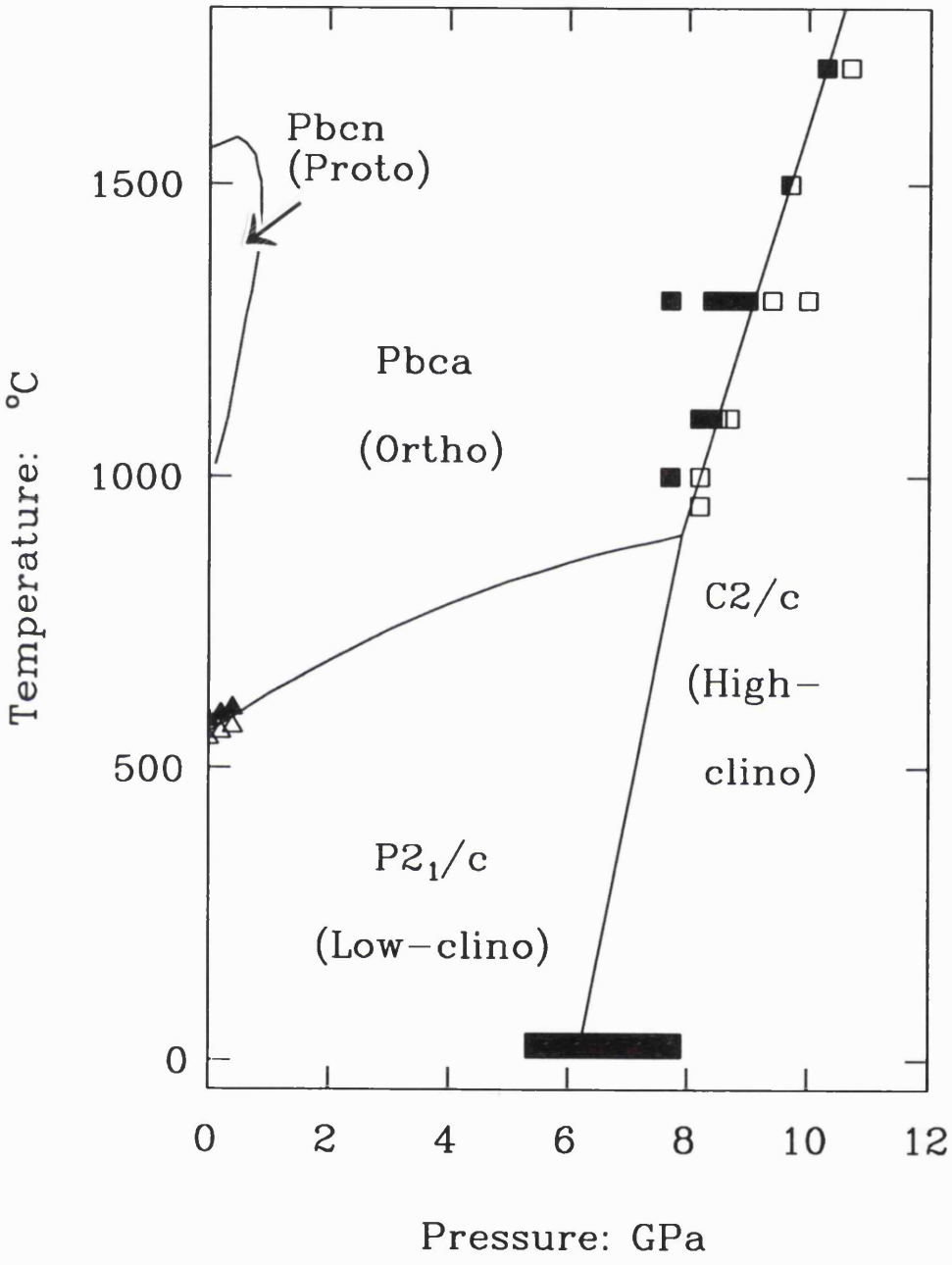

Figure 7.3: The currently accepted phase diagram of $MgSiO_3$ enstatite, showing the experimental reversals of Grover (1972; triangles), Angel et al., (1992a; large rectangle) and Pacalo and Gasparik (1990; squares). The protoenstatite field at very high temperatures shown here is that of Gasparik (1990).

Using the Clapeyron equation ($\delta P/\delta T = \Delta S/\Delta V$) and the experimentally determined phase boundaries in the $MgSiO_3$ system, it is possible to calculate the entropies and enthalpies accompanying the various transitions in this system. From the equations of state determined for the orthoenstatite (Chapter 4) and low-clinoenstatite (Chapter 6; Angel and Hugh-Jones, 1994), it is seen that ΔV for this transition initially decreases with pressure, before increasing after the change at 4 GPa in compression mechanism of the orthoenstatite (see Chapters 3 and 4). Although it was not possible to establish whether the apparent step in ΔV at 4 GPa is real or merely an artefact (see Chapter 4), ΔV remains positive at all pressures, indicating that the low-clinoenstatite is stabilised with respect to orthoenstatite at high pressures. The ΔV's for the ortho/high-P clino and low/high-P clinoenstatite transitions were obtained by comparing the volumes of the high-pressure phase with both the other two phases at the same pressures. There were no systematic variations of either set with pressure; the average values are given in Table 7.1. The slopes of the phase boundaries ($\delta P/\delta T$) of the low-clino/ortho (Grover, 1972) and ortho/high-pressure clinoenstatite (Pacalo and Gasparik, 1990) transitions are also given in Table 7.1.

	Low-clino →ortho	Low →high-P clino	ortho →high-P clino
$\delta P/\delta T$ (GPa K^{-1})	0.0222[a]	0.002[b]	0.0031[c]
ΔV_0 (cm^3 mol^{-1})	+0.056 (17)	-0.838 (11)[d]	-0.900 (11)[d]
ΔS_0 (J K^{-1} mol^{-1})	+1.2[e]	-1.4[f]	-2.59[g]
ΔH_0 (kJ mol^{-1})	+1.0[e]	+4.5[f]	+3.5[g]

Table 7.1. Thermodynamic parameters for phase changes in $MgSiO_3$ enstatite. Notes: a) From Grover (1972), data between 0 and 0.4 GPa; b) Calculated from ΔS and ΔV; c) From Pacalo and Gasparik (1990); d) From EOS of high-pressure clinoenstatite with $K_{0,T}$ = 111.1 GPa (see Chapter 6); e) From ΔV and boundary of Grover (1972); f) By difference from low-clino ⇌ ortho and ortho ⇌ high-P clino; g) From ΔV and boundary of Pacalo and Gasparik (1990).

The reversals of Pacalo and Gasparik (1990) of the ortho/high-P clinoenstatite transition give $dP/dT = 0.0031$ $GPaK^{-1}$ for the boundary between them, from which ΔS is calculated from the Clapeyron equation given above, to be -2.59(5) $JK^{-1}mol^{-1}$ (note that the quoted uncertainty in this value is propagated from ΔV alone). This is in good agreement with Raman data (Chopelas and Boehler, 1992), which gives a value of $\Delta S = -2.8$ $JK^{-1}mol^{-1}$. The reversals of the low-clino- to orthoenstatite phase boundary to 0.4 GPa (Grover, 1972) give a slope of 0.0222 $GPaK^{-1}$; thus the entropy change for this transition is calculated to be $\Delta S = +1.2$ $JK^{-1}mol^{-1}$. The entropy change for the low-/high-pressure clinoenstatite transition is obtained by the difference, and is therefore -1.4 $JK^{-1}mol^{-1}$.

Rearrangement of the equation for the Gibbs free energy of the system at a phase boundary:

$$\Delta G = \Delta H - T\Delta S + P\Delta V = 0 \qquad (7.3)$$

gives an expression for the equation of the boundary in terms of the entropy (ΔS), enthalpy (ΔH) and volume change (ΔV) of the transition:

$$P = T\frac{\Delta S}{\Delta V} - \frac{\Delta H}{\Delta V} \qquad (7.4)$$

Remembering to convert the temperatures from °C to Kelvin, the enthalpies, ΔH, of each transition may be calculated by using the equations of the phase boundaries from Grover (1972) and Pacalo and Gasparik (1990), and the values of ΔV calculated from the appropriate enstatite EOS's (Chapters 4 and 6). The enthalpy change for the transition of low- to high-pressure clinoenstatite is obtained by the difference between the other two ΔH's; they are all presented in Table 7.1.

Finally, from the reversed boundaries of Grover (1972) and Pacalo and Gasparik (1990), the triple point between ortho-, low- and high-pressure clinoenstatite is calculated to lie at approximately 7.9 GPa and 920°C. Allowing further for the effect of the change in compression mechanism of the orthoenstatite at 4 GPa on its EOS (Chapters 3 and 4), and therefore the variation in the value of ΔV for the low-clino- to orthoenstatite transition at pressures above 4 GPa, the triple point may be shifted to between 7.6 GPa and 800°C, and 7.9 GPa and 920°C.

7.3 $FeSiO_3$ FERROSILITE

7.3.1 Breakdown of Orthoferrosilite to Olivine and Quartz

The position of the equilibrium boundary between orthopyroxene and the olivine-quartz assembly is very well defined. Smith (1971) experimentally determined the pressure-dependence of the reaction $(Mg,Fe)SiO_3 \rightleftharpoons (Mg,Fe)_2SiO_4 + SiO_2$, concluding that at pressures less than ~ 0.1 GPa and at a given temperature (between 600°C and 1000°C), increasing the iron content of the pyroxene destabilises it with respect to the olivine-plus-quartz assemblage; similarly at a constant temperature within this range, the more iron-rich the orthopyroxene, the more stable the olivine-plus-quartz assemblage at any given pressure in the range 0 - 1.5 GPa.

Bohlen et al. (1980) reversed the boundary between orthoferrosilite and fayalite-plus-quartz using piston-cylinder apparatus, severely constraining the boundary in P-T space (Figure 7.4); the effect of introducing 5% Mg into the system merely reduced the pressure of the boundary by approximately 0.1 GPa at all temperatures analysed. The boundary was also found (Bohlen et al., 1980) to change its slope from $\delta P/\delta T = 1x10^{-3}$ GPa/°C to $\delta P/\delta T = 1.5x10^{-3}$ GPa/°C where it intersects the α-β quartz transition (Figure 7.4).

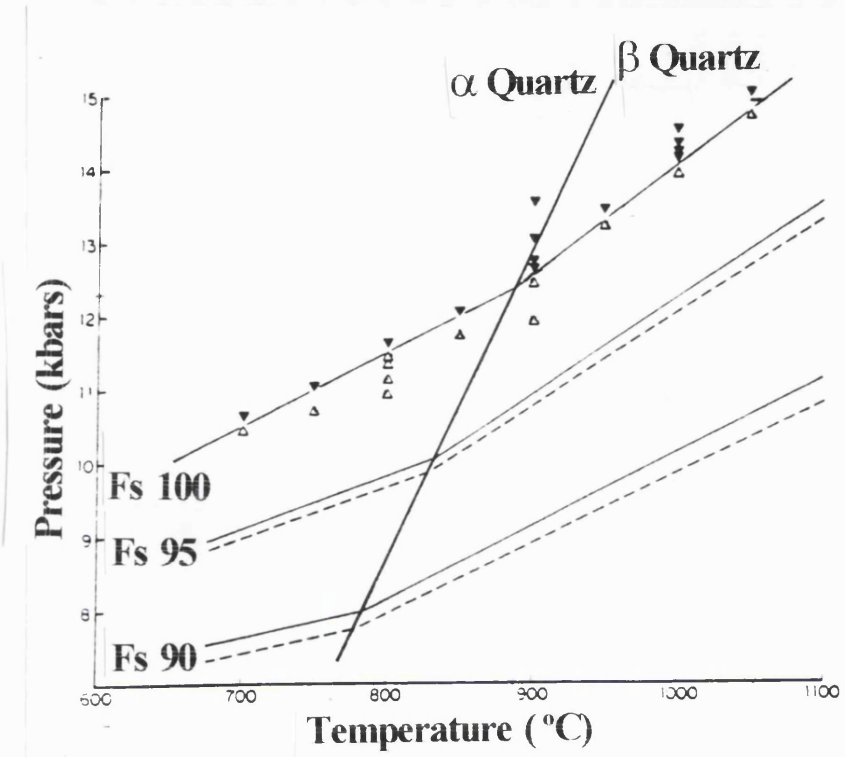

Figure 7.4: The well-constrained boundary between ferrosilite and fayalite + quartz, determined by Bohlen et al., 1980; showing the effect of introducing 5% or 10% Mg^{2+} into the cation sites of the pyroxene. Note the change in slope of the boundary as it intersects the α-β quartz transition.

7.3.2 Low-Clino to Orthoferrosilite Transition

The first syntheses of both the monoclinic and orthorhombic polymorphs of $FeSiO_3$ ferrosilite were achieved by Lindsley et al. (1964) using piston-cylinder apparatus. Although ferrosilite decomposes to fayalite (Fe_2SiO_4) and quartz (SiO_2) at pressures less than ~ 1 GPa (depending on the ambient temperature; see above), in 1965, he successfully reversed a phase boundary between orthoferrosilite and clinoferrosilite at pressures below ~ 4 GPa and a temperature of approximately 800°C, thus producing a phase boundary essentially independent of pressure (Figure 7.5). This phase boundary is generally accepted to be the true boundary between orthoferrosilite and low-clinoferrosilite, and is described by the equation:

$$T\ (°C) = 785 + 8.75\ P\ (GPa) \qquad (7.5)$$

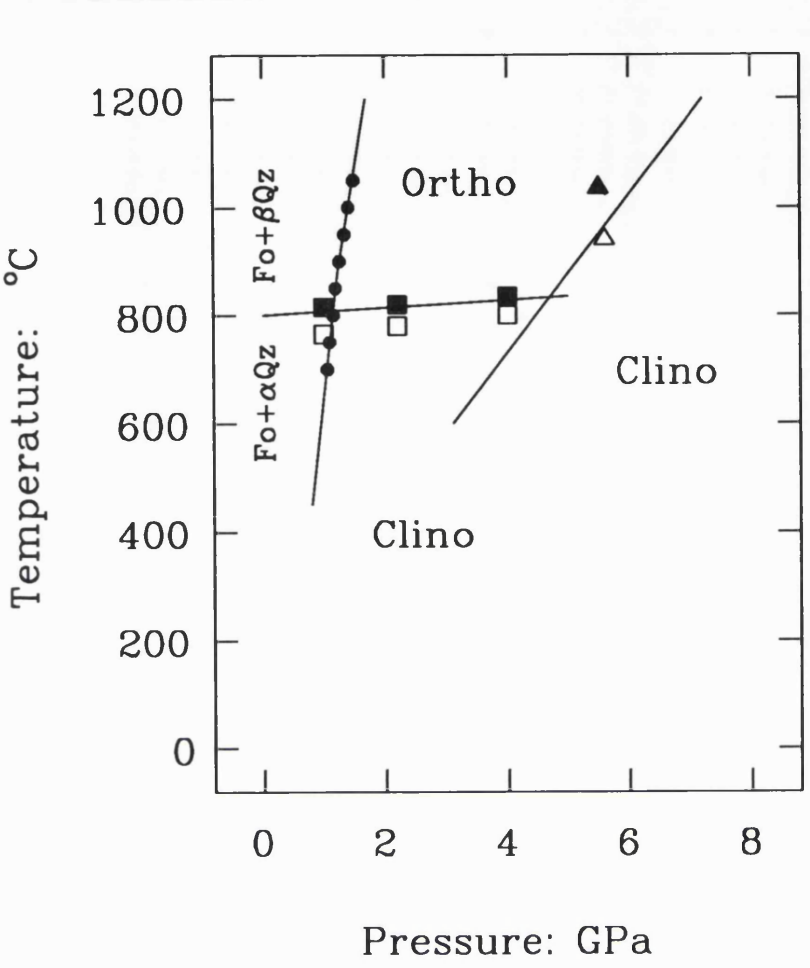

Figure 7.5: The conflicting ortho/clino phase boundaries of $FeSiO_3$ ferrosilite, determined by Lindsley (1965; squares) and Akimoto et al. (1965; triangles). The boundary and reversals (circles) of the transition between ferrosilite and the fayalite + quartz assemblage of Bohlen et al. (1980) are also shown.

Burnham (1965) measured the unit cell parameters for the clinoferrosilite and orthoferrosilite structures, deducing the space groups to be $P2_1/c$ and Pbca respectively, ie., space groups identical to those of the then-known enstatite polymorphs. Detailed structure refinements of these two polymorphs of $FeSiO_3$ led Burnham (1966b) to propose that since the structures differed predominantly in the stacking sequence of alternating layers of silicate chains and octahedral slabs parallel to a^*, the orthoferrosilite unit cells are built up of "double monoclinic units" related exactly by the *b*-glide, with a slight spatial mismatch due to structural adjustments associated with this glide. This structural relationship is identical to that previously observed for the $MgSiO_3$ polymorphs (eg. Ito, 1935; Atlas 1952).

7.3.3 Ortho- to High-Pressure Clinoferrosilite Transition

In 1965, Akimoto et al. independently reversed an ortho- to clinoferrosilite phase boundary in the range ~ 3-7 GPa and 600-1100°C using multi-anvil apparatus, also observing the breakdown of ferrosilite to fayalite plus quartz at pressures below ~ 1-2 GPa in the temperature range 600°C to 1200°C (Figure 7.4). Problems arising from the large discrepancy between the stability fields of Lindsley's (1965) and Akimoto et al.'s (1965) clinoferrosilites (Figure 7.5) led Lindsley and Munoz (1969) to suggest that either the clinoferrosilite found at low temperatures was stabilised by shearing stresses or that two distinct clinoferrosilite stability fields could exist being separated by the orthoferrosilite field. They also suggested that small amounts of water contained within the orthoferrosilite structure could stabilise it, although their data showed no evidence of this.

Preliminary experiments using multi-anvil apparatus (Woodland, pers. comm.) have confirmed the position in P-T space of Akimoto et al.'s (1965) ortho- to high-pressure clinoferrosilite phase boundary (determined from synthesis runs and a single experimental reversal), and have provisionally determined the equation of the boundary to be:

$$T\ (°C) = -158 + 203\ P\ (GPa) \qquad (7.6)$$

Note that upon decompression the high-pressure clinoferrosilite formed during the above experiments transforms displacively to the low-clinoferrosilite phase below about 1.5 GPa (Chapter 5).

7.3.4 Ortho- to High-Temperature Clinoferrosilite Transition

The existence of a monoclinic phase of ferrosilite with space group C2/c stable above ~ 1025°C (at ambient pressure) was established by Sueno et al. (1984), who determined the structure of this clinoferrosilite to be analogous to the high temperature $MgSiO_3$ clinoenstatite of Perotta and Stephenson (1965). This ortho- to high-temperature clinoferrosilite transition was found to be rapid, reversible and topotactic in character, with relative orientation of the polymorphs determined by X-ray precession photography to be a^*_{ortho}// a^*_{clino} and c_{ortho}// c_{clino} (Sueno and Kimata, 1981). In Chapter 6 it was demonstrated that the structures of the high-temperature and high-pressure C2/c clinoferrosilites are significantly different. By reinterpretation of his earlier data for the phase relations of $FeSiO_3$ at high pressures and temperatures, Lindsley (1980, 1981) established a true stability field of this high-temperature C2/c phase at high temperatures and pressures above 1 atm.; this is illustrated by the dotted line in Figure 7.6.

7.3.5 Low-Clino to High-Pressure Clinoferrosilite Transition

In order to resolve the differences between the ortho/clino boundaries of Lindsley (1965) and Akimoto et al. (1965), an in-situ high-pressure single-crystal X-ray diffraction study of low-clinoferrosilite (with space group $P2_1/c$) was undertaken (Chapter 5) to discover whether a structurally distinct and non-quenchable phase of clinoferrosilite existed at high pressures, as already demonstrated to exist in the $MgSiO_3$ system at ~ 8 GPa (Angel et al., 1992a). The phase boundary between the low-clinoferrosilite and a new high-pressure clinoferrosilite phase (with space group C2/c) was reversed at room temperature between 1.48 and 1.75 GPa, demonstrating that the C2/c polymorph is indeed the stable phase of $FeSiO_3$ at high pressures, and is the iron analogue of the high-pressure C2/c enstatite phase characterised by Angel et al. (1992a; see Chapters 5 and 6 for structural details). Since the transformation is non-quenchable, with the C2/c polymorph reverting to the $P2_1/c$ low-clinoferrosilite form on pressure release, the previous experimental results may now be reconciled:

Lindsley's experiments are the reversals of the $P2_1/c$ to ortho phase boundary, while those of Akimoto et al. approximate the position of a phase boundary between ortho- and C2/c clinoferrosilite, the products from the latter side of the boundary quenching to low-clinoferrosilite on pressure release (Figure 7.6).

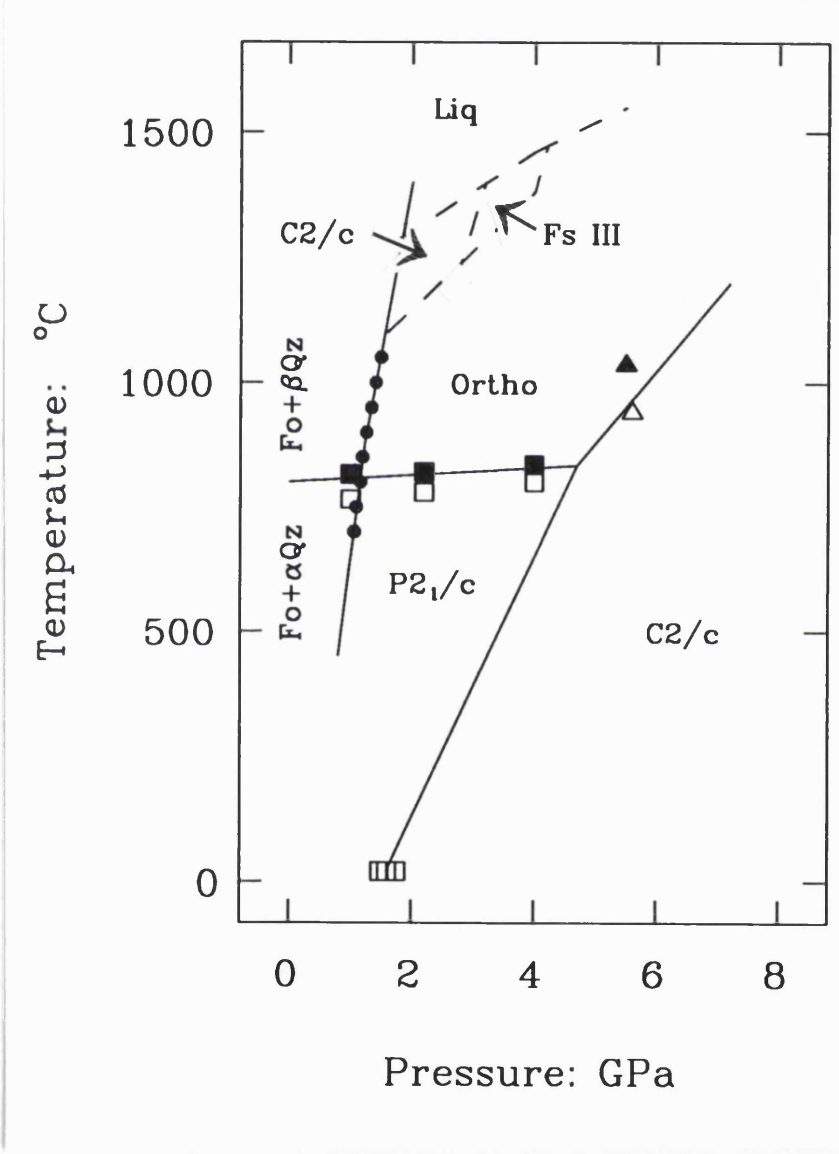

Figure 7.6: The equilibrium phase diagram for $FeSiO_3$ ferrosilite, showing the experimental reversals of Lindsley (1965; squares), Akimoto et al. (1965; triangles), and this work (rectangle; see Chapter 5). The transition from orthoferrosilite to high-temperature clinoferrosilite (Lindsley, 1980, 1981) is shown as a dotted line, and the stability field of ferrosilite III (determined by Lindsley, 1980, 1981) is also shown.

7.3.6 Other $FeSiO_3$ phases

By analogy with $MgSiO_3$ protoenstatite, Lindsley (1965) originally thought that the low pressure ($P < 4$ GPa) stability fields of ferrosilite III and high-symmetry C2/c clinoferrosilite (Figure 7.6) were inversion products of a "proto?-ferrosilite" phase. However, while establishing a true stability field for these two phases at high temperatures and pressures above ~1 GPa (1980, 1981), he determined that there is no stability field for an $FeSiO_3$ "proto?-ferrosilite" phase at any pressure or temperature (Figure 7.6).

Having indexed the X-ray diffraction pattern on precession photographs of the ferrosilite III phase on a triclinic cell, and by comparison of the unit cell parameters with those of the pyroxenoids rhodonite and pyroxmangite, Burnham (1965) determined its structure to be a pyroxenoid with a chain repeat of nine tetrahedra (according to the nomenclature of Liebau (1962), this is also known as a *Neunerketten* pyroxenoid).

7.3.7 $FeSiO_3$ Phase Diagram and Thermodynamic Calculations

The overall topology of the phase diagram of $FeSiO_3$ (ignoring the low-pressure breakdown to fayalite plus quartz (Figure 7.4) and the stability field of ferrosilite III (Lindsley, 1980)) that can be deduced from these experimental runs (details in Chapter 5) and those of Lindsley (1965) and Woodland (pers. comm.) is shown in Figure 7.6. From these latter two boundaries, the triple point is calculated to lie at approximately 4.85 GPa and 827°C. Note that although the topology of the $FeSiO_3$ phase diagram is very similar to that of $MgSiO_3$ (Angel et al., 1992a), the $FeSiO_3$ phase boundaries and the triple point are shifted to somewhat lower pressures.

Following the method outlined above in Section 7.2.7 for the $MgSiO_3$ phase boundaries, it is possible to calculate both ΔS and ΔH for the structural phase transitions occurring in the $FeSiO_3$ system. From the equations describing the low-clino/orthoferrosilite (Equation 7.5; Lindsley, 1965) and ortho-/high-P clinoferrosilite transitions (Equation 7.6; Woodland, pers. comm.), the slopes of the phase boundaries, $\delta P/\delta T$, are 0.1143 $GPaK^{-1}$ and 0.0049 $GPaK^{-1}$ respectively. The volume changes for these transitions are calculated from the EOS's of the $FeSiO_3$ polymorphs (Chapters 4 and 6) to be ΔV = +0.019(6) cm^3mol^{-1} for the low-clino- to orthoferrosilite transition, and ΔV = -0.937(6) cm^3mol^{-1} for the transition of orthoferrosilite to high-P clinoferrosilite (Table 7.2).

From these values, and by using the Clapeyron equation ($\delta P/\delta T = \Delta S/\Delta V$), the entropies of these transformations are calculated to be ΔS = +2.2(6) $JK^{-1}mol^{-1}$ and ΔS = -4.59(3) $JK^{-1}mol^{-1}$ respectively. Thus the entropy change for the low- to high-pressure clinoferrosilite transition is ΔS = -2.4(6) $JK^{-1}mol^{-1}$ (Table 7.2). Back calculation to the slope of the phase boundary gives $\delta P/\delta T$ = 0.0026(4) $GPaK^{-1}$ for the transition of low- to high-pressure clinoferrosilite. These values of ΔS are in good agreement with those determined for the phase relations in $MgSiO_3$, being of both the same signs and similar magnitudes.

	Low-clino →ortho	Low →high-P clino	ortho →high-P clino
$\delta P/\delta T$ GPa K^{-1}	0.1143[a]	0.0026[b]	0.0049[c]
ΔV_0 cm^3 mol^{-1}	+0.019 (6)[d]	- 0.937 (6)[d]	- 0.918 (6)
ΔS_0 J $K^{-1}mol^{-1}$	+2.2(6)[e]	-2.4(6)[f]	-4.59(3)[g]
ΔH_0 kJ mol^{-1}	+2.3(6)[e]	+0.8(2)[h]	- 1.5(6)[j]

Table 7.2 Thermodynamic parameters for phase changes in $FeSiO_3$ ferrosilite. Notes: a) From Lindsley (1965); b) Calculated from ΔS and ΔV; c) From Woodland (pers. comm.); d) Using EOS of low-pressure clinoferrosilite with K_0' = 4.3 (see Chapter 6); e) From ΔV and boundary of Lindsley (1965); f) By difference from low-clino ⇌ ortho and ortho ⇌ high-P clino; g) From ΔV and boundary of Woodland (pers. comm.). h) From $P2_1/c \rightarrow C2/c$ reversal (Chapter 5) and calculated $\delta P/\delta T$; j) By difference low-clino ⇌ ortho and low-clino ⇌ high-P clino.

Since the pressure of the low- to high-P clinoferrosilite transition is well constrained with little hysteresis (see Chapter 5), and the boundary of Lindsley (1965) has been reversed at several pressures and temperatures, the calculations of ΔH for the phase boundaries in the $FeSiO_3$ system have been calculated in a somewhat different manner to those of $MgSiO_3$.

Using the experimentally determined phase boundary of Lindsley (1965) and the thermodynamic equation (Equation 7.4) yields a value of $\Delta H = +2.3(6)$ kJmol^{-1} for the transition of low-clino to orthoferrosilite. Similarly, ΔH for the low-clino- to high-pressure clinoferrosilite transition may be calculated from the reversal data presented in Chapter 5 to be $+0.8(2)$ kJmol^{-1}. ΔH for the ortho- to high-pressure clinoferrosilite transformation is calculated from the difference between the two, and is thus $\Delta H = -1.5(6)$ kJmol^{-1}. These thermodynamic quantities for the phase transitions in the $FeSiO_3$ system are summarised in Table 7.2.

It is interesting to note that whilst the signs of the enthalpy changes for the low-clino- to orthoferrosilite and low-clino- to high-pressure clinoferrosilite transitions are the same as those of the corresponding transitions in the $MgSiO_3$ system, those of the ortho- to high-pressure clinopyroxene transformations are different: ΔH for the transition in $FeSiO_3$ is negative in sign (and therefore the transition is exothermic under these conditions), and in $MgSiO_3$ is positive (and thus endothermic). However, the relative differences in magnitude of the ΔH's between the three transformations are identical.

Finally, the equation describing the boundary between the two clinoferrosilite phases at high pressures and moderate temperatures is calculated to be:

$$P\ (GPa) = 0.0026(4)\ T\ (^{o}C) + 0.8(2) \qquad (7.7)$$

7.3.8 Metastable Phase Relations of $FeSiO_3$ Clinoferrosilite

Since the structures of the C2/c phases stable at high temperatures and high pressures respectively are substantially different (Chapter 6), and since the structural changes that must occur during a transition between such high-T and high-P C2/c phases are greater than any observed on heating or compression of a single clinopyroxene phase (Chapter 6), it is reasonable to expect a "crossover" transition between the two isosymmetric polymorphs at extremely high temperatures and pressures. This transition may, in fact, fall either in the equilibrium liquid field, or the orthopyroxene field. However, it is anticipated that the metastable phase diagram for the $FeSiO_3$ clinopyroxene polymorphs has the topology shown in Figure 7.7. The same topology is expected for the $MgSiO_3$ metastable phase relations (ignoring the stability field of protoenstatite at low pressures and very high temperatures), although the boundaries will be shifted to relatively higher pressures.

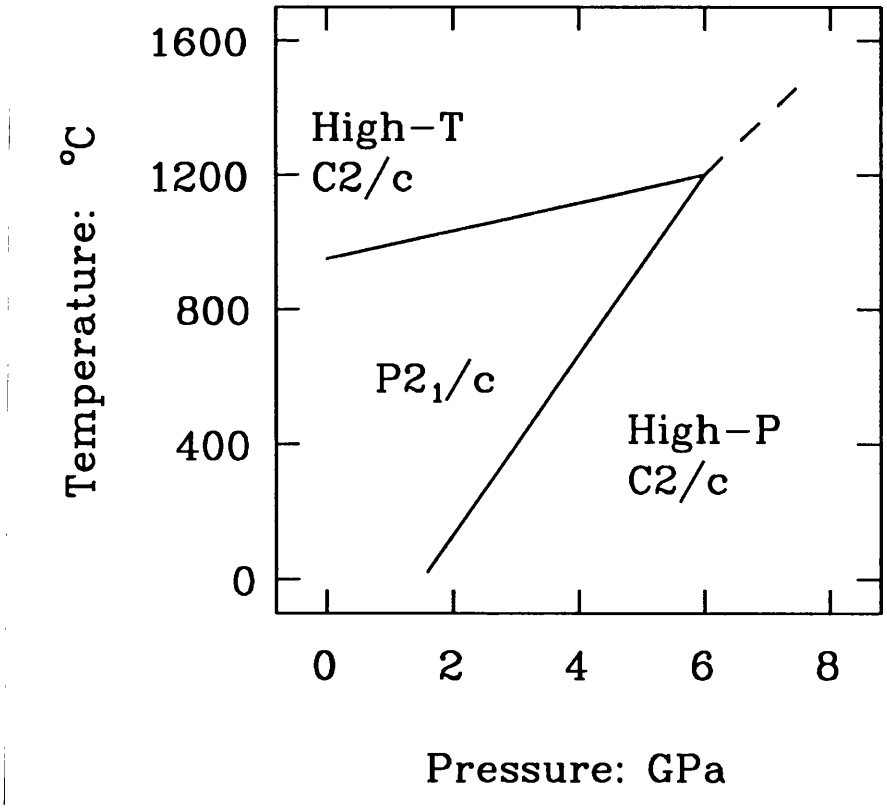

Figure 7.7: The proposed metastable phase diagram for the $FeSiO_3$ system, showing the inversion of low- to high- clinopyroxenes at both high pressures and temperatures. The possible position of the isosymmetric "crossover" transition between these C2/c high-clinoferrosilite phases is shown as a dotted line.

Evidence of several further "isosymmetric" or "crossover" phase transitions occurring in ceramics and other minerals has recently emerged. Amongst these are the first-order phase transition in potassium titanyl phosphate (KTP; Allan and Nelmes, 1992) at 5.5 GPa in the space group $Pna2_1$, where the major structural changes occurring during the transition include tilting of the PO_4 tetrahedra relative to the TiO_6 octahedra and displacements of the large potassium atoms by some 0.5Å along the *c*-axis, and also the $I\bar{1}$-$I\bar{1}$ transition in anorthite which occurs at high temperatures and $\sim$ 1.8 GPa (Hackwell, 1994; Hackwell and Angel, 1995). The latter "crossover" transition is characterised by a change in the conformation of the silicate framework of the feldspar, and the associated switching from a single Ca^{2+}-containing cation site to a split one as the high-temperature phase is formed.

The structural changes which would be involved in the transition from high-temperature C2/c clinopyroxene to high-pressure C2/c clinopyroxene are similarly well-defined; such changes involve extreme amounts of kinking (ie., more than 30°) of the silicate chains, which in turn cause the M2 sites to become significantly smaller and more regular in the high-P polymorph (ie., their coordination decreases from 8-fold in the high temperature polymorph to 6-fold in the high-pressure C2/c structure). Although the structures of the two C2/c phases have not been determined experimentally at simultaneous high-pressure and high-temperature conditions, it is expected that the change in the degree of kinking of the tetrahedral chains will cause approximately an 8% volume decrease, with an associated $\sim$ 7° change in the β angle of the monoclinic unit cell, during the isosymmetric transformation.

7.4 $(Mg,Fe)SiO_3$ PYROXENES OF INTERMEDIATE COMPOSITIONS

7.4.1 Ordering of Mg^{2+} and Fe^{2+} over the M1 and M2 Cation Sites

Because the $MgSiO_3$ and $FeSiO_3$ end-members of the $(Mg,Fe)SiO_3$ solid-solution do not exist in nature, there has also been a considerable amount of research in the last thirty years about pyroxenes of intermediate compositions along the enstatite-ferrosilite join. For such intermediate compositions, there must be at least two (and significantly more in natural pyroxenes) different cations in octahedral coordination, and therefore there must be a certain degree of order or disorder of these cations over the M1 and M2 sites at any given temperature or pressure. Ghose (1965) refined the structure of a natural orthopyroxene with approximate composition $Mg_{0.452}Fe_{0.54}SiO_3$ which showed a high degree of order of the Mg^{2+} and Fe^{2+} cations over the octahedral sites, with the M1 sites containing ~ 85% Mg^{2+} and ~ 15% Fe^{2+}, and the M2 sites containing ~ 10% Mg^{2+} and ~ 90% Fe^{2+}. Similar structure refinements (Kosoi et al., 1974) of two natural orthopyroxenes of approximate compositions $Mg_{0.56}Fe_{0.44}SiO_3$ and $Mg_{0.695}Fe_{0.20}Al_{0.11}(Si_{0.88}Al_{0.12})O_3$ also showed strong preferences of the Mg^{2+} (and Al^{3+}) for the M1 site, and the Fe^{2+} (and Ca^{2+} in other natural pyroxenes) for the M2 site.

This preference of Mg^{2+} for the M1 cation site has been confirmed in several synthetic $(Mg,Fe)SiO_3$ orthopyroxenes (eg. Cameron and Papike, 1980; Domeneghetti and Steffen, 1992). It is interesting to note that while the distortion of the M1 site does not significantly increase with increasing Fe^{2+} content, the corresponding distortion of the M2 site does increase considerably (Chapter 3). It is possible that changes in the Mg^{2+}/Fe^{2+} ordering scheme of orthopyroxenes of constant composition may slightly move the phase boundaries in P-T space, but since ordering is a non-convergent process (ie, the degree of order or disorder of the pyroxene does not change its symmetry), the symmetry changes involved during structural phase transitions will remain unchanged. Finally, it is important to note that although I will refer to the phase *boundaries* between pyroxenes of intermediate compositions throughout this section, these boundaries are really two-phase loops spread over a

finite pressure and temperature interval.

Recent Mössbauer and microprobe experiments (Woodland et al., unpublished data) to determine the relative occupancies of Fe^{2+} in the M1 and M2 sites of synthetic clinopyroxenes along the $(Mg,Fe)SiO_3$ join suggest that, at a given temperature, the high-pressure C2/c clinopyroxene phase is more ordered than orthopyroxene. Since the M1 sites in ortho- and high-pressure clinopyroxene are virtually identical in both size and degree of distortion, and the M2 sites are of similar size (see Chapters 5 and 6), the more ordered character of the high-pressure clinopyroxene is likely to be due to the somewhat less distorted nature of its M2 sites.

7.4.2 Low-Clino to Orthopyroxene Transition

Lindsley (1965) experimentally confirmed the low temperature stability field of $(Mg,Fe)SiO_3$ clinohypersthene, and observed the inversion of a natural orthopyroxene of approximate composition $Mg_{0.6}Fe_{0.4}SiO_3$ to clinopyroxene at 2 GPa and temperatures of up to 900°C, suggesting that the monoclinic to orthorhombic inversion occurred between 600°C and 900°C. Similarly, Schwab (1969) showed that the monoclinic polymorph of an intermediate pyroxene with composition $Mg_{0.75}Fe_{0.25}SiO_3$ was stable at temperatures below about 500°C, above which an orthorhombic phase was formed; this orthopyroxene was found to be stable up to the melting point at $\sim$1420°C.

Brown (1968) studied the ortho-clino inversion in natural pigeonitic pyroxenes at high temperatures, analysing the products of his experiments using optical methods as well as X-ray powder diffraction; he reported a stability field of a clinopyroxene above $\sim$1000°C. He also determined that the temperature of this orthorhombic to monoclinic transition increases with pressure, indicating a positive $\delta P/\delta T$ of the phase boundary for pyroxenes of intermediate composition along the $(Mg,Fe)SiO_3$ join as well as for the end-members (eg, Boyd and England, 1965; Grover, 1972; Lindsley, 1965). However, since high-clinopyroxene is now known to quench to the lower

symmetry form on rapid cooling (eg, Morimoto and Tokonami, 1969), this stability field of clinopyroxene at high temperatures may well represent that of high-clinopyroxene rather than (as Brown assumed) the low-clinopyroxene.

7.4.3 Ortho- to High-Temperature Clinopyroxene Transition

The earliest systematic heating experiments of $(Mg,Fe)SiO_3$ pyroxenes are those of Bowen and Schairer (1935), who discovered a time-dependent transition from orthorhombic to monoclinic structures on heating above about 1000°C, with the transition temperature depending on the relative iron content of the pyroxene. Further heating experiments on an iron-rich orthopyroxene (Smyth, 1973) demonstrated that the orthorhombic structure is stable up to 950°C, where it transforms to high-temperature clinopyroxene. Having confirmed the space group of orthopyroxene as Pbca, he showed that as a result of increasing the temperature and due the effect of differing rates of expansion of the M-O and T-O bonds, the tetrahedral silicate chains straighten, increasing the coordination of the M2 site to 7-fold at 850°C.

The presence of Fe^{2+} widens the orthopyroxene field to both higher and lower temperatures, thus increasing the thermal stability of the orthopyroxene relative to the high temperature clino- and protoenstatite phases, (Schwab, 1969). However, raising the pressure has the opposite effect (ie, increasing the pressure stabilises clinopyroxene structures (Schwab, 1969)). Ernst and Schwab (1970) also determined that the maximum stability of the orthorhombic phase (with symmetry Pbca) at one atmosphere pressure occurs for an $(Mg,Fe)SiO_3$ pyroxene containing about 25 mol% $FeSiO_3$.

7.4.4 Low-Clino to High-Temperature Clinopyroxene Transition

In 1972, Brown et al. determined the structure of a C2/c clinopyroxene with approximate composition $Mg_{0.65}Fe_{0.30}Ca_{0.05}SiO_3$ formed by heating crystals of the low-clinopyroxene phase. Similarly, Smyth (1974b) transformed crystals of a low-clinopyroxene with approximate composition $Mg_{0.31}Fe_{0.67}Ca_{0.015}SiO_3$ to high-clinopyroxene at ~725°C, noting that the transition was first order in character. Several

subsequent authors (eg, Shimobayashi and Kitamura, 1991) have confirmed the existence of this low- to high-temperature clinopyroxene transition, and determined the structural changes associated with it; these changes are very similar for pyroxenes of both natural and synthetic compositions along or near the $(Mg,Fe)SiO_3$ join.

7.4.5 Low-clino to High-Pressure Clinopyroxene Transition

Preliminary experiments using Raman Spectroscopy (Ross et al., pers. comm.) suggest that synthetic $P2_1/c$ clinopyroxenes of *all* compositions along the $(Mg,Fe)SiO_3$ join undergo a displacive phase transitoin to the high-pressure C2/c structure previously characterised for the $MgSiO_3$ and $FeSiO_3$ end-members (Angel et al., 1992a; Chapter 5). Whilst the pressure of such a transition varies essentially linearly with increasing magnesium content, from ~ 1.6 GPa for pure $FeSiO_3$ (Chapter 5) to ~8 GPa for pure $MgSiO_3$ (Angel et al., 1992a), it is expected that the structural changes occurring during the transition do not change significantly with compositional change. Finally, it is interesting to note that although there is very little hysteresis for the transition of low- to high-pressure clinopyroxenes containing more than ~85% Fe^{2+}, clinopyroxenes containing less Fe^{2+} than this tend to show greater hysteresis effects.

7.4.6 $(Mg,Fe)SiO_3$ Phase Relations

The relative pressures and temperatures of the various transformations between the ortho- and clino-pyroxene phases are highly dependent on both the relative Fe^{2+}- and Ca^{2+}-contents of the pyroxene. For example, while the pressure of the low- to high-pressure clinopyroxene phase transition decreases from ~ 8 GPa ($MgSiO_3$; Angel et al., 1992a) to ~ 1.6 GPa ($FeSiO_3$; see Chapter 5) with increasing Fe^{2+}-content, the temperature of the metastable low- to high-temperature clinopyroxene transformation ranges from > 1000°C for Mg^{2+}-rich pyroxenes to ~ 500°C for Fe^{2+}-rich ones (Prewitt et al., 1971). $(Mg,Fe)SiO_3$ pyroxenes are also able (Ohashi et al., 1975) to accommodate up to 15 mol% Ca^{2+} in their cation sites before their structures and properties are dramatically altered. In their study, Ohashi et al. (1975) found that clinopyroxenes with symmetry $P2_1/c$ transformed to clinopyroxenes with space group

C2/c when the Ca^{2+}-content was greater than 15%, since the relative increase in volume of the M2 sites at higher Ca^{2+}-concentrations maintained the more symmetric space group even at ambient conditions.

Kuno (1966) proposed a hypothetical phase diagram (Figure 7.8) for the Ca^{2+}-poor $(Mg,Fe)SiO_3$ pyroxene solid solution from experimental equilibrium data available at the time, distinguishing two types of clinopyroxene with stability fields at respectively higher and lower temperatures than the orthopyroxene field (cf. Lindsley and Munoz, 1969). Figure 7.8 shows this proposed phase diagram, with the more recent experimental data points for comparison. The agreement between the two is extremely good, with Kuno's (1966) estimated temperature of any given transformation being within ~ 50°C of the experimental data; ie., less than two estimated standard deviations (*esd*'s) away from the experimentally determined values, using the average *esd* from all the available published data.

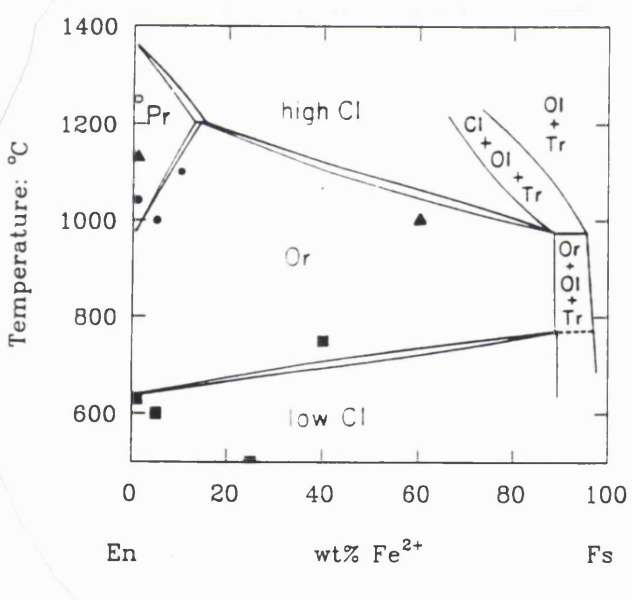

Figure 7.8: The phase diagram of $(Mg,Fe)SiO_3$ pyroxenes across the join, proposed by Kuno (1966), also showing the experimental data points collected since then; filled circles represent the ortho- to protopyroxene transition (Sadanaga et al., 1969; Smyth, 1974a; Murakami et al., 1982), squares the low-clino to orthopyroxene transition (Schwab, 1969; Smyth, 1974a; Lindsley, 1965), triangles the ortho- to high-temperature clinopyroxene transformation (Brown, 1968; Schrader et al., 1990) and the open circle the high-clino to protopyroxene transition (Schwab, 1969). The metastable reversals of the low- to high-temperature clinopyroxene boundary are not shown.

7.5 SUMMARY

The relative phase behaviour of both synthetic and natural Ca^{2+}-poor pyroxenes along or near the $(Mg,Fe)SiO_3$ solid solution join is very similar. The stable phase at ambient temperatures and pressures is the low-clinopyroxene phase with space group $P2_1/c$. At modest pressures and temperatures in the range 650 - 800°C depending on the iron-content of the pyroxene, there is a first order phase transition to the orthorhombic phase with space group Pbca. At ambient temperatures and high pressures in the range ~ 1.6 GPa to ~ 8.0 GPa (again depending on the relative Fe^{2+}-content of the pyroxene), the low-clinopyroxenes transform reversibly to a non-quenchable higher symmetry clinopyroxene, with space group C2/c. This high-pressure C2/c polymorph is stable for clinopyroxenes of all intermediate compositions along the $(Mg,Fe)SiO_3$ join (observed at ambient temperatures by infrared and Raman experiments; Sowerby and Ross, pers. comm.).

For pyroxenes containing more than ~ 85% Mg^{2+}, the stable phase below ~1 GPa and very high temperatures is protopyroxene, which has space group Pbcn and a triangular stability field in P-T space. It undergoes a highly time-dependent reversion to either ortho- or clinopyroxene upon cooling. Orthopyroxenes with more than 15% Fe^{2+} in their cation sites transform directly to a high symmetry C2/c clinopyroxene phase at temperatures in the range ~1000°C - 1200°C, rather than to a protopyroxene structure. Such a C2/c phase stable at high temperatures has a structure significantly different to that of the C2/c structure found at high pressures; there is likely to be a kind of "crossover" transition between the two polymorphs at extreme pressures and temperatures, involving significant kinking of the tetrahedral silicate chains and changes in the sizes and distortions of the M2 cation sites (see also Chapter 6).

The topology of the phase diagrams of both synthetic $MgSiO_3$ and $FeSiO_3$ are therefore very similar (see Figures 7.3 and 7.6), although the phase boundaries and triple point of the $FeSiO_3$ end-member lie at relatively lower pressures than those in

the $MgSiO_3$ system. Since all the available phase relations determined for pyroxenes of intermediate compositions are similar to those of the end-member phases, it is generally assumed that the phase diagrams for *all* Ca^{2+}-poor pyroxenes are essentially identical. The proposed phase diagram of Kuno (1966) appears to represent the high-temperature behaviour of Ca^{2+}-poor synthetic and natural pyroxenes across the $(Mg,Fe)SiO_3$ join very successfully, with the recent experimental data points for the relevant polymorphic phase transitions falling very close to his assumed boundaries.

Thermodynamic calculations for the transitions between ortho-, low- and high-pressure clinopyroxenes of both $MgSiO_3$ and $FeSiO_3$ compositions show that the values of ΔS and ΔH for a given transition in either end-member phase are of very similar magnitude. The ΔS calculated in this way for the ortho- to high-pressure C2/c $MgSiO_3$ clinoenstatite transition is also in good agreement with the ΔS of 2.8 $JK^{-1}mol^{-1}$ determined by Raman experiments (Chopelas and Boehler, 1992).

CHAPTER 8

CONCLUSIONS

Using single-crystal X-ray diffraction techniques with a diamond anvil cell, it has been possible to determine the compressional behaviour of both natural and synthetic ortho- and clinopyroxenes along or near the $MgSiO_3$ - $FeSiO_3$ join with a high degree of precision. There are first order phase transitions between low- and high-pressure clinopyroxene structures at pressures in the range ~ 1.8 to ~ 8 GPa (depending on the iron content of the pyroxene), and between Fe^{2+}-rich ortho- and high-pressure clinopyroxene structures above ~ 4.6 GPa. Note that whilst the low- to high-pressure clinopyroxene transition is an equilibrium transition, the ortho- to high-pressure clinopyroxene transition is metastable at ambient temperature.

The individual compression mechanisms operating above and below ~ 3.5 - 4 GPa in all synthetic orthopyroxenes along the $MgSiO_3$ - $FeSiO_3$ join are virtually identical, with the low-pressure regime being characterised simply by changes in the conformations of chains of essentially incompressible SiO_4 tetrahedra. Above this pressure, the Si-O bonds shorten in a regular way with no angular deformation of the tetrahedra. Associated with these changes, are changes in the degrees of kinking of the silicate chains and the amount of tilting of their bases from the (100) plane. On the other hand, compression of the M1 and M2 octahedra occurs steadily over the whole pressure range studied, with no observed discontinuity at any pressure. This change in compression mechanism occurring in the synthetic orthopyroxenes between ~ 3.5 and ~ 4 GPa causes a marked break in their equations of state (EOS's).

It is likely that comparable changes in compression mechanisms occur in other silicate minerals, but have not yet been identified due to insufficient data coverage or insufficient precision in high-pressure structure refinements. In addition, these kinds of changes may only occur in structures in which there are sufficient degrees of internal freedom to allow smooth compression of the cation polyhedra (semi-) independently of the discontinuous changes in the compressibilities of the silicate

tetrahedra. However, further high-precision structural analyses of other mantle minerals (such as olivines and garnets) at high pressures will be necessary to identify the possibility of such changes in compression mechanism being general phenomena.

Most mantle minerals have a K_0' in the range $4 < K_0' < 6$ (eg., Dietrich and Arndt, 1982; Kudoh and Takeuchi, 1985; Hazen and Finger, 1989; Hackwell, 1994). However, EOS's determined from the high-pressure X-ray diffraction data for *all* orthopyroxenes on or near the $(Mg,Fe)SiO_3$ join exhibit anomalously high values of K_0' in their low pressure compression regimes (ie., $P < 4$ GPa). This result is independent of the form chosen for the EOS. Since this high K_0' has also been observed in ultrasonic experiments using natural Ca^{2+}-poor orthopyroxenes (eg., Frisillo and Barsch, 1972; Webb and Jackson, 1993), it must therefore describe the true EOS behaviour of orthopyroxenes at low pressures, and cannot merely be an artefact of the chosen experimental technique. Structural data collected for such synthetic and natural Ca^{2+}-poor orthopyroxenes have demonstrated that the high K_0' at low pressures is due to the initial rapid compression of the long M2-O3 bonds followed by their stiffening at higher pressures. At pressures above ~ 3.5 - 4 GPa these K_0's decrease to more "normal" ones (generally between ~ 4 and ~ 6) as the M2-O3 bonds compress at a similar rate to the remaining M2-O bonds.

While the addition of Fe^{2+} to the octahedral sites of $MgSiO_3$ orthopyroxene has very little effect on either the bulk modulus, $K_{0,T}$, or its pressure derivative, K_0', addition of even very small amounts of Ca^{2+} (and also Al^{3+} and other natural impurities) to the orthopyroxene causes the bulk modulus to increase by some ~ 14%, and its pressure derivative to decrease by almost 35%. There is no evidence of any change in compression mechanism occurring in natural orthopyroxene below 6 GPa, with the silicate tetrahedra being incompressible to this pressure. This continuous behaviour of the Ca^{2+}-containing natural orthopyroxenes is explained in terms of the behaviour of the M2 cation site, where even small amounts (ie., less than 1%) of Ca^{2+} substitution cause the connectivity of the structure to be "braced" by a few stiffer M2 octahedra. As a result there is little change in the degree of kinking and tilting of either of the symmetrically distinct silicate chains, and the compression limit observed

in the Ca^{2+}-free orthopyroxenes at ~ 3.5 - 4 GPa (responsible for initiating the change in compression mechanism) is never reached in the natural samples.

Additional experiments are now needed to determine whether this change in the compressional properties of Ca^{2+}-containing $(Mg,Fe)SiO_3$ orthopyroxenes is solely due to the presence of calcium, as suggested by Shankland (1972), or whether small amounts of other dopants with similarly large ionic radii have the same effect of "bracing" the structure, and thus inhibiting changes in the compression mechanisms of the orthopyroxenes.

In either case, calculation of the volume and density differences between the synthetic and natural Ca^{2+}-containing orthopyroxenes has shown that the two compositions behave increasingly differently with increasing depth within the Earth's upper mantle; pure $MgSiO_3$ orthoenstatite is thus not a good representation of the pyroxene component at depth. In order to model the mineralogical and physical properties of the upper part of the upper mantle (ie., the region of stability of orthopyroxene rather than high-pressure C2/c clinopyroxene) of the Earth with more accuracy, use of the thermodynamic properties of natural orthopyroxenes, which already include the large effects of even small amounts of Ca^{2+} and Al^{3+} substitution, is more appropriate.

Both ortho- and low-clinopyroxenes undergo a first order phase transformation at high pressures (and ambient temperatures) to the high-pressure C2/c clinopyroxene polymorph. The transition of low-clinoferrosilite to high-pressure clinoferrosilite is first order and reversible, with the high-symmetry phase (C2/c) reverting to the low-symmetry phase ($P2_1/c$) on pressure release. This transition is characterised by a 3% volume decrease caused predominantly by a major reconfiguration of the tetrahedral silicate chains. The transformation of orthoferrosilite to high-pressure C2/c clinoferrosilite, observed at pressures in excess of 4.6 GPa, is highly time-dependent, irreversible and first order in character (with a ~2.6% volume discontinuity); the newly-formed C2/c clinoferrosilite reverts preferentially to the low-pressure $P2_1/c$ clinoferrosilite phase rather than orthoferrosilite upon pressure release. The proposed

mechanism for this transformation is highly reconstructive, involving the movement of slabs of the structure parallel to [001] with some associated exchange of the M1 and M2 cation sites.

More recent experiments (Ross and Sowerby, pers. comm.) have demonstrated that the C2/c pyroxene structure is also stable at high pressures for synthetic pyroxenes of all intermediate compositions along the $MgSiO_3$- $FeSiO_3$ join, with the pressure of the $P2_1/c \rightarrow C2/c$ transition depending on the relative iron content of the pyroxene. This high-pressure C2/c phase is therefore the stable polymorph of $(Mg,Fe)SiO_3$ pyroxene at the temperatures and pressures beyond the orthopyroxene stability field within the Earth's upper mantle. Although the transformation of orthopyroxene to this C2/c clinopyroxene has significant effects on the thermodynamic properties of the pyroxene, the relative sizes and distortions of the cation sites in both structures suggest that the solid solution limits of the pyroxene and its ability to take up trace elements remain essentially unchanged throughout the upper mantle. Furthermore, since there are no phase transformations in the $(Mg,Fe)_2SiO_4$ system at appropriate depths, it is likely that this high-pressure ortho/clino transformation could be related to the Lehmann discontinuity at $\sim$ 200 km depth in subcontinental mantle.

The compressional behaviour of the high-pressure C2/c polymorph of $FeSiO_3$ is very different to that of the corresponding orthopyroxene, although a similar change in compression mechanism is observed in both structures at $\sim$ 4 GPa. Unlike the orthopyroxenes, there is little kinking or tilting of the silicate chains in the C2/c clinopyroxene at any pressure below $\sim$ 7.5 GPa; increasing pressure is accommodated by the shortening of the M-O bonds over the whole pressure range studied, and by the considerable reduction of the Si-O bond lengths above $\sim$ 4 GPa. These differences in the compressional behaviour of the ortho- and high-pressure clinopyroxenes demonstrate that the physical properties of the pyroxene component of the Earth's upper mantle cannot be modelled purely on the behaviour of the orthopyroxene phase with depth; at depths greater than those of the transition between the two polymorphs (perhaps at the Lehmann discontinuity at $\sim$ 200 km?) the physical properties of the mantle will reflect those of the high-pressure C2/c clinopyroxene phase more closely

than those of orthopyroxene.

The high-pressure C2/c pyroxene structure differs considerably from both high-temperature and calcium-containing clinopyroxenes of the same space group. Because it is unlikely that the effect of temperature on a clinopyroxene equilibrated at high pressure would alter the structure sufficiently to become the high temperature C2/c structure, the $(Mg,Fe)SiO_3$ phase diagram probably contains two structurally distinct C2/c phases, whose stability fields may meet at a kind of "cross-over" transition at very high pressures and temperatures. While isosymmetric phase transitions have recently been detected in systems of different compositions and symmetries (eg., Allan and Nelmes, 1992; Hackwell and Angel, 1995), they may not have been identified previously due to insufficient precision in structural refinements at elevated pressures and/or temperatures. However, in order to confirm the existence of this (metastable?) C2/c $\rightarrow$C2/c clinopyroxene transition, *in situ* reversals of the boundary between the structurally distinct C2/c phases at very high pressures and temperatures are required.

Despite the present uncertainty about such (metastable?) behaviour of clinopyroxenes at extreme conditions, the topologies of the equilibrium phase diagrams of synthetic $MgSiO_3$ and $FeSiO_3$ at less extreme pressures and temperatures are very similar, with the phase boundaries and triple point of the $FeSiO_3$ end-member lying at relatively lower pressures than those in the $MgSiO_3$ system. Notwithstanding this, there are still several important aspects of these phase diagrams which remain unresolved.

Although preliminary compression experiments on synthetic clinopyroxenes of intermediate composition along the enstatite-ferrosilite solid solution have indicated that the high-pressure C2/c phase is the stable polymorph at high pressures (Ross and Sowerby, pers. comm.), it appears to be difficult to synthesise suitable single crystals for high-precision structure determinations. Since such crystals of intermediate compositions are synthesised in the stability field of the high-pressure C2/c clinopyroxene phase, and pass through the high $\rightarrow$low transition upon decompression, twins and/or a high density of stacking faults within the microstructure of the crystals

may be produced. Local chemical heterogeneities or local differences in the degree of order or disorder of the cations over the M1 and M2 sites may also broaden the X-ray diffraction peak profiles from the pyroxene, and thus reduce its quality for high pressure experiments. It is therefore imperative to discover the root cause of such poor X-ray diffraction data, and, having done so, to synthesise single clinopyroxene crystals of a higher quality on which to perform high-pressure structural analyses.

The position of the low-clinoferrosilite to high-pressure clinoferrosilite phase boundary shown in Chapter 7 represents the extrapolation of the pressure of the transition at ambient temperatures to its intersection with the ortho- to high-pressure-clino- and low-clino- to orthoferrosilite phase boundaries of Akimoto et al. (1965) and Lindsley (1965) respectively. The boundary between the corresponding $MgSiO_3$ clinopyroxene phases at high pressures and low-moderate temperatures is also simply an extrapolation from the room pressure reversal bracket to the calculated triple point, although thermodynamic calculations have given an indication of the slope and intersection on the temperature axis of both these boundaries. Use of a heated diamond anvil cell to determine the precise position of the low- to high-pressure clinopyroxene phase boundary would eliminate the uncertainties of its presently accepted position in P-T space. Unfortunately, such simultaneous high-pressure high-temperature experiments are currently difficult to perform (eg, Hackwell, 1994).

Similar high-pressure high-temperature experiments to determine the position of the low- to high-pressure clinopyroxene boundary for Mg^{2+}-rich $(Mg,Fe)SiO_3$ clinopyroxenes may raise practical problems due to the significantly higher pressures of the transformation, and the greater hysteresis observed (eg., Angel et al., 1992a). This significantly increased hysteresis in the transitions between Mg^{2+}-rich clinopyroxene phases has been observed during both high-pressure single crystal X-ray diffraction studies (Angel et al., 1992a) as well as Raman experiments (Ross et al., pers. comm.), and may be related to the crystal field stabilisation energy of the Fe^{2+} cation. However, further experiments (perhaps involving Raman or TEM techniques) are needed to eliminate any other possible explanations for this contrast in the hysteresis.

REFERENCES

Adams, D.M., Appleby, R. and Sharma, S.K. (1976) Spectroscopy at very high pressure: Part X. Use of ruby R-lines in the estimation of pressure at ambient and low temperatures. Journal of Physics, E9, 1140 - 1144.

Akaogi, M. and Akimoto, S. (1977) Pyroxene-garnet solid-solution equilibria in the systems $Mg_4Si_4O_{12}$ - $Mg_3Al_2Si_3O_{12}$ and $Fe_4Si_4O_{12}$ - $Fe_3Al_2Si_3O_{12}$ at high pressures and temperatures. Physics of the Earth and Planetary Interiors, 15, 90 - 105.

Akimoto, S., Katsura, T., Syono, Y., Fujisawa, H. and Komada, E. (1965) Polymorphic phase transition of pyroxenes $FeSiO_3$ and $CoSiO_3$ at high pressures and temperatures. Journal of Geophysical Research, 70, 5269 - 5278.

Allan, D.R. (1993) Crystal structure studies and techniques at high pressure. PhD thesis, University of Edinburgh.

Allan, D.R. and Nelmes, R.J. (1992) The crystal structure of potassium titanyl phosphate (KTP) in its high-pressure phase. Journal of Physics: Condensed Matter, 4, L395 - L398.

Allen, E.T., Wright, F.E. and Clement, J.K. (1906) Minerals of the composition $MgSiO_3$; a case of tetramorphism. American Journal of Science, 22, 385 - 438.

Anasatasiou, P. and Siefert, F. (1972) Solid solubility of Al_2O_3 in enstatite at high temperatures and 1-5 kb water pressure. Contributions to Mineralogy and Petrology, 34, 272 - 287.

Angel, R.J. (1986) Polytypes and polytypism. Zeitschrift für Kristallographie, 176, 193 - 204.

Angel, R.J., Chopelas, A. and Ross, N.L. (1992a) Stability of high-density clinoenstatite at upper mantle pressures. Nature, 358, 322 - 324.

Angel, R.J., Ross, N.L., Wood, I.G. and Woods, P.A. (1992b) Single-crystal X-ray diffraction with diamond-anvil cells. Phase Transitions, 39, 13 - 32.

Angel, R.J. and Hugh-Jones, D.A. (1994) Equations of state and thermodynamic properties of enstatite pyroxenes. Journal of Geophysical Research, 99, 19777 - 19783.

Atlas, L. (1952) The polymorphism of $MgSiO_3$ and solid-state equilibria in the system $MgSiO_3$ -$CaMgSi_2O_6$. Journal of Geology, 60, 125 - 147.

Barnett, J.D., Block, S., and Piermarini, G.J. (1973) An optical fluorescence system for quantitative pressure measurement in the diamond-anvil cell. Review of Scientific Instruments, 44, 1 - 9.

Bass, J.D. and Weidner, D.J. (1984) Elasticity of single-crystal orthoferrosilite. Journal of Geophysical Research, 89, 4359 - 4371.

Birch, F. (1947) Finite elastic strain of cubic crystals. Physical Review, 71, 809 - 824.

Birch, F. (1978) Finite strain isotherm and velocities for single crystal and polycrystalline NaCl at high pressures and 300°K. Journal of Geophysical Research, 83, 1257 - 1268.

Blessing, R.H. (1987) Data reduction and error analysis for accurate single crystal diffraction intensities. Crystallography Reviews, 1, 3 - 58.

Bohlen, S.R., Essene, E.J. and Boettcher, A.L. (1980) Reinvestigation and applications of spinel equilibria in the system FeO-Al_2O_3-SiO_2. Journal of Petrology, 27, 1143 - 1156.

Bohlen, S.R. and Boettcher, A.L. (1982) The quartz = coesite transformation: A precise determination and the effects of other components. Journal of Geophysical Research, 87, 7073 - 7078.

Bowen, N.L. and Schairer, J.F. (1935) The system MgO-FeO-SiO_2. American Journal of Science, 29, 151 - 217.

Boyd, F.R., England, J.L and Davis, B.T.C. (1964) Effects of pressure on the melting and polymorphism of enstatite, $MgSiO_3$. Journal of Geophysical Research, 69, 2101 - 2109.

Boyd, F.R. and England, J.L. (1965) The rhombic enstatite - clinoenstatite transition. Carnegie Institution of Washington Yearbook, 64, 117 - 120.

Brown, G.M. (1968) Experimental studies on inversion relations in natural pigeonitic pyroxenes. Carnegie Institution of Washington Yearbook, 66, 347 - 353.

Brown, G.E., Prewitt, C.T., Papike, J.J. and Sueno, S. (1972) A comparison of the structures of low and high pigeonite. Journal of Geophysical Research, 77, 5778 - 5789.

Burnham, C.W. (1965) Ferrosilite. Carnegie Institution of Washington Yearbook, 64, 202 - 204

Burnham, C.W. (1966a) Computation of absorption corrections and the significance of end effects. American Mineralogist, 51, 159 - 167.

Burnham, C.W. (1966b) Ferrosilite. Carnegie Institution of Washington Yearbook, 65, 285 - 290.

Buseck, P.R., Nord, G.L., Jr. and Veblen, D.R. (1980) Subsolidus phenomena in pyroxenes. MSA Reviews in Mineralogy, 7, p117 - 220.

Büssem, W., Schusterius, C. and Stuckardt, K. (1938) Über die Konstitution des Steatits. Wiss. Veröff. Siemenswerken, 17, 64 - 94.

Cameron, M. and Papike, J.J. (1980) Crystal chemistry of silicate pyroxenes. MSA Reviews in Mineralogy, 7, 5 - 92.

Cameron, M., Sueno, S., Prewitt, C.T. and Papike, J.J. (1973) High-temperature crystal chemistry of acmite, diopside, hedenbergite, jadeite, spodumene and ureyite. American Mineralogist, 58, 594 - 618.

Carpenter, M.A. (1979) Experimental coarsening of antiphase domains in a silicate mineral. Science, 206, 681 - 683.

Champness, P.E. (1973) Nucleation of augite at antiphase boundaries in pigeonite. Physics and Chemistry of Minerals, 2, 237 - 251.

Chen, C.-H. and Presnall, D.C. (1975) The system Mg_2SiO_4-SiO_2 at pressures up to 25 kilobars. American Mineralogist, 60, 398 - 406.

Chopelas, A. and Boehler, R. (1992) Raman spectroscopy of high pressure $MgSiO_3$ phases synthesised in a CO_2 laser heated diamond anvil cell. High-pressure research: Application to Earth and Planetary Sciences, ed. Y. Syono and M.H. Manghnani, p101 - 108.

Coe, R.S. and Kirby, S.H. (1975) The orthoenstatite to clinoenstatite transformation by shearing and reversion be annealing: Mechanism and potential applications. Contributions to Mineralogy and Petrology, 52, 29 - 55.

Dallwitz, W.B., Green, D.H. and Thompson, J.E. (1966) Clinoenstatite in a volcanic rock from the Cape Vogel area, Papua. Journal of Petrology, 7, 375 - 403.

Dietrich, P. and Arndt, J. (1982) Effects of pressure and temperature on the physical behaviour of mantle-relevant olivine, orthopyroxene and garnet: 1. Compressibility, thermal properties and macroscopic Grüneisen Parameters. High Pressure Researches in Geoscience (ed. W. Schreyer), pp293 - 306.

Domeneghetti, M.C. and Steffen, G. (1992) M1, M2 site populations and distortion parameters in synthetic Mg-Fe orthopyroxenes from Mössbauer spectra and X-ray structure refinements. Physics and Chemistry of Minerals, 19, 298 - 306.

Duffy, T.S., and Vaughan, M.T. (1988) Elasticity of enstatite and its relationship to crystal structure, Journal of Geophysical Research, 93, 383 - 391.

Dziewonski, M.A. and Anderson, D.L. (1981) Preliminary Reference Earth Model. Physics of the Earth and Planetary Interiors, 25, 297 - 356.

Ernst, T. and Schwab, R. (1970) Stability and structural relations of (Mg,Fe) metasilicates. Physics of the Earth and Planetary Interiors, 3, 451 - 455.

Finger, L.W. and Prince, E. (1975) A system of Fortran IV computer programs for crystal structure computations. U.S. National Bureau of Standards Technical Note, 854, 128p.

Finger, L.W. and King, H. (1978) A revised method of operation of the single-crystal diamond-anvil cell and refinement of the structure of NaCl at 32 kbar. American Mineralogist, 63, 337 - 342.

Forman, R.A., Piermarini, G.J., Barnett, J.D. and Block, S. (1972) Pressure measurement made by utilisation of ruby sharp-line luminescence. Science, 176, 284 - 286.

Frisillo, A.L. and Barsch, G.R. (1972) Measurement of single-crystal elastic constants of bronzite as a function of pressure and temperature, Journal of Geophysical Research, 77, 6360 - 6384.

Gasparik, T. (1989) Transformation of enstatite - diopside - jadeite pyroxenes to garnet. Contributions to Mineralogy and Petrology, 102, 389 - 405.

Gasparik, T. (1990) A thermodynamic model for the enstatite-diopside join. American Mineralogist, 75, 1080 - 1091.

Ghose, S. (1965) Mg^{2+}-Fe^{2+} order in an orthopyroxene, $Mg_{0.93}Fe_{1.07}Si_2O_6$, Zeitschrift für Kristallographie, 122, 81 - 99.

Grant, D.F. and Gabe, E.J. (1978) The analysis of single-crystal Bragg reflections from profile measurements. Journal of Applied Crystallography, 11, 114 - 120.

Grover, J. (1972) The stability of low-clinoenstatite in the system $Mg_2Si_2O_6$ - $CaMgSi_2O_6$ (abstract). EOS, Transactions of the American Geophysical Union, 53, 539.

Hackwell, T.P. (1994) The structural behaviour of aluminosilicate frameworks at high pressures and temperatures. PhD thesis, University College London.

Hackwell, T.P. and Angel, R.J. (1995) Reversed brackets for the P1 ⇌ I1 transition in anorthite at high pressures and temperatures. American Mineralogist, 80, 239 - 246.

Hales, A.L., Muirhead, K.J. and Rynn, J.M. (1980) A compressional velocity distribution for the upper mantle. Tectonophysics, 63, 309 - 348.

Hamilton, W.C. (1965) Significance tests on the crystallographic R-factor. Acta Crystallographica, 18, 502 - 510.

Haraldsen, H. (1930) Beiträge zur Kenntnis de thermiscen Umbildung del Talks. Neues Jahrbuch, Beilage-Band 61, 139 - 164.

Harlow, G.E., Nehru, C.E., Prinz, M., Taylor, G.J. and Keil, K. (1979) Pyroxenes in Serra de Magé: Cooling history in comparison with Moama and Moore country. Earth and Planetary Science Letters, 43, 173 - 181.

Hazen, R.M. and Finger, L.W. (1977) Compressibility and structure of Angra dos Reis fassaite. Carnegie Institution of Washington Yearbook, 76, 512 - 515.

Hazen, R.M. and Finger, L.W. (1982) Comparative Crystal Chemistry. John Wiley and Sons, New York.

Hazen, R.M. and Finger, L.W. (1989) High-pressure crystal chemistry of andradite and pyrope: Revised procedures for high-pressure diffraction experiments. American Mineralogist, 74, 352 - 359.

Herzberg, C. and Gasparik, T. (1991) Garnet and pyroxenes in the mantle: A test of the mantle fractionation hypothesis. Journal of Geophysical Research, 96, 16263 - 16274.

Holland, T.J.B. (1980) The reaction albite = jadeite + quartz determined experimentally in the range 600 - 1200 °C. American Mineralogist, 65, 129 - 134.

Ito, T. (1935) On the symmetry of rhombic pyroxenes. Zeitschrift für Kristallographie, 90, 151 - 160.

Ito, T. (1950) X-ray studies on Polymorphism. Maruzen Co., Tokyo.

Ito E., Takahashi, E. and Matsui, Y. (1984) The mineralogy and chemistry of the lower mantle: An implication of the ultra-high pressure phase relations in the system MgO-FeO-SiO_2. Earth and Planetary Science Letters, 67, 238 - 248.

Jackson, I., Niesler, H. and Weidner, D.J. (1981) Explicit correction of ultrasonically determined elastic wave velocities for transducer-bond phase shifts. Journal of Geophysical Research, 86, 3736 - 3748.

Jayaraman, A. (1983) Diamond anvil cell and high-pressure physical investigations. Review of Modern Physics, 55, 65 - 108.

Jeanloz, R., and Hazen, R.M. (1991) Finite-strain analysis of relative compressibilities: Application to the high-pressure wadsleyite phase as an illustration, American Mineralogist, 76, 1765 - 1768.

Jephcoat, A.P., Mao, H.K. and Bell, P.M. (1987) Operation of the megabar diamond-anvil cell. In G.C. Ulmer and H.L.Barnes (Eds), Hydrothermal Experimental Techniques, John Wiley and Sons, New York, pp469 - 506.

Kandelin, J. and Wiedner, D.J. (1988a) Elastic properties of hedenbergite. Journal of Geophysical Research, 93, 1063 - 1072.

Kandelin, J. and Wiedner, D.J. (1988b) The single-crystal elastic properties of jadeite. Physics of the Earth and Planetary Interiors, 50, 251 - 260.

Kanzaki, M. (1991) Ortho/clinoenstatite transition. Physics and Chemistry of Minerals, 17, 726 - 730.

Karato, S. (1992) On the Lehmann discontinuity. Geophysical Research Letters, 19, 2255 - 2258.

Kato, T. and Kumazawa, M. (1985) Garnet phase of $MgSiO_3$ filling the gap at very high temperature. Nature, 316, 803 - 805.

Katsura, T. and Ito, E. (1989) The system Mg_2SiO_4 - Fe_2SiO_4 at high pressures and temperatures: precise determination of stabilities of olivine, modified spinel and spinel. Journal of Geophysical Research, 94, 15663 - 15670.

King, H.E. and Finger, L.W. (1979) Diffracted beam crystal centring and its application to high-pressure crystallography. Journal of Applied Crystallography, 12, 374 - 378.

Kosoi, A.L., Malkova, L.A. and Frank-Kamenetskii, V.A. (1974) Crystal-chemical characteristics of rhombic pyroxenes. Soviet Physical Crystallography, 19, 171 - 174.

Kudoh, Y. and Takéuchi, Y. (1985) The crystal structure of forsterite Mg_2SiO_4 under high pressure up to 149 kb. Zeitschrift für Kristallographie, 171, 291 - 302.

Kumazawa, M., (1969) The elastic constants of single-crystal orthopyroxene, Journal of Geophysical Research, 74, 5973 - 5980.

Kuno, H. (1966) Review of pyroxene relations in terrestrial rocks. Mineralogical Journal, 5, 21 - 43.

Kushiro, I. (1972) Determination of liquidus relations in synthetic silicate systems with electron probe analysis: the system forsterite-diopside-silica at 1 atmosphere. American Mineralogist, 57, 1260 - 1271.

Lange, P.A. and Koltermann, M. (1966) Hochtemperatur-Röntgenuntersuchungen zur Frage des Umwandlungsverhaltens von Enstatit, Protoenstatit und Klinoenstatit. Neues Jahrbuch für Mineralogie, Montash (1966), 153 - 160.

Levien, L. and Prewitt, C.T. (1981) High-pressure structural study of diopside. American Mineralogist, 66, 315 - 323.

Levien, L., Weidner, D.J. and Prewitt, C.T. (1979) Elasticity of diopside. Physics and Chemistry of Minerals, 4, 105 - 113.

Liebau (1962) Die Systematik der Silikate. Naturwissenschaften, 49, 481 - 491.

Lindsley, D.H. (1965) Ferrosilite. Carnegie Institution of Washington Yearbook, 64, 148 - 150.

Lindsley, D.H. (1980) Phase equilibria of pyroxenes at pressures >1 atmosphere. MSA Reviews in Mineralogy, 7, 289 - 307.

Lindsley, D.H. (1981) The formation of pigeonite on the join hedenbergite-ferrosilite at 11.5 and 15 kbar: experiments and a solution model. American Mineralogist, 66, 1175 - 1182.

Lindsley, D.H., Davis, B.T. and MacGregor, I.D. (1964) Ferrosilite ($FeSiO_3$): Synthesis at high pressures and temperatures. Science, 144, 73 - 74.

Lindsley, D.H. and Munoz, J.L. (1969) Ortho-clino inversion in ferrosilite. Carnegie Institution of Washington Yearbook, 67, 86 - 88.

Luo, G., Xue, J., Xu, H., Xu, H. and Hu, M. (1992) Confirmation of the terrestrial existence of orthopyroxene with space group $P2_1ca$. American Mineralogist, 77, 115 - 120.

Malinowski, M. (1987) A diamond-anvil high-pressure cell for X-ray diffraction on a single crystal. Journal of Applied Crystallography, 20, 379 - 382.

Mao, H.K. and Bell, P.M. (1978) Design and varieties of the megabar cell. Carnegie Institution of Washington Yearbook, 77, 904 - 908.

Mao, H.K., Xu, J. and Bell, P.M. (1986) Calibration of the ruby pressure gauge to 800 kbar under quasi-hydrostatic conditions. Carnegie Institution of Washington Yearbook, 78, 659 - 660.

McCormick, T.C., Hazen, R.M. and Angel, R.J. (1989) Compressibility of omphacite to 60 kbar: Role of vacancies. American Mineralogist, 74, 1287 - 1292.

Merrill, L. and Bassett, W.A. (1974) Miniature diamond anvil pressure cell for single crystal X-ray diffraction studies. Review of Scientific Instruments, 45, 290 - 294.

Morimoto, N. (1956) The existence of monoclinic pyroxenes with the space group C^5_{2h} - $P2_1/c$. Proceedings of the Japan Academy, 32, 750 - 752.

Morimoto, N. and Tokonami, M. (1969) Domain structure of pigeonite and clinoenstatite. American Mineralogist, 54, 725 - 740.

Munoz, J.L. (1968) Effect of shearing on enstatite polymorphism. Carnegie Institution of Washington Yearbook, 66, 369 - 370.

Murakami, T., Takeuchi, Y., Yamanaka, T. (1982) The transition of orthoenstatite to protoenstatite and the structure at 1080°C. Zeitschrift für Kristallographie, 160, 299 - 312.

Murnaghan (1937) Finite deformations of an elastic solid. American Journal of Mathematics, 59, 235 - 260.

Nord, G.L. (1992) Imaging transformation-induced microstructures. MSA Reviews in Mineralogy, 27, pp 455 - 508.

Nye, J.F. (1957) Physical Properties of Crystals, Oxford University Press.

Ohashi Y. (1984) Polysynthetically-twinned structures of enstatite and wollastonite. Physics and Chemistry of Minerals, 10, 217 - 229.

Ohashi, Y., Burnham, C.W. and Finger, L.W. (1975) The effect of Ca-Fe substitution on the clinopyroxene crystal; structure. American Mineralogist, 60, 423 - 434.

Pacalo, R.E.G. and Gasparik, T. (1990) Reversals of the orthoenstatite-clinoenstatite transition at high pressures and temperatures. Journal of Geophysical Research, 95, 15853 - 15858.

Pannhorst W. (1979) Structural relationships between pyroxenes. Neues Jahrbuch für Mineralogie Abhandlungen, 135, 1 - 17.

Pannhorst, W. (1981) Comparison between topological classifications of pyroxenes. Neues Jahrbuch für Mineralogie Abhandlungen, 143, 1 - 14.

Papike, J.J., Prewitt, C.T., Sueno, S. and Cameron M. (1973) Pyroxenes: comparisons of real and ideal structural topologies. Zeitschrift für Kristallographie, 138, 254 - 273.

Perrotta, A.J. and Stephenson, D.A. (1965) Clinoenstatite: high-low inversion. Science, 148, 1090 - 1091.

Phakey, P.P. and Ghose, S. (1973) Direct observation of antiphase domain structure in omphacite. Contributions to Mineralogy and Petrology, 39, 239 - 245.

Prewitt, C.T., Brown, G.E. and Papike, J.J. (1971) Apollo 12 clinopyroxenes: High temperature X-ray diffraction studies. Proceedings of the Lunar Science Conference, 2, 59 - 68.

Putnis, A. (1992) Introduction to Mineral Science. Cambridge University Press.

Ralph, R.L. and Finger, L.W. (1982) A computer program for refinement of crystal orientation matrix and lattice constants from diffractometer data with lattice symmetry constraints. Journal of Applied Crystallography, 15, 537 - 539.

Ralph R.L., and Ghose, S. (1980) Enstatite, $Mg_2Si_2O_6$: Compressibility and crystal structure at 21 kbar (abs.), EOS, 61, 409.

Revenaugh, J. and Jordan, T.H. (1991) Mantle layering from ScS reverberations, 3. The upper mantle. Journal of Geophysical Research, 96, 19781 - 19810.

Riecker, R.E. and Rooney, T.P. (1966) Shear strength, polymorphism and mechanical behaviour of olivine, enstatite, diopside, labradorite and pyrope garnet: tests to 920°C and 60 kb. U.S. Clearinghouse federation of Science and Technology Info. Doc. AD642925.

Ringwood, A.E. (1975) Composition and Petrology of the Earth's mantle. McGraw-Hill, New York.

Robinson, K., Gibbs, G.V. and Ribbe, P.H. (1971) Quadratic elongation: A quantitative measure of distortion in coordination polyhedra. Science, 172, 567 - 570.

Ross, N., Akaogi, M., Navrotsky, A., Susaki, J., and McMillan, P., (1986) Phase transitions among the $CaGeO_3$ polymorphs (wollastonite, garnet and perovskite structures): Studies by high pressure synthesis, high temperature calorimetry and vibrational spectroscopy and calculation. Journal of Geophysical Research, 91, 4685 - 4696.

Ross, N.L. and Hazen, R.M. (1990) High-pressure crystal chemistry of $MgSiO_3$ perovskite. Physics and Chemistry of Minerals, 17, 228 - 237.

Ross, N.L. and Navrotsky, A. (1987) The Mg_2GeO_4 olivine-spinel phase transition. Physics and Chemistry of Minerals, 14, 473 - 481.

Ross, N.L. and Navrotsky A. (1988) Study of $MgGeO_3$ polymorphs (orthopyroxene, clinopyroxene and ilmenite structures) by calorimetry, spectroscopy and phase equilibria. American Mineralogist, 73, 1355 - 1365.

Ross, N.L. and Sowerby, J.R. (1995) Electronic absorption spectra of synthetic clinoferrosilite. R.G. Burns Memorial Volume, Geochimica Cosmochimica Acta, in press.

Sadanaga, R., Okamura, F.P. and Takeda, H. (1969) X-ray study of the phase transformations of enstatite. Mineralogical Journal, 6, 111 - 129.

Sarver, J.F. and Hummel, F.A. (1962) Stability relations of magnesium metasilicate polymorphs. Journal of the American Ceramic Society, 45, 152 - 157.

Sasaki, S., Prewitt, C.T. and Harlow, G.E. (1984) Alternative interpretation of diffraction patterns attributed to low ($P2_1ca$) orthopyroxene. American Mineralogist, 69, 1082 - 1089.

Saxena, S.K. (1988) Assessment of thermal expansion, bulk modulus and heat cpacity of enstatite and forsterite. Physics and Chemistry of Solids, 49, 1233 - 1235.

Saxena, S.K. and Eriksson, G. (1983) Theoretical computation of mineral assemblages in pyrolite and lherzolite. Journal of Petrology, 27, 843 - 852.

Schrader, H., Boysen, H., Frey, F. and Convert, P. (1990) On the phase transformation proto- clino-/orthoenstatite: Neutron powder investigation. Physics and Chemistry of Minerals, 17, 409 - 415.

Schwab, R.G. (1969) Die Phasenbeziehungen der Pyroxene im System $CaMgSi_2O_6$ - $CaFeSi_2O_6$ - $MgSiO_3$ - $FeSiO_3$. Fortschr. Mineralogie, 46, 188 - 273.

Sclar, C.B., Carrison, L.C. and Schwartz, C.M. (1964) High-pressure stability field of clinoenstatite and the orthoenstatite - clinoenstatite transition. Transactions of the American Geophysical Union, 45, 121.

Shankland, T.J. (1972) Velocity-density systematics: Deviation from Debye theory and the effect of ionic size. Journal of Geophysical Research, 77, 3750 - 3758.

Shearer, P.M. (1990) Constraints on upper-mantle discontinuities from observations of long-period reflected and converted phases, Journal of Geophysical Research, 96, 18147 - 18182.

Shimobayashi, N. and Kitamura, M. (1991) Phase transition in Ca-poor clinopyroxenes. Physics and Chemistry of Minerals, 18, 153 - 160.

Skinner, B.J. (1966) Thermal expansion, in Handbook of Physical Constants, ed. S.P.Clark, Jr., pp75 - 95, Geological Society of America, Boulder, Colorado.

Smith, D., (1971) Stability of the assemblage iron-rich orthopyroxene-olivine-quartz. American Journal of Science, 271, 370 - 382.

Smith, J.V. (1969a) Crystal structure and stability of the $MgSiO_3$ polymorphs; Physical properties and phase relations of Mg,Fe pyroxenes. Mineralogical Society of America Special Papers, 2, 3 - 29.

Smith, J.V. (1969b) Magnesium pyroxenes at high temperature: inversion in clinoenstatite. Nature, 222, 256 - 257.

Smith, J.V., Stephenson, D.A., Howie, R.A. and Hey, M.H. (1969) Relations between cell dimensions, chemical composition, and site preference of orthopyroxene. Mineralogical Magazine, 37, 90 - 114.

Smyth, J.R. (1971) Protoenstatite: a crystal structure refinement at 1100°C. Zeitschrift für Kristallographie, 143, 262 - 274.

Smyth, J.R. (1973) An orthopyroxene structure up to 850°C. American Mineralogist, 58, 636 - 648.

Smyth, J.R. (1974a) The high temperature crystal chemistry of clinohypersthene. American Mineralogist, 59, 1069 - 1082.

Smyth, J.R. (1974b) Experimental study on the polymorphism of enstatite. American Mineralogist, 59, 345 - 352.

Sueno, S., Cameron, M. and Prewitt, C.T. (1976) Orthoferrosilite: high-temperature crystal chemistry. American Mineralogist, 61, 38 - 53.

Sueno, S. and Kimata, M. (1981) On the ortho-clino phase transition of ferrosilite ($FeSiO_3$) and Fe-rich pyroxenes. Acta Crystallographica, A37 (supplement), C-111.

Sueno, S., Kimata, M. and Prewitt, C.T. (1984) The crystal structure of high clinoferrosilite. American Mineralogist, 69, 264 - 269.

Sueno, S. and Prewitt, C.T. (1983) Models for the phase transition between orthoferrosilite and high clinoferrosilite. Fortschritte für Mineralogie, 61, 223 - 241.

Thilo, E. and Rogge, G. (1939) Chemische Untersuchungen von Silikaten. VIII Mitt. Über die thermische Umwandlung des Anthophyllits $Mg_7Si_8O_{22}(OH)_2$. Über die Polymorphie des Magnesium Metasilikates und über den Mechanismus der Umwandlung von Anthophyllit und Talk beim Erhitzen. Deutsche chem. Gesell. Ber., 72, 341 - 362.

Thompson, Jr., J.B. (1970) Geometrical possibilities for amphibole structures: model biopyriboles. American Mineralogist, 55, 292 - 293.

Vidale, J.E. and Benz, H.M. (1992) Upper mantle seismic discontinuities and the thermal structure of subduction zones. Nature, 356, 678 - 682.

Vinet, P., Ferrante, J., Smith, J.R. and Rose, J.H. (1986) A universal equation of state for solids. Journal of Physics C: Solid state Physics, 19, L467 - L473.

Warren, B.E. and Modell, D.I. (1930) The structure of enstatite $MgSiO_3$. Zeitschrift für Kristallographie, 72, 42 - 57.

Watt, J.P. and Ahrens, T.J. (1986) Shock wave equations of state of enstatite. Journal of Geophysical Research, 91, 7495 - 7503.

Webb, S.L. (1989) The elasticity of the upper mantle orthosilicates olivine and garnet to 3 GPa. Physics and Chemistry of Minerals, 16, 684 - 692.

Webb, S.L., and Jackson, I. (1993) The pressure dependence of the elastic moduli of single-crystal orthopyroxene $(Mg_{0.8}Fe_{0.2})SiO_3$, European Journal of Mineralogy, 5, 1111 - 1119.

Weidner, D.J. (1986) Mantle models based on measured physical properties of minerals. In Chemistry and physics of terrestrial planets, S.K. Saxena, Ed. Berlin: Springer, 251 - 274.

Weidner, D.J.,Wang, H. and Ito, J. (1978) Elasticity of orthoenstatite, Physics of the Earth and Planetary Interiors, 17, 7 - 13.

Wilson, A.J.C. (1949) The probability distribution of X-ray intensities. Acta Crystallographica, 2, 318 - 321.

Wood, I.G., Welber, B., David, W.I.F. and Glazer, A.M. (1980) Ferroelastic phase transition in $BiVO_4$. II. Birefringence at simultaneous high pressure and temperature. Journal of Applied Crystallography, 13, 224 - 229.

Woodland, A.B. and O'Neill, H.St.C. (1993) Synthesis and Stability of $Fe^{2+}{}_3Fe^{3+}{}_2Si_3O_{12}$ garnet and phase relations with $Fe_3Al_2Si_3O_{12}$-$Fe^{2+}{}_3Fe^{3+}{}_2Si_3O_{12}$ solutions. American Mineralogist, 78, 1000 - 1013.

Yagi, T. and Akimoto, S. (1976) Direct determination of coesite-stishovite transition by in situ X-ray measurements. Tectonophysics, 35, 259 - 270.

Yagi, T., Akaogi, M., Shimomura, O., Suzuki, T. and Akimoto, S. (1987) In-situ observation of the olivine spinel transformation in Fe_2SiO_4 using synchrotron radiation. Journal of Geophysical Research, 92, 6207 - 6213.

Yang, H. and Ghose, S. (1993) Thermal expansion, Grüneisen parameter and Debye temperature of synthetic $(Fe,Mg)SiO_3$ orthopyroxene. AGU Spring Meeting Abstracts, M12A - 8.

Yang, H. and Ghose, S. (1995) A transitional structural state and anomalous Fe-Mg order-disorder in Mg-rich orthopyroxene, $(Mg_{0.75}Fe_{0.25})_2Si_2O_6$. American Mineralogist, 80, 21 - 26.

Zhang, L. and Hafner, S.S. (1992) High-pressure ^{57}Fe γ resonance and compressibility of $Ca(Mg,Fe)Si_2O_6$ clinopyroxenes. American Mineralogist, 77, 462 - 473.

APPENDIX 1

POSITIONAL PARAMETERS, BOND LENGTHS AND ANGLES OF $(Mg,Fe)SiO_3$ ORTHOPYROXENES

P (GPa)		0.00	1.04	1.95	3.27	4.09
Mg1	x	0.3763 (2)	0.3768 (2)	0.3760 (4)	0.3762 (2)	0.3758 (2)
	y	0.6541 (4)	0.6545 (6)	0.6556 (9)	0.6557 (4)	0.6557 (6)
	z	0.8663 (5)	0.8627 (6)	0.862 (1)	0.8598 (5)	0.8596 (8)
	B_{iso}	0.67 (6)	0.51 (7)	0.24 (12)	0.39 (6)	0.36 (7)
Mg2	x	0.3769 (2)	0.3770 (2)	0.3768 (4)	0.3774 (2)	0.3774 (3)
	y	0.4872 (4)	0.4860 (5)	0.4843 (8)	0.4856 (4)	0.4844 (6)
	z	0.3589 (6)	0.3556 (7)	0.355 (1)	0.3532 (6)	0.3512 (8)
	B_{iso}	0.82 (6)	0.64 (7)	0.54 (13)	0.63 (7)	0.45 (8)
TA	x	0.2715 (2)	0.2716 (2)	0.2707 (3)	0.2715 (2)	0.2708 (2)
	y	0.3418 (3)	0.3421 (6)	0.3436 (8)	0.3429 (4)	0.3438 (5)
	z	0.0506 (5)	0.0482 (6)	0.046 (1)	0.0447 (5)	0.0433 (7)
	B_{iso}	0.58 (4)	0.49 (6)	0.22 (9)	0.34 (4)	0.24 (6)
TB	x	0.4736 (2)	0.4737 (2)	0.4732 (3)	0.4729 (2)	0.4727 (2)
	y	0.3374 (3)	0.3365 (6)	0.3359 (9)	0.3377 (4)	0.3368 (6)
	z	0.7981 (4)	0.7997 (5)	0.8013 (9)	0.8015 (4)	0.8021 (6)
	B_{iso}	0.59 (4)	0.41 (6)	0.21 (9)	0.33 (5)	0.24 (6)
O1a	x	0.1835 (4)	0.1823 (5)	0.1826 (7)	0.1824 (4)	0.1828 (5)
	y	0.3407 (7)	0.338 (1)	0.342 (1)	0.3397 (7)	0.339 (1)
	z	0.034 (1)	0.032 (1)	0.031 (1)	0.027 (1)	0.023 (1)
	B_{iso}	0.64 (10)	0.87 (14)	0.23 (24)	0.34 (11)	0.25 (15)
O2a	x	0.3111 (4)	0.3111 (5)	0.3094 (8)	0.3097 (4)	0.3097 (5)
	y	0.5029 (7)	0.504 (1)	0.507 (1)	0.5070 (7)	0.507 (1)
	z	0.043 (1)	0.043 (1)	0.040 (1)	0.037 (1)	0.039 (1)
	B_{iso}	0.61 (11)	0.59 (15)	0.16 (24)	0.46 (12)	0.31 (15)
O3a	x	0.3025 (4)	0.3030 (5)	0.3038 (7)	0.3035 (4)	0.3034 (5)
	y	0.2224 (7)	0.223 (1)	0.223 (1)	0.2223 (8)	0.224 (1)
	z	0.832 (1)	0.829 (1)	0.825 (1)	0.825 (1)	0.825 (1)
	B_{iso}	0.43 (12)	0.18 (14)	0.12 (24)	0.51 (12)	0.21 (16)
O1b	x	0.5622 (4)	0.5627 (4)	0.5622 (8)	0.5620 (4)	0.5621 (5)
	y	0.3414 (8)	0.340 (1)	0.340 (1)	0.3402 (8)	0.340 (1)
	z	0.798 (1)	0.800 (1)	0.804 (1)	0.807 (1)	0.804 (1)
	B_{iso}	0.95 (12)	0.63 (14)	0.38 (24)	0.58 (11)	0.72 (16)
O2b	x	0.4324 (4)	0.4315 (4)	0.4327 (7)	0.4322 (4)	0.4323 (4)
	y	0.4836 (7)	0.483 (1)	0.483 (1)	0.4837 (7)	0.483 (1)
	z	0.690 (1)	0.686 (1)	0.691 (1)	0.687 (1)	0.690 (1)
	B_{iso}	0.57 (11)	0.37 (14)	0.22 (26)	0.18 (12)	0.30 (16)
O3b	x	0.4483 (5)	0.4472 (5)	0.4482 (7)	0.4464 (4)	0.4472 (5)
	y	0.1951 (7)	0.194 (1)	0.193 (1)	0.1921 (7)	0.192 (1)
	z	0.603 (1)	0.607 (1)	0.611 (1)	0.612 (1)	0.612 (1)
	B_{iso}	0.57 (12)	0.52 (15)	0.23 (23)	0.42 (13)	0.05 (10)

Table 1: Variation of the positional parameters and isothermal temperature factors of synthetic $MgSiO_3$ orthoenstatite with pressure.

P (GPa)		4.95	5.85	7.00	8.10
Mg1	x	0.3760 (4)	0.3763 (3)	0.3762 (3)	0.3766 (3)
	y	0.6552 (9)	0.6576 (7)	0.6560 (6)	0.6589 (7)
	z	0.859 (1)	0.8569 (8)	0.8567 (8)	0.8558 (9)
	B_{iso}	0.28 (11)	0.51 (8)	0.33 (7)	0.56 (10)
Mg2	x	0.3774 (4)	0.3772 (3)	0.3775 (3)	0.3774 (3)
	y	0.4848 (8)	0.4837 (6)	0.4845 (6)	0.4834 (8)
	z	0.350 (1)	0.3489 (8)	0.3472 (6)	0.3462 (9)
	B_{iso}	0.51 (13)	0.40 (8)	0.47 (8)	0.51 (10)
TA	x	0.2705 (3)	0.2710 (2)	0.2711 (2)	0.2704 (3)
	y	0.3432 (8)	0.3436 (5)	0.3431 (7)	0.3436 (7)
	z	0.041 (1)	0.0414 (7)	0.0399 (6)	0.0385 (8)
	B_{iso}	0.32 (9)	0.27 (6)	0.32 (6)	0.27 (8)
TB	x	0.4728 (3)	0.4727 (2)	0.4725 (2)	0.4730 (3)
	y	0.3383 (8)	0.3368 (6)	0.3373 (6)	0.3383 (7)
	z	0.8022 (9)	0.8032 (6)	0.8031 (5)	0.8042 (7)
	B_{iso}	0.15 (9)	0.28 (6)	0.26 (6)	0.28 (7)
O1a	x	0.1827 (7)	0.1821 (5)	0.1828 (5)	0.1814 (6)
	y	0.339 (1)	0.344 (1)	0.340 (1)	0.344 (1)
	z	0.024 (1)	0.024 (1)	0.021 (1)	0.022 (1)
	B_{iso}	0.33 (23)	0.23 (15)	0.41 (15)	0.27 (20)
O2a	x	0.3085 (7)	0.3098 (6)	0.3088 (6)	0.3082 (7)
	y	0.508 (1)	0.508 (1)	0.509 (1)	0.509 (1)
	z	0.035 (1)	0.032 (1)	0.033 (1)	0.031 (2)
	B_{iso}	0.09 (22)	0.61 (17)	0.48 (17)	0.41 (20)
O3a	x	0.3042 (7)	0.3034 (5)	0.3044 (5)	0.3036 (6)
	y	0.223 (1)	0.222 (1)	0.223 (1)	0.222 (1)
	z	0.826 (1)	0.820 (1)	0.817 (1)	0.820 (2)
	B_{iso}	0.11 (24)	0.02 (16)	0.30 (17)	0.62 (20)
O1b	x	0.5611 (7)	0.5613 (5)	0.5627 (5)	0.5602 (7)
	y	0.340 (1)	0.338 (1)	0.336 (1)	0.340 (1)
	z	0.805 (2)	0.811 (1)	0.812 (1)	0.812 (2)
	B_{iso}	0.34 (22)	0.52 (16)	0.55 (15)	0.56 (17)
O2b	x	0.4325 (7)	0.4324 (5)	0.4330 (6)	0.4330 (6)
	y	0.484 (1)	0.485 (1)	0.485 (1)	0.486 (1)
	z	0.685 (2)	0.686 (1)	0.686 (1)	0.682 (2)
	B_{iso}	0.34 (24)	0.20 (17)	0.16 (16)	0.19 (18)
O3b	x	0.4470 (7)	0.4460 (5)	0.4479 (5)	0.4451 (7)
	y	0.190 (1)	0.190 (1)	0.190 (1)	0.191 (1)
	z	0.613 (2)	0.613 (1)	0.613 (1)	0.615 (2)
	B_{iso}	0.07 (24)	0.20 (17)	0.19 (16)	0.10 (21)

Table 1: (cont.) Variation of the positional parameters of synthetic $MgSiO_3$ orthoenstatite with pressure.

P (GPa)	0.00	1.04	1.95	3.27
Mg1-O1a	2.156 (7)	2.12 (1)	2.132 (9)	2.106 (7)
Mg1-O1a	2.039 (7)	2.020 (8)	2.011 (9)	2.011 (7)
Mg1-O2a	2.008 (8)	2.01 (1)	1.996 (9)	1.989 (7)
Mg1-O1b	2.069 (7)	2.059 (9)	2.05 (1)	2.045 (7)
Mg1-O1b	2.171 (8)	2.14 (1)	2.14 (1)	2.138 (7)
Mg1-O2b	2.034 (7)	2.02 (1)	2.03 (1)	2.015 (7)
Mg2-O1a	2.082 (7)	2.09 (1)	2.07 (1)	2.071 (7)
Mg2-O2b	1.994 (6)	1.973 (8)	2.00 (1)	1.980 (7)
Mg2-O2a	2.034 (7)	2.018 (9)	2.044 (9)	2.043 (7)
Mg2-O3a	2.297 (7)	2.278 (9)	2.25 (1)	2.257 (8)
Mg2-O1b	2.045 (8)	2.05 (1)	2.07 (1)	2.046 (8)
Mg2-O3b	2.457 (7)	2.40 (1)	2.381 (9)	2.344 (7)
TA-O2a	1.593 (7)	1.590 (9)	1.597 (9)	1.590 (7)
TA-O3a	1.661 (6)	1.659 (8)	1.665 (9)	1.651 (7)
TA-O1a	1.608 (8)	1.626 (8)	1.599 (9)	1.615 (7)
TA-O3a	1.648 (6)	1.643 (9)	1.665 (9)	1.648 (7)
TB-O2b	1.593 (7)	1.608 (9)	1.589 (9)	1.584 (6)
TB-O1b	1.616 (7)	1.618 (9)	1.616 (9)	1.614 (8)
TB-O3b	1.675 (7)	1.669 (9)	1.651 (9)	1.671 (7)
TB-O3b	1.671 (6)	1.681 (7)	1.679 (8)	1.683 (6)
O1a-O2a	2.731 (9)	2.76 (1)	2.72 (1)	2.728 (9)
O1a-O3a	2.735 (9)	2.73 (1)	2.73 (1)	2.726 (9)
O1a-O3a	2.651 (9)	2.63 (1)	2.65 (1)	2.633 (9)
O1a-O1b	2.781 (9)	2.77 (1)	2.78 (1)	2.774 (9)
O1a-O2b	2.713 (9)	2.72 (1)	2.72 (1)	2.711 (9)
O2a-O3a	2.492 (8)	2.48 (1)	2.49 (1)	2.488 (9)
O2a-O3a	2.725 (9)	2.71 (1)	2.73 (1)	2.712 (9)
O3a-O3a	2.626 (2)	2.625 (3)	2.618 (3)	2.611 (3)

Table 2: Variation of bond lengths (< 2.8 Å) of synthetic $MgSiO_3$ orthoenstatite with pressure (P < 4 GPa).

P (GPa)	0.00	1.04	1.95	3.27
O1b-O2b	2.734 (9)	2.76 (1)	2.73 (1)	2.733 (9)
O1b-O3b	2.635 (9)	2.65 (1)	2.63 (1)	2.66 (1)
O1b-O3b	2.626 (9)	2.65 (1)	2.62 (1)	2.628 (9)
O2b-O3b	2.606 (9)	2.59 (1)	2.59 (1)	2.584 (9)
O2b-O3b	2.689 (8)	2.69 (1)	2.67 (1)	2.676 (8)
O3b-O3b	2.764 (4)	2.762 (6)	2.761 (7)	2.758 (5)

Table 2: (cont.) Variation of bond lengths (< 2.8 Å) of synthetic $MgSiO_3$ orthoenstatite with pressure (P < 4 GPa).

P (GPa)	4.09	4.95	5.85	7.00	8.10
Mg1-O1a	2.087 (9)	2.09 (1)	2.13 (1)	2.09 (1)	2.08 (1)
Mg1-O1a	2.025 (9)	2.01 (1)	2.00 (1)	2.010 (9)	1.99 (1)
Mg1-O2a	1.986 (9)	1.98 (1)	2.01 (1)	1.97 (1)	1.99 (1)
Mg1-O1b	2.05 (1)	2.06 (1)	2.04 (1)	2.015 (9)	2.03 (1)
Mg1-O1b	2.13 (1)	2.14 (1)	2.08 (1)	2.09 (1)	2.11 (1)
Mg1-O2b	2.01 (1)	2.01 (1)	1.99 (1)	2.00 (1)	2.00 (1)
Mg2-O1a	2.08 (1)	2.08 (1)	2.03 (1)	2.06 (1)	2.02 (1)
Mg2-O2b	2.004 (9)	1.98 (1)	1.983 (9)	1.992 (8)	1.98 (1)
Mg2-O2a	2.024 (9)	2.04 (1)	2.03 (1)	2.034 (9)	2.04 (1)
Mg2-O3a	2.25 (1)	2.24 (1)	2.23 (1)	2.22 (1)	2.21 (1)
Mg2-O1b	2.04 (1)	2.04 (1)	2.10 (1)	2.05 (1)	2.05 (1)
Mg2-O3b	2.332 (9)	2.31 (1)	2.29 (1)	2.29 (1)	2.26 (1)
TA-O2a	1.582 (9)	1.58 (1)	1.58 (1)	1.58 (1)	1.58 (1)
TA-O3a	1.663 (9)	1.68 (1)	1.66 (1)	1.635 (9)	1.65 (1)
TA-O1a	1.594 (9)	1.59 (1)	1.59 (1)	1.59 (1)	1.60 (1)
TA-O3a	1.640 (9)	1.63 (1)	1.63 (1)	1.65 (1)	1.64 (1)
TB-O2b	1.575 (9)	1.57 (1)	1.60 (1)	1.57 (1)	1.59 (1)
TB-O1b	1.62 (1)	1.59 (1)	1.59 (1)	1.62 (1)	1.57 (1)
TB-O3b	1.659 (9)	1.68 (1)	1.67 (1)	1.67 (1)	1.67 (1)
TB-O3b	1.670 (8)	1.67 (1)	1.67 (1)	1.659 (8)	1.67 (1)

Table 2: (cont.) Variation of bond lengths (< 2.8 Å) of synthetic $MgSiO_3$ orthoenstatite with pressure (P > 4 GPa).

P (GPa)	4.09	4.95	5.85	7.00	8.10
O1a-O2a	2.72 (1)	2.70 (1)	2.67 (1)	2.69 (1)	2.68 (1)
O1a-O3a	2.73 (1)	2.73 (1)	2.72 (1)	2.71 (1)	2.72 (1)
O1a-O3a	2.60 (1)	2.61 (1)	2.63 (1)	2.63 (1)	2.64 (1)
O1a-O1b	2.75 (1)	2.76 (1)	2.78 (1)	2.75 (1)	2.76 (1)
O1a-O2b	2.73 (1)	2.72 (1)	2.65 (1)	2.70 (1)	2.65 (1)
O2a-O3a	2.48 (1)	2.49 (1)	2.48 (1)	2.47 (1)	2.47 (1)
O2a-O3a	2.70 (1)	2.69 (1)	2.70 (1)	2.70 (1)	2.69 (1)
O3a-O3a	2.601 (3)	2.597 (3)	2.593 (4)	2.588 (4)	2.586 (4)
O1b-O2b	2.72 (1)	2.70 (1)	2.74 (1)	2.74 (1)	2.69 (1)
O1b-O3b	2.63 (1)	2.63 (1)	2.62 (1)	2.64 (1)	2.63 (2)
O1b-O3b	2.62 (1)	2.60 (1)	2.59 (1)	2.60 (1)	2.59 (1)
O2b-O3b	2.58 (1)	2.59 (1)	2.60 (1)	2.58 (1)	2.57 (1)
O2b-O3b	2.65 (1)	2.66 (1)	2.68 (1)	2.65 (1)	2.68 (1)
O3b-O3b	2.754 (6)	2.762 (8)	2.751 (8)	2.750 (7)	2.737 (8)

Table 2: (cont.) Variation of bond lengths (< 2.8 Å) of synthetic $MgSiO_3$ orthoenstatite with pressure ($P > 4$ GPa).

P (GPa)	0.00	1.04	1.95	3.27
O1a-Mg1-O1a	93.0 (3)	93.0 (4)	94.2 (5)	93.8 (3)
O1a-Mg1-O2a	91.4 (3)	90.5 (4)	90.5 (5)	90.3 (3)
O1a-Mg1-O1b	85.5 (3)	84.5 (4)	85.1 (5)	85.5 (3)
O1a-Mg1-O1b	80.7 (3)	81.2 (4)	81.3 (4)	81.6 (3)
O1a-Mg1-O2b	177.0 (3)	177.5 (4)	178.0 (5)	177.9 (3)
O1a-Mg1-O2a	94.8 (3)	95.6 (4)	94.3 (6)	94.7 (3)
O1a-Mg1-O1b	177.6 (3)	176.6 (4)	177.8 (7)	177.5 (3)
O1a-Mg1-O1b	85.8 (3)	85.1 (4)	86.0 (5)	85.5 (3)
O1a-Mg1-O2b	84.7 (3)	84.6 (4)	84.7 (5)	84.7 (3)
O2a-Mg1-O1b	87.2 (3)	86.8 (4)	87.8 (5)	87.7 (3)
O2a-Mg1-O1b	172.1 (3)	171.6 (5)	171.8 (6)	71.9 (3)
O2a-Mg1-O2b	90.6 (3)	90.5 (5)	91.2 (5)	91.1 (3)
O1b-Mg1-O1b	92.0 (3)	92.2 (4)	91.9 (5)	92.0 (3)
O1b-Mg1-O2b	96.8 (3)	97.8 (4)	95.9 (5)	96.0 (3)
O1b-Mg1-O2b	97.3 (3)	97.8 (4)	96.9 (5)	96.9 (3)
O1a-Mg2-O2b	84.6 (3)	83.9 (4)	83.7 (5)	84.0 (3)
O1a-Mg2-O2a	89.3 (3)	89.2 (4)	87.9 (5)	87.8 (2)
O1a-Mg2-O3a	107.5 (3)	108.5 (4)	108.4 (5)	108.0 (3)
O1a-Mg2-O1b	85.5 (3)	83.9 (5)	84.5 (4)	84.7 (3)
O1a-Mg2-O3b	172.6 (3)	172.6 (4)	172.8 (4)	172.9 (3)
O2b-Mg2-O2a	173.6 (3)	172.7 (4)	171.6 (6)	171.5 (3)
O2b-Mg2-O3a	109.9 (3)	109.7 (4)	110.7 (5)	110.2 (3)
O2b-Mg2-O1b	94.5 (3)	94.6 (4)	94.3 (5)	94.9 (3)
O2b-Mg2-O3b	100.6 (3)	100.7 (4)	100.2 (5)	100.7 (3)
O2a-Mg2-O3a	69.9 (3)	70.3 (4)	70.9 (5)	70.5 (3)
O2a-Mg2-O1b	87.1 (3)	86.9 (4)	86.1 (5)	86.3 (3)
O2a-Mg2-O3b	85.6 (3)	86.5 (3)	88.3 (5)	87.7 (3)
O3a-Mg2-O1b	153.0 (3)	153.4 (4)	152.7 (5)	152.6 (3)
O3a-Mg2-O3b	75.7 (2)	75.7 (3)	76.0 (4)	75.6 (3)
O1b-Mg2-O3b	88.9 (3)	89.9 (4)	89.2 (4)	89.6 (3)

Table 3: Variation of the bond angles of synthetic $MgSiO_3$ orthoenstatite with pressure.

Angle\P(GPa)	0.00	1.04	1.95	3.27
O2a-TA-O3a	99.9 (4)	99.6 (5)	99.1 (6)	100.3 (4)
O2a-TA-O1a	117.1 (4)	118.1 (6)	116.6 (6)	116.7 (4)
O2a-TA-O3a	113.4 (4)	113.6 (5)	113.4 (6)	113.8 (4)
O3a-TA-O1a	112.7 (4)	112.4 (5)	113.6 (6)	113.2 (4)
O3a-TA-O3a	105.6 (3)	105.3 (4)	103.7 (5)	104.6 (3)
O1a-TA-O3a	107.5 (4)	107.1 (5)	108.8 (5)	107.6 (4)
O2b-TB-O1b	116.9 (4)	117.7 (6)	116.7 (6)	117.5 (4)
O2b-TB-O3b	105.4 (3)	104.2 (4)	106.0 (6)	105.1 (3)
O2b-TB-O3b	109.9 (4)	109.6 (5)	109.8 (6)	110.0 (4)
O1b-TB-O3b	107.0 (4)	107.6 (5)	107.1 (6)	107.9 (4)
O1b-TB-O3b	106.2 (4)	106.7 (5)	105.3 (6)	105.7 (4)
O3b-TB-O3b	111.5 (3)	111.1 (4)	112.1 (6)	110.6 (3)
O3a-O3a-O3a	158.7 (5)	158.9 (8)	159.1 (9)	158.7 (6)
TA-O3a-TA	134.8 (5)	134.5 (7)	133.0 (8)	133.8 (5)
O3b-O3b-O3b	139.0 (5)	138.3 (7)	137.7 (7)	137.1 (5)
TB-O3b-TB	128.5 (5)	126.8 (6)	127.1 (7)	125.9 (4)

Table 3: (cont.) Variation of the bond angles of synthetic $MgSiO_3$ orthoenstatite with pressure.

P (GPa)	4.09	4.95	5.85	7.00	8.10
O1a-Mg1-O1a	93.3 (4)	93.2 (5)	95.1 (5)	93.5 (4)	95.4 (6)
O1a-Mg1-O2a	90.4 (4)	89.8 (5)	90.2 (5)	89.7 (4)	90.4 (5)
O1a-Mg1-O1b	85.8 (4)	86.0 (4)	85.2 (4)	85.1 (4)	86.6 (5)
O1a-Mg1-O1b	81.5 (4)	81.7 (4)	82.6 (5)	82.3 (4)	82.3 (5)
O1a-Mg1-O2b	178.0 (4)	177.5 (4)	177.5 (5)	177.7 (4)	177.5 (5)
O1a-Mg1-O2a	95.4 (4)	94.6 (5)	92.7 (6)	94.0 (4)	92.8 (5)
O1a-Mg1-O1b	177.1 (5)	176.9 (6)	178.4 (6)	176.9 (6)	177.6 (6)
O1a-Mg1-O1b	85.5 (4)	85.8 (5)	87.3 (5)	85.3 (4)	86.9 (5)
O1a-Mg1-O2b	85.2 (4)	84.8 (5)	83.1 (5)	85.0 (4)	83.0 (5)
O2a-Mg1-O1b	87.4 (4)	88.4 (5)	88.9 (5)	88.7 (4)	88.6 (6)
O2a-Mg1-O1b	171.9 (5)	171.5 (5)	172.8 (7)	171.9 (5)	172.7 (6)
O2a-Mg1-O2b	91.1 (4)	92.0 (5)	91.7 (6)	92.1 (5)	91.6 (5)
O1b-Mg1-O1b	91.6 (4)	91.1 (5)	91.2 (5)	91.8 (4)	91.9 (5)
O1b-Mg1-O2b	95.7 (4)	95.9 (5)	96.6 (5)	96.4 (4)	95.0 (5)
O1b-Mg1-O2b	97.1 (4)	96.5 (5)	95.5 (5)	95.9 (4)	95.6 (5)
O1a-Mg2-O2b	84.1 (4)	84.0 (5)	82.6 (4)	83.7 (4)	82.8 (5)
O1a-Mg2-O2a	87.0 (4)	87.0 (4)	87.2 (5)	86.7 (4)	87.2 (5)
O1a-Mg2-O3a	108.0 (4)	108.0 (5)	107.3 (5)	107.9 (4)	107.3 (6)
O1a-Mg2-O1b	83.8 (4)	84.4 (5)	84.7 (6)	83.9 (5)	85.2 (5)
O1a-Mg2-O3b	172.4 (4)	172.6 (4)	173.6 (5)	173.1 (4)	173.9 (5)
O2b-Mg2-O2a	170.8 (5)	170.8 (5)	169.8 (5)	170.4 (4)	169.9 (6)
O2b-Mg2-O3a	110.1 (4)	109.9 (5)	111.4 (5)	110.8 (4)	111.3 (6)
O2b-Mg2-O1b	94.4 (5)	93.8 (5)	93.1 (5)	94.5 (4)	93.1 (5)
O2b-Mg2-O3b	100.6 (4)	100.3 (5)	101.0 (4)	100.3 (4)	100.7 (5)
O2a-Mg2-O3a	70.8 (4)	71.1 (4)	71.2 (5)	70.8 (4)	70.9 (5)
O2a-Mg2-O1b	86.6 (4)	87.4 (4)	86.5 (5)	86.0 (4)	86.8 (5)
O2a-Mg2-O3b	88.5 (4)	88.9 (4)	89.2 (5)	89.3 (4)	89.4 (5)
O3a-Mg2-O1b	153.6 (4)	154.0 (5)	153.7 (5)	152.8 (4)	153.4 (5)
O3a-Mg2-O3b	76.3 (3)	76.4 (4)	76.6 (5)	76.0 (4)	76.2 (4)
O1b-Mg2-O3b	89.8 (4)	89.3 (5)	89.8 (4)	90.2 (4)	89.6 (5)

Table 3: (cont.) Variation of the bond angles of synthetic $MgSiO_3$ orthoenstatite with pressure.

P (GPa)	4.09	4.95	5.85	7.00	8.10
O2a-TA-O3a	99.9 (5)	99.8 (6)	100.1 (7)	100.2 (5)	99.9 (6)
O2a-TA-O1a	117.8 (5)	117.0 (6)	114.7 (8)	116.0 (6)	115.2 (7)
O2a-TA-O3a	113.6 (5)	113.5 (6)	114.4 (7)	113.4 (5)	113.9 (6)
O3a-TA-O1a	113.6 (5)	113.7 (6)	113.6 (6)	114.4 (5)	114.2 (6)
O3a-TA-O3a	103.9 (4)	103.4 (5)	103.9 (5)	104.0 (4)	103.8 (5)
O1a-TA-O3a	107.2 (5)	108.5 (6)	109.5 (6)	108.3 (5)	109.2 (5)
O2b-TB-O1b	116.9 (5)	117.2 (6)	118.6 (7)	117.8 (6)	117.1 (6)
O2b-TB-O3b	105.8 (5)	105.5 (5)	105.1 (5)	105.7 (4)	104.4 (6)
O2b-TB-O3b	109.7 (5)	110.4 (6)	110.1 (6)	110.3 (4)	110.6 (6)
O1b-TB-O3b	107.1 (5)	106.9 (6)	106.9 (6)	106.8 (5)	108.8 (6)
O1b-TB-O3b	105.7 (5)	105.8 (6)	105.3 (6)	104.6 (5)	106.0 (6)
O3b-TB-O3b	111.6 (4)	111.1 (5)	110.8 (5)	111.6 (4)	109.9 (6)
O3a-O3a-O3a	159.7 (8)	159.4 (9)	159.3 (9)	159.0 (9)	158.2 (9)
TA-O3a-TA	133.6 (7)	131.9 (8)	133.4 (8)	132.7 (6)	132.4 (9)
O3b-O3b-O3b	136.8 (7)	135.4 (8)	136.1 (9)	135.5 (7)	136.2 (8)
TB-O3b-TB	126.4 (6)	125.6 (7)	125.3 (7)	125.6 (6)	124.5 (7)

Table 3: (cont.) Variation of the bond angles of synthetic $MgSiO_3$ orthoenstatite with pressure.

P (GPa)		0.00	0.83	1.71	2.84	3.65
M1	x	0.3758 (1)	0.3758 (1)	0.3760 (1)	0.3757 (1)	0.3759 (2)
	y	0.6539 (1)	0.6542 (2)	0.6555 (3)	0.6559 (3)	0.6563 (4)
	z	0.8741 (2)	0.8717 (3)	0.8692 (4)	0.8660 (4)	0.8644 (5)
	B_{iso}	0.36 (2)	0.53 (4)	0.44 (4)	0.31 (5)	0.44 (5)
M2	x	0.3777 (1)	0.3779 (1)	0.3783 (1)	0.3784 (1)	0.3787 (2)
	y	0.4855 (1)	0.4843 (2)	0.4831 (3)	0.4820 (3)	0.4812 (3)
	z	0.3662 (2)	0.3638 (4)	0.3596 (4)	0.3579 (4)	0.3557 (6)
	B_{iso}	0.54 (2)	0.54 (4)	0.45 (5)	0.35 (5)	0.46 (6)
TA	x	0.2724 (1)	0.2721 (2)	0.2716 (2)	0.2717 (3)	0.2715 (3)
	y	0.3390 (1)	0.3396 (5)	0.3397 (7)	0.3410 (8)	0.3418 (8)
	z	0.0486 (4)	0.0466 (6)	0.0438 (7)	0.0405 (8)	0.037 (1)
	B_{iso}	0.29 (3)	0.32 (6)	0.24 (6)	0.20 (7)	0.28 (9)
TB	x	0.4732 (1)	0.4733 (2)	0.4728 (2)	0.4727 (2)	0.4726 (3)
	y	0.3346 (1)	0.3350 (5)	0.3332 (7)	0.3339 (8)	0.3343 (9)
	z	0.7890 (5)	0.7904 (6)	0.7909 (6)	0.7929 (8)	0.7943 (9)
	B_{iso}	0.22 (3)	0.19 (6)	0.21 (7)	0.24 (8)	0.32 (9)
O1a	x	0.1847 (2)	0.1856 (5)	0.1859 (5)	0.1848 (6)	0.1839 (7)
	y	0.3340 (4)	0.342 (1)	0.340 (1)	0.342 (2)	0.341 (2)
	z	0.039 (1)	0.036 (1)	0.031 (2)	0.029 (2)	0.029 (2)
	B_{iso}	0.47 (6)	0.32 (15)	0.26 (17)	0.18 (20)	0.61 (23)
O2a	x	0.3119 (2)	0.3118 (5)	0.3118 (5)	0.3107 (7)	0.3098 (8)
	y	0.4961 (4)	0.499 (1)	0.500 (1)	0.501 (2)	0.502 (2)
	z	0.060 (1)	0.058 (1)	0.052 (2)	0.049 (2)	0.046 (2)
	B_{iso}	0.52 (6)	0.63 (17)	0.77 (20)	0.42 (21)	0.53 (25)
O3a	x	0.3023 (2)	0.3021 (5)	0.3016 (5)	0.3022 (6)	0.3025 (7)
	y	0.2360 (4)	0.234 (1)	0.234 (1)	0.234 (1)	0.238 (2)
	z	0.818 (1)	0.813 (2)	0.810 (2)	0.807 (2)	0.804 (3)
	B_{iso}	0.58 (6)	0.34 (16)	0.02 (17)	0.09 (19)	0.17 (21)
O1b	x	0.5611 (2)	0.5611 (5)	0.5599 (6)	0.5588 (6)	0.5605 (8)
	y	0.3374 (4)	0.337 (1)	0.336 (1)	0.335 (2)	0.337 (2)
	z	0.785 (1)	0.787 (1)	0.789 (2)	0.788 (2)	0.792 (2)
	B_{iso}	0.35 (6)	0.42 (14)	0.68 (18)	0.17 (18)	0.67 (23)
O2b	x	0.4330 (2)	0.4316 (5)	0.4329 (5)	0.4334 (6)	0.4329 (6)
	y	0.4804 (4)	0.480 (1)	0.481 (1)	0.483 (1)	0.484 (2)
	z	0.693 (1)	0.693 (2)	0.691 (2)	0.686 (2)	0.686 (2)
	B_{iso}	0.55 (7)	0.41 (16)	0.33 (18)	0.02 (19)	0.15 (23)
O3b	x	0.4477 (2)	0.4467 (7)	0.4477 (7)	0.4466 (7)	0.4467 (8)
	y	0.2027 (4)	0.204 (1)	0.199 (1)	0.197 (1)	0.197 (1)
	z	0.584 (1)	0.590 (2)	0.591 (1)	0.594 (2)	0.599 (2)
	B_{iso}	0.48 (6)	0.67 (20)	0.12 (18)	0.08 (23)	0.30 (26)

Table 4: Positional parameters of synthetic $FeSiO_3$ orthoferrosilite at high pressure.

Table 5: (overleaf, Page 281) Bond lengths (< 2.8 Å) of synthetic $FeSiO_3$ orthoferrosilite at high pressure.

P (GPa)	0.00	0.83	1.71	2.84	3.65
Fe1-O1a	2.200(4)	2.212(9)	2.19(1)	2.17(1)	2.16(1)
Fe1-O1a	2.080(5)	2.085(9)	2.097(9)	2.07(1)	2.05(1)
Fe1-O2a	2.092(4)	2.08(1)	2.06(1)	2.06(1)	2.06(1)
Fe1-O1b	2.134(5)	2.129(9)	2.136(9)	2.16(1)	2.13(1)
Fe1-O1b	2.194(4)	2.19(1)	2.17(1)	2.16(1)	2.15(2)
Fe1-O2b	2.119(4)	2.099(9)	2.10(1)	2.10(1)	2.08(1)
Fe2-O1a	2.156(4)	2.16(1)	2.17(1)	2.15(1)	2.16(1)
Fe2-O2a	2.014(5)	2.012(9)	2.02(1)	2.03(1)	2.05(1)
Fe2-O3a	2.456(4)	2.43(1)	2.42(1)	2.40(1)	2.42(1)
Fe2-O1b	2.116(4)	2.12(1)	2.13(1)	2.14(1)	2.11(2)
Fe2-O2b	1.993(5)	1.983(9)	1.998(9)	1.98(1)	1.98(1)
Fe2-O3b	2.600(4)	2.56(1)	2.503(9)	2.45(1)	2.42(1)
TA-O1a	1.615(4)	1.59(1)	1.57(1)	1.60(1)	1.61(1)
TA-O2a	1.602(4)	1.62(1)	1.62(1)	1.60(1)	1.60(1)
TA-O3a	1.661(5)	1.64(1)	1.63(1)	1.64(1)	1.65(1)
TA-O3a	1.624(5)	1.65(1)	1.64(1)	1.64(1)	1.63(1)
TB-O1b	1.620(4)	1.62(1)	1.60(1)	1.58(1)	1.61(1)
TB-O2b	1.597(4)	1.60(1)	1.60(1)	1.61(1)	1.62(1)
TB-O3b	1.674(5)	1.66(1)	1.66(1)	1.67(1)	1.66(1)
TB-O3b	1.652(6)	1.677(8)	1.654(9)	1.66(1)	1.67(1)
O1a-O2a	2.739(5)	2.72(1)	2.72(1)	2.72(2)	2.72(2)
O1a-O3a	2.701(6)	2.68(1)	2.66(1)	2.68(2)	2.69(2)
O1a-O3a	2.630(5)	2.63(1)	2.60(1)	2.63(2)	2.63(2)
O2a-O3a	2.510(6)	2.50(1)	2.50(1)	2.50(2)	2.53(2)
O2a-O3a	2.684(6)	2.72(1)	2.71(2)	2.71(2)	2.68(2)
O3a-O3a	2.632(1)	2.629(2)	2.620(3)	2.612(3)	2.599(2)
O1b-O2b	2.734(5)	2.76(1)	2.72(1)	2.70(1)	2.74(2)
O1b-O3b	2.637(5)	2.64(1)	2.61(1)	2.60(2)	2.63(2)
O1b-O3b	2.639(6)	2.66(1)	2.61(1)	2.62(2)	2.63(2)
O2b-O3b	2.597(6)	2.57(1)	2.61(1)	2.62(2)	2.62(2)
O2b-O3b	2.653(7)	2.67(1)	2.65(1)	2.67(1)	2.69(2)
O3b-O3b	2.756(2)	2.744(6)	2.764(6)	2.764(6)	2.756(8)

P (GPa)	0.00	0.83	1.71	2.84	3.65
O1a-Fe1-O1a	92.3(1)	92.2(4)	91.6(4)	92.7(5)	93.1(5)
O1a-Fe1-O2a	93.3(2)	92.7(4)	92.4(4)	92.4(5)	91.7(6)
O1a-Fe1-O1b	85.3(2)	85.7(4)	86.4(4)	86.1(5)	85.7(5)
O1a-Fe1-O1b	80.5(1)	80.7(3)	81.9(4)	81.8(5)	81.4(6)
O1a-Fe1-O2b	176.5(2)	176.4(3)	176.5(4)	176.5(4)	176.9(6)
O1a-Fe1-O2a	96.2(2)	95.7(4)	95.2(4)	95.0(5)	94.6(5)
O1a-Fe1-O1b	176.3(1)	176.9(4)	176.7(5)	177.0(5)	177.5(6)
O1a-Fe1-O1b	86.8(2)	87.5(3)	87.8(4)	88.7(4)	87.8(5)
O1a-Fe1-O2b	84.7(2)	84.4(4)	85.0(4)	84.4(5)	84.4(5)
O2a-Fe1-O1b	86.7(2)	86.6(4)	87.5(4)	87.9(5)	87.6(6)
O2a-Fe1-O1b	173.2(2)	172.8(4)	173.7(5)	173.3(5)	172.8(6)
O2a-Fe1-O2b	88.8(2)	88.8(4)	88.9(4)	89.9(5)	90.3(6)
O1b-Fe1-O1b	90.1(1)	90.0(4)	89.4(4)	88.3(5)	89.9(5)
O1b-Fe1-O2b	97.6(2)	97.7(4)	97.0(4)	96.7(4)	96.8(5)
O1b-Fe1-O2b	97.5(2)	97.9(4)	97.0(4)	96.1(5)	96.7(6)
O1a-Fe2-O2b	85.9(2)	85.5(4)	85.7(4)	85.2(4)	84.1(5)
O1a-Fe2-O2a	88.8(2)	87.5(4)	86.7(4)	86.3(5)	86.1(5)
O1a-Fe2-O3a	110.0(1)	109.1(4)	108.6(4)	108.9(4)	109.7(5)
O1a-Fe2-O1b	83.3(2)	83.5(3)	83.0(4)	82.8(5)	82.2(5)
O1a-Fe2-O3b	170.2(2)	170.7(3)	170.2(3)	170.3(4)	171.1(5)
O2b-Fe2-O2a	173.6(2)	172.2(4)	172.0(4)	171.3(5)	170.0(6)
O2b-Fe2-O3a	111.0(2)	111.4(4)	112.0(4)	113.1(4)	113.5(5)
O2b-Fe2-O1b	93.8(2)	94.2(4)	93.1(4)	91.6(4)	92.1(5)
O2b-Fe2-O3b	102.6(2)	103.1(4)	102.7(4)	102.9(4)	103.0(5)
O2a-Fe2-O3a	67.5(2)	67.7(4)	68.0(4)	68.1(4)	68.5(5)
O2a-Fe2-O1b	89.3(2)	88.6(4)	88.7(4)	89.2(5)	88.3(5)
O2a-Fe2-O3b	82.9(2)	84.2(4)	85.0(4)	85.8(5)	87.0(5)
O3a-Fe2-O1b	152.2(2)	151.9(4)	152.7(4)	153.0(4)	152.4(5)
O3a-Fe2-O3b	71.6(1)	71.5(3)	73.1(3)	73.0(4)	72.7(5)
O1b-Fe2-O3b	91.3(1)	92.1(4)	91.5(4)	91.7(4)	92.0(5)

Table 6: Bond angles of synthetic $FeSiO_3$ orthoferrosilite at high pressure.

P (GPa)	0.00	0.83	1.71	2.84	3.65
O2a-TA-O3a	100.6(2)	100.2(6)	100.6(6)	101.1(7)	102.2(7)
O2a-TA-O1a	116.8(2)	116.2(5)	116.9(6)	116.3(7)	116.4(7)
O2a-TA-O3a	112.6(2)	113.2(5)	112.6(6)	112.9(7)	112.6(8)
O3a-TA-O1a	111.1(3)	111.8(5)	112.0(6)	112.0(6)	111.1(7)
O3a-TA-O3a	106.5(1)	106.3(4)	106.3(4)	105.5(5)	104.8(6)
O1a-TA-O3a	108.6(2)	108.6(5)	107.9(5)	108.4(6)	109.1(7)
O2b-TB-O1b	116.5(2)	117.7(5)	116.3(5)	115.8(6)	115.6(7)
O2b-TB-O3b	105.1(3)	104.1(5)	106.0(5)	105.5(6)	105.7(7)
O2b-TB-O3b	109.5(2)	109.1(5)	108.8(5)	109.5(6)	109.8(6)
O1b-TB-O3b	106.4(2)	107.3(5)	106.4(6)	106.3(6)	107.0(8)
O1b-TB-O3b	107.5(3)	107.8(5)	106.7(5)	107.8(6)	107.1(8)
O3b-TB-O3b	112.0(2)	110.7(5)	112.8(5)	112.1(6)	111.8(7)
TA-O3a-TA	139.1(3)	138.8(7)	138.7(7)	138.3(8)	138.3(9)
TB-O3b-TB	131.8(3)	130.7(7)	129.8(7)	128.5(7)	128.4(8)
O3a-O3a-O3a	168.9(3)	167.2(9)	167.2(1.0)	167.6(1.0)	170.3(1.2)
O3b-O3b-O3b	143.7(3)	144.4(8)	140.9(8)	139.9(9)	140.1(9)

Table 6: (cont.) Bond angles of synthetic $FeSiO_3$ orthoferrosilite at high pressure.

P (GPa)		0.00	1.54	2.50†	3.17
M1	x	0.3759 (4)	0.3763 (5)	0.3758 (1)	0.3758 (5)
	y	0.6547 (3)	0.6547 (3)	0.6568 (3)	0.6553 (4)
	z	0.8729 (8)	0.8682 (8)	0.8663 (4)	0.8650 (8)
	B_{iso}	0.77 (8)	0.61 (10)	0.36 (6)	0.54 (9)
M2	x	0.3782 (3)	0.3780 (4)	0.3783 (1)	0.3776 (4)
	y	0.4852 (2)	0.4840 (3)	0.4826 (2)	0.4819 (3)
	z	0.3652 (5)	0.3606 (5)	0.3597 (3)	0.3569 (6)
	B_{iso}	0.77 (6)	0.61 (8)	0.33 (4)	0.57 (7)
TA	x	0.2713 (4)	0.2706 (5)	0.2711 (1)	0.2698 (6)
	y	0.3413 (3)	0.3419 (5)	0.3418 (4)	0.3428 (5)
	z	0.0536 (8)	0.0489 (8)	0.0458 (5)	0.0455 (8)
	B_{iso}	0.77 (7)	0.58 (8)	0.26 (5)	0.46 (8)
TB	x	0.4744 (5)	0.4736 (6)	0.4732 (1)	0.4732 (5)
	y	0.3363 (4)	0.3362 (5)	0.3353 (4)	0.3361 (4)
	z	0.7946 (7)	0.7969 (7)	0.7980 (5)	0.7980 (7)
	B_{iso}	0.83 (8)	0.63 (10)	0.24 (5)	0.44 (8)
O1a	x	0.182 (1)	0.181 (1)	0.1832 (3)	0.181 (1)
	y	0.3385 (8)	0.341 (1)	0.3393 (9)	0.340 (1)
	z	0.039 (1)	0.034 (2)	0.034 (1)	0.027 (2)
	B_{iso}	0.71 (17)	0.78 (21)	0.36 (12)	0.51 (19)
O2a	x	0.3088 (9)	0.311 (1)	0.3103 (3)	0.312 (1)
	y	0.5002 (9)	0.500 (1)	0.5023 (8)	0.5034 (9)
	z	0.050 (1)	0.047 (2)	0.047 (1)	0.044 (2)
	B_{iso}	0.75 (18)	0.50 (19)	0.29 (11)	0.37 (20)
O3a	x	0.3012 (8)	0.303 (1)	0.3037 (3)	0.3023 (9)
	y	0.2280 (9)	0.2296 (9)	0.2282 (8)	0.230 (1)
	z	0.821 (2)	0.825 (2)	0.823 (1)	0.821 (2)
	B_{iso}	1.17 (20)	0.45 (21)	0.07 (10)	0.83 (22)
O1b	x	0.563 (1)	0.562 (1)	0.5617 (3)	0.564 (1)
	y	0.3382 (8)	0.337 (1)	0.3364 (8)	0.341 (1)
	z	0.798 (2)	0.805 (2)	0.801 (1)	0.821 (2)
	B_{iso}	1.48 (20)	0.99 (23)	0.45 (11)	0.76 (22)
O2b	x	0.4327 (9)	0.434 (1)	0.4335 (3)	0.4337 (9)
	y	0.4839 (8)	0.487 (1)	0.4828 (8)	0.4862 (9)
	z	0.692 (1)	0.694 (2)	0.691 (1)	0.692 (2)
	B_{iso}	0.77 (17)	0.59 (21)	0.40 (11)	0.27 (21)
O3b	x	0.4486 (9)	0.448 (1)	0.4471 (3)	0.4479 (9)
	y	0.1995 (9)	0.1968 (8)	0.1962 (8)	0.196 (1)
	z	0.596 (1)	0.600 (2)	0.603 (1)	0.603 (2)
	B_{iso}	0.90 (19)	0.64 (22)	0.26 (12)	0.18 (20)

Table 7: Positional parameters of synthetic $Mg_{0.6}Fe_{0.4}SiO_3$ orthopyroxene at high pressure. Note that data marked with a cross (†) was collected from crystal #2; unmarked data was obtained from crystal #1.

P (GPa)		4.14	4.76	5.77†	6.59†	7.50†
M1	x	0.3758 (3)	0.3761 (3)	0.3760 (1)	0.3763 (2)	0.3764 (2)
	y	0.6561 (7)	0.6570 (6)	0.6566 (6)	0.6576 (5)	0.6576 (4)
	z	0.8647 (9)	0.8626 (9)	0.8625 (5)	0.8612 (6)	0.8595 (5)
	B_{iso}	0.69 (11)	0.47 (13)	0.07 (6)	0.06 (7)	0.23 (7)
M2	x	0.3784 (2)	0.3782 (2)	0.3784 (1)	0.3783 (1)	0.3783 (1)
	y	0.4827 (4)	0.4813 (4)	0.4809 (2)	0.4802 (3)	0.4797 (3)
	z	0.3570 (6)	0.3570 (6)	0.3350 (3)	0.3544 (4)	0.3534 (4)
	B_{iso}	0.50 (10)	0.55 (9)	0.05 (4)	0.06 (5)	0.21 (5)
TA	x	0.2719 (3)	0.2710 (3)	0.2710 (1)	0.2712 (2)	0.2706 (2)
	y	0.3438 (7)	0.3419 (9)	0.3432 (8)	0.3431 (6)	0.3434 (5)
	z	0.0430 (9)	0.0424 (9)	0.0407 (5)	0.0393 (6)	0.0381 (6)
	B_{iso}	0.31 (9)	0.49 (10)	0.01 (5)	0.01 (6)	0.24 (6)
TB	x	0.4729 (3)	0.4731 (3)	0.4729 (1)	0.4729 (2)	0.4732 (2)
	y	0.3359 (8)	0.3363 (7)	0.3373 (7)	0.3377 (6)	0.3374 (4)
	z	0.8000 (9)	0.8000 (9)	0.7996 (5)	0.8010 (5)	0.8018 (6)
	B_{iso}	0.40 (9)	0.32 (10)	0.01 (4)	0.02 (5)	0.28 (6)
O1a	x	0.1827 (6)	0.1830 (7)	0.1826 (3)	0.1827 (4)	0.1834 (4)
	y	0.338 (1)	0.340 (1)	0.340 (1)	0.340 (1)	0.338 (1)
	z	0.028 (2)	0.031 (2)	0.030 (1)	0.028 (1)	0.027 (1)
	B_{iso}	0.28 (20)	0.27 (21)	0.04 (11)	0.05 (13)	0.50 (15)
O2a	x	0.3108 (6)	0.3085 (8)	0.3097 (3)	0.3091 (4)	0.3087 (5)
	y	0.507 (1)	0.509 (1)	0.507 (1)	0.506 (1)	0.508 (1)
	z	0.042 (2)	0.038 (2)	0.040 (1)	0.040 (1)	0.038 (1)
	B_{iso}	0.39 (24)	0.69 (26)	0.24 (12)	0.10 (14)	0.47 (15)
O3a	x	0.3031 (8)	0.3023 (6)	0.3038 (3)	0.3043 (4)	0.3042 (4)
	y	0.232 (1)	0.230 (1)	0.229 (1)	0.230 (1)	0.2273 (9)
	z	0.820 (2)	0.813 (2)	0.817 (1)	0.815 (1)	0.815 (1)
	B_{iso}	0.43 (23)	0.02 (20)	0.03 (11)	0.07 (14)	0.25 (14)
O1b	x	0.5605 (5)	0.5619 (7)	0.5611 (3)	0.5614 (4)	0.5596 (4)
	y	0.339 (2)	0.337 (1)	0.337 (1)	0.339 (1)	0.339 (1)
	z	0.798 (2)	0.801 (2)	0.804 (1)	0.806 (1)	0.803 (1)
	B_{iso}	0.54 (20)	0.68 (22)	0.18 (11)	0.06 (12)	0.33 (13)
O2b	x	0.4334 (6)	0.4330 (5)	0.4334 (3)	0.4337 (4)	0.4342 (4)
	y	0.487 (1)	0.486 (1)	0.481 (1)	0.485 (1)	0.485 (1)
	z	0.688 (2)	0.688 (2)	0.689 (1)	0.687 (1)	0.688 (1)
	B_{iso}	0.18 (22)	0.02 (21)	0.04 (12)	0.07 (14)	0.30 (14)
O3b	x	0.4454 (7)	0.4458 (7)	0.4455 (3)	0.4454 (4)	0.4450 (5)
	y	0.194 (1)	0.195 (1)	0.190 (1)	0.194 (1)	0.1921 (9)
	z	0.607 (2)	0.605 (2)	0.605 (1)	0.608 (2)	0.611 (1)
	B_{iso}	0.24 (22)	0.01 (24)	0.00 (11)	0.24 (15)	0.35 (15)

Table 7: (cont.) Positional parameters of synthetic $Mg_{0.6}Fe_{0.4}SiO_3$ orthopyroxene at high pressure. Note that data marked with a cross (†) was collected from crystal #2; unmarked data was obtained from crystal #1.

P (GPa)	0.00	1.54	2.50†	3.17
M1-O1a	2.13(1)	2.13(1)	2.134(7)	2.10(1)
M1-O1a	2.04(1)	2.03(1)	2.025(6)	2.03(1)
M1-O2a	2.06(1)	2.04(1)	2.025(7)	1.99(1)
M1-O1b	2.05(1)	2.03(2)	2.057(6)	2.02(1)
M1-O1b	2.17(1)	2.16(1)	2.145(7)	2.15(1)
M1-O2b	2.07(1)	2.03(1)	2.052(7)	2.03(1)
M2-O1a	2.12(1)	2.09(1)	2.126(7)	2.09(1)
M2-O2a	2.08(1)	2.04(2)	2.049(5)	2.01(1)
M2-O3a	2.37(1)	2.34(1)	2.303(6)	2.32(1)
M2-O1b	2.09(1)	2.11(1)	2.099(7)	2.07(1)
M2-O2b	1.98(1)	2.00(1)	1.986(5)	2.01(1)
M2-O3b	2.52(1)	2.46(1)	2.398(6)	2.41(1)
TA-O1a	1.64(1)	1.63(2)	1.602(6)	1.62(2)
TA-O2a	1.57(1)	1.58(1)	1.602(8)	1.61(1)
TA-O3a	1.63(1)	1.67(1)	1.664(6)	1.67(1)
TA-O3a	1.67(1)	1.64(1)	1.639(6)	1.63(1)
TB-O1b	1.62(1)	1.62(2)	1.611(6)	1.65(2)
TB-O2b	1.61(1)	1.61(1)	1.596(7)	1.60(1)
TB-O3b	1.67(1)	1.67(1)	1.665(7)	1.66(1)
TB-O3b	1.67(1)	1.66(1)	1.674(6)	1.66(1)
O1a-O2a	2.74(2)	2.75(2)	2.725(9)	2.79(2)
O1a-O3a	2.72(2)	2.75(2)	2.712(7)	2.75(2)
O1a-O3a	2.67(2)	2.66(2)	2.640(8)	2.63(2)
O1a-O1b	2.79(2)	2.79(2)	-	2.74(2)
O1a-O2b	2.74(2)	2.72(2)	2.749(9)	2.72(2)
O2a-O3a	2.48(1)	2.50(1)	2.496(9)	2.51(1)
O2a-O3a	2.70(1)	2.66(1)	2.71(1)	2.67(1)
O3a-O3a	2.634(2)	2.617(2)	2.617(2)	2.604(2)

Table 8: Variation of bond lengths (< 2.8 Å) of synthetic $Mg_{0.6}Fe_{0.4}SiO_3$ orthopyroxene with pressure (P < 4 GPa). Note that data marked with a cross (†) was collected from crystal #2; unmarked data was obtained from crystal #1.

P (GPa)	0.00	1.54	2.50†	3.17
O1b-O2b	2.77(2)	2.75(2)	2.728(8)	2.76(2)
O1b-O3b	2.65(2)	2.64(3)	2.644(8)	2.68(2)
O1b-O3b	2.63(2)	2.60(3)	2.622(8)	2.62(2)
O2b-O3b	2.60(1)	2.62(1)	2.61(1)	2.61(1)
O2b-O3b	2.68(1)	2.67(1)	2.667(9)	2.67(1)
O3b-O3b	2.755(5)	2.757(6)	2.761(5)	2.751(6)

Table 8: (cont.) Variation of bond lengths (< 2.8 Å) of synthetic $Mg_{0.6}Fe_{0.4}SiO_3$ orthopyroxene with pressure (P < 4 GPa). Note that data marked with a cross (†) was collected from crystal #2; unmarked data was obtained from crystal #1.

P (GPa)	4.14	4.76	5.77†	6.59†	7.50†
M1-O1a	2.09 (1)	2.12 (1)	2.10 (1)	2.09 (1)	2.083 (9)
M1-O1a	2.03 (1)	2.01 (1)	2.008 (6)	2.010 (7)	2.015 (8)
M1-O2a	1.98 (1)	2.00 (1)	1.99 (1)	2.01 (1)	2.002 (9)
M1-O1b	2.09 (1)	2.07 (1)	2.057 (7)	2.046 (8)	2.076 (8)
M1-O1b	2.15 (1)	2.11 (1)	2.12 (1)	2.12 (1)	2.121 (9)
M1-O2b	2.03 (1)	2.03 (1)	2.06 (1)	2.03 (1)	2.026 (9)
M2-O1a	2.11 (1)	2.11 (1)	2.12 (1)	2.11 (1)	2.129 (9)
M2-O2a	2.05 (1)	2.08 (1)	2.054 (6)	2.049 (7)	2.057 (7)
M2-O3a	2.33 (1)	2.32 (1)	2.28 (1)	2.275 (9)	2.248 (8)
M2-O1b	2.08 (1)	2.09 (1)	2.09 (1)	2.08 (1)	2.093 (9)
M2-O2b	1.98 (1)	1.97 (1)	1.981 (6)	1.978 (7)	1.988 (7)
M2-O3b	2.35 (1)	2.36 (1)	2.31 (1)	2.317 (9)	2.283 (8)
TA-O1a	1.62 (1)	1.59 (1)	1.601 (6)	1.600 (8)	1.575 (9)
TA-O2a	1.60 (1)	1.61 (1)	1.59 (1)	1.58 (1)	1.587 (9)
TA-O3a	1.67 (1)	1.63 (1)	1.659 (7)	1.660 (8)	1.660 (8)
TA-O3a	1.61 (1)	1.63 (1)	1.63 (1)	1.628 (9)	1.637 (8)
TB-O1b	1.59 (1)	1.61 (1)	1.595 (6)	1.599 (8)	1.559 (8)
TB-O2b	1.61 (1)	1.61 (1)	1.55 (1)	1.58 (1)	1.571 (9)
TB-O3b	1.67 (1)	1.67 (1)	1.70 (1)	1.67 (1)	1.674 (9)
TB-O3b	1.68 (1)	1.67 (1)	1.662 (7)	1.672 (8)	1.679 (8)

Table 8: (cont.) Variation of bond lengths (< 2.8 Å) of synthetic $Mg_{0.6}Fe_{0.4}SiO_3$ orthopyroxene with pressure (P > 4 GPa). Note that data marked with a cross (†) was collected from crystal #2; unmarked data was obtained from crystal #1.

P (GPa)	4.14	4.76	5.77†	6.59†	7.50†
O1a-O2a	2.77(2)	2.71(2)	2.72(1)	2.70(1)	2.70(1)
O1a-O3a	2.72(1)	2.68(2)	2.707(8)	2.71(1)	2.69(1)
O1a-O3a	2.61(1)	2.62(2)	2.634(9)	2.63(1)	2.62(1)
O1a-O1b	2.78(1)	2.78(2)	2.788(8)	2.781(9)	2.80(1)
O1a-O2b	2.73(2)	2.72(2)	2.74(1)	2.72(1)	2.75(1)
O2a-O3a	2.54(2)	2.53(2)	2.50(2)	2.49(1)	2.49(1)
O2a-O3a	2.67(2)	2.70(2)	2.69(2)	2.67(1)	2.69(1)
O3a-O3a	2.594(3)	2.596(3)	2.592(3)	2.585(3)	2.587(2)
O1b-O2b	2.71(1)	2.74(2)	2.69(1)	2.70(1)	2.66(1)
O1b-O3b	2.63(2)	2.64(2)	2.66(1)	2.65(1)	2.62(1)
O1b-O3b	2.64(2)	2.64(2)	2.611(8)	2.62(1)	2.61(1)
O2b-O3b	2.61(1)	2.59(1)	2.58(2)	2.57(1)	2.58(1)
O2b-O3b	2.69(2)	2.68(1)	2.61(1)	2.67(1)	2.66(1)
O3b-O3b	2.753(7)	2.745(7)	2.770(9)	2.740(7)	2.748(5)

Table 8: (cont.) Variation of bond lengths (< 2.8 Å) of synthetic $Mg_{0.6}Fe_{0.4}SiO_3$ orthopyroxene with pressure (P > 4 GPa). Note that data marked with a cross (†) was collected from crystal #2; unmarked data was obtained from crystal #1.

P (GPa)	0.00	1.54	2.50†	3.17
O1a-M1-O1a	93.9(6)	94.3(7)	93.7(3)	94.4(7)
O1a-M1-O2a	92.1(5)	92.6(6)	90.8(3)	92.9(5)
O1a-M1-O1b	84.6(5)	84.6(5)	85.3(2)	85.4(6)
O1a-M1-O1b	80.9(4)	81.2(5)	82.3(3)	80.0(5)
O1a-M1-O2b	176.5(4)	176.4(5)	177.7(3)	176.3(5)
O1a-M1-O2a	95.4(5)	95.7(6)	94.9(3)	96.8(6)
O1a-M1-O1b	176.0(5)	176.0(6)	177.3(3)	177.0(7)
O1a-M1-O1b	83.8(5)	84.2(6)	85.8(3)	83.7(5)
O1a-M1-O2b	83.9(5)	84.2(6)	84.8(3)	84.2(6)
O2a-M1-O1b	88.4(6)	88.3(6)	87.7(3)	86.3(6)
O2a-M1-O1b	172.9(6)	173.7(6)	173.1(3)	172.9(5)
O2a-M1-O2b	90.7(4)	90.8(5)	91.1(3)	90.7(4)
O1b-M1-O1b	92.3(7)	91.8(7)	91.5(3)	93.3(7)
O1b-M1-O2b	97.4(6)	96.6(6)	96.1(3)	95.8(6)
O1b-M1-O2b	96.2(6)	95.4(6)	95.8(3)	96.4(6)
O1a-M2-O2b	84.1(5)	83.2(6)	83.8(2)	83.3(6)
O1a-M2-O2a	88.4(5)	88.8(6)	86.8(3)	88.1(5)
O1a-M2-O3a	109.4(6)	109.4(7)	108.1(2)	109.6(7)
O1a-M2-O1b	83.2(4)	83.3(6)	83.6(3)	82.5(5)
O1a-M2-O3b	170.9(3)	171.4(4)	171.4(3)	170.8(3)
O2b-M2-O2a	171.9(7)	171.8(7)	170.6(3)	171.4(5)
O2b-M2-O3a	112.1(4)	112.0(6)	112.1(3)	112.5(4)
O2b-M2-O1b	95.6(6)	94.6(6)	94.3(3)	94.5(6)
O2b-M2-O3b	102.7(5)	102.6(6)	102.7(2)	102.2(5)
O2a-M2-O3a	67.4(4)	69.1(5)	69.7(3)	70.4(5)
O2a-M2-O1b	86.8(5)	86.3(6)	86.0(3)	84.5(6)
O2a-M2-O3b	85.1(4)	85.6(5)	86.8(2)	86.4(5)
O3a-M2-O1b	150.3(4)	151.4(4)	151.8(2)	151.2(4)
O3a-M2-O3b	73.9(4)	74.7(5)	74.9(2)	75.4(4)
O1b-M2-O3b	90.1(5)	89.8(5)	90.2(2)	89.7(5)

Table 9: Variation of bond angles of synthetic $Mg_{0.6}Fe_{0.4}SiO_3$ orthopyroxene with pressure (P < 4 GPa). Note that data marked with a cross (†) was collected from crystal #2; unmarked data was obtained from crystal #1.

P (GPa)	0.00	1.54	2.50†	3.17
O2a-TA-O3a	101.7(6)	100.2(7)	99.6(3)	99.9(7)
O2a-TA-O1a	116.6(7)	117.8(8)	116.5(4)	119.5(8)
O2a-TA-O3a	112.8(7)	111.6(8)	113.7(3)	110.8(7)
O3a-TA-O1a	112.4(7)	113.0(8)	112.3(3)	113.5(7)
O3a-TA-O3a	106.0(5)	104.5(7)	104.8(3)	104.1(6)
O1a-TA-O3a	107.0(6)	108.8(7)	109.1(3)	108.0(7)
O2b-TB-O1b	118.0(7)	117.3(8)	116.6(3)	115.9(8)
O2b-TB-O3b	104.9(7)	106.5(8)	106.0(3)	106.4(7)
O2b-TB-O3b	109.4(7)	109.5(7)	109.3(4)	109.8(7)
O1b-TB-O3b	107.4(7)	107.1(8)	107.6(3)	108.2(7)
O1b-TB-O3b	106.0(7)	104.7(8)	105.9(3)	104.7(8)
O3b-TB-O3b	111.3(6)	111.9(7)	111.6(3)	111.9(6)
TA-O3a-TA	137.1(1.0)	135.2(1.2)	134.7(4)	135.3(1.1)
TB-O3b-TB	130.0(9)	129.2(1.0)	127.4(4)	128.6(9)
O3a-O3a-O3a	162.9(7)	164.1(7)	162.0(6)	164.7(8)
O3b-O3b-O3b	141.9(6)	140.1(7)	138.8(5)	139.4(7)

Table 9: (cont.) Variation of bond angles of synthetic $Mg_{0.6}Fe_{0.4}SiO_3$ orthopyroxene with pressure ($P < 4$ GPa). Note that data marked with a cross (†) was collected from crystal #2; unmarked data was obtained from crystal #1.

P (GPa)	4.14	4.76	5.77†	6.59†	7.50†
O1a-M1-O1a	93.5(5)	94.0(5)	94.0(3)	94.0(4)	93.2(3)
O1a-M1-O2a	91.0(6)	89.8(6)	90.4(4)	90.2(4)	89.1(4)
O1a-M1-O1b	86.0(5)	85.0(5)	85.4(4)	85.8(3)	86.3(3)
O1a-M1-O1b	82.0(5)	82.3(5)	82.6(4)	82.6(4)	83.5(4)
O1a-M1-O2b	176.7(6)	177.7(5)	178.4(4)	178.1(4)	178.6(3)
O1a-M1-O2a	95.6(5)	93.7(6)	94.6(4)	94.3(4)	94.2(4)
O1a-M1-O1b	176.6(6)	177.7(6)	177.0(5)	177.9(4)	177.5(4)
O1a-M1-O1b	86.0(5)	86.4(5)	85.9(4)	86.1(4)	86.9(3)
O1a-M1-O2b	84.5(5)	84.4(5)	84.9(4)	84.6(4)	85.7(3)
O2a-M1-O1b	87.8(5)	88.4(5)	88.3(3)	87.8(3)	88.3(3)
O2a-M1-O1b	172.9(7)	172.1(6)	173.0(5)	172.8(4)	172.5(4)
O2a-M1-O2b	91.7(6)	92.0(6)	91.0(5)	91.3(4)	91.8(4)
O1b-M1-O1b	90.6(5)	91.4(5)	91.0(4)	91.9(3)	90.7(3)
O1b-M1-O2b	95.9(5)	96.6(5)	95.8(4)	95.5(4)	94.8(3)
O1b-M1-O2b	95.3(5)	95.9(5)	96.2(4)	95.9(4)	95.7(4)
O1a-M2-O2b	83.8(5)	83.3(4)	84.0(3)	83.4(3)	83.7(3)
O1a-M2-O2a	86.5(5)	86.0(5)	86.4(4)	86.1(3)	85.3(3)
O1a-M2-O3a	109.0(5)	108.6(5)	108.7(3)	109.2(3)	108.7(3)
O1a-M2-O1b	83.1(5)	82.8(5)	83.0(4)	83.0(4)	83.0(3)
O1a-M2-O3b	171.1(5)	171.3(4)	170.8(3)	171.4(4)	171.0(3)
O2b-M2-O2a	170.2(5)	169.3(5)	170.3(5)	169.5(4)	169.0(3)
O2b-M2-O3a	112.5(5)	113.6(4)	111.8(4)	113.0(4)	113.2(3)
O2b-M2-O1b	92.8(5)	93.2(5)	94.3(4)	93.4(3)	92.4(3)
O2b-M2-O3b	103.0(4)	103.0(4)	102.5(3)	102.6(3)	102.5(3)
O2a-M2-O3a	70.6(5)	69.9(5)	70.3(4)	70.2(3)	70.5(3)
O2a-M2-O1b	86.3(5)	85.5(5)	85.7(4)	85.8(3)	86.4(3)
O2a-M2-O3b	86.8(4)	87.6(5)	87.3(4)	87.9(3)	88.5(3)
O3a-M2-O1b	152.7(5)	151.5(5)	152.1(3)	151.7(3)	152.5(3)
O3a-M2-O3b	74.1(4)	74.5(4)	75.2(3)	74.4(3)	75.1(3)
O1b-M2-O3b	90.7(5)	90.9(5)	89.9(4)	90.4(3)	90.1(3)

Table 9: (cont.) Variation of bond angles of synthetic $Mg_{0.6}Fe_{0.4}SiO_3$ orthopyroxene with pressure (P > 4 GPa). Note that data marked with a cross (†) was collected from crystal #2; unmarked data was obtained from crystal #1.

P (GPa)	4.14	4.76	5.77†	6.59†	7.50†
O2a-TA-O3a	102.1(7)	102.4(7)	100.7(4)	100.7(5)	100.0(5)
O2a-TA-O1a	117.9(6)	115.3(7)	117.1(7)	116.8(5)	117.5(5)
O2a-TA-O3a	112.8(7)	112.8(7)	112.8(5)	112.8(5)	113.2(4)
O3a-TA-O1a	111.5(6)	112.1(6)	112.2(4)	112.5(4)	112.7(4)
O3a-TA-O3a	104.3(6)	105.3(6)	103.9(4)	103.6(4)	103.4(4)
O1a-TA-O3a	107.4(6)	108.4(6)	109.1(5)	109.4(4)	109.0(4)
O2b-TB-O1b	115.5(6)	116.8(6)	117.8(6)	116.7(5)	116.3(4)
O2b-TB-O3b	105.4(6)	104.7(6)	105.0(5)	104.8(5)	105.2(4)
O2b-TB-O3b	109.6(6)	109.8(6)	109.0(5)	110.4(5)	109.6(4)
O1b-TB-O3b	107.9(6)	107.5(6)	107.5(5)	108.1(4)	108.2(4)
O1b-TB-O3b	107.8(6)	107.2(7)	106.6(3)	106.5(4)	107.4(4)
O3b-TB-O3b	110.8(6)	110.9(6)	111.0(4)	110.2(4)	110.0(4)
TA-O3a-TA	136.9(9)	136.6(8)	134.7(4)	134.4(5)	133.3(6)
TB-O3b-TB	126.2(7)	126.9(7)	125.2(6)	126.3(6)	124.9(5)
O3a-O3a-O3a	166.0(1.2)	164.5(1.0)	163.6(1.1)	164.6(9)	162.5(7)
O3b-O3b-O3b	138.5(8)	139.1(8)	135.8(9)	138.4(8)	137.1(6)

Table 9: (cont.) Variation of bond angles of synthetic $Mg_{0.6}Fe_{0.4}SiO_3$ orthopyroxene with pressure (P > 4 GPa). Note that data marked with a cross (†) was collected from crystal #2; unmarked data was obtained from crystal #1.

P (GPa)		0.00	1.04	1.90	3.00
M1	x	0.3757(6)	0.3754(6)	0.376(1)	0.374(1)
	y	0.6529(5)	0.6542(5)	0.6541(6)	0.6541(6)
	z	0.8652(8)	0.8623(8)	0.863(1)	0.861(1)
	B_{iso}	0.08(8)	0.06(12)	0.10(9)	0.23(10)
M2	x	0.3785(6)	0.3780(5)	0.3792(9)	0.3783(8)
	y	0.4842(3)	0.4844(4)	0.4830(5)	0.4821(5)
	z	0.3582(7)	0.3572(6)	0.3546(9)	0.3523(9)
	B_{iso}	0.08*	0.07(10)	0.10*	0.23*
TA	x	0.2701(6)	0.2703(6)	0.268(1)	0.269(1)
	y	0.3424(4)	0.3429(4)	0.3424(6)	0.3433(5)
	z	0.0491(7)	0.0479(7)	0.0458(9)	0.0435(9)
	B_{iso}	0.00(6)	0.01(5)	0.05(7)	0.09(7)
TB	x	0.4740(6)	0.4752(5)	0.4752(9)	0.4750(9)
	y	0.3377(4)	0.3369(5)	0.3371(5)	0.3379(5)
	z	0.8013(6)	0.8022(7)	0.8025(8)	0.8031(9)
	B_{iso}	0.16(8)	0.01*	0.05*	0.09*
O1a	x	0.182(1)	0.181(1)	0.179(2)	0.177(2)
	y	0.340(1)	0.3399(9)	0.343(1)	0.339(1)
	z	0.031(2)	0.032(2)	0.024(2)	0.029(2)
	B_{iso}	0.20(8)	0.07(8)	0.27(12)	0.25(13)
O2a	x	0.312(1)	0.308(1)	0.309(2)	0.311(2)
	y	0.502(1)	0.5036(9)	0.506(2)	0.506(1)
	z	0.050(2)	0.046(2)	0.042(3)	0.036(2)
	B_{iso}	0.20*	0.07*	0.27*	0.25*
O3a	x	0.303(1)	0.303(1)	0.301(2)	0.303(2)
	y	0.2254(9)	0.225(1)	0.223(1)	0.228(1)
	z	0.826(2)	0.825(2)	0.819(2)	0.821(2)
	B_{iso}	0.20*	0.07*	0.27*	0.25*
O1b	x	0.565(1)	0.568(1)	0.566(2)	0.567(2)
	y	0.338(1)	0.338(1)	0.339(1)	0.341(1)
	z	0.806(2)	0.804(2)	0.814(3)	0.809(2)
	B_{iso}	0.20*	0.07*	0.27*	0.25*
O2b	x	0.435(1)	0.432(1)	0.429(2)	0.432(2)
	y	0.4856(8)	0.483(1)	0.485(2)	0.488(1)
	z	0.691(2)	0.689(2)	0.692(2)	0.691(2)
	B_{iso}	0.20*	0.07*	0.27*	0.25*
O3b	x	0.446(1)	0.445(1)	0.445(2)	0.451(2)
	y	0.1943(9)	0.191(1)	0.192(1)	0.191(1)
	z	0.605(2)	0.606(2)	0.609(2)	0.611(2)
	B_{iso}	0.20*	0.07*	0.27*	0.25*

Table 10: Positional parameters of the natural orthopyroxene OPX2 at $P < 4$ GPa. Note that the isotropic temperature factors (B_{iso}) denoted by an asterisk (*) were fixed during the final refinement of the orthopyroxene structure.

P (GPa)		4.03	4.93	6.01
M1	x	0.377(1)	0.378(1)	0.376(1)
	y	0.6550(8)	0.6558(7)	0.6583(9)
	z	0.860(1)	0.858(1)	0.856(1)
	B_{iso}	0.16(13)	0.01(18)	0.16(10)
M2	x	0.378(1)	0.3762(8)	0.3771(9)
	y	0.4818(5)	0.4815(5)	0.4804(7)
	z	0.3525(9)	0.3522(9)	0.351(1)
	B_{iso}	0.16*	0.03(12)	0.16*
TA	x	0.271(1)	0.270(1)	0.268(1)
	y	0.3431(7)	0.3441(6)	0.3423(8)
	z	0.040(1)	0.040(1)	0.040(1)
	B_{iso}	0.04(8)	0.11(7)	0.22(10)
TB	x	0.473(1)	0.472(1)	0.475(1)
	y	0.3385(8)	0.3389(6)	0.3365(8)
	z	0.804(1)	0.8033(9)	0.804(1)
	B_{iso}	0.04*	0.11*	0.22*
O1a	x	0.181(2)	0.179(2)	0.178(3)
	y	0.338(1)	0.339(1)	0.342(2)
	z	0.031(2)	0.021(1)	0.027(3)
	B_{iso}	0.27(14)	0.27(13)	0.47(17)
O2a	x	0.310(2)	0.304(2)	0.306(3)
	y	0.508(1)	0.509(1)	0.509(2)
	z	0.039(3)	0.040(3)	0.034(3)
	B_{iso}	0.27*	0.27*	0.47*
O3a	x	0.305(2)	0.302(2)	0.304(3)
	y	0.227(1)	0.228(1)	0.225(2)
	z	0.819(3)	0.819(2)	0.818(3)
	B_{iso}	0.27*	0.27*	0.47*
O1b	x	0.562(2)	0.562(2)	0.567(3)
	y	0.336(2)	0.337(1)	0.337(2)
	z	0.809(3)	0.811(2)	0.812(3)
	B_{iso}	0.27*	0.27*	0.47*
O2b	x	0.433(2)	0.430(2)	0.432(2)
	y	0.486(2)	0.487(1)	0.487(2)
	z	0.691(3)	0.690(2)	0.689(3)
	B_{iso}	0.27*	0.27*	0.47*
O3b	x	0.444(2)	0.448(2)	0.446(3)
	y	0.192(2)	0.191(1)	0.190(2)
	z	0.609(3)	0.613(2)	0.611(3)
	B_{iso}	0.27*	0.27*	0.47*

Table 10: Positional parameters of the natural orthopyroxene OPX2 at P > 4 GPa. Note that the isotropic temperature factors (B_{iso}) denoted by an asterisk (*) were fixed during the final refinement of the orthopyroxene structure.

P (GPa)	0.00	1.04	1.90	3.00
M1-O1a	2.14 (2)	2.11 (2)	2.11 (2)	2.05 (2)
M1-O1a	2.03 (2)	2.00 (2)	2.01 (2)	1.95 (2)
M1-O2a	2.01 (2)	2.03 (2)	2.01 (2)	1.94 (3)
M1-O1b	2.02 (2)	2.01 (2)	1.97 (2)	2.00 (2)
M1-O1b	2.15 (2)	2.10 (2)	2.13 (2)	2.13 (2)
M1-O2b	2.04 (2)	2.03 (1)	1.97 (2)	1.99 (2)
M2-O1a	2.10 (2)	2.08 (2)	2.05 (3)	2.06 (2)
M2-O2a	2.02 (2)	2.06 (2)	2.07 (2)	2.04 (2)
M2-O3a	2.31 (2)	2.29 (2)	2.30 (2)	2.28 (3)
M2-O1b	2.06 (2)	2.03 (1)	2.04 (2)	2.01 (3)
M2-O2b	2.01 (1)	1.98 (1)	1.97 (2)	2.00 (2)
M2-O3b	2.39 (1)	2.36 (2)	2.32 (2)	2.36 (2)
TA-O1a	1.61 (2)	1.63 (2)	1.62 (3)	1.68 (3)
TA-O2a	1.60 (1)	1.57 (1)	1.61 (2)	1.61 (2)
TA-O3a	1.67 (1)	1.66 (1)	1.64 (2)	1.66 (2)
TA-O3a	1.66 (1)	1.66 (1)	1.68 (2)	1.65 (2)
TB-O1b	1.66 (2)	1.69 (2)	1.65 (3)	1.67 (4)
TB-O2b	1.59 (1)	1.61 (1)	1.64 (2)	1.63 (2)
TB-O3b	1.70 (1)	1.72 (1)	1.71 (2)	1.68 (2)
TB-O3b	1.68 (1)	1.68 (1)	1.69 (2)	1.66 (1)
O1a-O2a	2.76 (2)	2.73 (3)	2.76 (4)	-
O1a-O3a	2.76 (3)	2.75 (3)	2.75 (4)	2.79 (5)
O1a-O3a	2.66 (3)	2.66 (3)	2.67 (4)	2.71 (5)
O1a-O1b	2.78 (2)	2.72 (3)	2.72 (4)	2.67 (4)
O1a-O1b	2.76 (3)	2.69 (3)	2.69 (4)	2.64 (5)
O1a-O2b	2.75 (3)	2.70 (3)	2.62 (4)	2.62 (4)
O2a-O3a	2.45 (1)	2.48 (1)	2.47 (2)	2.50 (2)
O2a-O3a	2.70 (1)	2.70 (1)	2.73 (2)	2.69 (2)
O3a-O3a	2.630 (3)	2.623 (3)	2.622 (4)	2.608 (3)

Table 11: Bond lengths (< 2.8 Å) of natural orthopyroxene OPX2 at P < 4 GPa.

P (GPa)	0.00	1.04	1.90	3.00
O1b-O3b	2.72 (3)	2.77 (3)	2.76 (4)	2.67 (4)
O1b-O3b	2.68 (3)	2.74 (3)	2.69 (4)	2.63 (4)
O2b-O3b	2.61 (1)	2.61 (1)	2.62 (2)	2.65 (2)
O2b-O3b	2.68 (1)	2.66 (1)	2.66 (2)	2.69 (2)
O3b-O3b	2.773 (6)	2.783 (6)	2.775 (9)	2.773 (9)

Table 11: (cont.) Bond lengths (< 2.8 Å) of natural orthopyroxene OPX2 at P < 4 GPa.

P (GPa)	4.03	4.93	6.01
M1-O1a	2.10 (3)	2.07 (3)	2.06 (3)
M1-O1a	1.99 (3)	2.01 (3)	1.94 (3)
M1-O2a	1.99 (3)	2.06 (3)	2.02 (3)
M1-O1b	2.03 (3)	2.01 (3)	1.97 (3)
M1-O1b	2.10 (3)	2.09 (2)	2.04 (3)
M1-O2b	1.98 (2)	1.94 (2)	1.99 (3)
M2-O1a	2.10 (3)	2.04 (3)	2.04 (3)
M2-O2a	2.04 (2)	2.07 (3)	2.08 (3)
M2-O3a	2.24 (3)	2.26 (2)	2.21 (3)
M2-O1b	2.09 (3)	2.10 (3)	2.05 (3)
M2-O2b	2.00 (2)	1.98 (2)	2.00 (2)
M2-O3b	2.30 (2)	2.33 (2)	2.29 (3)
TA-O1a	1.63 (3)	1.64 (3)	1.63 (4)
TA-O2a	1.59 (2)	1.56 (2)	1.59 (3)
TA-O3a	1.68 (2)	1.67 (2)	1.66 (3)
TA-O3a	1.65 (2)	1.63 (2)	1.66 (3)
TB-O1b	1.60 (4)	1.62 (4)	1.67 (4)
TB-O2b	1.58 (2)	1.60 (2)	1.62 (2)
TB-O3b	1.70 (2)	1.67 (2)	1.68 (2)
TB-O3b	1.68 (2)	1.67 (2)	1.67 (2)

Table 11: (cont.) Bond lengths (< 2.8 Å) of natural orthopyroxene OPX2 at P > 4 GPa.

P (GPa)	4.03	4.93	6.01
O1a-O2a	2.76 (4)	2.70 (4)	2.71 (6)
O1a-O3a	2.75 (5)	2.76 (5)	2.77 (6)
O1a-O3a	2.68 (5)	2.64 (5)	2.70 (7)
O1a-O1b	2.75 (5)	2.74 (5)	2.65 (6)
O1a-O1b	2.77 (5)	2.71 (5)	2.65 (6)
O1a-O2b	2.69 (4)	2.63 (4)	2.61 (5)
O2a-O3a	2.50 (2)	2.50 (2)	2.49 (2)
O2a-O3a	2.69 (2)	2.68 (2)	2.69 (2)
O3a-O3a	2.599 (4)	2.590 (3)	2.594 (4)
O1b-O3b	2.67 (5)	2.63 (4)	2.73 (5)
O1b-O3b	2.64 (5)	2.59 (4)	2.67 (6)
O2b-O3b	2.59 (2)	2.61 (2)	2.61 (2)
O2b-O3b	2.65 (2)	2.68 (2)	2.66 (2)
O3b-O3b	2.76 (1)	2.758 (8)	2.76 (1)

Table 11: (cont.) Bond lengths (< 2.8 Å) of natural orthopyroxene OPX2 at $P > 4$ GPa.

P (GPa)	0.00	1.04	1.90	3.00
O1a-M1-O1a	93.8 (8)	94.9 (8)	95.5 (1.3)	97.7 (1.3)
O1a-M1-O2a	91.9 (6)	91.0 (7)	91.9 (1.1)	93.8 (1.1)
O1a-M1-O1b	83.8(6)	82.3 (6)	83.8 (8)	82.2 (1.0)
O1a-M1-O1b	80.1 (6)	79.4 (6)	78.9 (9)	78.2 (1.1)
O1a-M1-O2b	175.7 (6)	177.2 (6)	176.5 (6)	174.2 (1.4)
O1a-M1-O2a	97.2 (7)	96.2 (7)	96.0 (1.1)	98.5 (1.2)
O1a-M1-O1b	175.8 (6)	176.5 (4)	176.6 (1.1)	175.2 (1.3)
O1a-M1-O1b	83.5 (6)	83.2 (6)	82.1 (1.0)	81.5 (1.1)
O1a-M1-O2b	85.3 (7)	84.3 (7)	82.3 (1.1)	83.3 (1.0)
O2a-M1-O1b	86.4 (8)	86.1 (6)	87.4 (1.1)	86.3 (1.0)
O2a-M1-O1b	172.0 (7)	170.2 (7)	170.3 (1.1)	171.9 (1.2)
O2a-M1-O2b	92.4 (6)	91.8 (6)	91.0 (8)	91.7 (9)
O1b-M1-O1b	92.7 (8)	94.1 (8)	94.5 (1.2)	93.8 (1.3)
O1b-M1-O2b	96.9 (7)	98.4 (7)	98.3 (1.0)	96.3 (1.2)
O1b-M1-O2b	95.6 (7)	97.8 (7)	98.1 (1.0)	96.4 (1.1)
O1a-M2-O2b	84.1 (7)	83.4 (6)	81.6 (9)	80.3 (9)
O1a-M2-O2a	88.0 (6)	87.8 (6)	86.8 (8)	89.3 (9)
O1a-M2-O3a	108.0 (9)	108.6 (9)	107.4 (1.3)	110.0 (1.4)
O1a-M2-O1b	83.0 (6)	81.8 (6)	82.2 (9)	80.8 (1.0)
O1a-M2-O3b	171.7 (4)	171.6 (4)	171.6 (5)	170.6 (9)
O2b-M2-O2a	171.9 (7)	170.6 (8)	167.7 (1.1)	169.6 (1.0)
O2b-M2-O3a	111.8 (4)	110.8 (5)	111.2 (6)	112.1 (7)
O2b-M2-O1b	95.3 (6)	96.8 (7)	98.5 (9)	95.7 (1.0)
O2b-M2-O3b	102.2 (6)	102.5 (7)	104.5 (9)	101.7 (1.0)
O2b-M2-O3a	69.3 (5)	69.1 (5)	68.6 (7)	70.6 (7)
O2a-M2-O1b	85.3 (7)	85.1 (6)	83.8 (1.0)	83.4 (1.1)
O2a-M2-O3b	85.8 (5)	86.7 (6)	87.5 (8)	88.7 (8)
O3a-M2-O1b	151.4 (4)	151.3 (4)	149.7 (7)	151.3 (8)
O3a-M2-O3b	74.9 (6)	75.2 (6)	76.1 (9)	77.9 (1.1)
O1b-M2-O3b	91.0 (7)	91.5 (6)	91.1 (9)	89.9 (9)

Table 12: Variation of bond angles with pressure (P < 4 GPa) of natural orthopyroxene OPX2.

P (GPa)	0.00	1.04	1.90	3.00
O2a-TA-O3a	98.1 (8)	99.8 (8)	98.9 (1.2)	99.8 (1.1)
O2a-TA-O1a	118.9 (9)	116.9 (8)	117.1 (1.1)	119.2 (1.2)
O2a-TA-O3a	112.0 (9)	113.4 (9)	112.3 (1.2)	111.0 (1.4)
O3a-TA-O1a	114.1 (9)	113.4 (9)	115.1 (1.4)	113.2 (1.4)
O3a-TA-O3a	104.1 (9)	104.3 (9)	104.7 (1.3)	103.8 (1.3)
O1a-TA-O3a	108.5 (9)	108.2 (9)	108.0 (1.3)	108.7 (1.4)
O2b-TB-O1b	116.8 (8)	119.0 (8)	121.0 (1.1)	118.1 (1.3)
O2b-TB-O3b	105.1 (7)	102.7 (8)	102.8 (1.2)	106.5 (1.2)
O2b-TB-O3b	109.8 (7)	107.5 (8)	106.0 (1.2)	109.6 (1.3)
O1b-TB-O3b	108.0 (8)	108.9 (8)	110.3 (1.3)	106.2 (1.5)
O1b-TB-O3b	107.0 (8)	108.7 (9)	106.9 (1.3)	104.1 (1.5)
O3b-TB-O3b	110.1 (7)	109.8 (8)	109.4 (1.2)	112.4 (1.1)
TA-O3a-TA	133.4 (1.5)	133.9 (1.5)	133.6 (2.2)	133.5 (2.3)
TB-O3b-TB	126.4 (9)	124.0 (1.1)	123.6 (1.6)	127.7 (1.6)
O3a-O3a-O3a	161.1 (7)	160.7 (8)	159.5 (1.0)	161.4 (8)
O3b-O3b-O3b	138.5 (6)	136.7 (7)	136.8 (9)	136.3 (9)

Table 12: (cont.) Variation of bond angles with pressure (P < 4 GPa) of natural orthopyroxene OPX2.

P (GPa)	4.03	4.93	6.01
O1a-M1-O1a	93.9 (1.4)	94.3 (1.4)	97.6 (1.9)
O1a-M1-O2a	89.3 (1.2)	88.4 (1.1)	90.5 (1.4)
O1a-M1-O1b	83.6 (1.1)	84.4 (1.1)	82.1 (1.3)
O1a-M1-O1b	82.4 (1.1)	81.3 (1.2)	80.5 (1.4)
O1a-M1-O2b	178.6 (8)	177.5 (8)	177.4 (1.9)
O1a-M1-O2a	95.0 (1.3)	94.2 (1.2)	94.3 (1.5)
O1a-M1-O1b	175.9 (8)	176.4 (9)	178.3 (1.4)
O1a-M1-O1b	84.5 (1.3)	83.7 (1.2)	83.2 (1.5)
O1a-M1-O2b	85.4 (1.1)	83.3 (1.1)	83.2 (1.3)
O2a-M1-O1b	88.4 (1.0)	89.2 (1.1)	87.4 (1.3)
O2a-M1-O1b	171.6 (1.4)	169.3 (1.2)	170.1 (1.7)
O2a-M1-O2b	92.0 (1.0)	92.6 (1.0)	92.0 (1.2)
O1b-M1-O1b	91.9 (1.5)	92.8 (1.4)	95.1 (1.7)
O1b-M1-O2b	97.0 (1.3)	98.0 (1.2)	97.0 (1.5)
O1b-M1-O2b	96.3 (1.3)	97.6 (1.2)	97.2 (1.5)
O1a-M2-O2b	81.9 (1.0)	81.4 (1.0)	80.6 (1.2)
O1a-M2-O2a	87.4 (1.0)	86.3 (1.0)	87.5 (1.2)
O1a-M2-O3a	109.8 (1.5)	111.0 (1.5)	110.3 (1.9)
O1a-M2-O1b	82.6 (1.1)	81.7 (1.1)	80.7 (1.4)
O1a-M2-O3b	172.0 (6)	170.2 (8)	171.2 (1.1)
O2b-M2-O2a	169.3 (1.0)	167.5 (1.0)	168.1 (1.2)
O2b-M2-O3a	111.7 (7)	111.8 (7)	112.5 (8)
O2b-M2-O1b	94.4 (1.0)	94.2 (1.0)	95.2 (1.2)
O2b-M2-O3b	103.1 (1.1)	101.8 (1.0)	102.1 (1.2)
O2b-M2-O3a	71.1 (8)	70.4 (8)	70.6 (9)
O2a-M2-O1b	85.2 (1.0)	86.4 (1.0)	83.8 (1.3)
O2a-M2-O3b	87.6 (9)	90.8 (8)	89.7 (1.2)
O3a-M2-O1b	152.2 (7)	152.1 (7)	151.2 (9)
O3a-M2-O3b	74.4 (1.0)	76.7 (1.0)	76.6 (1.3)
O1b-M2-O3b	90.8 (1.1)	88.8 (8)	90.7 (1.2)

Table 12: (cont.) Variation of bond angles with pressure (P > 4 GPa) of natural orthopyroxene OPX2.

P (GPa)	4.03	4.93	6.01
O2a-TA-O3a	99.5 (1.2)	101.8 (1.2)	99.8 (1.5)
O2a-TA-O1a	117.6 (1.3)	115.3 (1.3)	115.2 (1.8)
O2a-TA-O3a	112.4 (1.4)	114.6 (1.5)	112.0 (1.7)
O3a-TA-O1a	113.0 (1.4)	113.3 (1.4)	114.9 (1.9)
O3a-TA-O3a	103.0 (1.4)	103.6 (1.3)	102.9 (2.0)
O1a-TA-O3a	110.1 (1.4)	107.7 (1.5)	111.0 (1.9)
O2b-TB-O1b	118.9 (1.5)	119.8 (1.2)	118.7 (1.6)
O2b-TB-O3b	104.2 (1.2)	105.8 (1.2)	104.3 (1.6)
O2b-TB-O3b	108.8 (1.4)	110.0 (1.3)	108.2 (1.6)
O1b-TB-O3b	108.0 (1.4)	105.8 (1.4)	108.5 (1.9)
O1b-TB-O3b	107.2 (1.4)	103.9 (1.4)	106.2 (1.8)
O3b-TB-O3b	109.4 (1.3)	111.4 (1.1)	110.9 (1.6)
TA-O3a-TA	132.0 (2.4)	134.4 (2.4)	130.6 (3.3)
TB-O3b-TB	124.7 (1.7)	127.2 (1.5)	124.4 (2.1)
O3a-O3a-O3a	162.1 (1.1)	163.3 (1.0)	160.7 (1.2)
O3b-O3b-O3b	137.2 (1.1)	136.6 (9)	135.9 (1.1)

Table 12: (cont.) Variation of bond angles with pressure (P > 4 GPa) of natural orthopyroxene OPX2.

APPENDIX 2

POSITIONAL PARAMETERS, BOND LENGTHS AND ANGLES OF LOW- AND HIGH-PRESSURE CLINOFERROSILITES

		"A" chain	"B" chain
Fe 1	x	0.2512 (3)	
	y	0.6538 (2)	
	z	0.2262 (5)	
	B_{iso}	0.92 (5)	
Fe 2	x	0.2256 (3)	
	y	0.0145 (3)	
	z	0.2239 (5)	
	B_{iso}	1.13 (5)	
Si	x	0.0454 (5)	0.5531 (5)
	y	0.3384 (5)	0.8334 (5)
	z	0.2915 (9)	0.2431 (9)
	B_{iso}	0.64 (7)	0.77 (7)
O1	x	0.871 (1)	0.379 (1)
	y	0.338 (1)	0.837 (1)
	z	0.178 (2)	0.137 (2)
	B_{iso}	0.62 (17)	0.59 (16)
O2	x	0.125 (1)	0.633 (1)
	y	0.496 (1)	0.981 (1)
	z	0.335 (2)	0.387 (3)
	B_{iso}	0.70 (17)	1.17 (21)
O3	x	0.106 (1)	0.608 (1)
	y	0.266 (1)	0.702 (1)
	z	0.597 (3)	0.470 (2)
	B_{iso}	1.45 (21)	1.60 (22)

Table 1: Positional parameters of synthetic $FeSiO_3$ low-clinoferrosilite (space group $P2_1/c$) at ambient conditions.

	"A"-chain	"B"-chain
Fe1-O1	2.08 (1)	2.09 (1)
Fe1-O1	2.20 (1)	2.20 (1)
Fe1-O2	2.11 (1)	2.13 (1)
Fe2-O1	2.16 (1)	2.13 (1)
Fe2-O2	2.04 (1)	1.99 (1)
Fe2-O3	2.45 (1)	2.57 (1)
Si-O1	1.62 (1)	1.61 (1)
Si-O2	1.58 (1)	1.59 (1)
Si-O3	1.63 (1)	1.65 (1)
Si-O3	1.65 (1)	1.69 (1)
O1-O2	2.74 (1)	2.73 (1)
O1-O3	2.69 (1)	2.65 (1)
O1-O3	2.64 (2)	2.64 (1)
O2-O3	2.63 (1)	2.58 (1)
O2-O3	2.52 (2)	2.67 (1)
O3-O3	2.634 (2)	2.751 (7)

Table 2: Bond lengths of synthetic $FeSiO_3$ low-clinoferrosilite ($P2_1/c$) at ambient conditions.

	Bond angle (degrees)
O1a-M1-O1a	92.3 (4)
O1a-M1-O2a	94.8 (4)
O1a-M1-O1b	81.0 (4)
O1a-M1-O1b	85.5 (4)
O1a-M1-O2b	176.9 (4)
O1a-M1-O2a	96.0 (4)
O1a-M1-O1b	86.1 (4)
O1a-M1-O1b	176.0 (4)
O1a-M1-O2b	85.2 (4)
O2a-M1-O1b	175.4 (4)
O2a-M1-O1b	87.6 (4)
O2a-M1-O2b	87.3 (4)
O1b-M1-O1b	90.2 (4)
O1b-M1-O2b	97.0 (4)
O1b-M1-O2b	96.9 (4)
O1a-M2-O2a	89.5 (4)
O1a-M2-O3a	108.7 (4)
O1a-M2-O1b	83.5 (4)
O1a-M2-O2b	86.7 (4)
O1a-M2-O3b	170.2 (4)
O2a-M2-O3a	67.7 (4)
O2a-M2-O1b	88.1 (4)
O2a-M2-O2b	174.6 (4)
O2a-M2-O3b	81.7 (4)
O3a-M2-O1b	152.2 (4)
O3a-M2-O2b	110.0 (4)
O3a-M2-O3b	72.1 (4)
O1b-M2-O2b	95.3 (4)
O1b-M2-O3b	91.7 (4)
O2b-M2-O3b	102.4 (4)

Table 3: Bond angles of synthetic $FeSiO_3$ low-clinoferrsosilite at ambient conditions.

	Bond angle (degrees)
O2a-SiA-O3a	110.1 (6)
O2a-SiA-O1a	117.7 (6)
O2a-SiA-O3a	102.5 (6)
O3a-SiA-O1a	108.3 (6)
O3a-SiA-O3a	106.7 (4)
O1a-SiA-O3a	111.0 (5)
O1b-SiB-O2b	117.1 (6)
O1b-SiB-O3b	108.4 (5)
O1b-SiB-O3b	106.5 (5)
O2b-SiB-O3b	105.0 (6)
O2b-SiB-O3b	109.0 (6)
O3b-SiB-O3b	110.8 (4)
O3a-O3a-O3a	167.1 (9)
SiA-O3a-SiA	139.1 (8)
O3b-O3b-O3b	130.1 (7)
SiB-O3b-SiB	144.1 (9)

Table 3: (cont.) Bond angles of synthetic $FeSiO_3$ low-clinoferrsosilite at ambient conditions.

P (GPa)		1.87	2.83	3.49 ‡
Fe1	x	0.00	0.00	0.00
	y	0.9054 (6)	0.905 (1)	0.9117 (9)
	z	0.25	0.25	0.25
	B_{iso}	0.38 (6)	0.07 (7)†	0.13 (10)†
Fe2	x	0.00	0.00	0.00
	y	0.2721 (4)	0.2744 (9)	0.2769 (9)
	z	0.25	0.25	0.25
	B_{iso}	0.28 (7)	0.07 (7)†	0.13 (10)†
Si	x	0.2988 (4)	0.2985 (7)	0.298 (1)
	y	0.0882 (8)	0.087 (2)	0.085 (1)
	z	0.2225 (6)	0.220 (1)	0.220 (2)
	B_{iso}	0.05 (5)	0.11 (12)	0.05 (15)
O1	x	0.126 (1)	0.122 (2)	0.123 (2)
	y	0.095 (2)	0.093 (3)	0.096 (4)
	z	0.154 (2)	0.150 (3)	0.156 (4)
	B_{iso}	0.30 (11)*	0.09 (17)*	0.17 (26)*
O2	x	0.377 (1)	0.376 (2)	0.378 (2)
	y	0.233 (2)	0.234 (3)	0.235 (3)
	z	0.373 (2)	0.375 (3)	0.376 (4)
	B_{iso}	0.30 (11)*	0.09 (17)*	0.17 (26)*
O3	x	0.352 (1)	0.355 (2)	0.353 (3)
	y	0.053 (1)	0.050 (2)	0.053 (4)
	z	0.934 (2)	0.937 (3)	0.927 (4)
	B_{iso}	0.30 (11)*	0.09 (17)*	0.17 (26)*

Table 4: Variation of the positional parameters of C2/c $FeSiO_3$ clinoferrosilite with pressure ($P < 4$ GPa). Data collected from crystal #2 is marked by a double cross (‡), whilst the unmarked data was collected from crystal #1. Note that the isotropic temperature factors, B_{iso}, marked with an asterisk (*) or a cross (†) were constrained to be identical during the final structure refinement.

P (GPa)		4.28	4.94 ‡	6.51 ‡
Fe1	x	0.00	0.00	0.00
	y	0.907 (1)	0.9067 (7)	0.908 (1)
	z	0.25	0.25	0.25
	B_{iso}	0.13 (12)†	0.16 (8)†	0.03 (8)†
Fe2	x	0.00	0.00	0.00
	y	0.276 (1)	0.2743 (7)	0.274 (1)
	z	0.25	0.25	0.25
	B_{iso}	0.13 (12)†	0.16 (8)†	0.03 (8)†
Si	x	0.298 (2)	0.2996 (8)	0.303 (1)
	y	0.087 (2)	0.0893 (9)	0.089 (1)
	z	0.217 (2)	0.218 (1)	0.215 (2)
	B_{iso}	0.01 (21)	0.20 (10)	0.26 (13)
O1	x	0.122 (5)	0.130 (2)	0.135 (3)
	y	0.088 (4)	0.087 (3)	0.097 (3)
	z	0.160 (5)	0.155 (4)	0.156 (5)
	B_{iso}	0.06 (29)*	0.18 (17)*	0.65 (23)*
O2	x	0.379 (5)	0.386 (2)	0.382 (2)
	y	0.229 (3)	0.230 (2)	0.231 (3)
	z	0.372 (5)	0.370 (3)	0.365 (4)
	B_{iso}	0.06 (29)*	0.18 (17)*	0.65 (23)*
O3	x	0.353 (4)	0.353 (2)	0.356 (2)
	y	0.053 (3)	0.056 (2)	0.052 (3)
	z	0.929 (5)	0.934 (3)	0.937 (4)
	B_{iso}	0.06 (29)*	0.18 (17)*	0.65 (23)*

Table 4: (cont.) Variation of the positional parameters of C2/c $FeSiO_3$ clinoferrosilite with pressure (P > 4 GPa). Data collected from crystal #2 is marked by a double cross (‡), whilst the unmarked data was collected from crystal #1. Note that the isotropic temperature factors, B_{iso}, marked with an asterisk (*) or a cross (†) were constrained to be identical during the final structure refinement.

P (GPa)	1.87	2.83	3.49 ‡
M1-O1	2.20 (2)	2.16 (3)	2.14 (3)
M1-O2	2.109 (8)	2.08 (1)	2.11 (2)
M1-O3	2.12 (1)	2.11 (3)	2.13 (3)
M2-O1	2.12 (2)	2.12 (3)	2.11 (3)
M2-O2	1.990 (9)	1.98 (2)	1.97 (2)
M2-O3	2.43 (1)	2.41 (2)	2.36 (3)
Si-O1	1.61 (1)	1.64 (2)	1.63 (2)
Si-O2	1.60 (1)	1.62 (2)	1.65 (3)
Si-O3	1.67 (1)	1.65 (2)	1.68 (2)
Si-O3	1.66 (1)	1.65 (2)	1.62 (3)
O1-O1	2.78 (2)	2.71 (3)	2.71 (4)
O1-O2	2.70 (1)	2.74 (2)	2.73 (3)
O1-O3	2.66 (1)	2.69 (3)	2.70 (3)
O1-O3	-	2.69 (3)	2.66 (3)
O2-O3	2.70 (2)	2.71 (3)	2.74 (3)
O2-O3	2.60 (1)	2.58 (3)	2.61 (4)
O2-O3	2.678 (8)	2.65 (2)	2.65 (2)

Table 5: Variation of the bond lengths (< 2.8 Å) of C2/c $FeSiO_3$ clinoferrosilite with pressure (P < 4 GPa). Data collected from crystal #2 is marked by a double cross (‡), whilst the unmarked data was collected from crystal #1.

P (GPa)	4.28	4.94 ‡	6.51 ‡
M1-O1	2.09 (4)	2.14 (2)	2.21 (3)
M1-O1	2.12 (3)	2.12 (2)	2.14 (3)
M1-O2	2.12 (4)	2.07 (2)	2.07 (3)
M2-O1	2.14 (4)	2.18 (2)	2.14 (3)
M2-O2	1.98 (3)	1.96 (2)	2.00 (2)
M2-O3	2.36 (3)	2.36 (2)	2.36 (2)
Si-O1	1.63 (4)	1.57 (2)	1.55 (3)
Si-O2	1.59 (3)	1.60 (2)	1.57 (3)
Si-O3	1.66 (3)	1.62 (2)	1.59 (2)
Si-O3	1.64 (3)	1.69 (2)	1.66 (3)
O1-O2	2.74 (5)	2.75 (3)	2.63 (4)
O1-O3	2.70 (5)	2.59 (2)	2.57 (3)
O1-O3	2.63 (5)	2.60 (3)	2.61 (3)
O2-O3	2.67 (4)	2.62 (3)	2.61 (3)
O2-O3	2.55 (4)	2.60 (3)	2.55 (4)
O3-O3	2.66 (2)	2.68 (1)	2.64 (2)

Table 5: (cont.) Variation of the bond lengths (< 2.8 Å) of C2/c $FeSiO_3$ clinoferrosilite with pressure (P > 4 GPa). Data collected from crystal #2 is marked by a double cross (‡), whilst the unmarked data was collected from crystal #1.

P (GPa)	1.87	2.83	3.49 ‡
O1-M1-O1	78.5 (7)	77.6 (1.3)	78.7 (1.5)
O1-M1-O1	90.8 (5)	89.1 (8)	91.8 (1.0)
O1-M1-O1	89.3 (5)	90.2 (9)	91.2 (1.0)
O1-M1-O2	175.1 (5)	174.8 (1.0)	175.3 (9)
O1-M1-O2	97.9 (4)	97.8 (7)	98.6 (9)
O1-M1-O1	179.9 (9)	179.2 (1.7)	176.1 (1.8)
O1-M1-O2	92.5 (4)	93.5 (8)	92.0 (9)
O1-M1-O2	87.5 (5)	87.1 (8)	85.1 (9)
O2-M1-O2	85.9 (7)	86.8 (1.4)	84.4 (1.4)
O1-M2-O1	82.2 (7)	79.7 (1.4)	80.0 (1.5)
O1-M2-O2	87.3 (4)	87.2 (7)	86.0 (1.0)
O1-M2-O2	90.7 (4)	89.4 (8)	89.2 (9)
O1-M2-O3	89.6 (4)	91.3 (8)	90.3 (1.0)
O1-M2-O3	169.2 (4)	166.7 (8)	168.3 (1.0)
O2-M2-O2	177.4 (8)	175.5 (1.5)	173.7 (1.8)
O2-M2-O3	96.0 (4)	97.0 (8)	96.6 (9)
O2-M2-O3	85.7 (4)	85.9 (8)	87.4 (9)
O3-M2-O3	99.3 (6)	98.5 (1.1)	100.1 (1.5)
O1-Si-O2	114.6 (8)	114.2 (1.3)	113.0 (1.5)
O1-Si-O3	108.6 (5)	109.9 (9)	109.3 (1.3)
O1-Si-O3	108.4 (6)	109.6 (1.2)	109.9 (1.5)
O2-Si-O3	111.3 (6)	111.8 (1.1)	110.8 (1.5)
O2-Si-O3	106.3 (5)	104.0 (1.0)	105.7 (1.3)
O3-Si-O3	107.4 (5)	107.0 (1.0)	108.0 (1.1)
O3-O3-O3	138.4 (9)	140.4 (1.8)	138.1 (2.6)
Si-O3-Si	126.3 (7)	126.1 (1.3)	124.8 (1.9)

Table 6: Variation of the bond angles of C2/c $FeSiO_3$ clinoferrosilite with pressure ($P < 4$ GPa). Data collected from crystal #2 is marked by a double cross (‡), whilst the unmarked data was collected from crystal #1.

P (GPa)	4.28	4.94 ‡	6.51 ‡
O1-M1-O1	78.8 (2.1)	82.2 (1.1)	81.5 (1.5)
O1-M1-O1	89.6 (1.5)	90.9 (8)	94.2 (1.1)
O1-M1-O1	88.7 (1.4)	86.9 (8)	87.4 (1.1)
O1-M1-O2	175.7 (1.3)	175.6 (7)	176.1 (1.0)
O1-M1-O2	99.1 (1.3)	98.6 (7)	98.6 (1.0)
O1-M1-O1	177.7 (1.8)	177.1 (1.3)	178.0 (1.8)
O1-M1-O2	94.1 (1.3)	93.5 (7)	89.7 (1.0)
O1-M1-O2	87.6 (1.2)	88.7 (8)	88.8 (1.1)
O2-M1-O2	83.3 (2.0)	80.9 (1.0)	81.5 (1.2)
O1-M2-O1	76.9 (2.1)	80.3 (1.0)	84.9 (1.6)
O1-M2-O2	87.2 (1.3)	88.4 (8)	87.1 (1.0)
O1-M2-O2	90.7 (1.2)	89.8 (8)	90.9 (1.0)
O1-M2-O3	92.1 (1.2)	90.0 (6)	88.8 (9)
O1-M2-O3	166.9 (1.0)	167.5 (7)	169.0 (9)
O2-M2-O2	177.3 (1.8)	177.7 (1.3)	177.3 (1.6)
O2-M2-O3	96.0 (1.4)	97.8 (7)	97.8 (8)
O2-M2-O3	85.8 (1.4)	83.7 (7)	84.0 (8)
O3-M2-O3	99.7 (1.5)	100.7 (9)	98.8 (1.2)
O1-Si-O2	116.5 (2.3)	120.1 (1.0)	115.0 (1.5)
O1-Si-O3	110.6 (2.0)	108.7 (9)	109.8 (1.3)
O1-Si-O3	107.0 (2.0)	105.8 (1.1)	108.0 (1.4)
O2-Si-O3	110.7 (2.1)	109.5 (1.0)	111.7 (1.4)
O2-Si-O3	103.9 (1.8)	104.2 (9)	104.1 (1.3)
O3-Si-O3	107.5 (1.8)	107.9 (7)	107.9 (9)
O3-O3-O3	138.3 (1.9)	136.1 (1.5)	139.1 (2.3)
Si-O3-Si	125.1 (2.4)	126.0 (1.2)	128.1 (1.5)

Table 6: (cont.) Variation of the bond angles of C2/c $FeSiO_3$ clinoferrosilite with pressure (P > 4 GPa). Data collected from crystal #2 is marked by a double cross (‡), whilst the unmarked data was collected from crystal #1.

APPENDIX 3

POSITIONAL PARAMETERS, BOND LENGTHS AND ANGLES OF THE FICTIVE Hd-LIKE $FeSiO_3$ CLINOFERROSILITE

	x	y	z
Fe1	0.0	0.901	0.25
Fe2	0.0	0.263	0.25
Si	0.296	0.085	0.252
O1	0.124	0.090	0.159
O2	0.375	0.240	0.362
O3	0.359	0.031	0.045

Table 1: Calculated positional parameters for the Hd-like C2/c phase of $FeSiO_3$ clinoferrosilite.

Bond	Bond length (Å)
Fe1-O1	2.07 (1)
Fe1-O1	2.22 (1)
Fe1-O2	2.105 (9)
Fe2-O1	2.10 (1)
Fe2-O2	2.005 (5)
Fe2-O3	2.91 (3)
7/8th Fe2-O3	3.00 (3)
Si-O1	1.625 (5)
Si-O2	1.605 (1)
Si-O3	1.64 (1)
Si-O3	1.641 (1)

Table 2: Calculated bond lengths for the fictive Hd-like C2/c phase of $FeSiO_3$ clinoferrosilite.

Bond	Bond length (Å)
O1-O2	2.75
O1-O3	2.65
O1-O3	2.66
O2-O3	2.59
O2-O3	2.65
O3-O3	2.674

Table 2: (cont.) Calculated bond lengths for the fictive Hd-like C2/c phase of $FeSiO_3$ clinoferrosilite. The reported estimated standard deviations of some of the above bond lengths represent the differences between the results for the structure calculations performed in two independent ways (see Chapter 6)

	Bond angle (degrees)
O1-M1-O1	85.52
O1-M1-O1	80.41
O1-M1-O1	91.27
O1-M1-O2	174.83
O1-M1-O2	94.85
O1-M1-O1	175.79
O1-M1-O2	96.71
O1-M1-O2	86.28
O2-M1-O2	89.96

Table 3: Calculated bond angles for the fictive Hd-like C2/c phase of $FeSiO_3$ clinoferrosilite. The reported estimated standard deviations of some of the above bond angles represent the differences between the results for the structure calculations performed in two independent ways (see Chapter 6)

	Bond angle (degrees)
O1-M2-O1	85.75
O1-M2-O2	92.62
O1-M2-O2	88.91
O1-M2-O3	137.88
O1-M2-O3	89.24
O1-M2-O3	119.22
O1-M2-O3	167.95
O2-M2-O2	177.92
O2-M2-O3	119.10
O2-M2-O3	102.28
O2-M2-O3	58.88
O2-M2-O3	76.32
O3-M2-O3	59.09
O3-M2-O3	65.92
O3-M2-O3	53.79
O3-M2-O3	97.68
O1-Si-O2	116.58
O1-Si-O3	108.48
O1-Si-O3	108.14
O2-Si-O3	109.09
O2-Si-O3	105.56
O3-Si-O3	108.74
Si-O3-Si	136.7 (5)
O3-O3-O3	156.3 (4)

Table 3: Calculated bond angles for the fictive Hd-like C2/c phase of $FeSiO_3$ clinoferrosilite. The reported estimated standard deviations of some of the above bond angles represent the differences between the results for the structure calculations performed in two independent ways (see Chapter 6).